Contents

Chapter 1
Introduction

Particle physics aims at the study of the fundamental constituents of matter and of their interactions. In order to probe a scale as small as the dimensions of the constituents of the nucleon, it is necessary to produce interactions between particles at the highest possible energy and to study the dynamics of the interaction. This requires high energy particle accelerators as well as giant detectors.

Our present knowledge in high energy physics is based upon the standard model, a set of theories which provide a successful description of the phenomenology of high energy particle physics at the present available energies. The quark model postulates that matter is made up of six quarks, six leptons and their antiparticles. The interactions between these particles are described by means of gauge theories in which these interactions are mediated by the exchange of integer spin particles, the gauge bosons. These theories are: the electroweak theory of Glashow-Salam-Weinberg unifying the weak and electromagnetic interactions and the Quantum ChromoDynamics (QCD) describing the strong interactions. Gravitation is not introduced in the standard model. This model has been extremely successful in describing particles and their interactions and no contradictions with the experimental data have been found so far. However in these gauge theories the particles are treated as massless, which is clearly not the case in reality. The Higgs mechanism was proposed to generate the particle masses which implies the existence of a new particle, not yet discovered, the Higgs boson. In addition, there are arguments suggesting that new physics might be discovered at very high collision energies. Extensions of the standard model have been proposed such as the Minimal Supersymmetric Standard Model (MSSM) predicting the existence of new particles, supersymmetric particles. There are other unanswered questions:*e.g* do all interactions unify at very high energies, and how can we then describe the unified force?

The Large Hadron Collider (LHC) project has been proposed to answer or to shed light on the above questions. The LHC is a proton-proton accelerator which will be installed in the existing LEP tunnel at CERN, the European laboratory for particle physics, in Geneva. Since the proton constituents carry only a fraction of the proton momentum, the proton beams will be accelerated up to 7 TeV in order to reach about 1 TeV in the centre of mass at the constituent scale.

The cross sections of physics channels of interest at the LHC are very small compared to the total proton-proton cross section and hence the LHC must operate with the highest possible luminosity, 10^{34} Hz/cm^2, and with a very short time between bunches of accelerated protons, 25 ns. This leads to about 10^9 interactions per second and to high radiation levels putting stringent constraints on the detectors to be used.

The Compact Muon Solenoid (CMS) experiment is one of the two general purpose experiments designed to run at the highest LHC luminosity. It consists of a magnet system, providing a uniform 4 Tesla magnetic field inside a central volume containing a tracker system, an electromagnetic and a hadronic calorimeter. The magnet is surrounded by a muon detection system interleaved in the magnet return yoke.

The CMS tracker will be equipped with three types of detectors: pixel detectors, silicon strip counters and microstrip gas counters. Five Belgian research groups (UCL, UIA, ULB, UMH and VUB) participate to the design and the construction of the CMS endcap MSGC tracker, together with groups from France, Germany, Russia and more recently Switzerland.

The present work is a contribution to the study and optimization of microstrip gas counters (MSGC) for the CMS tracker, mainly in the endcap parts. Microstrip gas counters are proportional gas counters for which the electrode pattern is made with microelectronics technology. This permits small inter-anode distances, typically 200 μm, allowing the construction of detectors with the small granularity needed to cope with the high track density at the LHC. MSGC's can also sustain higher counting rates than the MWPC and have a faster response. Their low cost, with respect to that of solid state detectors, makes them attractive for large detection surfaces. Thus, in CMS, the outermost part of the tracker system is foreseen to be equipped with MSGC's.

In order to use the MSGC in a high rate experiment such as CMS, an extensive research program to optimize this device has been carried out during the last years, in particular by the RD28 collaboration and by the CMS collaboration. Many topics have been covered: improvement of its high rate capability and long term stability by an adequate choice of the construction materials; choice of the operating gas and study of its behaviour in a magnetic field; study of its response to heavily ionizing particles (HIP's) and neutrons,etc. However at the beginning of this work several problems had still to be solved. Among them were: the optimization of the choice of the gas mixture taking into account the requirements for CMS and the behaviour of MSGC's under a high rate of hadrons leading to HIP's. In addition, the consequences of the specific design of the MSGC endcap tracker on the MSGC response had to be carefully studied. These subjects constitute the main topics studied in this thesis.

Before the start of the gas study for CMS in Brussels, several candidates were present: DME/CO_2 was shown to have a good spatial resolution, to be efficient and fast enough for operation at the LHC, Ar/DME was shown to reach full efficiency at a lower cathode strip voltage, which is safer, and was producing no ageing of the counter. Ne/DME mixtures were found to lead to very high gas gains also at a low cathode strip voltage but the minimum ionizing particle detection efficiency in the 3 mm gas gap of the counter was questioned, due to the low primary ionization density of neon. The detection efficiency in several Ne/DME gas mixtures was first measured in a cosmic rays hodoscope in Brussels; they were shown to be adequate for CMS. However the drift velocity of these gas mixtures needed to be measured to check if they were fast enough for operation at the LHC. Due to the high price of neon, other mixtures were tried either by replacing the neon by argon or helium or by adding amounts of CO_2 to the binary mixtures. Adding CO_2 was expected to increase the drift velocity. We have measured the detection efficiency, the spatial resolution and the signal to noise ratio for all the new mixtures in the cosmic rays hodoscope in Brussels. Using a set of simulation programs, we have computed the drift velocity and the transverse diffusion coefficient in these mixtures and compared the results to the measurements done by the MSGC group of the university of Antwerp. This analysis leads to the choice of a gas suited for CMS. The implication of this choice on the Lorentz angle in the barrel part of CMS and on the spatial resolution is also discussed.

One of the characteristics of gaseous detectors is the appearance of discharges if the gas amplification is pushed beyond a certain value. This is not a problem in counters with robust electrodes like MWPC's, provided the discharge rate is kept low enough to avoid a significant dead time. In MSGC's, these discharges might damage the strip pattern since the strips are thin, typically 7 μm wide and 1-2 μm thick. Even a low rate of discharges can rapidly destroy the counter. A scheme that was proposed to suppress the discharges or to limit the subsequent

damage is the so called "advanced passivation" technique, shown to be efficient in laboratory tests of MSGC's with α-particles. In this technique the edges of the MSGC cathode strips are coated by a 4 μm wide dielectric layer. However its efficiency had to be proven in a high intensity beam of hadrons. Within the CMS collaboration, we have carried out a test of five MSGC's, in such a beam during two weeks. We have investigated the uniformity of the response with the time of exposure to the beam and scrutinized the possible damages to strips by discharges.

The last part of this work consists in a study of some particular aspects of MSGC operation related to the design of the CMS MSGC endcap tracker. In this design the counters have a trapezoidal shape with a varying anode pitch, an approach never attempted before. In order to obtain a uniform response along the strips, a rule was proposed by NIKHEF to vary the cathode width and the anode-cathode distance with the anode pitch . We have studied the limits of validity of this rule together with the stability of operation of such wedge shaped counters. In addition, in order to minimize the amount of dead space, the Belgian groups have proposed to place several trapezoidal MSGC counters side by side in a module with a single gas volume. The stability of operation, the uniformity of the response of these multisubstrates modules and the detection efficiency between adjacent counters were still to be studied. These questions have been addressed using data taken with dedicated prototypes. First, dedicated prototypes were tested in the cosmic rays hodoscope. Then the groups participating to the MSGC endcap tracker built one full scale MSGC module each, with a total of 38 trapezoidal MSGC counters. Together they were exposed to a low intensity muon beam at CERN and read out. The analysis of the experimental data was complemented by a simulation.

The LHC project and the CMS experiment are presented in chapter 2. Chapter 3 introduces fundamental principles of operation of gaseous detectors. In chapter 4, the MSGC's working principles are discussed and the design of the forward MSGC tracker is described. In chapter 5, we present the studies we have performed on MSGC's for operation at the LHC: the search for a gas mixture satisfying all CMS requirements and the study of the behaviour of advanced passivated counters in the presence of heavily ionizing particles. In chapter 6, the particular aspects of MSGC operation related to the endcap tracker design, the wedged shape and the contiguous counters, are developed. Finally, conclusions on this work are summarized in chapter 7.

Chapter 2
The future CMS experiment at the LHC

Introduction

This work is a contribution to the study of the forward Micro Strip Gas Counter (MSGC) tracker of the future Compact Muon Solenoid (CMS) experiment at the Large Hadron Collider (LHC). The aim of this chapter is to introduce the LHC project and to describe the CMS experiment. A brief description of the LHC machine is given in section 2.1. Section 2.2 gives an overview of the physics that will be addressed at the LHC. The various components of the CMS experiment are outlined in section 2.3, with some emphasis on the tracker system.

2.1 The Large Hadron Collider

The Large Hadron Collider (LHC) [1] is a machine in which bunches of protons will be accelerated before entering in frontal collision. Since in proton-proton collisions the partons carry only a fraction of the total proton momentum, the proton-proton centre of mass energy must be high enough to produce quark and gluon interactions at the TeV energy scale. The proton beams are thus accelerated up to an energy of 7 TeV per beam.

The LHC will be installed in the existing 27 km long tunnel of the Large Electron-Positron (LEP) collider at CERN, in Geneva. It will use the available CERN injection infrastructure system as shown in figure 2.1. A small linear accelerator and the Proton Synchrotron (PS) booster give the proton beams an energy of 1.4 GeV. The PS will accelerate the beams up to 25 GeV and will inject them to the Super Proton Synchrotron (SPS) where they are accelerated to an energy of 450 GeV. The beams are then injected in the LHC ring for the final acceleration up to an energy of 7 TeV per beam. In the LHC ring, the two proton beams will circulate in opposite directions, in two separate vacuum tubes; they consist in bunches of protons every 25 ns. They will be guided by a magnetic field of 8.4 Tesla created by superconducting coils cooled at 1.9 K by superfluid helium. The beams intersect in four experimental interaction regions.

The production cross sections of physics channels of interest are very small relative to the total proton-proton cross section. Therefore it is necessary to observe a large number of collisions to see a significant number of such rare interesting events. The rate of occurrence R of a certain process is related to its cross section σ by: $R{=}\mathcal{L}\sigma$, where $\mathcal{L}$ is the collider luminosity given by:

$$\mathcal{L} = \frac{1}{4\pi}\frac{N_1 N_2 f}{\sigma_x \sigma_y} \quad (cm^{-2}s^{-1}), \tag{2.1}$$

where N_1 and N_2 are the numbers of particles per bunch in the two colliding beams, f is the bunch crossing frequency, and σ_x and σ_y are the RMS of the particle distribution in the bunches, in the x and y directions, transverse to the beam. The design parameters of the LHC

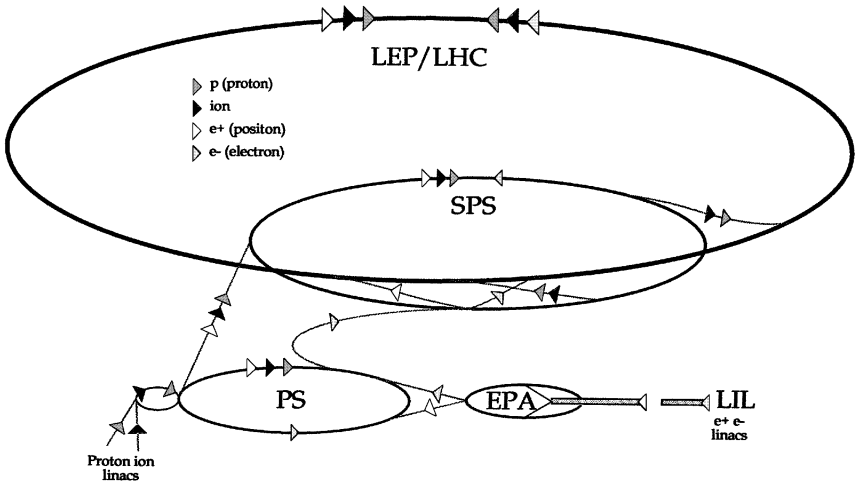

Figure 2.1: *Layout of the CERN accelerator network used as injection chain for the LHC.*

at nominal luminosity are given in table 2.1. However the LHC will not start with its nominal luminosity, but a low luminosity start-up phase will precede the high luminosity operation. It is suggested that the luminosity during the first year will be 10 % of the nominal value and will rise to 33 % in the second year and 67 % in the third year. From the fourth year onwards the LHC is assumed to operate at its nominal luminosity.

Luminosity	10^{34} cm^{-2} s^{-1}
Number of protons per bunch	1.05×10^{11}
Frequency	40 MHz
Beam energy	7 TeV
RMS bunch width	15 μm
Bunch crossing interval	25 ns
Interaction rate	$\simeq10^{9}$Hz

Table 2.1: *Standard LHC parameters.*

Two general purpose detectors will be designed to study the Higgs boson and possible extensions of the Standard Model, ATLAS and CMS. Figure 2.2 shows the overall layout of the LHC machine and its detectors. The two other intersections will be equipped with dedicated detectors, ALICE, conceived for heavy ion collisions study, and LHC-B devoted to the B-physics.

2.2 Physics potential at LHC

The LHC will provide a rich program of physics. In this section we present briefly some selected topics of the LHC physics program of the ATLAS and CMS experiments.

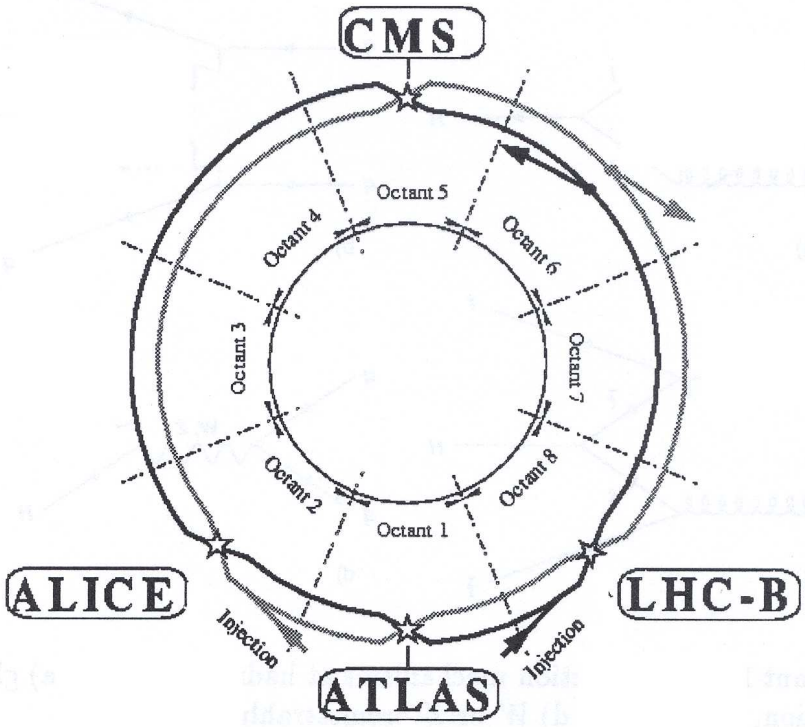

Figure 2.2: *Schematic layout of the LHC and the location of the experiments.*

2.2.1 Search for the Standard Model Higgs

Elementary particles and their interactions are described by the standard model, a theoretical framework combining the quark-parton model of particles, the Glashow-Salam-Weinberg model of electroweak interactions and the quantum chromodynamics describing the strong interactions. The predictions of the standard model have been tested in a large number of experiments and, so far, no confirmed contradictions have been reported. Recently, another experimental evidence supporting the standard model came from the discovery of the last missing quark predicted by the standard model, the top quark [2, 3].

In spite of the great phenomenological success of the standard model, some problems have still to be solved, mainly the gauge symmetry breaking in the electroweak sector of the model. Indeed, the standard model is a set of gauge theories in which particles have no mass. If this works well for the photon, it is no longer the case for massive particles as the weak interaction exchange bosons $W^{\pm}$ and Z^0 which have a mass of 80 and 91 GeV/c^2 respectively. Introducing mass terms breaks the gauge invariance symmetry of the electroweak Lagrangian. In order to have still a gauge invariant theory, a theoretical solution has been proposed independently by F. Englert and R. Brout [4] and by P. Higgs [5]. They introduced a new field, the Higgs field, which gives rise to a mass term for $W^{\pm}$ and Z^0 via an interaction with the Higgs field, but leaves the photon massless. A new massive particle of spin 0 called Higgs boson is associated to this new field. Fermion masses can also be generated by introducing a coupling term between fermions and the Higgs field. Up to now, there is no experimental evidence for the existence of this particle. Therefore it is one of the most important tasks to be performed within the LHC project.

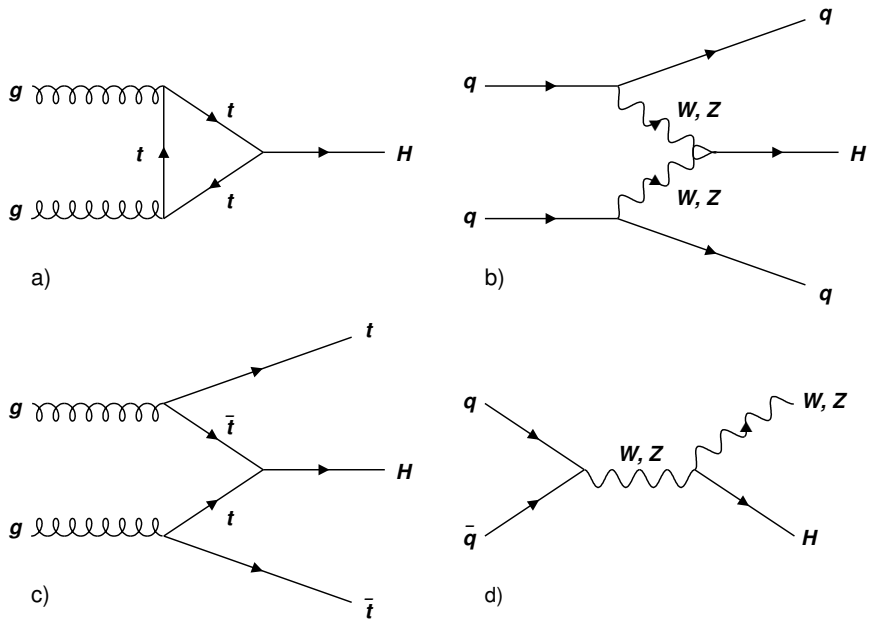

Figure 2.3: *Dominant Higgs production diagrams at the LHC: a) gluon-gluon fusion, b) WW or ZZ fusion, c) $t\bar{t}$ fusion, d) W or Z bremsstrahlung.*

Higgs decay mode	Mass interval
H$\rightarrow \gamma\gamma$	95 or 110 GeV/c$^2 \leq m_H \leq$ 150 GeV/c^2
H$\rightarrow ZZ^* \rightarrow 4l^{\pm}$	120 GeV/c$^2 \leq m_H \leq$ 180 GeV/c^2
H$\rightarrow ZZ \rightarrow 4l^{\pm}$	180 GeV/c$^2 \leq m_H \leq$ 650 GeV/c^2
H$\rightarrow ZZ \rightarrow 2l^{\pm}2\nu$	500 GeV/c$^2 \leq m_H \leq$ 1 TeV/c^2
H$\rightarrow W^+W^- \rightarrow l\nu jj$ H$\rightarrow ZZ \rightarrow 2l^{\pm}2\nu$	$m_H \sim$ 1TeV/c^2

Table 2.2: *The most promising decay channels for Higgs discovery at the LHC with the corresponding mass range. l denotes an electron or a muon, ν a neutrino and j a jet.*

The mass m_H of the Higgs boson can not be predicted accurately from present experimental data. However, the consistency with the standard model requires an upper limit of 1 TeV/c^2. Direct searches for the Higgs boson in LEP experiments exclude the mass region below $m_H \simeq$ 95 GeV/c^2 (see for example [7]). At the end of the data taking at LEP, this limit will be pushed to 110 GeV/c^2 if the Higgs is not discovered. Because it is heavy and its coupling to elementary particles is proportional to their mass, the Higgs essentially does not couple to light particles. The dominant Higgs production will thus involve either W$^{\pm}$ or Z^0 bosons, or top quarks(t) produced in quark-quark(qq) or gluons-gluons(gg) interactions. The diagrams of the dominant production mechanisms are shown in figure 2.3. The Higgs production expected at the LHC ranges from 10^6 to 10^4 events per year, at the nominal luminosity, for Higgs masses between 0.1 and 1 TeV/c^2. Detection of the Higgs boson at the LHC will be made on the basis of its decay modes. However, not all the decay modes provide experimentally distinguishable signature, and the decay channels that provide the best experimental signature have very small branching ratios, of the order of 10^{-3}. The most promising decay channels of the Higgs boson

are summarized in table 2.2 with the corresponding Higgs mass range. In the mass range above the lower limit put by LEP and below 150 GeV/c^2, the signature will be the decay into a photon pair giving a signal of two isolated electromagnetic showers pointing to the vertex. In the mass range $120 \leq m_H \leq 2m_Z$, an important signal is the channel H$\rightarrow ZZ^* \rightarrow 4l^{\pm}$, where l denotes an electron or a muon and Z^* a virtual Z boson since the Higgs mass is below $2m_Z$. With masses larger than $2m_Z$, the decays into real Z's can be exploited. However the Higgs production cross section decreases rapidly at large values of m_H and therefore the four lepton mode of H$\rightarrow ZZ$ at high masses ($m_H > 600$ GeV/c^2) becomes difficult because of the lack of statistics. Other more frequent decay modes of Z and W have to be considered. These are the processes H$\rightarrow W^+W^- \rightarrow l\nu jj$ and H$\rightarrow ZZ \rightarrow 2l^{\pm}2\nu$, where ν is a neutrino and j a jet of particles.

2.2.2 Heavy flavour quark physics

At LHC large amounts of heavy quarks (beauty and top) will be produced even at the low luminosity foreseen at the beginning of the LHC operation.

A rich field of top quark physics and detailed studies of the properties of the top will be made, including the measurements of its mass through different channels and the branching ratios for various decay modes. This will enable more precise calculations of the cross sections for various processes.

In B physics, the measurement of CP violation in the (B^0-$\bar{B}^0$) system will be of particular interest. C and P are transformations of the particle wave function under the exchange of particles by their antiparticles (Charge conjugation) and by the reversal of the space coordinates (Parity) respectively. CP violation in weak interactions has been observed, thirty years ago, in the decay of neutral kaons. Analogously, it is expected to occur in the B-system (see for example [6])[1]. Other topics include rare B decay modes and general studies of systems containing b-quarks. B physics study will be the main topic at the low luminosity start-up phase of the LHC.

2.2.3 Beyond the Standard Model

Although the standard model is extremely successful in describing the phenomenology of particle physics at the energies achieved in current experiments, there are arguments that new physics may be discovered at higher energies. Thus extensions of the standard model exist that are consistent with the present data, and predict the existence of new particles at masses below 1 TeV. Among these extensions is the Minimal Supersymmetric Standard model (MSSM) which introduces a new symmetry between fermions and bosons. Each particle should have a supersymmetric partner, with a spin differing by 1/2. This model has several attractive features, as it provides a mean of incorporating gravity and predicts the unification of all forces at very high energies. In this model, there are five physical Higgs bosons, namely two charged scalars (H$^+$,H$^-$), a light (h) and a heavier neutral (H^0) scalar particle, and a neutral pseudo scalar particle (A).

According to the predictions of the MSSM, the lightest supersymmetric Higgs, h, should have a mass below 130 GeV/c^2 [7]. Thus the absence of a fundamental scalar particle below this mass limit is often considered to be the proof of the failure of the MSSM. In addition, to prove the MSSM, physicists are forced to discover at least one supersymmetric particle. A review of the direct search for supersymmetric particles to be done at LHC can be found in reference [9].

[1] There are recent indications of CP violation in the (B^0-$\bar{B}^0$) system [8].

2.3 The CMS experiment

The Compact Muon Solenoid (CMS) detector is designed to run at the highest LHC luminosity but is also adapted for studies at the initial lower luminosities. The physics objectives at LHC together with the harsh experimental environment dictate the design of the experiment. The CMS detector must have [10]:

- a very good muon identification and momentum measurement;
- a high resolution electromagnetic calorimeter for the energy measurement of photons and electrons;
- an inner tracking system capable of measuring high p_t charged tracks with very good momentum resolution;
- a large detector acceptance;
- fast and radiation hard detectors.

The CMS detector is composed of several subdetectors that can be classified in three main categories: the tracking system, the calorimeters and the muon chambers. To achieve the above requirements, CMS has chosen to have a compact detector with the tracker and the calorimeters inside a solenoidal producing a high magnetic field of 4 T. The high field will enable a good momentum measurement in the tracker, reduce the charged particles in the electromagnetic calorimeter and enable a clean environment for the muon detection.

Due to the huge number of events 10^9 Hz that will be produced at the LHC, online data selection called "triggering", is needed in order to reduce this number to only 100 Hz. In CMS, this will be achieved with a multilevel trigger system selecting candidate events with a clear signature (high p_t leptons and photons, missing energy,..).

Figure C.1 shows a three dimensional schematic representation of the CMS detector[1]. The overall dimensions of the detector are 21 m in length and 15 m in diameter. The total weight amounts to 14500 Tons. It has an almost complete solid angle coverage and is composed of three regions: a central "barrel" region and two identical "endcaps" regions, placed forward and backward, on each side of the barrel.

2.3.1 Magnet

The magnet plays an important role in the CMS detector. A long superconducting solenoid of 13 m length and an inner radius of 2.95 m, with a uniform magnetic field of 4 T was chosen. The inner radius is large enough to accommodate the tracker, the electromagnetic and hadronic calorimeters. The magnetic flux is returned via a 1.5 m thick saturated iron yoke which is instrumented with the muon chambers. The magnet is used as the principal support structure for all the detectors.

2.3.2 The muon subdetector

The signature of several interesting processes at LHC involves muons. The muon system [11] is placed in the outermost part of the detector, outside the solenoid[2]. Indeed, contrary to hadrons,

[1] Figures labelled C are colour figures and can be found in appendix C at the end of this manuscript.

[2] Muons are subject to only weak and electromagnetic interactions. In addition, due to their mass they are less sensitive to bremsstrahlung than electrons.

muons have no strong interactions; they can thus traverse all the material inside the coil with almost no deviation of their trajectory. The detection of a particle in the muon system, with a position in agreement with the extrapolation of a track from the central tracker, allows to identify it as a muon. The muon system should measure the muon momentum with an accuracy between 8 and 40 % for muons of transverse momentum p_t between 10 and 10^3 GeV/c. The muon detection system consists in four stations interleaved with the iron return yoke of the magnet, and a pseudorapidity (see appendix A) coverage from 0 to 2.4. In the barrel region, drift tubes are used, providing a 250 μm spatial resolution in the (R,ϕ) plane and less than 1 mrad angular resolution. In the endcap regions, use is made of cathode strip chambers. They measure the $R\phi$ coordinate with an accuracy of 75 μm and are able to assign a bunch crossing to the track detected. Since the muon subdetector participate to the CMS trigger system, this requires detectors capable of reacting in less than 25 ns, the time between two bunch crossings. To achieve this, there are resistive plate chambers both in the barrel and in the endcaps. These chambers have an excellent time resolution of 3 ns.

2.3.3 The electromagnetic calorimeter

The major task of the electromagnetic calorimeter (ECAL) is to absorb the energy of electrons and photons and to give a signal proportional to the initial energy [12]. To be able to discover a low mass Higgs decaying into two photons, the ECAL must have the best possible energy resolution. In addition, some cascade decays of supersymmetric particles produce several electrons. There also, the energy resolution must be excellent which can only be beaten by an homogeneous crystal calorimeter. Indeed the energy resolution of an electromagnetic calorimeter can be parametrized as:

$$(\frac{\sigma_E}{E})^2 = (\frac{a}{\sqrt{E}})^2 + (\frac{\sigma_n}{E})^2 + c^2 \qquad (2.2)$$

where a, σ_n and c are constant. $a/\sqrt{E}$ is a stochastic term corresponding to statistical fluctuations in the number of primary processes that generate the signal, σ_n/E is a noise term including mainly the electronic noise and the pile-up, and c is a constant term accounting for other contributions as the calorimeter non uniformity. For an homogeneous electromagnetic calorimeter, the stochastic term is of the order of $2\%/\sqrt{E}$, compared to 10 $\%/\sqrt{E}$ in the case of a sampling calorimeter. For the CMS barrel ECAL, σ_n is estimated to be 210 MeV and c is 0.55 %.

A response within a single bunch crossing interval is also required since the ECAL information will be needed for trigger purposes.

The ECAL is divided into a central part covering the pseudorapidity range $|\eta| < 1.48$ and a forward region covering the range $1.48 < |\eta| < 3$.

Lead tungstate ($PbWO_4$) has been chosen as an active material for the CMS ECAL since it has shorter radiation length and smaller Molière radius than those of commonly used crystals. Its short radiation length (0.89 cm) means that the thickness of material required to contain the shower longitudinally is small (23 cm). This enables the whole calorimetry to be placed inside the superconducting coil, leading to a compact detector. The small Molière radius (2.2 cm) results in fewer crystals being required to contain the shower laterally, improving the shower isolation efficiency, reducing pile-up and leading to a spatial resolution of $\sqrt{(2.02\sqrt{E})^2 + (0.29)^2}$ mm, which is needed for the angular resolution. More than 60 % of the crystal light is emitted within 15 ns matching thus the bunch crossing time of 25 ns.

2.3.4 The hadron calorimeter

The signatures for the discovery of a high mass Higgs include jets and missing energy. In addition, most of the supersymmetric signatures include missing energy or b-jets. The task of the CMS hadron calorimeter (HCAL) [13] is to measure quark and gluon jet directions and energies by measuring the energy and the location of the hadronic showers produced by the particles in jets. The neutrinos are to be identified by the missing energy which is reconstructed as the difference between the centre of mass energy and the total energy of all the other particles emitted. This is done by measuring all energy deposited in the calorimeter system, combining both the ECAL and the HCAL systems. This implies an angular acceptance near to 4π. The HCAL also provides a trigger signal for jets and missing energy. It is a sampling calorimeter with active plastic scintillator layers interleaved with copper layers. It is placed inside the solenoidal magnet and covers the pseudorapidity range up to 3. A separate forward calorimeter extends the pseudorapidity coverage from 3 to 5. Beam test results showed that the HCAL resolution is $(100\%/\sqrt{E})^2+(4.3\%)^2$ and simulation studies indicated that it is adequate.

2.3.5 The CMS tracker

The central tracker is described in some details, since this work is a contribution to the study of this part of the expriment.

Placed close to the interaction region, the CMS central tracker [14] will need to cope with an enormeous track density and survive in a very hostile radiation environment. This, together with the CMS physics goals, puts stringent demands on the performances of the tracker detector elements.

2.3.5.1 Radiation environment

The greatest challenges in the design of the CMS tracker is the radiation hardness of the detector elements and their electronics. The radiation within the tracker is characterized by two distinct components: a direct particle flux emerging from the interaction region, and neutrons produced in nuclear interactions in the surrounding material.

Figure 2.4 shows the expected radiation dose (a), neutron (b) and charged hadron (c) fluences in the tracker as a function of z, the distance from the interaction point along the beam, at various distances R from the beam pipe, for an integrated luminosity corresponding to ten years of LHC operation. The charged particle flux is almost independent of z coordinate and behaves roughly as $1/R^2$. The neutron fluence rises when approaching the endcap due to the contribution of the ECAL endcap. As an illustration, this figure shows that the average rate of charged hadrons at a radius of 75 cm from the interaction point is 2×10^3 Hz/mm^2.

2.3.5.2 Momentum resolution of charged particles

The task of the central tracker system is to measure the momentum and direction of charged particles as well as their production vertices.

In a uniform magnetic field B, charged particles have a helicoidal trajectory around the field axis. The radius of curvature R_c of the particle track is related to the component of the momentum in the plane transverse to the beam, p_t, by:

$$p_t[GeV/c] = 0.3B[T]R_c[m] \tag{2.3}$$

The transverse momentum can be determined by measuring the coordinates (x,y) or (R,ϕ) of a set of points along the particle track in the plane transverse to the magnetic field, and by

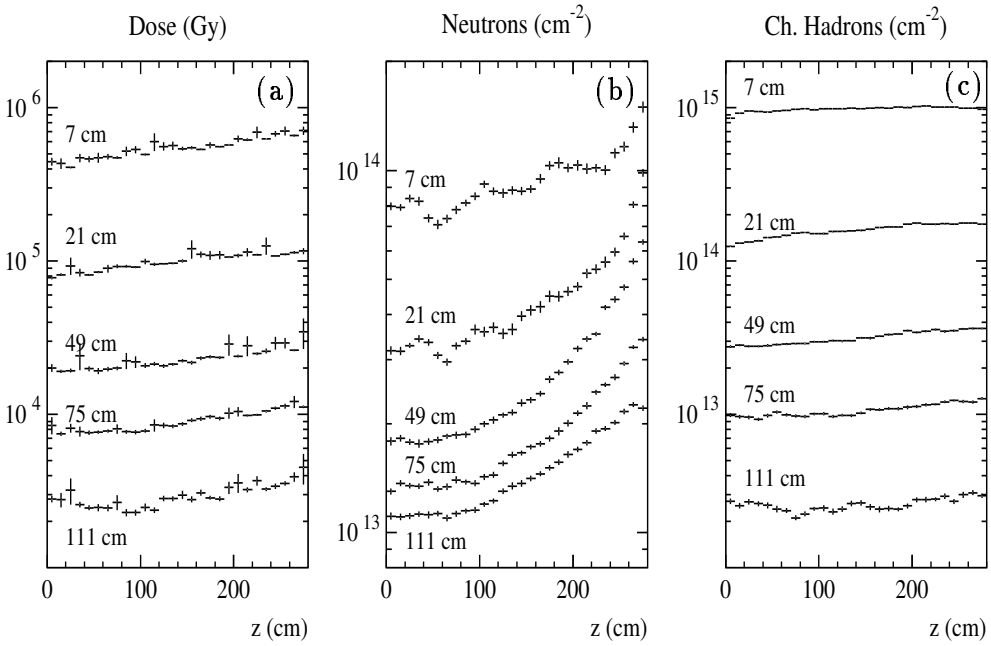

Figure 2.4: *Radiation levels along the z axis, at various radii in the CMS tracker region. All values correspond to an integrated luminosity of* $5\times 10^5 pb^{-1}$.

fitting a circle through these measured points to obtain the radius of curvature of the track. The particle momentum is thus computed as:

$$p = p_t / sin\theta \tag{2.4}$$

where θ is the emission angle of the particle with respect to the magnetic field axis (z axis); it is calculated from the z-coordinates of the measured points. Equations (2.3) and (2.4) show that the charged particle momentum resolution has contributions from the errors on the track curvature and on the polar angle θ. In addition, the momentum resolution suffers also from multiple Coulomb scattering in the material traversed by the particle. Thus the momentum resolution can be written as:

$$(\frac{\Delta p}{p})^2 = (\frac{\Delta p_t}{p_t})^2 + (\frac{cos\theta}{sin\theta}\Delta\theta)^2 + (\frac{\Delta p}{p})^2_{m.s}. \tag{2.5}$$

In practice, the second term is small, compared to the two other ones, and can be neglected. The first term is due to the error on the track curvature reconstructed by the tracking detectors and is given by [15]:

$$(\frac{\Delta p_t}{p_t}) = \frac{a_n \sigma_{R\phi}}{0.3 B L_T^2} p_t \tag{2.6}$$

where $\sigma_{R\phi}$ is the spatial resolution of the tracking detector in $R\phi$ and L_T is the length of the particle path projected onto the transverse plane. The factor a_n is given by:

$$a_n \simeq \sqrt{\frac{720}{n+4}} \quad for \quad n > 10 \tag{2.7}$$

in case of n uniformly spaced measurement points. Hence the momentum resolution will degrade linearly with increasing p_t but will improve for high magnetic field and large radial size of the tracking cavity.

The error due to multiple Coulomb scattering is given by:

$$(\frac{\Delta p}{p})_{m.s} = \frac{0.06[Tm]}{\beta B L_T}\sqrt{\frac{L}{X_0}} \tag{2.8}$$

where X_0 is the radiation length of the material traversed and $\beta=v/c$ is the particle velocity.

2.3.5.3 Objectives and requirements

The CMS tracker is designed to reconstruct most of the tracks of charged particles and to measure their momentum and direction down to the lowest transverse momentum possible (1 GeV/c at high luminosity). Simulation studies have shown that to reach the physics goals of CMS, the tracker must satisfy the following requirements:

- an intrinsic momentum resolution of $\Delta p_t/p_t \simeq 0.1 p_t$ (with p_t in TeV/c). Since the active envelope of the tracker extends up to a radius of 115 cm and will measure on average 12 points per track, it can be shown from equation (2.6) that an average $R\phi$-resolution of 25 μm is required;

- a reconstruction efficiency of 95 % for isolated tracks and 90 % for tracks in jets. Simulation studies showed that the detection cells must have a high detection efficiency, of the order of 98 %;

- a response time below 50 ns corresponding to two bunch crossing intervals;

- a granularity fine enough to cope with the high track density and to keep the occupancy of a single readout channel below a few percents.

- radiation hard detectors to meet the high level of radiation in the tracker;

- an amount of material as small as possible. Indeed, the presence of the tracker in front of the electromagnetic calorimeter causes bremsstrahlung of electrons and photon conversions which spoils the energy measurements of electrons and photons in the electromagnetic calorimeter. In addition, the momentum resolution is also affected by multiple Coulomb scattering mainly for low momentum charged particles.

2.3.5.4 Tracker description

Three detector technologies have been chosen to build the central tracker. Silicon pixel detectors are located at less than 20 cm from the beam pipe, silicon strip detectors are placed at a radius between 20 and 60 cm and microstrip gas counters (MSGC) occupy the region between 70 and 120 cm (see figures C.2 and C.3). Each subdetector is composed of a barrel part, with cylindrical detection layers, and two endcap parts made of disk shaped detection layers. The barrel counters measure the $R\phi$ and z coordinates of the particle impact point, the R coordinate being provided by the radius of the detection layers. The endcap counters measure the $R\phi$ and R coordinates, and the z position is provided by the position of the disk along the beam pipe. On average 12 to 13 points per track are measured. The central tracker covers the pseudorapidity region $|\eta|<2.6$.

Pixel detectors are capable of measuring two space coordinates with an accuracy of 15 μm. The pixel system has two barrel layers and two endcap disks on each side of the barrel. It should provide two hits per track which allow secondary vertices to be found for tagging long lived particles, like b or c quarks.

The silicon strip tracker is composed of five barrel layers and ten endcap disks on both sides of the barrel. The barrel counters are tilted by an angle of 9^o with respect to the radial direction in order to compensate for the effect of the magnetic field on the drift direction of the charge carriers. To provide the readout of the second coordinate, about half of the detection layers are double sided. In a single sided counter, the $R\phi$ coordinate is measured with an accuracy better than 20 μm. In double sided counters, the strips of the second readout side are tilted by an angle of 100 mrad with respect to the $R\phi$ strips, allowing to measure the second coordinate with an accuracy of less than 1 mm. For stable long term operation at the LHC, the CMS solid state detectors will be kept at a temperature of -10^0.

The outermost volume of the CMS tracker will be equipped with microstrip gas counters. These detector have larger detector cells (200 μm), which matches the lower track density in this region, but have a lower cost than that of solid state detectors. The MSGC tracker consists of six barrel layers and eleven endcap disks on each side. The detector elements will be arranged in such a way that the $R\phi$ coordinate of particle trajectories are determined with the highest precision, better than 50 μm including positioning of the counters. A second coordinate measurement, with an accuracy of 1 mm, will be made possible in some layers with small angle stereo strips. In the barrel part, the counters will be tilted by 14^0 in the radial direction to compensate for the Lorentz angle.

Since the present work is a contribution to the design of the endcap MSGC tracker, the theory and experimental work results underlying the functioning of gaseous detectors are given in chapter 3. The MSGC counter technique itself with the various research and development results relevant for this work are presented in chapter 4 together with a description of the CMS forward MSGC tracker.

Chapter 3
Particle detection with gaseous detectors

Introduction

In this chapter we present various aspects of physics that are relevant to particle detection with gaseous detectors. Since the detection and identification of particles are based on their interactions with matter, section 3.1 describes the most important of these interactions. Special emphasis is given to electromagnetic interactions and ionization mechanisms in gases. Indeed in gas filled detectors, the incoming particle loses part or all of its energy in collisions with the gas atoms or molecules leading in some cases to electron-ion pair production. Section 3.2 deals with the drift of electrons and ions in gases. The avalanche process and signal development in gaseous detectors are discussed in section 3.3. Finally, two examples of gaseous detectors are shown in section 3.4.

3.1 Particle interactions with matter

For particle detection the electromagnetic and the nuclear interactions are of great importance, resulting in the loss of all or part of the incoming particle energy. Since in gaseous detectors the electromagnetic interaction is the most important process, it will be described with some details. The electromagnetic processes involved depend on the type of the particle and therefore charged particles and photons will be treated separately in sections 3.1.1 and 3.1.2 respectively. In section 3.1.3, a brief description of nuclear interactions is given with an emphasis on the processes affecting tracking detectors.

3.1.1 Electromagnetic interactions of charged particles with matter

Charged particles can undergo the following electromagnetic processes:

- collisions with atomic electrons, leading to either excited atoms or electron-ion pairs. Since the particle detection depends ultimately on this process, it will be described in detail in sections 3.1.1.1 and 3.1.1.2.
- elastic scattering on the nuclei and on the atomic electrons, leading to modifications in the particle direction and position.

In addition to these two processes, electrons and positrons can lose energy by the emission of electromagnetic radiation in the Coulomb field of the nuclei and of the atomic electrons. The electrons will be treated in section 3.1.1.3.

3.1.1.1 Energy loss of charged particles by atomic collisions

An energetic charged particle heavier than the electron traversing a medium loses its energy via collisions with atomic electrons. These collisions lead to excitation and ionization of the atoms or molecules that constitute the medium. In case of a particle with charge ze and velocity $\beta = v/c$, the mean rate of energy loss per unit length of the traversed material, normalized to the density of the medium, is given by the Bethe-Bloch formula:

$$-\frac{dE}{\rho dx} = \frac{Kz^2}{\beta^2}\frac{Z}{A}\left(\frac{1}{2}\ln\frac{2m_e c^2\beta^2\gamma^2 T_{max}^2}{I^2} - \beta^2 - \frac{\delta}{2}\right) \tag{3.1}$$

where ρ, A and Z are respectively the density, atomic weight and atomic number of the medium traversed, $m_e c^2$ is the rest energy of the electron and $\gamma = (1-\beta^2)^{-1/2}$ is the Lorentz factor. The constant K is equal to 0.307 $MeV g^{-1} cm^2$. In this equation T_{max} denotes the maximum kinetic energy that can be transferred to a free electron in a single collision. It is given by:

$$T_{max} = \frac{2m_e c^2\beta^2\gamma^2}{1 + 2\gamma m_e/M + (m_e/M)^2} \tag{3.2}$$

where M is the mass of the incident particle. The symbol I denotes the mean excitation energy of the atom. The term $\delta/2$ is a correction due to the polarization of the medium as will be explained below.

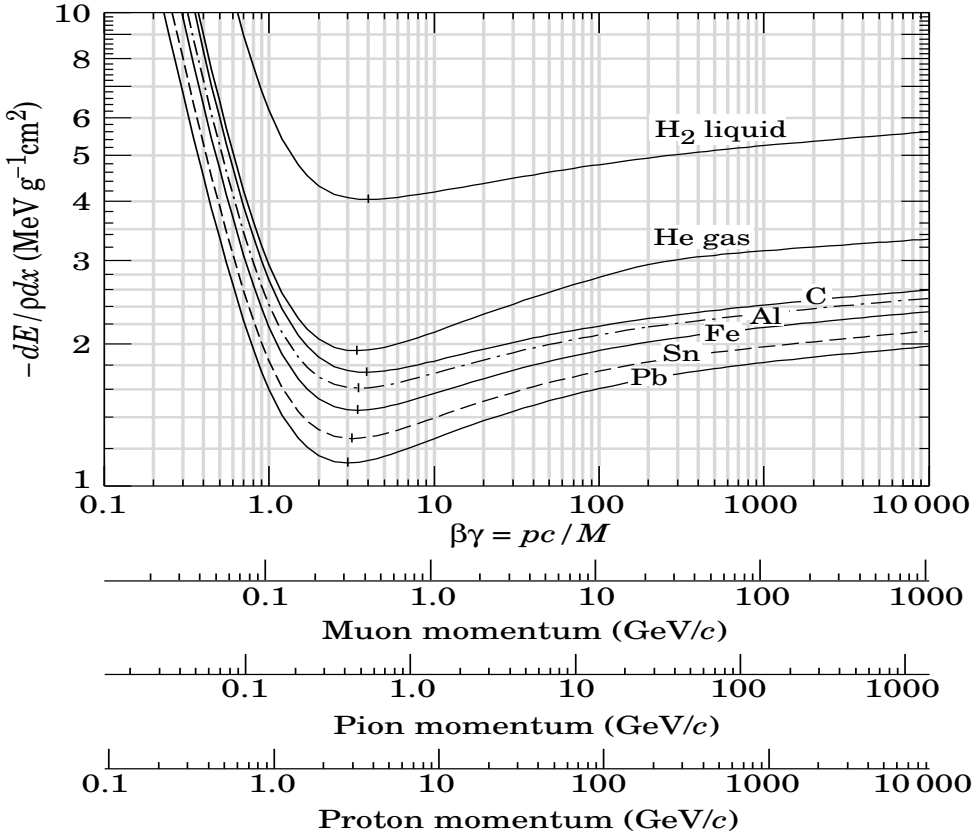

Figure 3.1: *Mean energy loss as a function of the particle momentum, for muons, pions and protons, in various mediums.*

The function (3.1) is shown in figure 3.1, for various materials and various particles. Some important features of these curves are:

- the ionization loss in a given medium depends on the charge and velocity β of the ionizing particle; the dependence on its mass through T_{max} is negligible;
- at low energies, the ionization loss falls with $1/\beta^2$, then goes through a broad minimum at $\beta\gamma = 3-4$. Particles having energy close to this minimum are called minimum ionizing particles (MIP's). Slow particles undergo a huge ionization and are called highly ionizing particles (HIP's);
- at relativistic velocities ($\gamma >> 1$), a slow logarithmic increase of the energy loss occurs. This is called the relativistic rise;
- at highly relativistic energies, a plateau is reached which is called the Fermi plateau. Indeed the electric field of the particle polarizes the medium leading to shielding effect. This is the origin of the term $\delta/2$ in relation (3.1). More details can be found for example in references [15, 16, 17, 18].

In practice, for any given particle, the amount of energy lost is not, in general, equal to the mean value given by relation (3.1) because of the statistical fluctuations which are due to the fluctuations of the number of collisions and of the energy transferred in each collision. For a beam of particles, this will result in a distribution in the energy lost by the particle after a given thickness of material traversed.

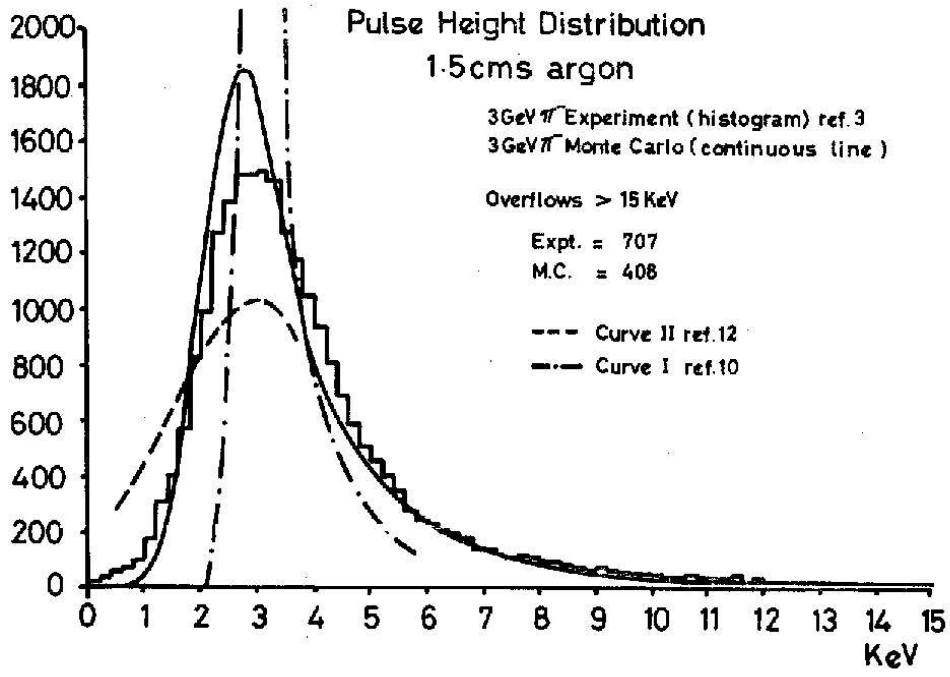

Figure 3.2: *Experimental energy loss distribution of 3 GeV π^- in 1.5 cm of argon (histogram). The dot-dashed curve represents the Landau theory. The solid curve corresponds to the model of Cobb et al., [18] and the dashed curve represents the model of Blunck and Leisegang [20].*

Landau was the first to calculate the energy loss distribution for the case of thin absorbers [19]. Experimental data have shown considerable discrepancies with this theory. Indeed, in his theory Landau considered the electron as free and the energy transferred to this electron was supposed to be larger than its binding energy. Several groups worked then to solve this

problem [18, 20, 21]. Figure 3.2 shows a comparison between the experimental energy loss distribution for 3 GeV π in 1.5 cm of Ar at atmospheric pressure and the distributions predicted by the Landau theory, the model of Cobb et al. and the one proposed by Blunck and Leisang. It shows that the model of Cobb et al. is the closest to reality. In this model, a monte carlo simulation was used to simulate realistic energy loss distributions and the relativistic rise.

3.1.1.2 Primary and secondary ionizations

We have seen that a particle traversing a gas loses energy by excitation and ionization. The electrons ejected by the incident particle itself are called primary electrons or δ-rays. The number of ionizing collisions initiated by the incident particle, per centimetre of gas traversed, is called the primary ionization density n_p. These primary electrons can be emitted with kinetic energy large enough to cause further secondary ionizations of the atom A by the process:

$$e^- + A \rightarrow e^- + A^+ + e^-$$

Another source of secondary ionization is the Penning effect. An intermediate excited state A^* of atom A can be created either by the incident radiation itself (*e.g.* a π meson) or by primary electrons:

$$\pi^{\pm} + A \rightarrow \pi^{\pm} + A^* \quad \text{or} \quad e^- + A \rightarrow e^- + A^*,$$

and the deexcitation of atom A may occur through a collision with a second atom B resulting in the ionization of B.

A primary electron will travel through the gas and produce secondary electrons until its energy is below the lowest ionization potential of the atoms in the gas. The distance the primary electron can travel and still being able to ionize atoms or molecules is called the range. An empirical formula exists that parametrizes the range of δ-rays with their energy [15]. In argon, at normal temperature and pressure (N.T.P), a primary electron of 1 keV is stopped in about 65 μm, and one of 10 keV in about 1.5 mm, but only 0.05 % of the collisions produce primary electrons with kinetic energy equal to or larger than 10 keV.

The number of primary ionizations follows Poisson statistics, *i.e* the probability of having k primary electrons in a distance x traversed by the incident particle is:

$$P(k) = \frac{(n_p x)^k}{k!} \exp(-n_p x) \tag{3.3}$$

The theoretical inefficiency of a detector of thickness x is thus equal to the probability of having no primary electron inside the detector material traversed by a charged particle, *i.e* $P(0)=exp(-n_p x)$. A high enough ionization density n_p is thus required to keep the theoretical detector inefficiency negligible.

The sum of primary and secondary ionization densities lead to the total ionization density n_T. In proportional gaseous detectors the signal amplitude increases with n_T and the energy resolution improves. One therefore has to choose a gas with the highest possible n_T.

For our application the choice of n_p and n_T will be discussed in chapters 4 and 5.

3.1.1.3 Electrons

Like heavy charged particles, electrons suffer energy loss via collisions with atoms or molecules of the material traversed. However, for energies above a few MeV, electrons lose their kinetic

energies essentially by photon emission (bremsstrahlung), in the Coulomb field of the nuclei and electrons of the medium[1].

The radiation length, X_0, is defined as that thickness of material required to reduce the energy of an electron by a factor e, by bremsstrahlung. Normalized to the material density, X_0 is given by the empirical formula [22]:

$$X_0 = \frac{716.4A}{Z(Z+1)\ln(287)\sqrt{Z}} g cm^{-2} \tag{3.4}$$

where A and Z are respectively the atomic weight and atomic number of the medium. In an experiment such as CMS, this process affects the detector performances. On one hand, it increases the photon background in the calorimeters. On the other hand, it makes difficult the reconstruction of the electron trajectories and degrades the electron momentum measurements, because of the discontinuities of curvature at the emission point of the photons [12, 14].

3.1.1.4 Multiple Coulomb scattering

When passing through matter, charged particles also suffer elastic Coulomb scatterings from nuclei. The particle is then deflected several times from its original direction. For small angle single scatterings the distribution of the total deflection angle is Gaussian and its standard deviation, projected onto a plane parallel to the direction of the scattered particle, is given by [22]:

$$\theta_0 = \frac{13.6 MeV}{\beta cp} z \sqrt{\frac{x}{X_0}} [1 + 0.038 \ln(\frac{x}{X_0})] \tag{3.5}$$

where β, p and z are the velocity, the momentum and the charge of the incident particle, and x and X_0 are the material thickness and radiation length respectively.

Multiple Coulomb scattering puts severe limitations on the detector performances mainly for the reconstruction of tracks of low momentum particles. Materials with short radiation length should therefore be avoided when building a high precision tracker (see chapters 2 and 5).

3.1.2 Electromagnetic interactions of photons with matter

Three main processes are responsible for the photon absorption in matter:

- absorption of the photon energy by an atomic electron: the photoelectric effect;
- the Compton effect, in which the photon is scattered by a stationary, free electron;
- the conversion of the photon into an electron-positron pair, in the Coulomb field of a nucleus or an electron.

Figure 3.3 shows the absorption coefficient of γ-rays in matter as a function of their energy [23]. Above 10 MeV, the important process for photons is the production of an electron-positron pair in the electromagnetic field of a nucleus or electron. It is convenient to define a quantity called the conversion length λ_{pair}. It is the distance after which a photon beam is

[1] At very high energies, muons also are subject to bremsstrahlung. However, the cross section of this process is proportional to the inverse squared of the particle mass and therefore the radiation lost by muons is 40 000 times smaller than that for electrons.

High energy electrons can also produce electron-positron pairs, but this process is very rare, compared to bremsstrahlung.

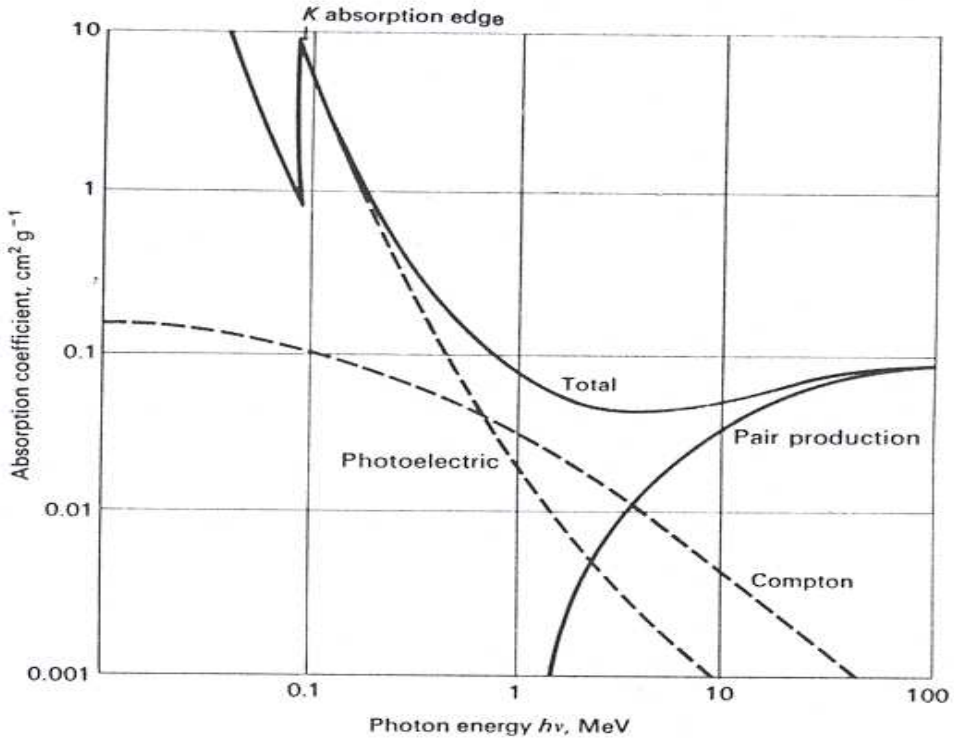

Figure 3.3: *Absorption coefficient per g per cm² of lead for γ-rays as a function of their energy.*

attenuated by a factor e by creation of $e^{\pm}$ pairs. In high energy physics experiments, photon conversion degrades the detector performances in particular the calorimeter since it renders photon identification and detection difficult. It also increases the number of charged particles inside the tracker. In CMS, 32 % of the photons produced in $H \rightarrow \gamma\gamma$ decays convert before leaving the tracker sensitive volume so that in only 46 % of these decays both photons reach the calorimeter. About 60 % of the conversion occurs in the Pixel and Silicon sub-trackers [14, 12].

3.1.3 Nuclear interactions

Hadronic interactions are a major concern in the CMS tracker because they produce charged, low energy particles that are thus highly ionizing.

Neutrons are also capable of causing ionization by indirect processes such as: (a) collisions that produce recoil atoms or ions, (b) collisions that excite atomic nuclei which de-excite by emitting either Auger electrons or γ-rays and (c) reaction of type (n,α) and (n,p) where a neutron is absorbed by a nucleus, subsequently emitting a charged particle.

All these low energy particles deposit into the tracker gas, more than 100 times the energy at the minimum of function (3.1). A low energy proton for instance can deposit an energy about 300 times the energy deposited by a MIP. In gaseous detectors a large energy deposition can initiate discharges and even produce detector damage as will be seen below.

Hadron interactions can also induce radioactivity. Two mechanisms are responsible for it:

- low energy neutron interactions such as (n,α),(n,p),(n,γ),etc;
- creation of long-lived radionuclides (30 % of the high energy interactions) [14].

In addition to safety issues, the induced radioactivity represents an additional contribution to the detector background.

3.2 Drift and diffusion in gases

The behaviour of gaseous filled detectors (see section 3.4) depends crucially on the drift of the electrons and ions that are released in the gas. Liberated electrons drift towards the anodes under the influence of the electric field E, positive ions drift towards the cathodes.

In a microscopic point of view, the drift of a particle (electron or ion) can be seen as a succession of short travels during which it acquires kinetic energy from the accelerating electric field, and collisions with gas atoms or molecules, where it loses part of its kinetic energy. This leads to a macroscopic drift at an average speed u called the drift velocity. It is related to the electric field by: $u{=}\mu E$, where μ is the particle mobility. Because of numerous collisions with gas molecules, the particle will also change in direction, resulting in a diffusion of the ionizing cloud. As a result the drift of electrons and ions is mainly described by the drift velocity and the diffusion coefficient, often called transport parameters. Because of their different masses, electrons and ions are treated separately, in sections 3.2.1 and 3.2.3 respectively.

3.2.1 Electrons

In a gaseous detector, the electron drift velocity determines the detector response time. Due to the diffusion of the electrons, the ionization cloud is spread, influencing thus the impact point determination.

It will be shown that, in the presence of a magnetic field, the electrons are deviated from their trajectory by an angle α_L called the Lorentz angle. This affects both the drift velocity and the diffusion, and consequently the detection efficiency and the spatial resolution of the counter. Another process which may happen is the capture of free electrons by molecules. For detailed calculations, important references are [15, 16, 17, 24, 25]

Very often, a quantity called the reduced electric field E/P, where P stands for the pressure, is used instead of the electric field E.

3.2.1.1 Drift velocity, diffusion and Lorentz angle

The motion of electrons in gases is often described in two ways: from the macroscopic and microscopic points of view.

- In the macroscopic model, the electron is first treated as any charged particle moving under the influence of the electric and magnetic fields $\mathbf{E}$ and $\mathbf{B}$. In this case, the equation of motion is written as:

$$m\frac{d\mathbf{u}}{dt} = e\mathbf{E} + e[\mathbf{u}\times\mathbf{B}] - K\mathbf{u} \tag{3.6}$$

  where m and e are the mass and electric charge of the electron, $\mathbf{u}$ its velocity vector and $K\mathbf{u}$ is a friction force caused by the interaction of the electron with the gas; the factor $\tau{=}m/K$ has the dimension of a time. The drift velocity $u{=}|<\mathbf{u}>|$, which is the average speed of all drifting electrons, is thus also a solution of equation (3.6). For large t ($t >> \tau$), the increasing friction force compensates the accelerating electromagnetic force leading to a constant drift velocity u. It is a solution of the steady state equation , $d{<}\mathbf{u}{>}/dt = 0$:

$$\frac{<\mathbf{u}>}{\tau} = \frac{e}{m}(\mathbf{E}+<\mathbf{u}>\times\mathbf{B}) \tag{3.7}$$

  In this equation, the right hand side corresponds to the acceleration of the electron between two collisions, due to the electromagnetic force, and therefore τ can be considered as the average time between two collisions.

In the absence of a magnetic field, equation (3.7) gives the drift velocity:

$$u = \frac{e}{m} E\tau = \mu_e E. \tag{3.8}$$

The electron mobility μ_e is thus given by:

$$\mu_e = \frac{e\tau}{m} \tag{3.9}$$

In the presence of a magnetic field, the drift behaviour of charged particles changes. The Lorentz force acts on a moving charged particle when the electric field **E** is not parallel to the magnetic field **B**. In the case of **E** perpendicular to **B** (*e.g* **B**= (0,0,B_z) and **E**=(E_x,0,0)), the drift velocity is given by:

$$u = \frac{\varepsilon\tau}{\sqrt{1+\omega^2\tau^2}} \tag{3.10}$$

where $\varepsilon = \frac{eE_x}{m}$ and $\omega = \frac{eB_z}{m}$. In this case the drift velocity is reduced by a factor $\sqrt{1+\omega^2\tau^2}$ with respect to its value in the absence of the magnetic field (equation (3.8)).

The deviation angle α_L between the electric field lines and the direction of motion of the electron, due to the magnetic field, is:

$$\alpha_L = -\omega\tau = -\mu_e B_z \tag{3.11}$$

Combining equations (3.8) and (3.11), the Lorentz angle can be expressed as:

$$\alpha_L = -\frac{u}{E_x} B_z \tag{3.12}$$

and therefore, the Lorentz angle can be minimized by working at the highest possible electric field and the smallest possible drift velocity.

In the case of **E** parallel to **B**, the drift velocity is not affected. This is the situation in the forward-backward tracker of CMS whereas in the barrel, where the 4 T magnetic field is perpendicular to the electric field, the Lorentz angle amounts to 0.25 *rad* and the drift velocity is found to be reduced by 3 % in a Ne/DME 30/70 % gas mixture at an electric field of 10 kV/cm.

Although the macroscopic treatment gives a global understanding of the electrons behaviour under an electric and a magnetic field, it is not able to describe the diffusion of the electrons nor the drift velocity dependence on the electric field intensity as for electrons τ may depend on E. To have a deep insight onto these parameters, a microscopic treatment is mandatory.

- In the microscopic model, the electrons are scattered randomly on the gas molecules. Thus it is assumed that there is no correlation between the electron direction before and after the collision. The average kinetic energy of an electron, in the presence of an electric field of strength E, can be given as:

$$\varepsilon = \varepsilon_E + \varepsilon_T \tag{3.13}$$

where ε_E is the average electron energy acquired from the electric field and ε_T is the electron average thermal energy in the absence of the electric field. This latter is equal to $3/2kT$, where k is the Boltzmann constant and T is the gas temperature.

In a time interval τ between two consecutive collisions, the electrons acquire, from the electric field, a drift speed u given by equation 3.8. It can be shown, that u is related to the fraction λ of the electron energy ε_E lost in a collision and to the collision cross section σ by:

$$u^2 = \frac{2E}{mN\sigma}\sqrt{\frac{\lambda}{2}} \tag{3.14}$$

where N is the gas molecular density. The average time between collisions is then given by:

$$\tau^2 = \frac{m}{e^2 N\sigma E}\sqrt{2\lambda} \tag{3.15}$$

and therefore depends also on the electric field. The collisions with gas molecules cause also a random diffusion of the electrons. As a consequence, a point-like cloud of electrons starting to drift in the z direction at time $t = 0$ will have a Gaussian spread in a direction x, perpendicular to z, of standard deviation σ_x equal to $\sqrt{2Dt}$, where D is the transverse diffusion coefficient and $t = z/u$ is the drift time. It can be shown that the diffusion coefficient is related to the electron kinetic energy ε by [15]:

$$D = \frac{2}{3}\frac{\varepsilon}{m}\tau. \tag{3.16}$$

Very often, the diffusion is expressed in centimetres per unit of drift distance:

$$D' = \frac{\sigma_x}{\sqrt{z}} \tag{3.17}$$

and therefore $D'=\sqrt{2D/u}$. Thus the width of the electron cloud is proportional to the square root of the drift distance.

Expressions (3.14) and (3.16) reflect the importance of the electron average kinetic energy ε, the fractional energy loss λ and the collision cross section σ to understand the behaviour of the drift velocity and diffusion as a function of the electric field E. As an illustration, figure 3.4 shows the drift velocity in argon with different content of methane as a function of the reduced electric field. It is observed that the behaviour depends strongly on the gas composition. To explain this, consider figure 3.5 where the so-called characteristic energy, $\varepsilon_K=(2/3)\varepsilon$, is shown as a function of the electric field. In the range of electric fields between 100 and 3000 V/cm, for argon it varies slowly between 3 and 10 eV. Since these energies are well below the threshold excitation of argon, the only possible collisions are elastic with very small energy losses of the order of 10^{-4} eV, leading to a constant fractional energy loss as can be seen in figure 3.6(b). Also at these energies, the collision cross section is at its maximum value (see figure 3.6(a)) leading to a small drift velocity.

Adding a small amount of methane to argon increases the drift velocity as can be seen from figure 3.4. Indeed, the threshold of excitation for methane is 0.03 eV which increases the fractional energy as illustrated in 3.6(b). This results in an increase of the drift velocity.

The diffusion coefficient increases with the electron kinetic energy. In some gases, such as Di-Methyl-Ether (DME) and CO_2, the average kinetic energy remains constant around $(3/2)kT$ in a large range of electric fields, up to 1 kV/cm and rises slowly after this limit called thermal limit. In this case, the diffusion coefficient is very small and constant. We will see later the influence of such gases on the detector performances.

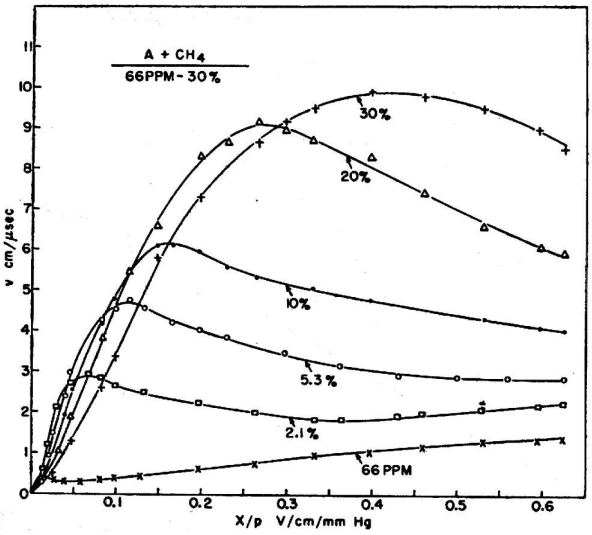

Figure 3.4: *Drift velocity in argon with various CH_4 contents as a function of the reduced electric field [24].*

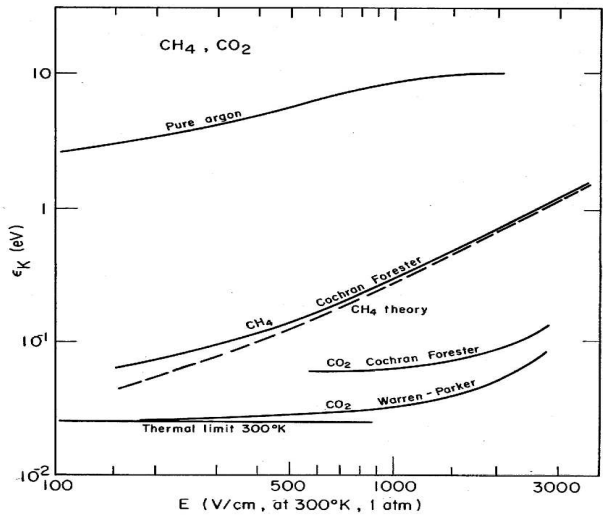

Figure 3.5: *Characteristic energy as a function of the electric field intensity [24].*

Experimentally, it has been observed that, in the non-thermal case, the electric field alters the diffusion and it is necessary to introduce two diffusion coefficients D_L and D_T respectively for the longitudinal and the transverse directions with respect to the electric field. This is demonstrated in figure 3.7 where D_L/μ_e and D_L/μ_e are shown as a function of the reduced electric field E/P for an Ar-CH_4-C_4H_{10} gas mixture [26].

In the presence of a magnetic field, the transverse diffusion coefficient D_T is reduced by a factor $1+(\omega\tau)^2$, while the longitudinal diffusion is not affected. This is illustrated in figure 3.8 where the transverse diffusion coefficient is shown as a function of the magnetic field [26].

A compilation of experimental data on drift velocity, diffusion coefficients and other drift properties can be found in reference [27].

3.2.2 The Boltzmann transport equation

The simple classical theory described above leads to qualitatively correct results. In order to obtain rigourous quantitative results one has to apply the full theory of electron transport in gases. The idea is to write down diffusion equations describing the dynamics of electrons distribution functions, rather than considering the motion of single electrons. This theory is based on the Boltzmann transport equation, which expresses the conservation of the number of electrons. If f($\mathbf{r}$,$\mathbf{v}$,t) is the distribution of electrons at the point $\mathbf{r}$, $\mathbf{v}$ of the phase space at time t, this equation reads [28]:

$$\frac{\partial f}{\partial t} + \frac{\partial f}{\partial \mathbf{r}}\frac{\partial \mathbf{r}}{\partial t} + \frac{\partial f}{\partial \mathbf{v}}\frac{\partial \mathbf{v}}{\partial t} - \frac{\partial f}{\partial t}|_{collision} = 0 \tag{3.18}$$

Here $\partial f/\partial t$ represents the time evolution of f($\mathbf{r}$,$\mathbf{v}$,t), $(\partial f/\partial \mathbf{r})(\partial \mathbf{r}/\partial t)$ represents the loss of electrons in interval $d\mathbf{r}$ due to diffusion, $(\partial f/\partial \mathbf{v})(\partial \mathbf{v}/\partial t)$ represents the modification of the electrons density due to the acceleration by the electric field E and $\partial f/\partial t|_{collision}$ is the change of the electrons density, due to collisions with gas molecules, which should contain the full dynamics of the elastic and inleastic processes that could take place.

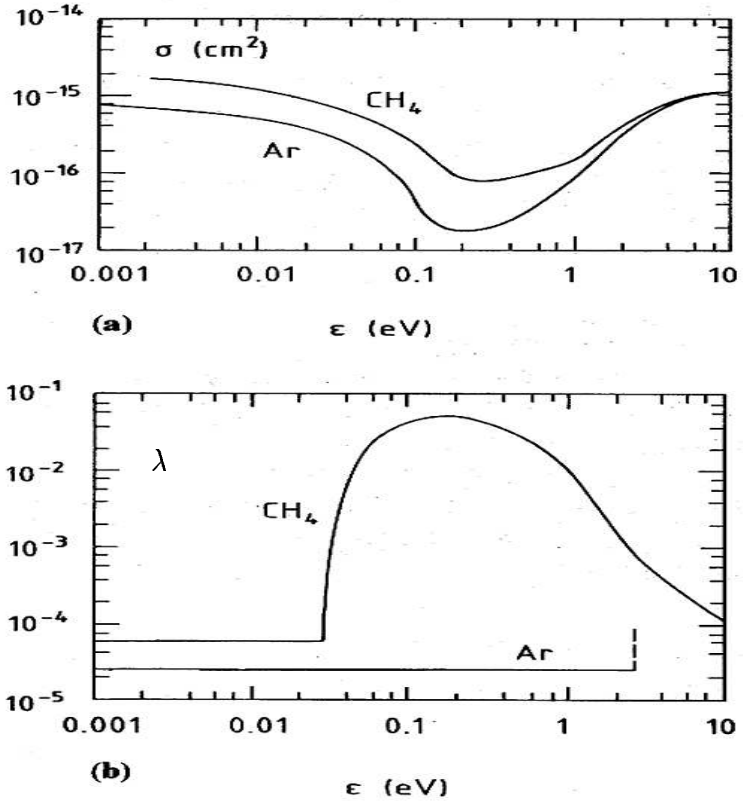

Figure 3.6: *Collision cross section (a) and fractional energy loss (b) in argon and in methane [15].*

The solution of this equation has been studied by many authors [29, 30]

Following the work of Morse et al. [31], V. Palladino and B. Sadoulet considered the stationary case of equation (3.18), without t dependance and with a uniform distribution in space $\partial f/\partial \mathbf{r}$=0. In this case it is possible to work only with the distribution function $f(\varepsilon, cos\theta)$, where θ is the angle between the direction of motion of the electron and the E-field, and ε is the energy of the electron. The resulting equation is then expanded in Legendre polynomials:

$$f(\varepsilon, cos\theta) = f_0(\varepsilon) + f_1(\varepsilon)cos\theta + ... \tag{3.19}$$

Let us assume the electrons are drifting along the x axis, the electric field being parallel to this axis and the magnetic field perpendicular to it. If only two terms are considered for the expansion (3.19), calculations showed that the solution of equation (3.18) is [25]:

$$f_0(\varepsilon) = C\sqrt{\varepsilon}exp[-\int_0^{\varepsilon} \frac{3\Lambda(\varepsilon')G(B)\varepsilon'}{[(eEl(\varepsilon'))^2 + 3\Lambda(\varepsilon')kTG(B))]}d\varepsilon'] \tag{3.20}$$

where C is a constant obtained from the normalization condition:

$$\int_0^{\varepsilon_{max}} f_0(\varepsilon)d\varepsilon = 1, \tag{3.21}$$

and $l(\varepsilon)$ is the mean free path between two elastic collisions. The expression $\Lambda(\varepsilon)$ is the contribution of inelastic collisions and is given by:

$$\Lambda(\varepsilon) = \frac{2m}{M} + \sum_i \frac{\varepsilon_i}{\varepsilon}\frac{l(\varepsilon)}{l_i(\varepsilon)} \tag{3.22}$$

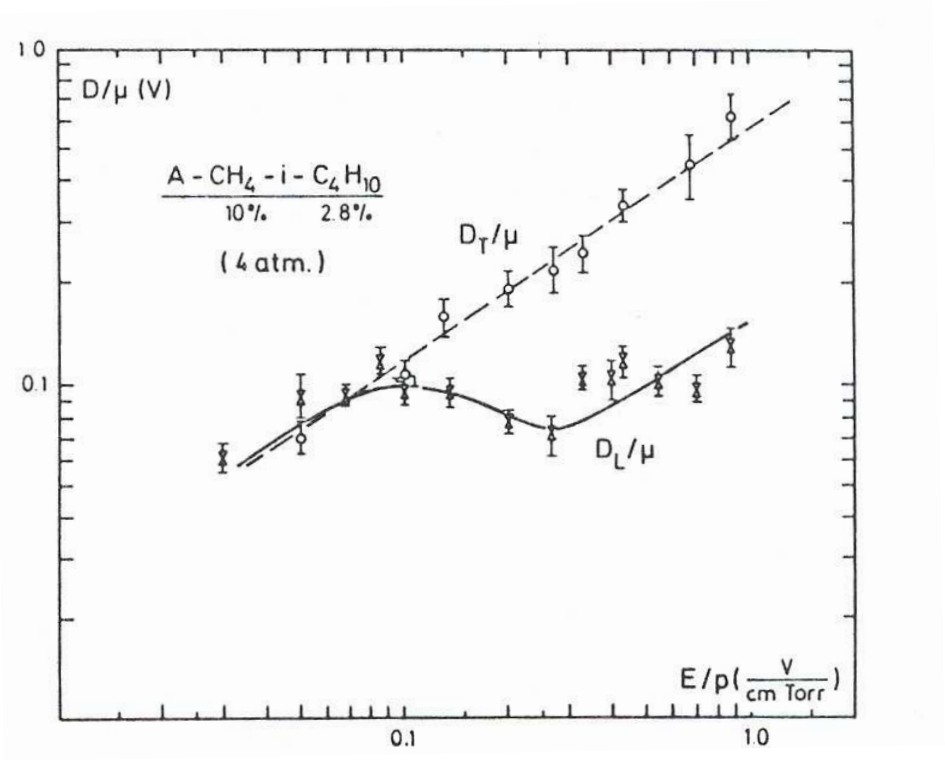

Figure 3.7: *Longitudinal and transverse diffusion coefficients normalized to the electron mobility as a function of the reduced electric field [26].*

where M is the mass of the molecule, ε_i is the excitation energy of the $i-th$ state and $l_i(\varepsilon)$ is the mean free path between two collisions which give rise to the excitation. The term $G(B)$ in expression (3.20) is the contribution of the magnetic field and is given by:

$$G(B) = 1 + \frac{e^2 B_z^2 l(\varepsilon)^2}{2m\varepsilon} \tag{3.23}$$

Once the function $f_0(\varepsilon)$ is obtained, the drift velocity, the Lorentz angle and the diffusion coefficient are derived. Thus the drift velocity v is given by:

$$v = \sqrt{v_x^2 + v_y^2} \tag{3.24}$$

where

$$v_x = -\frac{2}{3}\frac{eE}{m}\int_0^{\varepsilon_{max}} \frac{\varepsilon l(\varepsilon)}{G(B)}\frac{\partial(f_0(\varepsilon)/v(\varepsilon))}{\partial\varepsilon}d\varepsilon \tag{3.25}$$

and

$$v_y = \frac{e^2 EB}{3m}\int_0^{\varepsilon_{max}} \frac{l(\varepsilon)^2 v(\varepsilon)}{G(B)}\frac{\partial(f_0(\varepsilon)/v(\varepsilon))}{\partial\varepsilon}d\varepsilon \tag{3.26}$$

The ratio of v_y and v_x gives the Lorentz angle, and the transverse diffusion coefficient is given by:

$$D_T = \frac{1}{3}\int_0^{\varepsilon_{max}} \frac{l(\varepsilon)v(\varepsilon)}{G(B)} f_0(\varepsilon)d\varepsilon \tag{3.27}$$

To solve equation (3.18), a computer code has been written by S. Biagi [32, 33] taking into account Legendre polynomials up to the second order. In chapter 5, this program, called MAGBOLTZ, will be used to compute the drift velocity and the transverse diffusion coefficient in several gases.

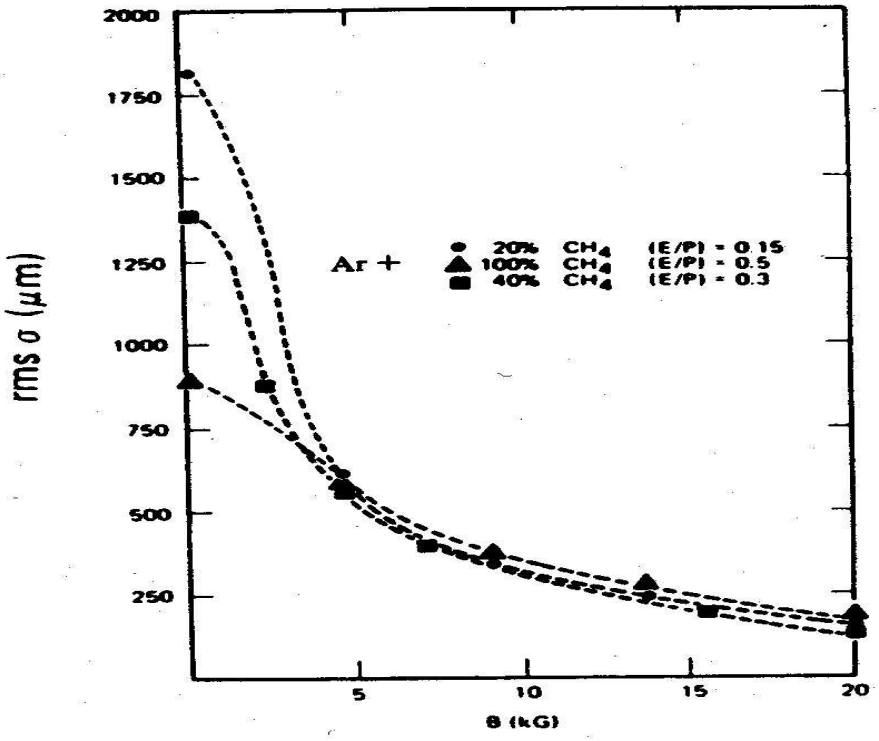

Figure 3.8: *Transverse diffusion coefficient (called σ in this figure) as a function of the magnetic field for different gas mixtures [26].*

3.2.3 Ions

The behaviour of ions differs from that of electrons because of their much larger mass. On one mean free path, ions acquire an amount of energy that is almost totally lost in the next collision. As a consequence their energy remains in the thermal limit up to high electric fields. This implies much smaller diffusion coefficients compared to that of electrons. This also implies that their mobility, μ_i is constant, and their drift velocity is a linear function of the electric field. Their mobility is also much smaller than that of electrons. To give an order of magnitude, in CH_4 the electron mobility is about 10^4 $cm^2s^{-1}V^{-1}$ while it is only 2.2 $cm^2s^{-1}V^{-1}$ for CH_4^+ ions [15]. This small mobility leads to a small Lorentz angle since $\alpha_L = \mu_i B$.

In proportional counters, the charges created in the avalanche induce electric signals that can be amplified and measured. It will be shown in section 3.3.2 that the contribution of ions to the induced signal is much larger than that of the electrons. Therefore the time development of the signal is mostly determined by the ions speed.

3.3 Avalanche process and signal development

In gaseous filled detectors, once the drifting electrons reach a region of high electric field, close to an anode (typically a hundred microns), they gain sufficient energy to ionize a gas molecule. Other electrons are then created which can, in turn, produce new ionizations. This process, called avalanche, continues until all the electrons are collected on the anode. The motion of electrons and ions induces signals on the electrodes.

3.3.1 Gas amplification factor

In gas filled detectors, electron multiplication occurs near the anode where the electric field is very high (typically more than 50 kV/cm). This multiplication is described by the first Townsend coefficient α. The increase by ionization of the number of electrons N on a distance dx is given by:

$$dN = \alpha N dx \tag{3.28}$$

This amplification is a very complicated process. Indeed, it involves several mechanisms as ionization, excitation, photoionization, recombination between electrons and positive ions, etc. Therefore α must be measured for every gas mixture, as a function of the electric field. Earlier experimental measurements have shown that the avalanche multiplication occurs in noble gases at much lower electric fields than in complex molecules [24]. Therefore, noble gases are used as the main components in gaseous detectors. The gas amplification factor G, called gas gain, is given by:

$$G = \frac{N}{N_0} = \exp[\int_{x_0}^{x_a} \alpha(x) dx] \tag{3.29}$$

where x_0 is the point where the electric field intensity is just sufficient to produce secondary electrons by ionization, N_0 is the number of electron-ion pairs created before reaching the point x_0 and x_a is the anode position.

The gas gain can not be increased at will. Gain limitations may occur because of three reasons.

First, at high gains when the avalanche grows and reaches a size of 10^7-10^8 electron-ion pairs, the slowly moving positive ions create, locally around the anode, an electric field that opposes to the external electric field and reduces it. The multiplication processes become slow and recombinations between electrons and positive ions inside the avalanche occur.

The second reason is the ageing. Gaseous counters that have been in use for some time may show a gain decrease. This behaviour is attributed to either the presence of some contaminants in the gas mixture or to the construction materials used. It was found that organic components of the gas can form insulating polymer deposits on the electrodes. This causes electric field and gain variations. Intensive studies have been conducted in order to understand the ageing phenomenon in wire chambers, which is found to depend strongly on the accumulated charge. A review of these studies can be found in references [25, 34, 35].

The third reason for gain limitations in proportional counters is the occurrence of secondary processes leading to detector breakdown. Two processes are known to be at the origin of breakdown:

- secondary emission of electrons: during the avalanche, excited and ionized atoms are created. Excited noble gases like argon can return to the ground state only by photon emission. The minimum energy of the emitted photon is 11.6 eV which is above the ionization potential of any cathode metal (5.9 eV for aluminium and 7.7 eV for copper). Electrons can therefore be extracted from the cathode by photoelectric effect and initiate new avalanches. This process is called photon feedback. It can lead to a permanent discharge. In order to stop electron extraction from the cathode , the photons have to be absorbed. This is ensured by adding polyatomic molecules to the gas, called quenchers. These molecules present a large amount of non-radiative excited states allowing the absorption of photons in a wide range of energy. At the cathode surface itself, the accumulation of positive ions may create a dipole field sufficient to extract electrons from the cathode (the Malter effect);

- development of streamers: since the avalanche increases in size, the space charge fields created increases and the total electric field is enhanced in the front and the back of the avalanche. Electrons that are released by photoionization or Penning effects inside the avalanche are accelerated by the high field created by the avalanche itself, amplified and lead to new avalanches. If this process continues, it will create a low resistivity filament of charges between the anode and the cathode, leading to a discharge. The physical processes leading to the transition from a proportional avalanche multiplication to a streamer have been discussed in many references [36, 37]. The explanation given here is due to Atac et al. [38]. In the case of MSGC's, the breakdown mechanism will be discussed with some details in section 4.2.4.

3.3.2 Signal formation

The motion of electrons and positive ions, created in the avalanche, induces currents on the electrodes which can be amplified and measured.

In a cylindrical proportional counter, if the avalanche takes place at a distance x_0 from the wire, it can be shown that the ratio of the total induced voltage from the electrons V^- and that from the positive ions V^+ is given by [17]:

$$\frac{V^-}{V^+} = \frac{\ln \frac{a+x_0}{a}}{\ln \frac{b}{a+x_0}} \tag{3.30}$$

where a and b are respectively the radius of the anode wire and of the cylinder. Taking some typical values, a=10μm, b=10mm and x_0=1μm, V^- is only 1 % of V^+. The induced signal is therefore due to the motion of the positive ions.

In case of several electrodes, the treatment is different and complicated because of capacitive couplings between the electrodes. The most general tool to calculate signal currents induced on electrodes is provided by Ramo's theorem. This theorem states that the current that flows into one particular electrode i under the influence of a moving charge q at x_1 with velocity v can be calculated from the electric field $E_i(x_1)$ created by putting this electrode at potential V_i and grounding all the others, in the absence of the charges. A complete derivation of this theorem can be found in reference [15].

3.4 Gaseous detectors

Before 1968, most tracking detectors in particle physics were visual devices , *e.g* photographic emulsions, bubble chambers, spark chambers, etc. In 1968, Charpak introduced an electronic gaseous tracking device providing the possibility of direct position determination of the incoming particle in large volumes [39]. This device is the MultiWire Proportional Counter (MWPC). Later the first drift chamber was operational [40]. Then, a large number of descendants, with different geometries and for different detection purposes, were introduced: time projection chambers, parallel plate chambers, etc.

In the two next sections, the MWPC and the drift chamber are described since they are the most relevant for the rest of this work.

3.4.1 The MultiWire Proportional Counter (MWPC)

The basic MWPC consists of a plane of equally spaced thin anode wires placed between two cathode planes as shown in figure 3.9. A typical wire spacing is 2 mm. For optimal operation,

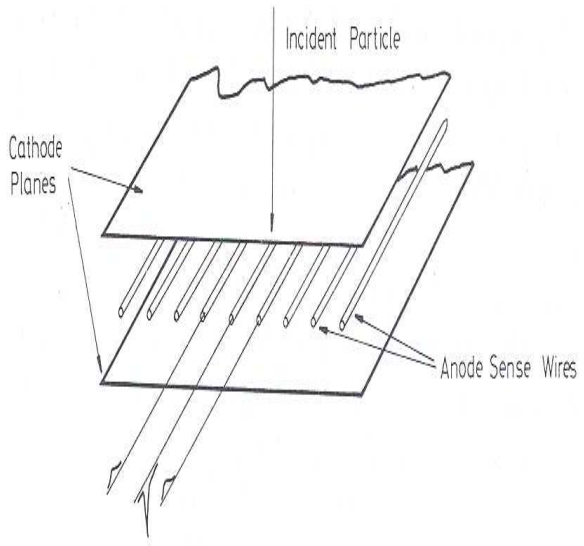

Figure 3.9: *Schematic view of a multiwire proportional counter.*

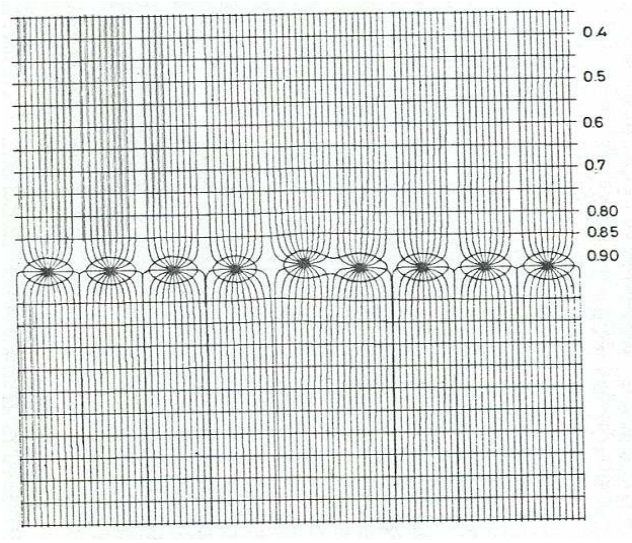

Figure 3.10: *Electric field lines and equipotential lines in an MWPC. The effect of a slight wire displacement is also shown.*

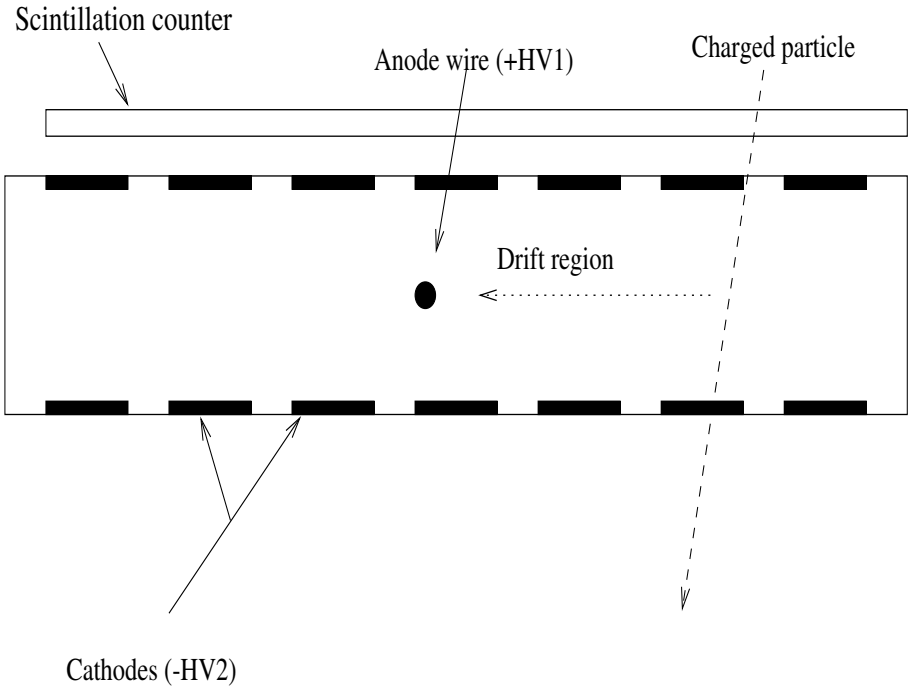

Figure 3.11: *Basic operating principle of a drift chamber.*

the anode cathode distance should be three or four times the wire spacing. The volume, between the cathodes and the anodes, is filled with a suitable gas mixture. A negative voltage is applied to the cathode planes, the anodes being grounded, leading to an electric field configuration as shown in figure 3.10. Electrons liberated in the gas volume by an ionizing particle, drift towards the nearest anode wire, ions drift towards the cathode. Near the anode the electrons are accelerated and an avalanche process takes place. The amplitude of the signals induced on the electrodes allows to determine the particle crossing point.

In a MWPC the alignment and positioning of the anode wires are critical for precise measurements. When a voltage is applied to the electrodes, electrostatic forces between the wires appear. If a wire is displaced from the middle plane, it will be attracted to the side of the displacement, when the voltage is applied, leading to electrostatic and mechanical instabilities. It has been shown that the distance between the anodes can not be less than 1 mm, which puts severe limitation on the detector performances, mainly its granularity [24]. Another constraint comes from the limited detector response time which is a few hundreds of nanoseconds. Therefore the counting rate of the MWPC, being the maximum particle flux the detector can sustain keeping a uniform response, can not be more than 10^4 particles per mm^2 per second.

3.4.2 The drift chamber

During the development of MWPC's, it was realized that spatial information could also be obtained from measurement of the electron drift time. A schematic view of a chamber exploiting this aspect is shown in figure 3.11. Such chamber is called drift chamber. It consists of a thin anode wire placed in the middle of a region of moderate uniform electric field. A scintillator, serving as a trigger, signals the arrival of an ionizing particle at time t_0. Since the electric field is uniform in the drift region, the electrons drift velocity u is constant. Therefore the distance from the anode wire to the origin of the ionization electrons produced by the incident particle is given by:

$$x = u(t_1 - t_0) \tag{3.31}$$

where t_1 is the time at which the signal is received at the anode.

The uniform electric field is obtained by setting the cathodes to appropriate voltages. However, close to the anode the electric field is not uniform and consequently, relation (3.31) does not hold. The advantage of drift chambers is the small amount of wires and electronics required and the large surface which can be covered. They have been and are used in many experiments [15]. However much more attention must be given to the gas choice to avoid electron losses during the larger drift and to the field uniformity. Due to the large drift distance the drift chambers deliver their signals with a certain delay and can stand only modest particle fluxes.

Chapter 4
The CMS Forward-Backward MSGC Tracker

Introduction

In the CMS experiment, Micro-Strip Gas Counters (MSGC's) are foreseen to equip the outermost part of the central tracking system. This work is a contribution to the study of the MSGC end-cap part of the CMS tracker. A general description of the MSGC is given in section 4.1.

In the last years, a wide effort has been undertaken to improve this device and in particular to meet the high rate requirements of an experiment as CMS. Section 4.2 gives a summary of these optimization studies of MSGC's for high rate experiments with an emphasis on the topics related to CMS. However, some problems persist, namely the damages that can be produced by accidental discharges induced by heavily ionizing particles (HIP's), putting thus severe limitations on the safety margin in gain before breakdown in MSGC's.

In the last few years, new types of micro-pattern gaseous detectors have been developed. Some of them yield similar performances as MSGC's and allow to work at lower voltages, reducing therefore the problem of safety margin limitation encountered in MSGC's. Among these new structures the Small Gap Chamber (SGC) and the Gas Electron Multiplier (GEM) are of particular interest within the CMS collaboration. These two detectors are described in section 4.3.

Finally section 4.4 describes the CMS forward-backward MSGC tracker.

4.1 The Micro Strip Gas Counter (MSGC)

Confronted with the increasingly demanding requirements of high energy physics experiments, the MWPC has met two major limitations: its limited granularity and counting rate capability. Below 1 mm wire spacing and below 2 mm anode-cathode gap, it is extremely difficult to operate a MWPC because of the electrostatic and mechanical instabilities. Moreover, the ions produced during the avalanche are slowly collected by the electrodes, generating thus a space charge that modifies the electric field at the level of the anodes. As a consequence, the gain drops quickly at a particle flux above 10^4 Hz/mm^2. In 1988 A. Oed introduced a detector built with microelectronics technology: the Micro-Strip Gas Counter (MSGC) [41]. A schematic view of this detector is drawn in figure 4.1. It consists of an insulating substrate (glass) on which thin (1 μm) metal anode and cathode strips are alternating. Typical strip widths are 10 μm for the anodes and 100 μm for the cathodes. The substrate thickness is typically between 200 and 300 μm. A typical inter-anode distance (pitch) is 200 μm. An upper drift electrode, at negative potential, delimits the sensitive gas volume. This region is filled with the detector active medium: a suitable gas mixture. Typical voltages applied to the detector are: -520 V for the cathode strips and -3000 V for the drift cathode, the anodes being grounded. The resulting electric field configuration, shown in figure 4.2, consists of a uniform electric field (up

to 10 kV/cm) and a dipole field ($\geq$ 100 kV/cm) near the strip electrodes. When a charged particle crosses the counter the ionization electrons drift towards the anodes under the uniform electric field. During their drift, the electrons are subject to diffusion. Therefore the electron cloud is spread over several anode strips. Close to the anodes they will start an avalanche multiplication in the strong electric field. The electrons from the gas multiplication process are quickly collected on the anodes, while the positive ions migrate towards the cathode strips and the drift cathode. The motion of these charges induces currents on the electrodes that can be amplified and measured with an appropriate circuitry.

Because of their much larger drift velocity and since the avalanche occurs close to the anode, the electrons are very quickly collected by the anode and induce currents on the electrodes in less than 1 ns. On the contrary, positive ions move towards the cathodes inducing thus a negative current on the nearby anode and positive currents on the cathodes. In MSGC's, more than 90 % of the signal is provided by the ion motion, the electrons contribute by only 10 % [42].

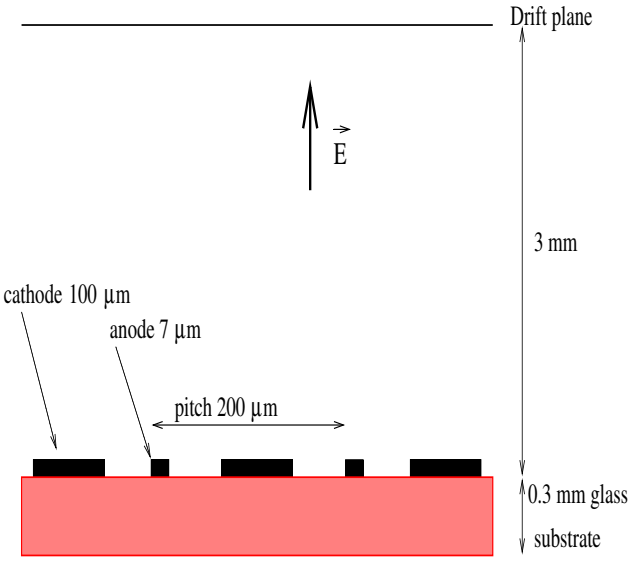

Figure 4.1: *Cross section of a MSGC with typical dimensions.*

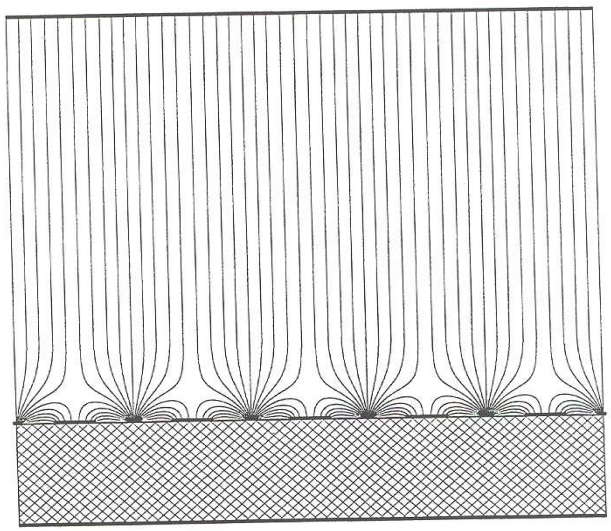

Figure 4.2: *Electric field lines in a MSGC.*

With its particular electrode geometry, the MSGC has substantially better performances than the MWPC:

- the high potential difference between the anode and cathode strips results in a high gas amplification. Proportional gains over 10^4 have been obtained [43]. Moreover the electric field is highly concentrated around the anode which leads to small fluctuations of the gas gain. An energy resolution of 11 % has been obtained for 5.9 keV X-rays [44];

- the particle impact point is determined with great accuracy thanks to the small strip spacing, made possible with the lithography technology, and to the diffusion which makes the charge spread over more than one strip. A position accuracy of 30 μm could be reached for MIP's with close to normal angle of incidence in detectors with 200 μm anode pitch;

- the time interval to evacuate ions produced in the avalanche around the anode strip is very short due to the presence of nearby cathode strips. The signal induction is thus

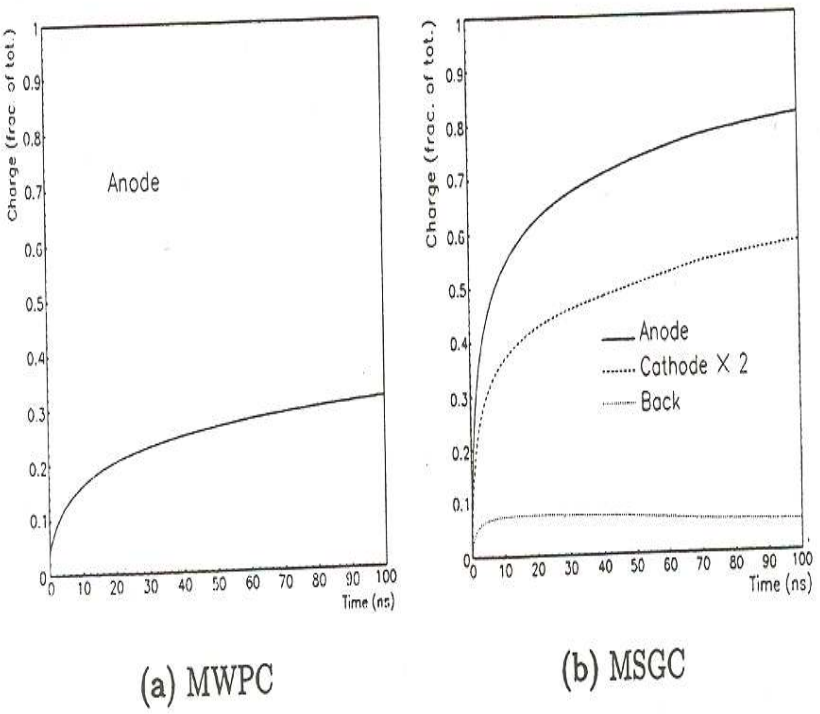

Figure 4.3: *Time development of the induced charge on the electrodes of a MWPC (a) and a MSGC (b) [42].*

faster in MSGC's than in MWPC's. This is illustrated in figure 4.3 where the fraction of charge collected by the strips is shown for a MWPC (a) and for a MSGC (b) as a function of time. It is clearly observed that after 50 ns, in the MSGC 70 % of the induced charge on the anode is already collected, while in the MWPC this is only 25 %. In this figure, the label *cathode* $\times$ 2 means that the corresponding signal is the sum of the signals induced on the two cathodes adjoining the anode where the avalanche develops. The cathode signal is clearly less than the anode one. This is the advantage of the anode readout for MSGC's;

- with this detector, high counting rates are achieved due to its high granularity and fast response. The MSGC can be operated at particle fluxes above 10^6 Hz/mm^2 [45, 46].

The MSGC has attracted a lot of interest since its introduction. Originally it was conceived as an X-rays or neutron imaging detector [47]. Its use has been extended to other fields mainly in high energy physics experiments as a tracking device. More details about the use of MSGC's as tracking devices will be given in the next chapter. Eight MSGC plates have been used in the NA12 experiment at CERN at proton fluxes up to 5.10^5 Hz/mm^2 [48]. Thanks to these detectors, the momentum of the 450 GeV/c proton beam has been measured with an accuracy of 2.1 GeV/c instead of 7 GeV/c measured before in the same experiment with MWPC's. At the fixed target experiment SMC, at CERN, 16 MSGC's of 10×10 cm^2 active area have been successfully used [49]. In the HERMES experiment at HERA, 12 MSGC's of large active area, up to 15×20 cm^2, constitute the vertex detector [50]. In all of these experiments MSGC's have proven their feasibility as tracking detectors. However, to be used in higher rate experiments, MSGC's had to be optimized. This is the subject of the next section.

4.2 MSGC optimization for high flux experiments

Due to their good features described in the preceding section, MSGC's have been chosen as tracking devices in some future high flux experiments. In the HERA-B experiment, MSGC's were foreseen to equip the vertex detector and to participate to the level-1 trigger [52]. In the CMS experiment, up to 20 000 detectors are planned to equip the outer part of the central tracking system. Meanwhile some stability problems were met during the test of MSGC's under high particle fluxes [53]. Indeed, gain degradation with time and with irradiation rate had been reported and great efforts have been undertaken to optimize this device in order to meet the high flux requirements.

The research programs focused on the following topics:

- development of large size substrates (more than 10×10 cm^2);
- choice of the electrode materials and the detector geometry;
- choice of the operating gas to achieve the highest possible stable gain, detection efficiency and the best spatial resolution. A high drift velocity is also required, to obtain a fast response, as well as a long term operation stability. For safety reasons, the amount of flammable components should be small;
- stability under irradiation with HIP's and neutrons;
- study of the detector response in the presence of an intense magnetic field (4 T);
- readout electronics.

These topics are linked to each other and will therefore not be described independently. First the influence of the detector material and geometry is discussed. Requirements on the gas mixture, the readout electronics and the high voltage scheme are then presented. Finally, breakdown mechanisms in MSGC's are described with an emphasis on those related to HIP's.

4.2.1 Detector material

4.2.1.1 Substrate

The material most commonly used as a substrate for MSGC's is the high resistivity (10^{15} Ωcm) DESAG D-263 glass. It is commercially available with good surface quality and can be produced in large size samples as required in high energy physics applications. However early studies of chambers made with D-263 glass have shown a gain drop up to 40 % after an accumulated charge of 100 mC/cm of strip [54, 55]. Another problem that has been reported is a gain instability at counting rates above 10^4 Hz/mm^2.

This last phenomenon is attributed to the charging up of the substrate. Indeed, with high resistivity substrates, ions produced in the avalanche may stick to the insulating surface between strips; if these ions are not neutralized, the electric field in the neighbourhood of the electrodes is modified and consequently the gain of the counter. As a consequence, at detector power on, an initial decrease of the gain is also observed before an equilibrium is reached. The value of the gain at this equilibrium is rate dependent. This is demonstrated is figure 4.4 where the gain is shown as a function of time for different counting rates of 5.9 keV X-rays for a plastic substrate, that is also insulating [56].

The charging up effect can be reduced by the use of substrates with moderate resistivity. Systematic studies have shown that the lower the surface resistivity the higher the rate capability [45, 57]. With a bulk resistivity in the range 10^9-10^{12} Ωcm or a surface resistivity of

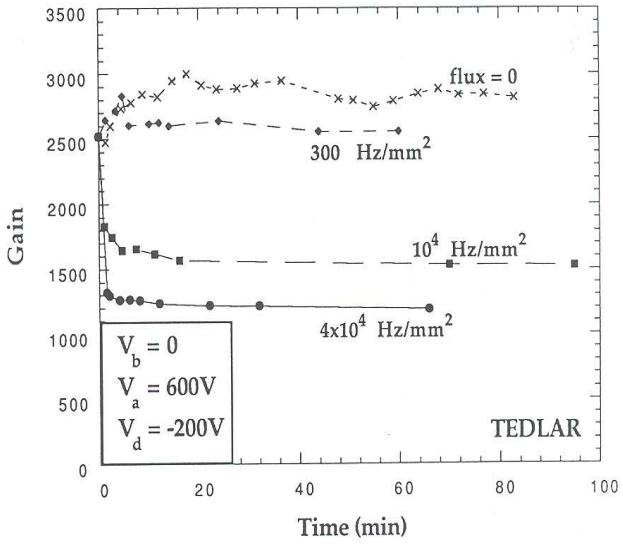

Figure 4.4: *Gain as function of time, at various X-ray fluxes, for an MSGC made with a Tedlar plastic substrate of resistivity 10^{14} Ωcm [56].*

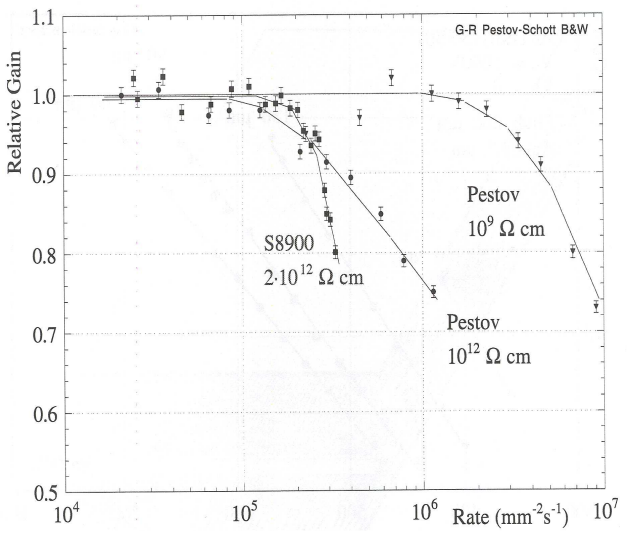

Figure 4.5: *Relative gain as a function of the irradiation rate for MSGC plates manufactured on semi-conducting glass in the range of resistivity 10^9-10^{12} Ωcm [59].*

10^{14}-10^{16} $\Omega/\Box$, several groups have obtained counting rates up to 10^6 Hz/mm^2 without significant gain drop [57, 58]. An example is given in figure 4.5 where the gain is reported as a function of the counting rate for three different types of glass [59].

Low resistivity substrates do not only solve the rate capability problem but also the ageing problem to an acceptable level. Several groups have reported results from ageing studies with substrates made of semi-conducting glass (Moscow, Pestov or Schott S-8900) where the counters could sustain radiation doses up to 100 mC/cm of strip without significant degradation of gain or energy resolution [54, 55]. This dose was estimated to be equivalent to the charge accumulated during 10 years of LHC operation [1]. An example of such results is reported in figure 4.6 for the Schott S-8900 glass [59]. The main drawback of these materials is that they contain heavy elements which would affect tracking performances in an experiment such as CMS.

A low resistivity support can also be obtained by coating a high resistivity substrate with a thin-film conductive layer reducing the surface resistivity to values in the range 10^{14}-10^{15} $\Omega/\Box$ (see for example [60, 61]). This can be done in two ways:

- by the chemical vapour deposition of thin ($\sim$ 1500 Å) diamond-like layers (DLC coating). Several plates of 300 μm thick D-263 glass, varying in size from 10×10 cm^2 to 10×25 cm^2, have been successfully coated [62, 63]. The resulting resistivity is in the range 10^{14}-10^{15} $\Omega/\Box$. The samples have shown stable operation and sustained radiation doses up to 80 mC/cm of strip as shown in figure 4.7. The detectors exhibit stable operation up to rates in excess of 10^6 Hz/mm^2.

- by the sputtering on standard glass (D-263 glass) of $\sim$ 1 μm of electronic conductive glass (Pestov glass for example). As shown in figure 4.8, this coating clearly improves the rate capability of the counter and allows to operate at counting rates in excess of

[1] This is an over-estimation. Indeed, it can be shown, taking the simulation results from [14], that the dose accumulated during 10 years of LHC operation is less than 50 mC/cm of strip.

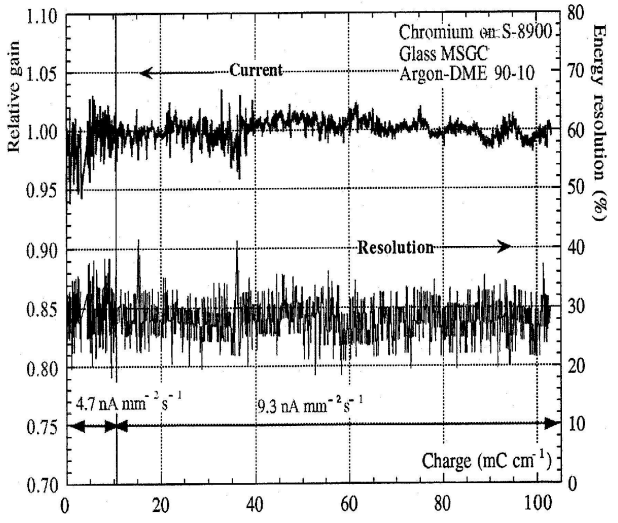

Figure 4.6: *Relative gain and energy resolution versus the accumulated charge per cm of strip, for an MSGC made of chromium strips deposited over a S-8900 glass substrate [59].*

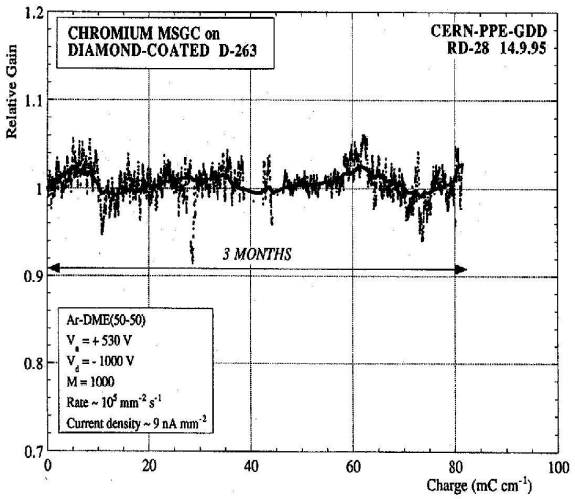

Figure 4.7: *Relative gain versus the accumulated charge per cm of strip for an MSGC made of diamond-coated D263 glass substrate [51].*

10^6 Hz/mm^2 [61]. Long term behaviour was also demonstrated with this type of coating [14].

Experimental studies have demonstrated the advantage of the Pestov glass coating over the DLC coating in terms of the high gas gain reached before breakdown in the presence of HIP's [14]. The Pestov coating was then chosen for MSGC's in the CMS experiment [14].

The main disadvantage of using low resistivity supports is that a higher voltage must be applied to the strips in order to reach the same gas gain as with high resistivity substrates [64, 65]. An example is given in figure 4.9(a) where the gain is shown as a function of the applied anode voltage for a coated and an uncoated substrate. A 50 V difference is seen between the two counters [65]. This could be understood by looking at the electric field strength between the anode and the cathode for the two counters as shown in figure 4.9(b) [66]. The avalanche is highly localized at the anode in the uncoated substrate. Due to the coating, the anode field is reduced by a factor 3 near the anode implying a higher voltage for the same gas amplification. In addition, in the case of the coated substrate, a high uniform field is created between the anode and the cathode strips. This would favour the development of unquenched streamers as will be explained in section 4.2.4.

4.2.1.2 Electrodes and detector geometry

Early observations suggested that the ageing rate of MSGC's could be affected by the nature of the metal used for the anode and the cathode strips [53]. The metal resistivity also plays an important role in the uniform detector response as will be seen below. Adherence of the strips to the substrate must be excellent.

It has been reported that detectors made with aluminium strips present a 10 % gain drop after less than 1 mC/cm of accumulated charge. On the contrary, identical detectors with gold strips sustained radiation doses in excess of 50 mC/cm of strips [67]. The MSGC group in

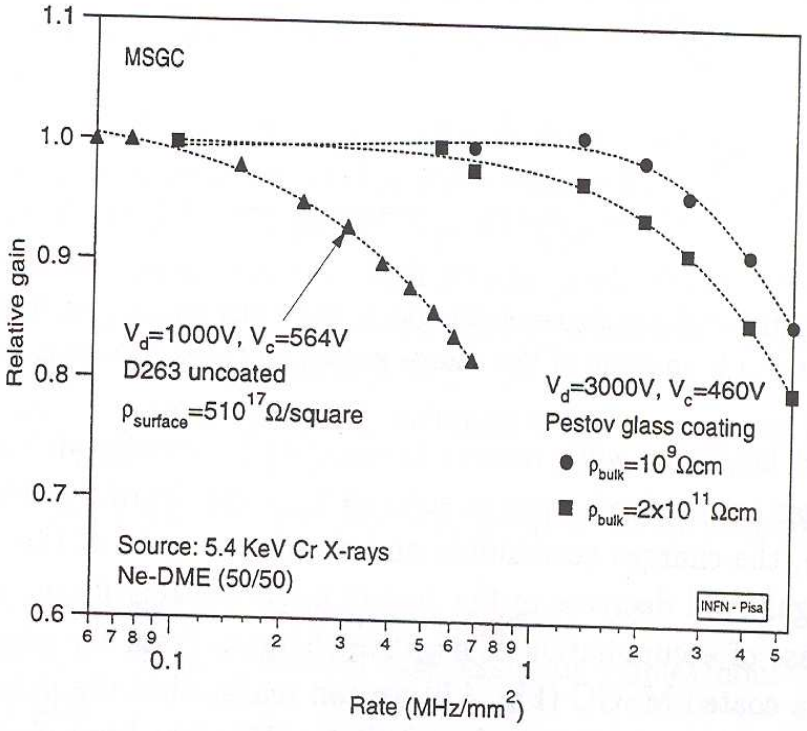

Figure 4.8: *Relative gain as a function of the irradiation rate for an uncoated (D263) MSGC and for MSGC's coated with a thin film layer of Pestov glass having two different bulk resistivities [14].*

NIKHEF has reported promising results with nickel strips but it needs further investigations to meet the LHC requirements [68]. As can be seen from figures 4.6 and 4.7 chromium strips also can sustain radiation doses up to 100 mC/cm of strip.

Strips made of high resistivity materials like chromium are limited to only a few centimetres in length since they generate a position-dependent response. This is demonstrated in figure 4.10 showing, for chromium strips, a comparison between the measurements and the calculations of the signal relative pulse height and peaking time versus the distance between the irradiation spot and the readout amplifier [69]. Due to the high resistivity of chromium, 30 % of signal attenuation and 30 % of increase in the signal peaking time are seen already at 6 cm. Use of low resistance metals for the strips ($\leq$ 40 Ω/cm) is mandatory when working with long strips, *e.g* gold. As a result gold has been chosen as the strips metallization for MSGC's in CMS [14]. Since its adherence to the substrate is difficult, gold is applied over a thin (0.1 μm thick) adhesion layer, like Ti.

The electrode width also influences the MSGC performances. Figure 4.11 shows the dependence of the detector gain on the applied anode strip voltage for different cathode widths [70]. Each measurement was stopped when a discharge occurred between the anode and cathode strips. The anode pitch is 200 μm and the anode width is 7 μm. For this pitch, the largest stable gain reached before breakdown is obtained with a cathode width in the range of 90-100 μm. A similar test was done for the anode width; the result is shown in figure 4.12 [57]. The anode voltage leading to breakdown does not depend on the anode width in the range 5-13 μm but the maximum gas gain increases significantly with decreasing anode widths. However, the anode width, for technological constraints, can not be less than 5 μm. In CMS, it will be either 7 or 10 μm.

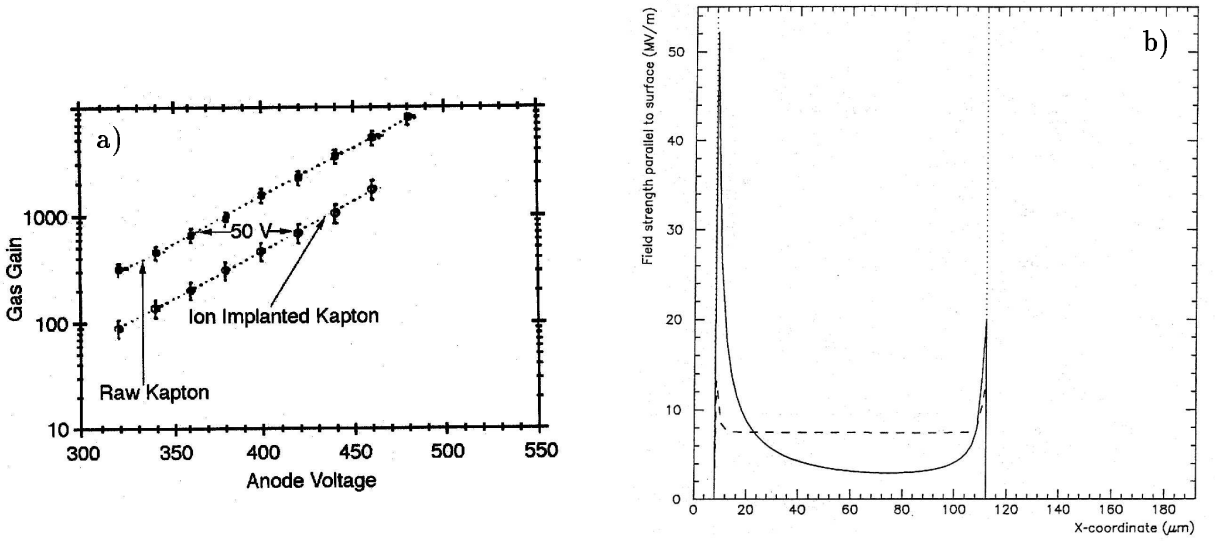

Figure 4.9: a) Gain as a function of the voltage difference between the anode and cathode strips in MSGC's made on substrates of surface resistivity of 10^{17} $\Omega/\Box$ and 10^{13} $\Omega/\Box$ [65]. b) Electric field strength as a function of the distance to the anode, for an uncoated (solid line) and a coated (dashed line) MSGC [66].

4.2.2 Gas mixtures

The detector performances are affected by the choice of the gas mixture for the MSGC system. In CMS, the gas mixture should have the following characteristics:

1. high primary (n_p) and total (n_T) ionization densities to ensure large signals and high detection efficiency ($\geq$ 98 %) in thin detectors (3 mm gas gap for MSGC's in CMS). Table 4.1 gives the values of (n_p) and (n_T) for gases commonly used in MSGC's [71, 72]. A theoretical efficiency of 99.9% can be ensured by a primary ionization density of more than 30 electrons per cm, which restricts the choice to gas mixtures with a high content of either CO_2, DME, CF_4, organic or heavy noble gases;

2. long efficiency plateau. Figure 4.13 shows a typical behaviour of the MSGC detection efficiency as a function of the cathode strip voltage. The efficiency plateau is defined as the range of cathode strip voltages where the efficiency is at its maximum. The length of this plateau is important since it presents a safety margin for long term operation. A gain drop of a few percents, due to ageing, can be compensated safely by an increase of the cathode strip voltage. One should thus choose the gas with the longest efficiency plateau;

3. high gas gain at modest strip voltages to make the efficiency plateau start at low strip voltages. This is important regarding possible sparks as the spark energy is proportional to the square of the applied strip voltage. A lower strip voltage thus decreases the risk of damaging the strips with discharges and also decreases the discharge rate;

4. high drift velocity to ensure a fast detector response. Simulations have shown that the CMS tracker will operate satisfactorily if the MSGC's can provide timing information within 50 ns, which is equivalent to two LHC bunch crossing intervals [73]. The electron drift velocity in the gas volume is the key parameter for the MSGC time resolution. In a

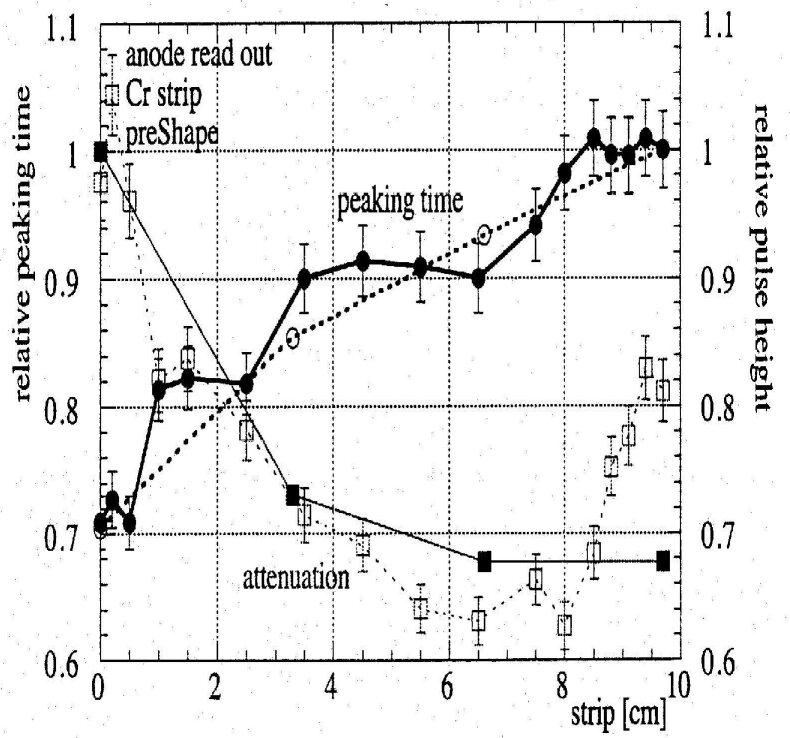

Figure 4.10: *Measured (points with error bars) and simulated relative peaking time and pulse height as a function of the distance to the readout side along chromium strips [69].*

3 mm gas gap, the gas mixture should have an electron drift velocity above 60 μm/ns to meet the above requirements;

5. no electronegative components. As an example, it is well known that the CF_4 molecule can absorb an electron and dissociate to form F^-, CF_3^+ ions together with F^*, CF_2^* and CF_3^* radicals [74]. At electric drift fields greater than 5 kV/cm, the attenuation of electrons by CF_4 is very high and can reach up to 8 dB/mm leading therefore to detection inefficiencies [75];

6. good quenching properties to ensure the detector stability. Use of high Z noble gases can initiate photon feedback processes since they present low energy excitation levels as was explained in section 3.3;

7. no detector ageing. Some gases, as organic compounds, lead to fast degradation due to polymer deposition on the strips. Long term tests have been successfully carried out with DME-based mixtures [10, 76];

8. appropriate transverse diffusion in order to spread the charge over more than one strip to achieve the required spatial localization. However a too large diffusion can also increase the strip occupancy;

9. small Lorentz angle for the 4 T magnetic field orthogonal to the electric field to keep the required spatial resolution in the barrel part of the CMS tracker. Since the magnetic field is parallel to the electric field in the end-cap tracker, this is not a concern in this region;

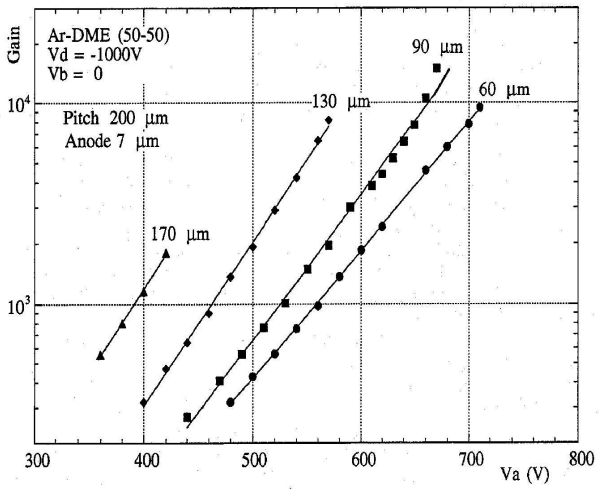

Figure 4.11: *Dependence of the gain on the voltage difference between the anode and cathode strips, for various cathode widths. The anode pitch is 200 µm and the anode width is 7 µm [70].*

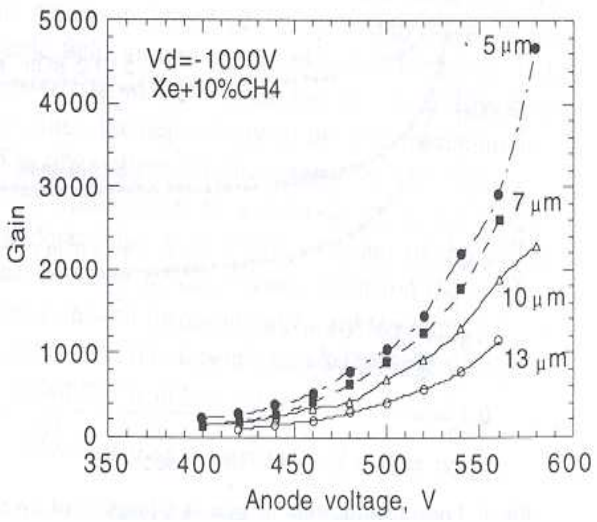

Figure 4.12: *Dependence of the gain on the voltage difference between the anode and cathode strips, for various anode widths [57].*

10. no or small amount of flammable components.

The gas mixture optimization for LHC conditions has been intensively studied. Due to its high primary and total ionization densities, good quenching properties and good radiation hardness, DME is often envisaged for MSGC operation [43, 75].

A first study of gas mixtures for MSGC's at LHC was carried out at NIKHEF [75]. The authors studied mixtures of Ar, CF_4, C_2H_4, Xe, CO_2 and DME with respect to the drift velocity, the detection efficiency and the spatial resolution. The best candidates at that time were CO_2/DME 40/60 % and Xe/CO_2/DME 30/40/30. This latter is much more expensive due to the high cost of Xe. Other groups used Ar/DME or pure DME as these two gases are known for their long term stability [43]. The advantage of adding an amount of a noble gas to DME is that one can reach a full detection efficiency at lower strip voltages than with CO_2/DME mixtures or pure DME.

More recently, the group of R. Bellazzini observed very large proportional gains, up to 2×10^4 with Ne/DME 70/30 % [77]. This behaviour is attributed to the good quenching properties of DME and to the very high excitation and ionization potentials of neon (16.6 eV and 21.5 eV respectively). The photon feedback is strongly suppressed as compared to argon. Still, the detection efficiency had to be checked since the neon primary ionization density is low. The drift velocity in these mixtures was not known either. This was one of the motivations for us to start studies of Ne/DME mixtures. This study has been extended to other binary and triple DME based mixtures. The complete work and the results are described in section 5.4 of chapter 5.

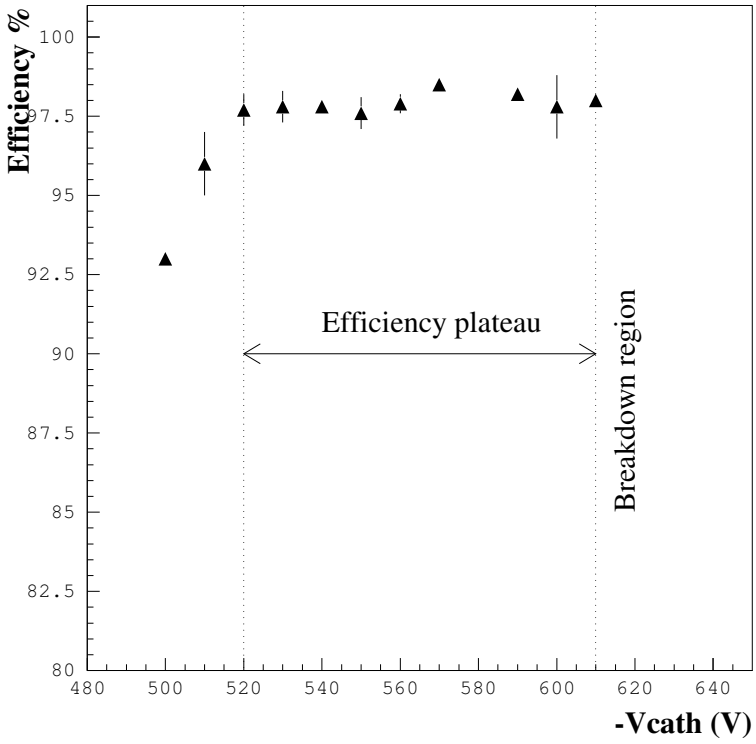

Figure 4.13: *Typical dependence of the MSGC detection efficiency on the cathode strip voltage.*

4.2.3 Readout electronics and high voltage supply

The MSGC signals are characterized by large fluctuations in duration and size. Indeed, the ionization being spread along the particle path, electrons generated close to the substrate will reach the anode before those created further away. The signal is thus extended in time; the time development of the signal in MSGC's is of the order of 50 ns. Moreover, since the ionization and the avalanche processes are of stochastic nature, MSGC signals vary in shape from one event to the next. The charge collected on the electrodes from a MIP is about 20000-50000 electrons, depending on the gas gain.

At LHC, the proton collision frequency will be 40 MHz. The MSGC readout system should perform a fast shaping of the signals into short pulses in order to assign each signal to the bunch crossing interval in which it has been produced. Low noise and sufficiently fast amplifiers are needed to amplify the MSGC signals. In CMS, the front-end electronics is based on the APV6, both for silicon and Micro-Strip Gas counters [78]. It consists of 128 amplifiers and a multiplexer for serial readout. Each channel of the APV6 contains a charge amplifier and a shaper of 50 ns RC-CR shaping time, and a 160 location deep memory into which samples are written at the LHC machine frequency of 40 MHz. Upon reception of a trigger, the channel output is computed as a weighted sum of three samples. The values of these weights are derived on the basis of the CR-RC impulse response of the amplifier. This method, called "deconvolution", has demonstrated the ability to confine the deconvoluted signal to only one LHC beam crossing interval in the case of silicon detectors [79]. In the case of MSGC's, a new version of the APV6 has been developed [80].

Gas	$\mathbf{n}_p$ (cm^{-1})	$\mathbf{n}_T$ (cm^{-1})
He	3.3	7.6
Ne	10.9	39.9
Ar	24.8	96.6
Kr	33.0	197.5
Xe	44.8	313.3
CO_2	33.6	100.0
CH_4	24.8	59.3
CF_4	51	-
DME	62	-

Table 4.1: *Primary and total ionization densities for gases commonly used in MSGC detectors [71, 72].*

The main factors that affect the readout performance at the LHC are the noise and the so called "ballistic deficit". The amplifier noise increases with the detector capacitance and should be minimum. The ballistic deficit is the charge reduction factor due to the use of shaping times shorter than or comparable to the intrinsic collection time of the counter. This results in a reduced signal. Because of their charge collection time, MSGC's equipped with APV's suffer from a ballistic deficit, after deconvolution, of 50 % at a shaping time of 50 ns [81].

The MSGC operation requires two negative voltages: the cathode strips and the drift cathode. The MSGC collaboration is developing a system to monitor and control these high voltages. Inside the MSGC, the cathode strips can not be grouped and powered all together. This is because the energy stored in the capacitance of the overall detector is so large that it could damage the strip pattern in case of a discharge. To limit the risk of damage, it was found safer to subdivide the detector into groups of 16 strips, each group being connected to the high voltage through a large current limiting resistor ($\sim$ 5 MΩ). In this case all electrodes that are grouped together and connected to the high voltage carry a signal of reverse polarity with respect to that of the electrode where the avalanche develops, due to capacitive couplings. The amount of this signal is equal to the total charge divided by the number of connected strips. Thus in case of 16 strips connected together, the cross talk results in a 6 % of the total charge reduction of the signal per strip.

4.2.4 Breakdown mechanisms in MSGC's

The appearance of discharges at some critical applied voltage is a permanent feature in gas proportional counters and has been intensively studied (see for example [82, 83, 84]).

In MSGC's, at pressure close to atmospheric, systematic studies have shown that the dominant mechanism of discharge is a fast transition from proportional multiplication mode to streamer mode [84]. Unquenched streamers must be avoided since the energy released in a discharge may be large enough to damage the strip pattern or even to produce local short circuits. Streamers can be triggered by the space charge field of large avalanches produced by HIP's. Indeed, a HIP, produced for instance by the interaction of a hadron with the detector materials, can release more than 100 times the ionization released by a MIP. In CMS, the neutron fluences at 50 cm from the interaction point is estimated to be about 10^3-10^4 Hz/mm^2, which generates a rate of HIP's of 0.1-1 Hz/cm^2 in the detectors.

Although they can survive a high flux of electrons or X-rays without problems, MSGC's are found to be instable in beams of low energy pions or protons [52, 83]. This confirms that the discharges are induced by the HIP's themselves. The presence of HIP's thus reduces the maximum attainable gain of the counter. This behaviour has been observed by other groups where the MSGC's were exposed to α-particles emitted from ^{220}Rn and presented a fast increase of the discharge rate with the cathode strip voltage [85]. The maximum gain that could be reached was 3500, less than a factor 2 above the gain required for efficient MIP detection. This margin between the voltage required for efficient detection of MIP's and the appearance of discharges in the presence of HIP's is small and is not satisfactory for long-term operation of a large MSGC system in the LHC environment.

These and other observations have stimulated detailed studies of the discharge mechanism in MSGC's in view of finding how to avoid them and how to extend the counter lifetime [52, 83, 84]. Various schemes have been proposed to suppress the discharges or to limit the subsequent

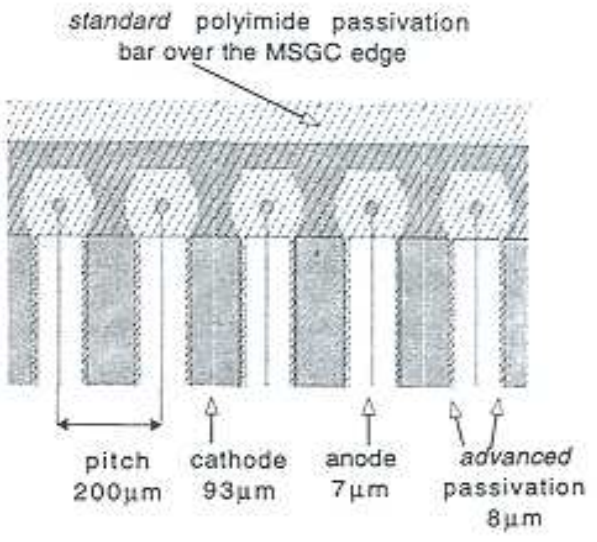

Figure 4.14: *Scheme of the standard and the advanced passivation techniques in a MSGC.*

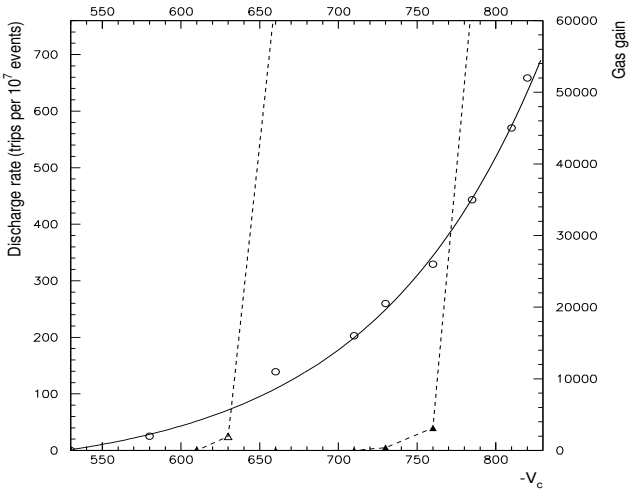

Figure 4.15: *Discharge rate as a function of the cathode strip voltage, in diamond coated MSGC's, with and without advanced passivation (closed and open triangles respectively). The gain dependence is also shown [86].*

damages.

It has been shown that the most critical part of the MSGC's are the electrode edges [14, 43]. In these regions, the electric field is reinforced which favours the extraction of electrons. To prevent this, the strip ends are made less sharp and, in addition, a 200 μm wide passivation layer (polyimide) has been added on top of the anode-cathode structure, at the detector borders. This is the so-called "standard passivation" procedure (see figure 4.14).

Another improvement has been made at the level of the cathode strips themselves since it is known from earlier tests that the presence of high field on the cathode edge (see figure 4.9(b)) limits the maximum attainable voltage in MSGC's, due to electron extraction from the cathodes. Moreover, the presence of this high field favours the streamer development which leads to breakdown. To prevent this phenomenon to take place, the group of R. Bellazzini has introduced the so-called "advanced passivation" technique in which the edges of the cathode strips are

coated by a narrow (4 μm wide) dielectric layer in order to reduce the electric field in this region [86] (see figure 4.14).

Figure 4.15 shows the gas gain and the discharge rate for diamond coated MSGC's with and without the advanced passivation, exposed to α-particles. It is clearly seen that the cathode strip voltage margin is increased by more than 100 V in the passivated counter.

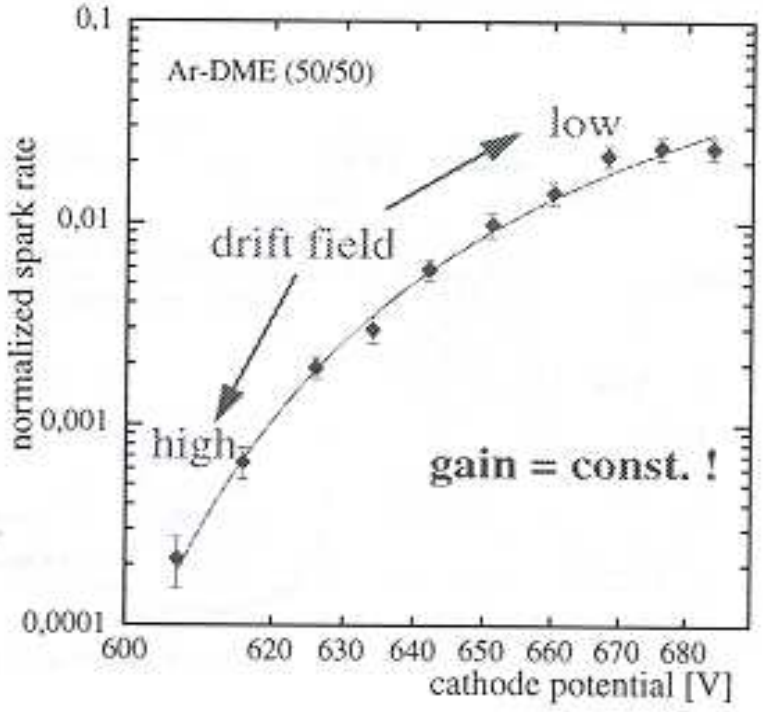

Figure 4.16: *Normalized discharge rate as a function of the cathode strip voltage for a fixed MSGC gain of 3000. The electric field varies between 1 and 10 kV/cm [87].*

For a given gas gain, a further reduction of the electric field at the cathode strip edges can be achieved by increasing the electric drift field [14]. This has a number of advantages. First, a high electric drift field contributes to the gas gain and therefore one can work with a lower cathode strip voltage minimizing thus the risk of damage due to discharges. Secondly, the discharge rate is decreased, at a constant gain, when the electric drift field is increased as can be seen from figure 4.16. The third advantage is that at high drift fields, the Lorentz angle is reduced.

In 1997, the MSGC group of CMS has carried out a program to test MSGC's with advanced passivation in a high intensity hadron beam in presence of HIP's. This test is described in section 5.5. The detectors that were tested in this beam correspond to the final CMS specification, the so-called "baseline counter" [14], which consists of:

- a substrate made of D263 glass, 300 μm thick, under coated with a 1 μm thick layer of Pestov glass with a surface resistivity in the range of 10^{15}-10^{16} $\Omega/\Box$;
- gold strips deposited on an adhesive Ti layer; the anode width is 7-10 μm;

- a standard passivation and an advanced passivation achieved with BCB [1] or polyimide;
- a gas gap of 3 mm;
- a drift cathode potential set between -3000 and -3500 V.

4.3 New Micro-pattern gas detectors

Triggered by the invention of the MSGC, a new generation of micro-pattern gas detectors has emerged during the last decade. A recent review of these new developments can be found in references [85, 88]. Among these new structures, the Small Gap Chamber (SGC) [89] and the Gas Electron Multiplier (GEM) [90] are of particular interest in experiments working in a high rate environment and might be envisaged as possible alternative to MSGC's for the CMS outer tracker. Both yield similar performances as the MSGC and allow to work at lower voltages.

4.3.1 Small Gap Chamber (SGC)

The Small Gap Chamber (SGC) is a variant of the MSGC structure as shown in figure 4.17. The main feature of this design is the reduction of the distance between the anode and cathode strips from the usual 50 μm to only 10 μm. In addition this space is covered by a passivating polyimide layer. The fraction of the exposed insulating area is thus reduced. As a consequence, charging-up of the substrate is minimized and the substrate coating is no longer needed. However the passivation of the strip edges is essential to obtain large gains. This particular design allows to work efficiently with lower cathode strip voltages, starting from -350 V. Prototypes of this design have been built and tested in the laboratory and in low and high intensity hadron beams [89, 91]. Promising results were obtained in terms of robustness in presence of HIP's. Further developments will focus on ageing studies and the production of large area prototypes.

4.3.2 Gas Electron Multiplier (GEM)

The Gas Electron Multiplier (GEM) consists of a thin polymer foil ($\sim$ 50 μm thick), metal coated on each side, and perforated regularly by a high density of holes [90]. The hole diameters can be between 40 and 140 μm, the hole spacings between 90 and 200 μm. With a suitable voltage of a few hundreds volts, applied between the two sides of the GEM foil, an electric field of up to 100 kV/cm is created in the holes.

Inserting the GEM foil in the gas volume of a gaseous detector (MSGC for instance as illustrated in figure 4.18) allows to pre-amplify the electrons released in the gas above the GEM by the ionizing particle, and to pass them through the holes. In case of a MSGC coupled to a GEM, this pre-amplification allows to reduce the cathode strip voltage by up to 200 V to reach the same total gain. This is extremely important since it increases the safety margin before breakdown.

Since its introduction by F. Sauli, the GEM has attracted a lot of interest. Actually it is planned to equip the MSGC's of the HERA-B experiment [52]. However, a full MIP detection efficiency, in the presence of a high intensity magnetic field, has still to be proven which is a major concern for the barrel part of the CMS tracker.

[1] Benzo-cyclo-Buthène.

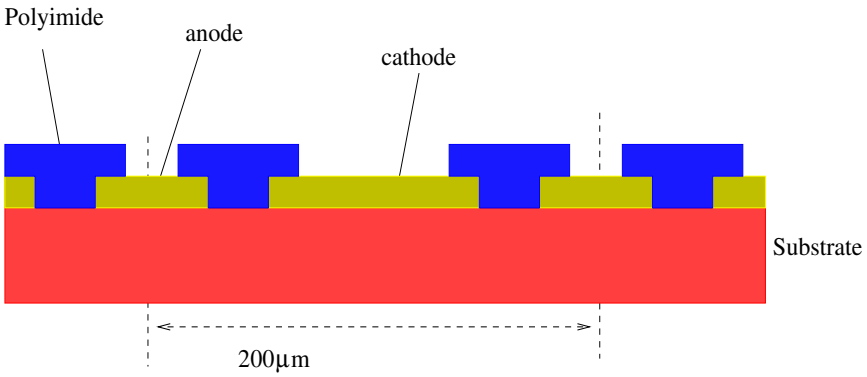

Figure 4.17: *Cross section of a Small Gap Chamber.*

4.4 The forward MSGC tracker design

The outermost part of the CMS central tracker is composed of MSGC's (see figure C.2). This part is divided in a barrel and in a forward-backward part (see section 2.3.5). The general layout of the end-cap part, subject of this work, is first given in section 4.4.1. Section 4.4.2 describes some specifications of the MSGC's foreseen in this region. The main design criteria to build this tracker are a full radial coverage of the entire area for each disk, minimization of dead space between the detector modules, rigidity of the disk assembly consistent with material budget constraints, and access for services. To equip the end-cap region with MSGC's, two approaches have been proposed. Both are described in section 4.4.3. Section 4.4.4 summarizes briefly the quality acceptance test of the substrates and of the modules before the final assembly.

4.4.1 General layout

The forward-backward region of the MSGC tracker consists of eleven disks, perpendicular to the beam pipe, on either side of the MSGC barrel part extending in z from $\pm$ 1215 mm to $\pm$ 2760 mm and covering the radial region from 700 mm to 1165 mm.

The disks are made of plates machined to the appropriate dimensions. These plates consist of honeycomb core material, 20 mm thick, embedded between two carbon fibre skins. All disks in one end-cap are connected together by means of carbon fibre bars to form super-modules as illustrated in figure 4.19.

The disks are equipped with gas boxes, called detector modules, having the shape of a sector of an annulus and housing several individual MSGC's. These modules are mounted on each disk in four concentric rings as shown in figure 4.20. All modules of a given ring are identical. Rings 2 and 4 are located on the front side of the disk (towards the interaction point), rings 1 and 3 on the back side. In the same figure, it can be seen that the front and the back rings overlap radially to guarantee a full detector coverage in the radial direction for high p_T particles. Table 4.2 gives some major parameters of the end-cap MSGC tracker and table 4.3

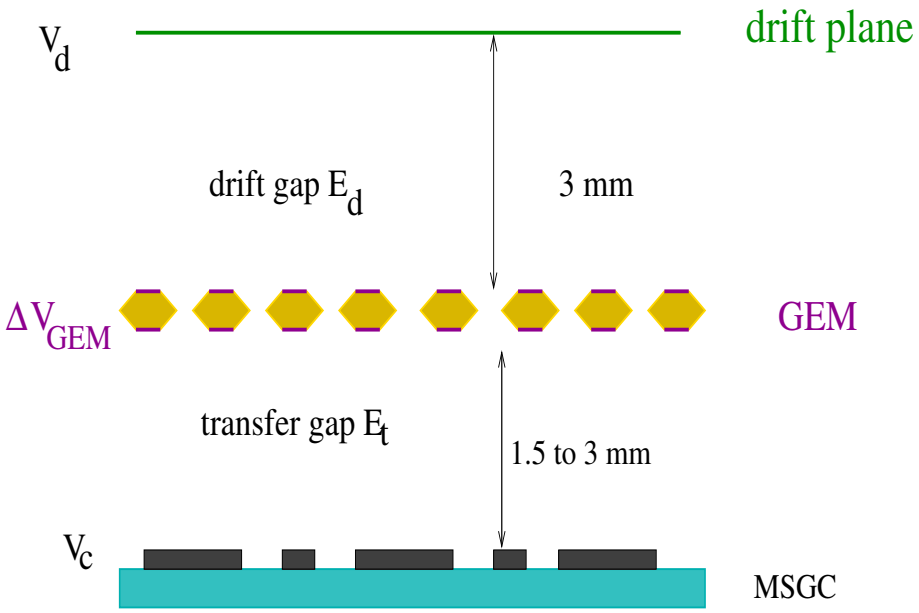

Figure 4.18: *Cross section of a MSGC equipped with a GEM.*

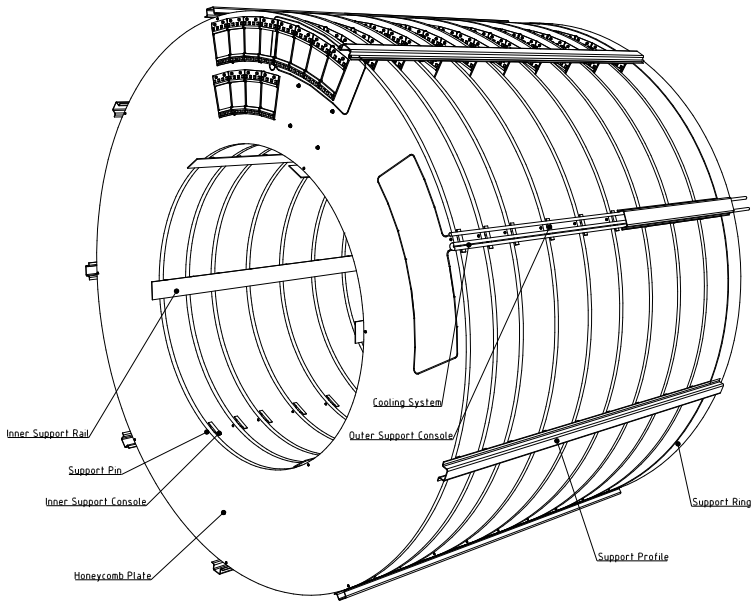

Figure 4.19: *CMS forward-backward disk structure.*

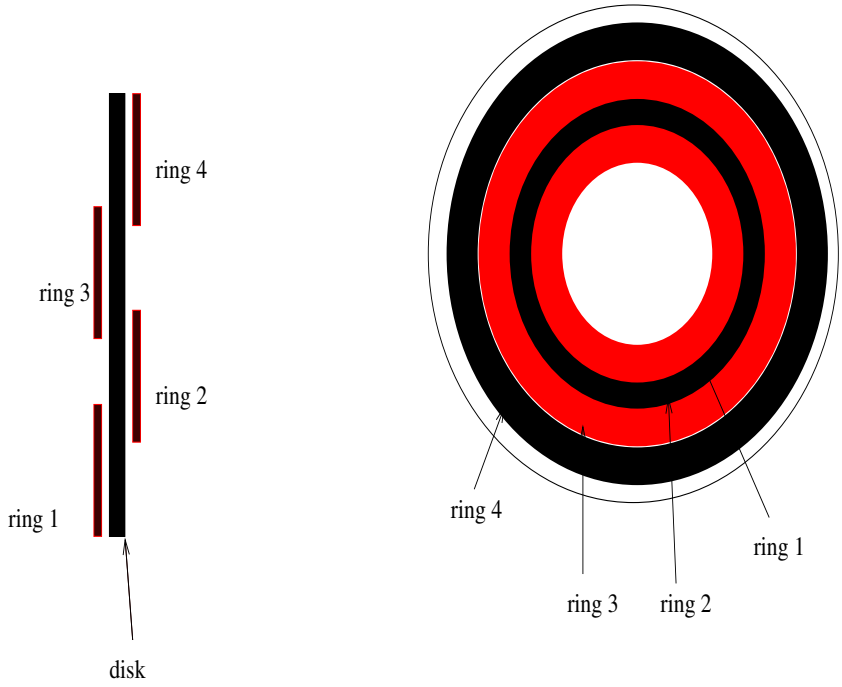

Figure 4.20: *Schematic view showing the arrangement of the four rings on a end-cap disk.*

minimum radius	700 mm
maximum radius	1165 mm
number of disks	11 each side
number of rings	4 per disk
active radius length	440 mm
ring overlap in radius	8.6 %

Table 4.2: *Some parameters of the MSGC end-cap tracker.*

summarizes the dimensions of the rings on the disks. The MSGC's of intermediate rings 2 and 3 have radial strips measuring the r-ϕ coordinate with a precision of 40 μm. The z position is given by the z position of the MSGC substrate. For pattern recognition purposes and vertex reconstruction needs, it is important to have at least two space points measurements for each track in the end-cap MSGC system. To ensure this, rings 1 and 4 are equipped with MSGC's with two layers of strips at a small stereo angle to enable also the measurement of the radial coordinate with an accuracy of 1 mm (see below). In each super-module, the outermost disk is entirely equipped with double-sided detectors.

More details about the mechanical aspects of this region can be found in reference [14].

4.4.2 Specificity of the end-cap MSGC's

As it is convenient for pattern recognition to have the strips pointing to the beam pipe in the forward and backward part of the tracker, the MSGC substrates will have a trapezoidal shape in that region. Therefore the anode pitch is not constant along the strips. This could lead to gain variations along the strips unless care is taken to compensate with an optimization of the strip geometry. In a first attempt, the authors of reference [92] have tested a MSGC with four

ring	location	type	r_{in}(mm)	r_{out}(mm)
4	front	double	1005.4	1150.0
3	back	single(double)	889.6	1033.1
2	front	single(double)	776.1	878.6
1	back	double	710.0	797.5

Table 4.3: *Dimensions of rings on the disks. The items between brackets refer to the outermost disks which are equipped with double sided counters.*

different sets of strip geometry. Gain variations along the strips up to 70 % have been reported when only the anode-cathode gap varies along the strips, the electrode width being constant. On the contrary, this variation could be minimized by varying the cathode width too. Later on, the MSGC NIKHEF group suggested to vary both the anode-cathode gap and the cathode width with the radial position following an homothetic rule given by:

$$G = \frac{P}{8} + 20\mu m \tag{4.1}$$

where G represents the anode-cathode gap and P the anode pitch; the anode width, being too small ($\sim$ 10 μm), is kept constant (see figure 4.21). In CMS the forward-backward MSGC's will be produced following this formula. For the other characteristics they will follow the

ring	strip length(mm)	lower pitch(μm)	Higher pitch(μm)
4	144.6	248	217
3	143.5	208	179
2	102.5	204	180
1	87.5	200	178

Table 4.4: *Some characteristics of the forward-backward MSGC strip pattern.*

specifications defined for the CMS "baseline counters" as given at the end of section 4.2. There will be 513 (512) cathode (anode) strips , per single sided substrate. In the inner ring substrates, the anode strip width is foreseen to be 7 μm instead of 10 μm elsewhere. Some parameters of the forward-backward MSGC strip pattern are summarized in table 4.4. The strip length is chosen so as to maintain the occupancy due to ionizing particles to the level of a few percents taking into account the increase of the particle rate with the pseudorapidity in this region [14].

About one half of the MSGC's will be designed to measure also the second coordinate in order to provide space points for charged particle tracking. Use will be made of the so-called "twin chambers". Such chamber consists of two counters mounted back-to-back. One has 512 radial anode strips and measures the r-ϕ coordinate with the usual accuracy (40 μm); the other has 256 anode strips tilted by a stereo angle of 50 mrad and provides measurements of the radial coordinate with a resolution of 1 mm, sufficient for tracking purposes. The MSGC end-cap tracker consists of 2240 single sided counters and 2512 twin chambers leading to a total number of readout channels of 3 076 096.

The high voltage and the readout electronics schemes were already described in section 4.2.3.

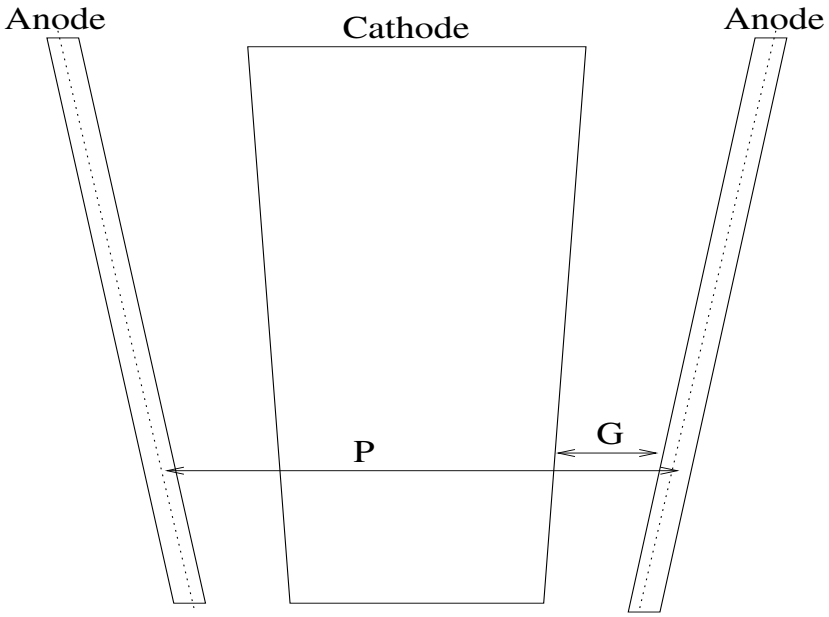

Figure 4.21: *A trapezoidal detector's cell showing the anode and cathode geometry. P denotes the anode pitch and G the anode-cathode gap.*

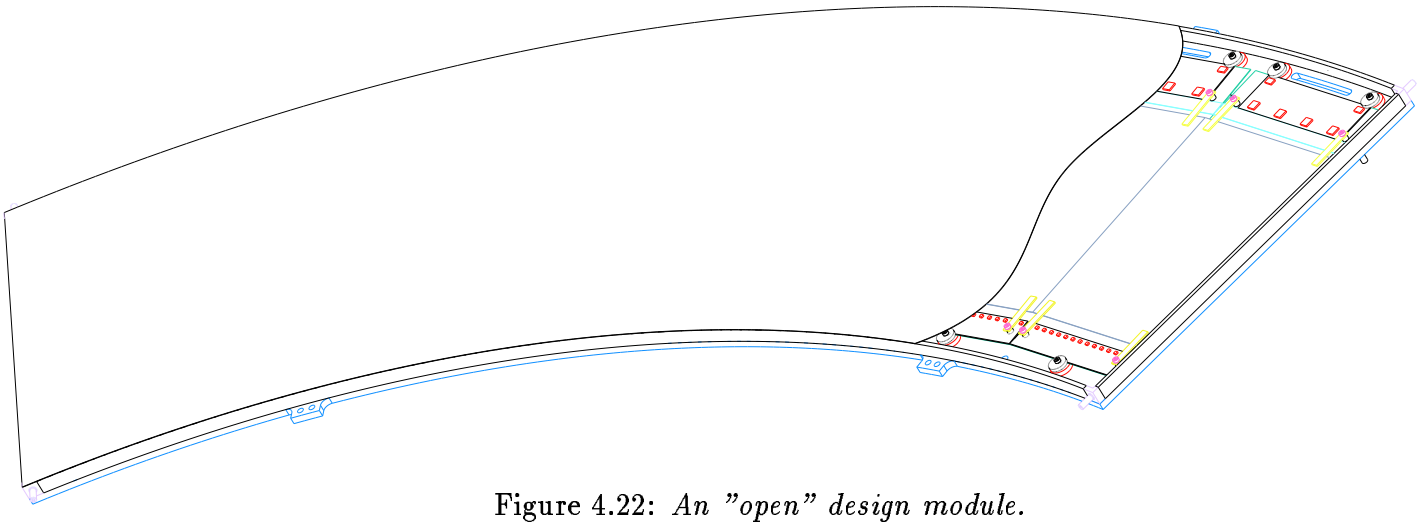

Figure 4.22: *An "open" design module.*

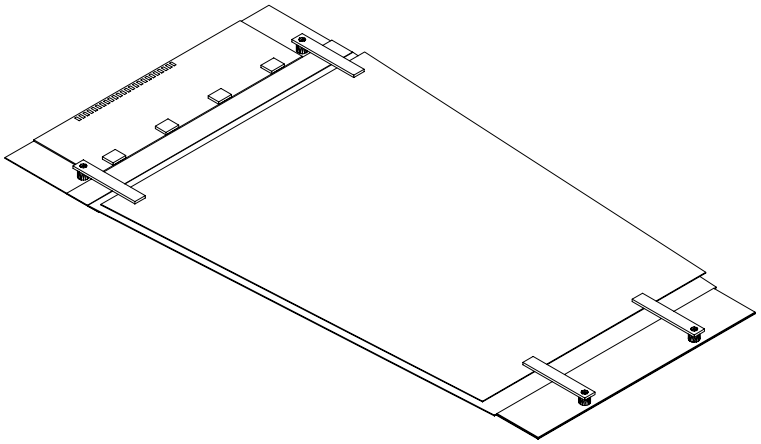

Figure 4.23: *Schematic view of a wedge shaped detector equipped with its high voltage and readout electronics hybrids.*

4.4.3 MSGC modules

In the MSGC end-cap design, each detector module is housing several MSGC's put side by side without a gas tight wall between them and without overlap in the azimuthal angle. The region between two adjacent counters in a given module is called "strip less region". The alignment of MSGC's inside a module is done in such a way that the distance between the two anodes adjoining the strip less region is twice the nominal pitch elsewhere in the substrate. This idea comes from the fact that no detection inefficiency has been noticed in the region of a single broken strip in an MSGC counter.

Two different approaches have been proposed to design the detector modules: the so-called "open" and "closed" designs.

4.4.3.1 The open design

This design allows to test MSGC counters including their electronics before mounting them inside a module [93].

Each detector module provides a common gas volume for 7 to 10 adjacent trapezoidal MSGC counters (see figure 4.22). The bottom plate of the gas box is made of aluminized carbon fibre-honeycomb composite structure [94, 95]. The curved edges of the gas box are made of aluminium tubes with a rectangular section of 3×10 mm^2 and a wall thickness of 200 μm. These are used as integrated gas distribution manifolds, the gas mixture being delivered via laser-drilled holes ($\sim$ 200 μm diameter) facing every MSGC inside the box.

Each MSGC counter is made of one substrate, one drift cathode, one front-end electronic hybrid and one high voltage hybrid (see figure 4.23). During the entire assembly and the test procedure of the individual counters all parts remain accessible for intervention and even replacement. Once the counter is fully tested and operational, it is aligned and held in place inside the detector module in a stress-free manner using 3 excentrics. Two alignment holes per MSGC are printed on the rigid bottom of the box along a radius of the disk. The MSGC is aligned under a microscope by centering two fiducial marks, printed in its central cathode strip, into these two small holes. The module is finally sealed by an aluminized kapton foil glued on top of the frame (see figure 4.22). Results from finite elements analysis calculations showed negligible deformation of the gas box when loaded with the counters (see references[94, 95]).

The cooling of the front-end electronics is achieved by water flow through a thin aluminium tube, identical to the one used for the gas distribution, but glued along its 10 mm side to the front side of the composite panel. Data lines and electrical services to the front-end hybrids are fed through the composite. Since the cathode strip voltage may require a fine tuning at the level of individual counters, there is one cathode strip voltage line per counter. The drift voltage does not require a fine tuning and therefore only one drift voltage line per module is planned.

On the external face of the box, six fiducial marks are printed for the alignment of the detector module with respect to its nominal position on the disk. The modules are placed side by side in a given ring, without overlapping in the azimuthal angle, which leads to a dead space of 1 %.

In case of a short circuit the detector module can be opened and repaired by replacing the faulty individual MSGC. The other counters within the module are therefore not lost. Although this is a good feature of the design, this will not be so easy during operation of CMS since the access to the central detector at LHC will be rare and difficult. Therefore, a complete test of the counters before mounting them into the module is mandatory. The drawbacks of this design is that the visual alignment procedure can not be easily automated and that the final electronics must be available before assembling the modules.

4.4.3.2 The closed design

The main feature of the closed design, now adopted by the CMS collaboration [14], is that it foresees the front-end electronics and the high voltage hybrids outside the gas volume to avoid undesired gas pollution by critical materials mainly during the bonding procedures. This means that the gas volume is closed at an early construction stage [96].

A schematic view of the detector module proposed in this design is shown in figure 4.24. It consists of three frames, aligned to each other, supporting four substrates, four drift planes, the electronics hybrid and the high voltage hybrid.

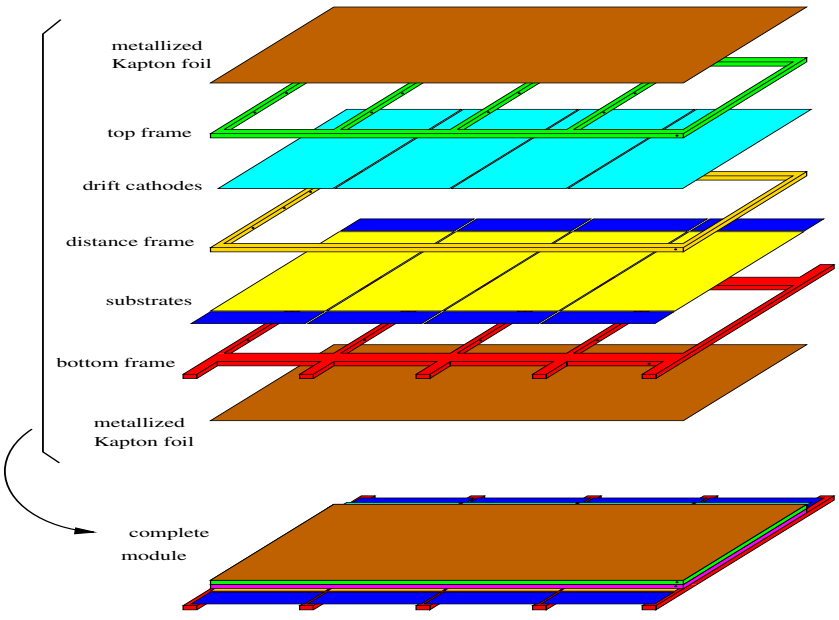

Figure 4.24: *Overview of the various elements forming a "closed" design module.*

The four substrates are glued to the 2.5 mm thick bottom frame after being aligned with respect to each other. Straps on the front and the back sides of this frame hold the readout and the high voltage hybrids [1]. Three stiffening bars inside this frame are foreseen to avoid deformation of the substrates through sagging.

Another frame, called the distance frame, having a 3 mm height and without internal bars, separates the substrates and the drift cathodes, defining thus the sensitive detector volume. This frame is glued onto the bonding pads of the substrates, which are bonded to the readout and to the high voltage hybrids, outside the gas volume. The top frame, equivalent to the bottom one, supports the drift cathodes. The module is closed by a kapton foil coated with aluminium on the outside. The substrate alignment and the glueing of the substrates to the bottom frame are done with a special tool which provides the possibility of controlling the substrate position and fixing the bottom frame to the aligned substrates (see reference [14]).

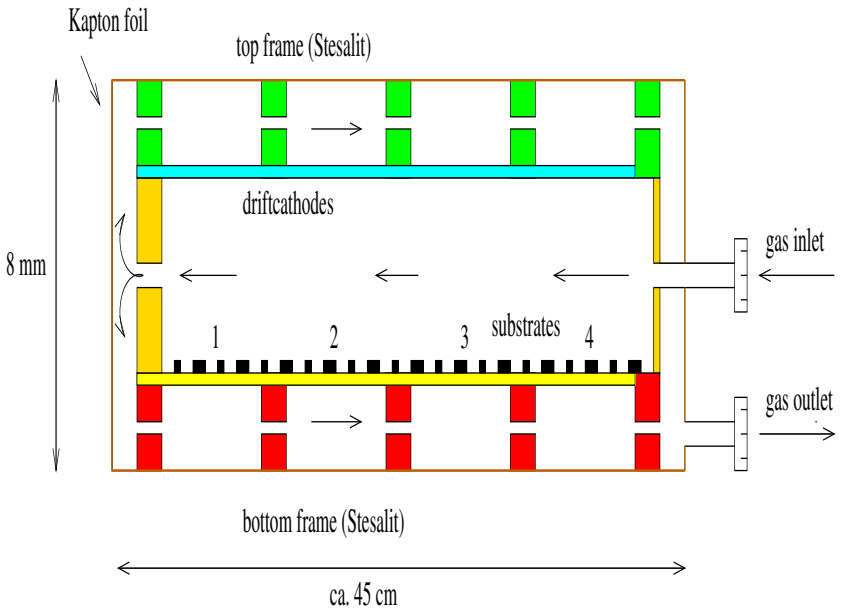

Figure 4.25: *Cross section of a closed design module showing the gas flow through the module.*

In each detector module, there is one common drift voltage line and four cathode strip voltage lines. The gas distribution principle within the module is illustrated in figure 4.25 where a cross section of such a module is shown. This gas flow provides equalization of the pressure on both sides of the substrates and of the drift cathodes.

The gas is delivered to the module via a hole in one side of the distance frame and passes through the detection volume. It leaves this volume via three holes in the other side of the distance frame and enters a gas diversion leading to two gas volumes on either side of the counter. Finally, the gas leaves the module through holes in the bars of the top and bottom frames.

Once the detector module is completed, it is mounted on the disk. In each detector module, the straps of the bottom frame are equipped with six precision holes in order to fix the module to the disk. These holes are aligned to the fiducial marks that are printed on the disk. Due

[1] For the final layout, the CMS collaboration is investigating the possibility to have only one support holding both hybrids, the readout electronics and the high voltage.

to the 3 mm thick frame, placing the modules side by side onto the disks will result in a dead space of 1.52 % and 1.24 % respectively for the innermost and the outermost rings.

Another design, based on the same concept as this of the closed design, is illustrated in figure 4.26. Here the gas volume is closed by the drift plane itself, a 3 mm thick metallized carbon fibre honeycomb plate. More details about this variant of the closed design can be found in reference [97].

Although the closed design involves less human intervention which prevents the substrates from possible accidental damage, the main worry is that a faulty counter in one module would require the replacement of the whole module. Indeed, the substrates are glued to the frames and therefore can not be removed.

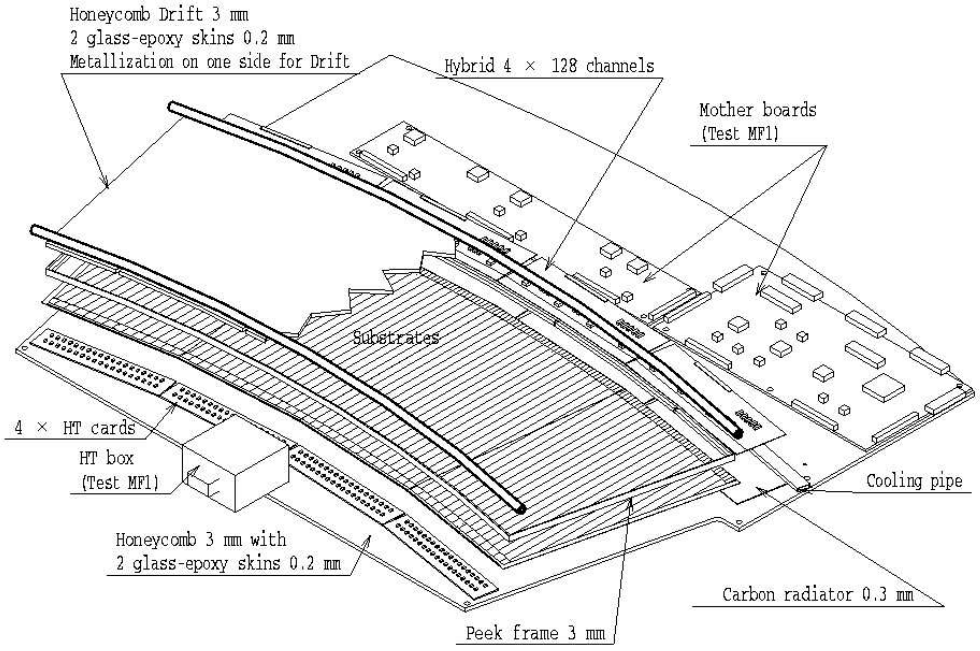

Figure 4.26: *Scheme of the module following a variant of the closed design.*

4.4.4 Quality control and final assembly

The acceptance test of the detecting elements and the assembly procedure which will be followed to build the MSGC end-cap tracker will be based on the experience acquired in the past.

In order to achieve the required performances, the following steps will be followed from the construction to the assembly phases [1]:

- after production, each substrate is fully inspected at the factory itself;
- upon reception of the substrate, an electrical test of all individual anode strips is performed in a computer-controlled probe station. Production failures and interrupted anode strips are thus detected;
- to check the quality of the lithography, a fast optical inspection is performed;

[1] Details can be found in reference [14].

- if the quality of the substrate fulfils the acceptance test (*i.e* less than 2 % defects), the substrate is cut to the correct size using a diamond scriber and cleaned in an ultrasonic bath;
- the substrate surface resistivity is then measured by applying a high voltage to the cathode strips and measuring the current between the anodes and the cathodes.
- the substrates are then aligned into the modules;
- a gas leak test is done;
- the readout chips are checked;
- the high voltage and the readout electronics are bonded to the strips.

Each module is then subject to an extensive test procedure including:

- a test of bonded electronic channels;
- a high voltage test;
- a test with radioactive sources and with cosmic rays.

The module is then mounted onto the corresponding disk.

4.5 Conclusions

Micro Strip Gas Counters have been subject to extensive studies. A large number and variety of prototypes have been manufactured and tested in the laboratory and in particle beams. Most of the conditions necessary to guarantee the detector lifetime at high flux experiments have been determined. Nevertheless, the weak point of these counters is their weakness against destructive sparks induced by heavily ionizing particles. The passivation technique, found to extend the gain range before sparks appear, in tests with α-particles, had to be tested in a high intensity hadron beam (see chapter 5). In the same chapter, a study of several gas mixtures will be presented aiming to identify the best gas mixture for the CMS application.

Some features of the MSGC end-cap system in CMS had still to be tested, mainly the behaviour resulting from the particular shape of the counters. Several tests of trapezoidal counters, mounted side by side in a common gas volume, have been carried out. The results of these tests are given in chapter 6.

Chapter 5
Studies on MSGC for future operation at LHC

Introduction

The development of MSGC's for the future CMS experiment at CERN poses severe challenges. For this reason, extensive studies have been carried out, as explained in chapter 4. Within the CMS collaboration itself we performed several tests of MSGC prototypes, both in a cosmic rays hodoscope and in test beams.

As the gas mixture plays a major role in MSGC performances, in particular in CMS, the Belgian groups have carried out a gas study of DME based gas mixtures, in a cosmic rays hodoscope in Brussels and in a laser setup in Antwerp. My personal contribution was the measurements of the particle detection efficiency, the signal over noise ratio and the spatial resolution, in the cosmic rays hodoscope, and the calculation, by means of a set of simulation programs, of the electron drift velocity, the transverse diffusion coefficient and the lorentz angle in the presence of a magnetic field. These calculations are compared to the measurement done in Antwerp. Three MSGC's were used to perform the gas study in the cosmic rays hodoscope.

The complete experimental setup is described in section 5.1. The method to calibrate the hodoscope drift chambers is also described and discussed in detail. Section 5.2 describes the procedure of MSGC data analysis and some results are given. Section 5.3 gives a description of the simulation program that is used in order to help to understand the experimental results. Results from our measurements of the signal to noise ratio, the detection efficiency and the spatial resolution are given in section 5.4. Measurements of the electron drift velocity and the transverse diffusion coefficient for the same gas mixtures, performed in the laser setup, are also presented. These measurements are compared to the calculations we have performed.

The greatest challenges in the design of the CMS MSGC system come from the high hadron rate environment leading to the presence of HIP's as explained in section 4.2.4. Many investigations of the MSGC's behaviour under high rates of HIP's have been made using radioactive sources. However, it turned out that these laboratory tests were not sufficient to simulate the conditions of high intensity hadron beams. Section 5.5 reports on the test of five MSGC's in a high intensity hadron beam.

5.1 The cosmic muon hodoscope at the IIHE

A cosmic rays hodoscope has been built in Brussels, in order to study the MSGC response to Minimum Ionizing Particles (MIP's).

Cosmic muons of energy above the energy corresponding to the minimum of ionization are selected, and their tracks are reconstructed thanks to a set of twelve drift chambers. In the middle of the hodoscope, a stack of MSGC's has been installed. In this section and in the next one, results of three prototypes are reported, one of them consists of two half substrates put side by side in order to test the behaviour of multi substrate modules. The two other ones are taken as a reference.

5.1.1 Description of the hodoscope

The cosmic rays hodoscope is shown schematically in figure 5.1. Cosmic muons are selected by means of a coincidence of two scintillators, 40×40 cm^2 large. A 10 cm lead absorber positioned immediately above the bottom scintillator allows to select muons of momentum above 300 MeV/c. The muon tracks are reconstructed by means of twelve drift chambers, 20×40 cm^2,

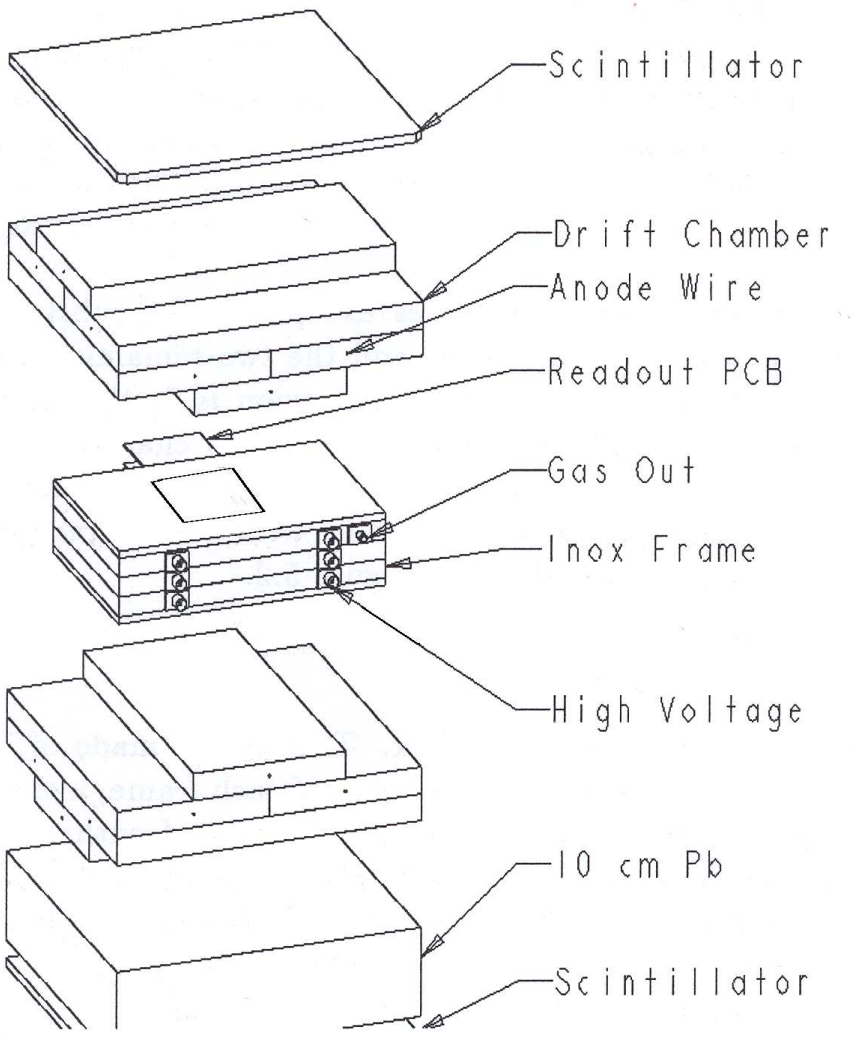

Figure 5.1: *Layout of the cosmic rays hodoscope and the MSGC stack.*

grouped three by three. The drift chambers are identical to the ones that were used for the DELPHI experiment [98]; they are shown schematically in figure 3.11. In each group, the third chamber , called the central chamber, is staggered over the two other ones placed side by side, to solve the left-right ambiguities. The groups are placed so as to provide four impact points along the muon track in two orthogonal projections, two on each side of the tested MSGC's. The selected tracks cover an area of up to 20×20 cm^2 in the mid plane of the hodoscope.

The drift chambers, filled with an Ar/CH_4-90/10 % gas mixture, are operated in proportional mode. The voltages applied to the chambers are -3.5 kV and + 2.2 kV respectively for the cathodes and the anode wire. The expected drift velocity is $\approx$45 $mm/\mu s$ [15].

5.1.2 MSGC prototypes

Three MSGC's were placed on top of each other. Two of them, the lowest one called the first one, and the highest one called the third one, are identical to the counters built for the SMC experiment [49]. These are 10×10 cm^2 chambers with 512 parallel anode strips. The substrates consist of DESAG D263 glass of 300 μm thickness. They are glued to a printed circuit board frame, together with the front-end electronics and the high voltage lines. The electrode strips, etched on the glass support, are made of aluminium, 1 μm thick. The anodes are 7 μm wide and the cathodes, 90 μm wide. The anode pitch is 200 μm. The anode strips were wire bonded to the readout electronics using an ultrasonic bonding machine. The current in the preamplifier is limited to less than 1 A by a 740 Ω protective resistor between the anode strips and the preamplifier. These resistors are made of short NiCr strips, 5 nm thick. The cathode strips are connected to the high voltage by groups of sixteen via a 4.7 MΩ resistor. This reduces the electrical energy released in case of sparks to 20 μJ; the capacitance of a cathode group is about 100 pF.

The drift planes consist of 300 μm thick aluminized glass, mounted on four spacers placed at each corner of the chamber. The gas gap is 3.3 and 2.7 mm for the first and third reference MSGC respectively.

The second counter is similar to the other ones except for the substrate where a piece containing 48 anode strips was cut from the centre and the two remaining pieces of substrate were placed side by side at a distance of 70 μm. This region is further called the strip less region. Its response to cosmic rays will be studied in the next chapter in section 6.2. The distance between the two anodes adjoining the strip less region is 400 μm instead of 200 μm elsewhere. These two anodes were adjusted to be parallel with an accuracy of 5 μm. The gas gap of this chamber is 3 mm. Its layout is shown in figure 5.2.

5.1.3 Gas and high voltage systems

The three MSGC's are placed in a common gas box. This box is made of individual frames 25×20 cm^2 and 2 cm thick, one per chamber. In the side of each frame, a slit is made to allow the connection of the counter to the data acquisition system via feedthrough printed circuit boards. A photograph of one of these chambers mounted in its frame is shown in figure 5.3. To minimize the Coulomb multiple scattering the gas volume is closed by two 50 μm aluminium foils of the size of the counters.

To avoid gas pollution, use of plastic materials was avoided. The gas box and the gas distribution tubes are made of stainless steel. A gas mixer, built by the group of Mons University, was used. It has four inputs and outputs, with massflowmeters calibrated for noble gases, CO_2, DME and isobutane respectively. Thus various gas mixtures can be tested and the desired gas mixture is delivered to the counters through one of the outputs.

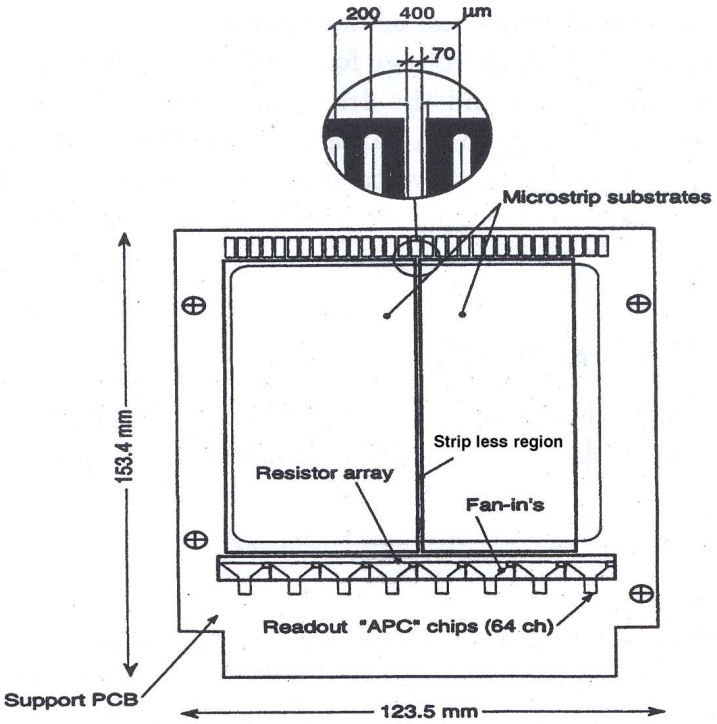

Figure 5.2: *Layout of the prototype with a substrate in two pieces.*

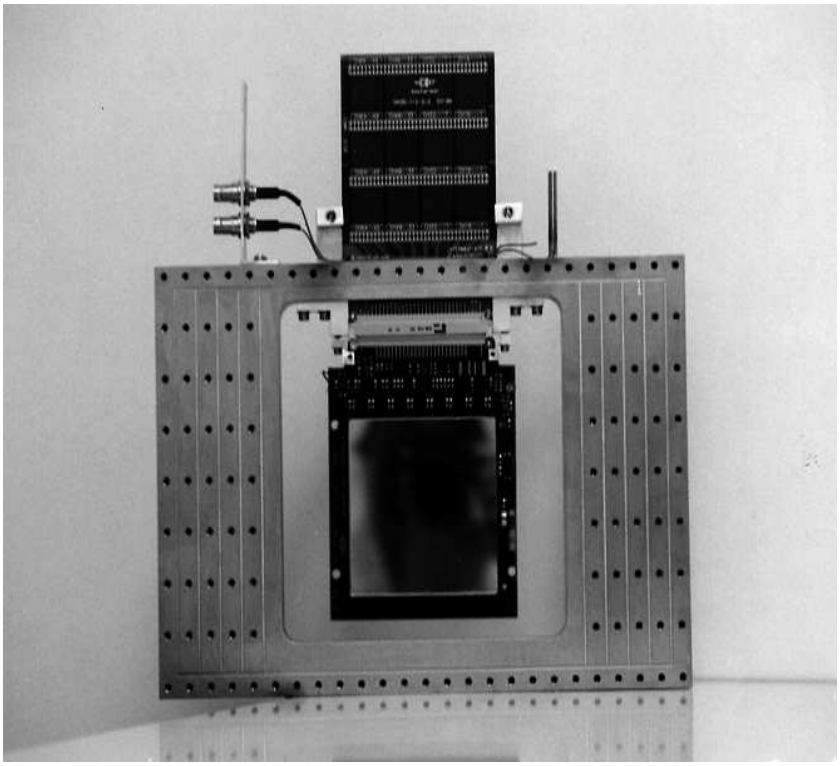

Figure 5.3: *Photograph of an MSGC mounted in a stainless steel frames.*

A CAEN power supply delivered the high voltage for the drift planes and the cathode strips. The currents drawn by the cathode strips and the drift planes are controlled by opto-coupled electrometers. In order to protect the strips from damage in case of a spark, the cathode strips are automatically disconnected from the high voltage as soon as the current drawn by the cathode strips exceeds a certain threshold. Typically, the leakage current was below 10 nA and the trip level was set to 80 nA.

5.1.4 Readout and DAQ system

The data acquisition system for the hodoscope and for the MSGC's is based on a Macintosh II-ci computer interfaced with a CAMAC (Computer Automated Measurements And Control) instrumentation bus.

5.1.4.1 Drift chambers

The anode signals in the drift chambers are read out and amplified by charge amplifiers, developed at CERN. The electrons drift time, in the twelve drift chambers of the hodoscope, is measured by two 12-bit Time-to-Digital Converters (LeCroy 2228A TDC's). Each TDC has eight channels measuring the time interval elapsed since a common start has been received from the coincidence of the hodoscope scintillator signals. A TDC channel is stopped by the anode signal of the drift chamber connected to it.

5.1.4.2 MSGC's

The MSGC anode signals are read out by integrated electronics: the Analogue Pipeline Chips (APC). Originally the APC chips have been designed for the silicon vertex detector of the H1 experiment at HERA [99]. Nevertheless it was used for MSGC readout [49], and is currently used in the HERMES experiment [50]. This chip contains 64 preamplifiers. As shown in figure 5.4, each channel is composed of two elements: a preamplifier mounted as a current integrator and a 32 cell switched capacitor pipeline, sampling the output of the preamplifier every 100 ns. Only the difference between the signal samples before and after the event are read out.

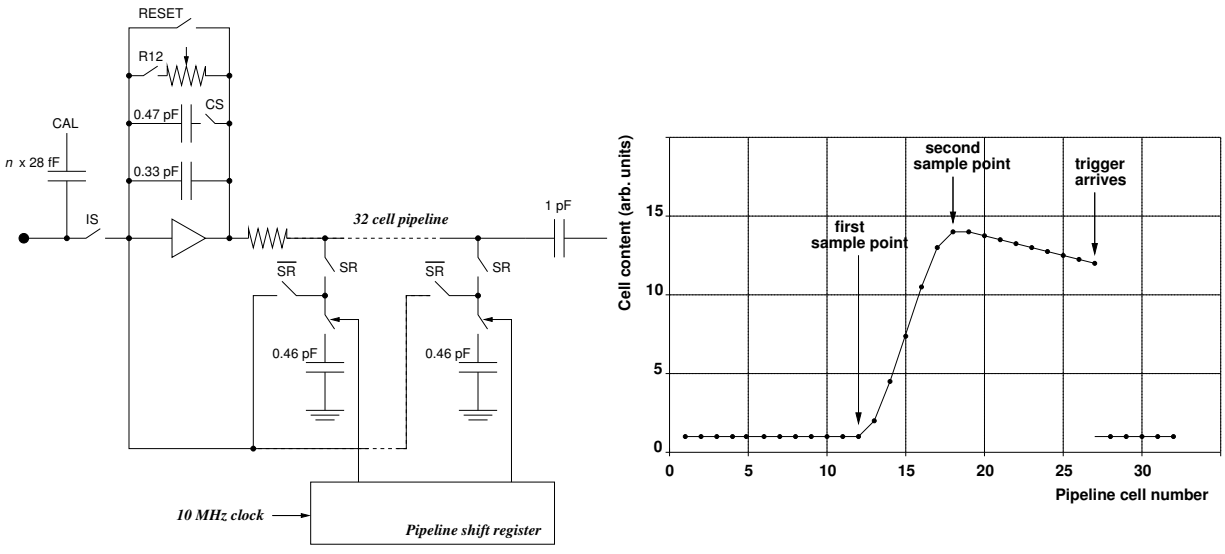

Figure 5.4: *Schematic diagram and principle of the APC chip.*

The standard operation of the APC chip consists of three phases. The first phase corresponds to the data recording phase. The charge of one anode strip is integrated and stored in the 0.33 pF capacitor. By enabling the switch R12 the capacitor is discharged by a feedback resistor. Sequentially, the output voltage of the preamplifier is stored into each of the 32 pipeline capacitors of 0.46 pF. This is made possible thanks to the pipeline shift register which contains 32 bits controlling the 32 capacitor switches, and shifts every 100 ns. The second phase starts when an event trigger is received. The detector signals are disconnected from the preamplifier input by opening the switch IS and the pipeline capacitors are disconnected from the preamplifier outputs to memorize the past 3.2 μs. The discharge resistor is disconnected by the R12 switch and the RESET closed in order to clear any injected charges from the SR and $\overline{SR}$ switches when changing from phase 1 to phase 2. The pipeline pointer is moved to the cell called the first sample point corresponding to the instant just before the rising edge of the anode signal. The RESET switch is then opened and the switch of the selected pipeline buffer is closed and opened. The buffer charge is then read back onto the preamplifier and stored into the latch capacitor of 1 pF. Then the preamplifier feedback capacitor is discharged again to reset the preamplifier. The readout of the second pipeline buffer is started by advancing the pipeline shift register to the second sample point which corresponds to the maximum of the anode signal. Again it is re-read through the preamplifier, and the difference of the two sample signals is stored into the latch capacitor. In the last phase, the signals of all channels are sequentially read out. The correct positions of the sample points are chosen by maximizing the signal amplitude. For our application, the optimum delay between the two samples is found to be 600 ns.

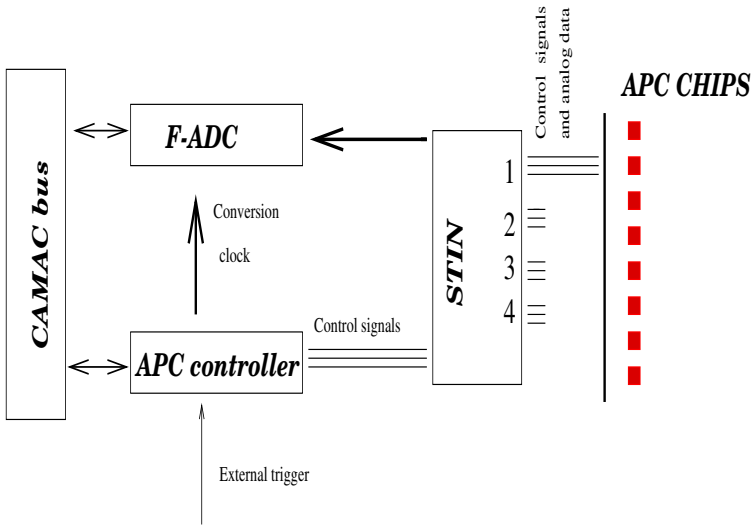

Figure 5.5: *Readout chain of the MSGC system.*

The MSGC readout chain is shown in figure 5.5. The APC controller provides the control signals that are required to operate the 64 APC preamplifiers [100]. It is triggered externally by a NIM signal. Most of the system settings are controlled by three programmable registers supplied under CAMAC control. The control signals are distributed to the counters by the STation INterface (STIN) [100]. This module forms also an interface between the chambers and a 10 bit Flash-Analog-to-Digital Converter F-ADC: the CAMAC Scirocco-II [101]. This later performed the digitization of the strips analog data, controlled by a clock signal synchronized with the data, generated by the APC controller. Pedestal subtraction can be done online in

the Scirocco-II. In our application, the pedestal subtraction has been chosen to be done offline because of common mode fluctuation. The calibration procedure of the APC chips is described in details in reference [102].

5.1.4.3 Trigger system and monitoring program

Figure 5.6 gives the principle of the hodoscope trigger system. All trigger and veto signals are sent to a 4-channel Programmable Logic Unit (PLU) which generates the pulses required by the various CAMAC modules. The coincidence of the two scintillators triggers the data readout cycle. Immediately after a coincidence, a fast veto of 2 ms duration is generated by a NIM timer in order to disable further triggers and to let the data acquisition system react. An additional start signal of 2Hz is required in order to reset the APC chips at regular intervals. These reset pulses, together with the scintillator triggers are sent to the APC controller, through output O_2 of the PLU unit. They are delayed by 1.2 μs to allow for integration and sampling of the anode signals in the chips. During the veto time, output O_4 provides a common start of the TDC's. Output O_3 transmits the reset pulses when there is no veto signal to the gate of a CAMAC ADC, and the data acquisition system reads this module to decide whether it is a real trigger or not. If it is a real trigger, the data acquisition system reads the TDC's and tries to reconstruct a straight track with the drift chambers. If such a track is reconstructed and crosses the MSGC box, the Scirocco-II is then read out and the event is written onto disk. The rate of event written onto disk is 3 events per minute.

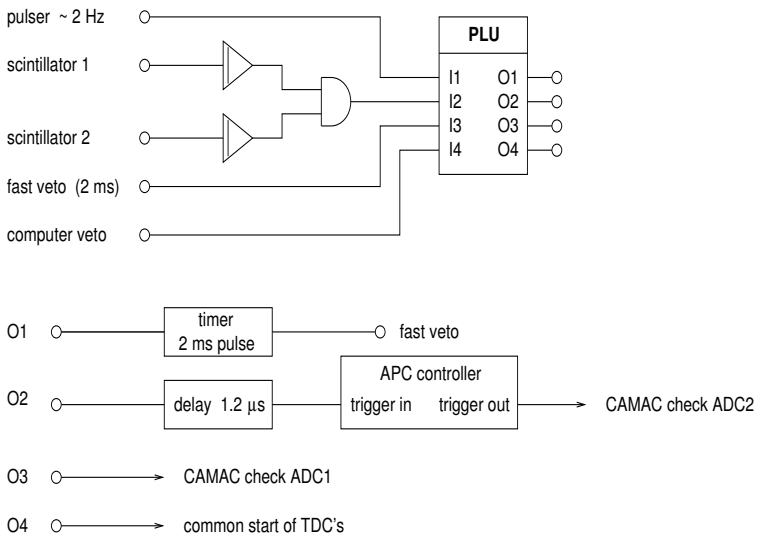

Figure 5.6: *Principle of the hodoscope trigger system.*

The data acquisition program has been written in Fortran in the MacUA1 environment which is a Macintosh based system for data acquisition, control and monitoring applications [103]. The program provides a graphic interface with an event display and a menu bar. In the event display, two windows have been made available. The first one shows the particle trajectory reconstructed by the drift chambers and the second shows the data recorded on the MSGC strips for each event. With the menu bar the user can initialize the parameters needed for data taking and steer the program. In the initialization menu, it is possible to introduce the number of required events, the number of counters to be tested, etc. During this initialization phase, the CAMAC crate and all modules are cleared. At the beginning of the run, 50 events

triggered by random pulses are taken in order to compute the pedestal and the RMS noise of the MSGC strips. This is done in order to allow an online pedestal subtraction if asked. Upon reception of a trigger, the computer reads the TDC's and checks that a signal has been detected in the four layers of drift chambers in each projection. The particle impact point coordinates are calculated using the time-distance relation (3.31). Events for which a hit is closer than 1.5 cm from an anode wire are rejected because of the non-uniformity of the electric field in this region. The particle impact point in the mid plane of the hodoscope is calculated and only those particles traversing the MSGC active area are kept.

5.1.5 Drift time-distance relation calibration

The cosmic muon hodoscope has been built in order to reconstruct the cosmic muon tracks and to predict their impact point in the MSGC's active area. To find the best estimate of the muon track parameters, knowledge of their impact point with the drift chambers and thus the corresponding drift distances are needed. For each event i, the drift time t_k^i is recorded for the kth drift chamber by the corresponding TDC channel. The drift distance d_k^i in that chamber can then be obtained by:

$$d_k^i = v_k t_k^i + d_k^0 \tag{5.1}$$

where v_k and d_k^0 are respectively the electron drift velocity and the anode signal delay due to cables and electronics of that chamber. The calibration consists of a precise determination of the drift chamber parameters. These parameters are not measured directly but are extracted from the recorded data with the help of a χ^2 technique using Lagrange multipliers. The use of Lagrange multipliers [104] comes from the fact that the unknown parameters are constrained by the hodoscope geometry itself as will be explained below. In the following, the method will be described, and its application to the hodoscope will be explained.

Consider a system determined by $J+N$ variables $\underline{\theta}=(\theta_j)$, $j=1,J$ and $\underline{\eta}=(\eta_n)$, $n=1,N$. The Variables $\underline{\theta}$ are not directly measurable while there exist measurements of $\underline{\eta}$: $\underline{y}=(y_n)$, $n=1,N$ with their covariance matrix V.

Suppose a model where $\underline{\theta}$ and $\underline{\eta}$ are subject to K constraint equations:

$$f_k(\underline{\eta},\underline{\theta}) = 0 \quad k = 1,K \quad with \quad K > J \tag{5.2}$$

An estimate of the parameters $\underline{\theta}$ is obtained by minimizing the following expression:

$$X^2(\underline{\eta},\underline{\theta},\underline{\lambda}) = \chi^2(\underline{\eta}) + 2\underline{\lambda}^T \underline{f}(\underline{\eta},\underline{\theta}) \tag{5.3}$$

where T denotes the transpose of a matrix and

$$\chi^2(\underline{\eta}) = (\underline{y}-\underline{\eta})^T V^{-1} (\underline{y}-\underline{\eta}) \tag{5.4}$$

is the least square estimate of the measurements and the second term is a linear combination of the constraint equations. The K coefficients of this linear combination $\underline{\lambda}$ are called the Lagrange multipliers.

Differentiating these quantities with respect to $\underline{\eta}$, $\underline{\theta}$ and $\underline{\lambda}$ gives $N+J+K$ equations to solve:

$$\begin{aligned} -V^{-1}(\underline{y}-\underline{\eta}) + f_\eta^T \underline{\lambda} &= 0 \\ f_\theta^T \underline{\lambda} &= 0 \\ \underline{f} &= 0 \end{aligned} \tag{5.5}$$

where $(f_\eta)_{kn}=\frac{\partial f_k}{\partial \eta_n}$ and $(f_\theta)_{kj}=\frac{\partial f_k}{\partial \theta_j}$.

Solving this set of equations requires numerical methods based on an iterative procedure. At the iteration $\nu+1$, the Taylor's series expansion of $\underline{f}(\underline{\eta},\underline{\theta})$ around $\underline{\eta}^\nu$ and $\underline{\theta}^\nu$ is:

$$f_k^{\nu+1} = f_k^\nu + \sum_{n=1}^{N}(\frac{\partial f_k}{\partial \eta_n})^\nu(\eta_n^{\nu+1}-\eta_n^\nu) + \sum_{j=1}^{J}(\frac{\partial f_k}{\partial \theta_j})^\nu(\theta_j^{\nu+1}-\theta_j^\nu) + .. = 0$$

At first order of this expansion, the set of equations (5.5) becomes:

$$V^{-1}(\underline{\eta}^{\nu+1}-\underline{y}) + f_\eta^{T\nu}\underline{\lambda}^{\nu+1} = 0 \tag{5.6}$$

$$f_\theta^{T\nu}\underline{\lambda}^{\nu+1} = 0 \tag{5.7}$$

$$\underline{f}^{\nu+1} = \underline{f}^\nu + f_\eta^\nu(\underline{\eta}^{\nu+1}-\underline{\eta}^\nu) + f_\theta^\nu(\underline{\theta}^{\nu+1}-\underline{\theta}^\nu) = 0 \tag{5.8}$$

which is a set of linear equations that can be solved to find the next iteration $\nu+1$. Equation (5.6) gives:

$$\underline{\eta}^{\nu+1} = \underline{y} - V f_\eta^{T\nu}\underline{\lambda}^{\nu+1} \tag{5.9}$$

Replacing in (5.8) gives:

$$\underline{\lambda}^{\nu+1} = (S^\nu)^{-1}[\underline{R}^\nu + f_\theta^\nu(\underline{\theta}^{\nu+1}-\underline{\theta}^\nu)] \tag{5.10}$$

where $\underline{\mathrm{R}}^\nu$ and S^ν are given by:

$$\underline{R}^\nu = \underline{f}^\nu + f_\eta^\nu\underline{y} - f_\eta^\nu\underline{\eta}^\nu \tag{5.11}$$

$$S^\nu = f_\eta^\nu V f_\eta^{T\nu} \tag{5.12}$$

Finally replacing $\underline{\lambda}^{\nu+1}$ in (5.7) gives the value of $\underline{\theta}$ at iteration $\nu+1$:

$$\underline{\theta}^{\nu+1} = \underline{\theta}^\nu - \underline{C}^\nu \tag{5.13}$$

with

$$\underline{C}^\nu = [f_\theta^{T\nu}(S^\nu)^{-1}f_\theta^\nu]^{-1}[f_\theta^{T\nu}(S^\nu)^{-1}\underline{R}^\nu] \tag{5.14}$$

The iteration procedure can be repeated until either the following conditions are fulfilled:

$$\Delta\underline{f} = \underline{f}^{\nu+1}-\underline{f}^\nu < \underline{tolf}$$

$$\Delta\underline{\eta} = (\underline{\eta}^{\nu+1}-\underline{\eta}^\nu) \quad or \quad (\frac{\Delta\underline{\eta}}{\underline{\eta}}) < \underline{tol\eta}$$

$$\Delta\underline{\theta} = (\underline{\theta}^{\nu+1}-\underline{\theta}^\nu) \quad or \quad (\frac{\Delta\underline{\theta}}{\underline{\theta}}) < \underline{tol\theta}$$

or the maximum number of iterations is reached: $\nu+1$=nitmax; $\underline{tolf}$, $\underline{tol\eta}$ and $\underline{tol\theta}$ are the tolerance values, given by the user, for $\underline{f}$, $\underline{\eta}$ and $\underline{\theta}$ respectively. A routine has been written based on this procedure [105] . To adapt the problem to this routine, the user has to provide:

1. the set of measurements $y_1,...,y_N$ as initial values for $\underline{\eta}$, and their covariance matrix V.

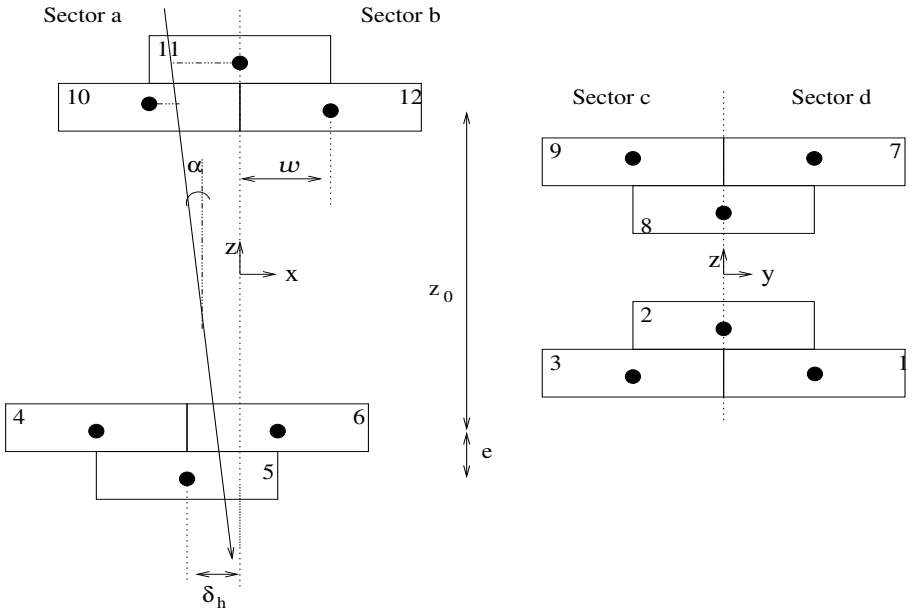

Figure 5.7: *Schematic view of the hodoscope projected in the xz and yz planes respectively, together with the definition of the four sectors a, b, c and d. For simplicity the horizontal shift δ_h is shown only for one projection.*

2. initial values for the unknown variables $\theta_1, ..., \theta_J$ of the problem.

3. the analytical form of the constraint equations $\underline{f}$ and their derivatives $\underline{f_\eta}$ and $\underline{f_\theta}$.

To apply this procedure to the calibration of the hodoscope, this later has been divided into four sectors as shown in figure 5.7. There are two sectors for each set of chambers measuring either the x coordinate (a and b) or the y coordinate (c and d). A sector is made of four half chambers on top of each other: $a(c)$ for the left side and $b(d)$ for the right side of the xz(yz) projection. This has been done in order to treat the two halves of each chamber independently and to choose tracks with a small incident angle with respect to the vertical z axis, which minimizes the effect of the errors on the chamber positions along that axis. In each drift chamber tracks passing close to the anode or close to the opposite edge to the anode are excluded from the analysis since in these regions the electric field is not uniform and relation (5.1) does not hold.

The z axis is assumed to pass through the anode wires of the two upper central chambers and the origin of the coordinate system is taken at the middle of the drift chamber system. The constraint equations come from the following assumptions:

- all chambers are perfectly horizontal. As a result, for a given projection, the particle incident angle α is the same for all four layers of chambers, provided the multiple Coulomb scattering can be neglected.

- all anode wires in a given projection are perfectly parallel; the maximum drift distance is w=99.0 $\pm$ 0.5 mm for all chambers; the vertical distance between the anode planes of the two layers of staggered chambers is always e=33.0 $\pm$ 0.5 mm; it is z_0=507 $\pm$ 2 mm for the closest layers of non contiguous chambers, in the xz projection (see figure 5.7).

- a horizontal shift δ_h of the lower group of chambers with respect to the upper one is allowed (see figure 5.7).

Consider, for instance, one sector, say sector a. For each track, the x coordinates of the four impact points, in each of the four chambers: 11, 10, 4 and 5, are given by:

$$\begin{aligned} x^i_{11} &= -v_{11}t^i_{11} - d^0_{11} \\ x^i_{10} &= -w + v_{10}t^i_{10} + d^0_{10} \\ x^i_4 &= -w + v_4 t^i_4 + d^0_4 - \delta_h \\ x^i_5 &= -v_5 t^i_5 - d^0_5 - \delta_h \end{aligned} \tag{5.15}$$

For simplicity, the parameters d^0_k can be neglected for the moment and the fit can be performed to find the v_k only. This will result in shifted residual distributions, the mean of which giving the parameters d^0_k.

As the particle incidence angle α is the same with all four layers and the origin of the coordinate system has been chosen in the middle of the hodoscope, we have , even with a non zero δ_h,:

$$tg\alpha = \frac{x^i_{10} - x^i_{11}}{e} = \frac{x^i_5 - x^i_4}{e} \tag{5.16}$$

leading therefore to a first constraint equation:

$$2w - v_{11}t^i_{11} - v_{10}t^i_{10} - v_4 t^i_4 - v_5 t^i_5 = 0 \tag{5.17}$$

In the absence of a horizontal shift and for vertical tracks (α=0), the drift distances in symmetric chambers with respect to z=0 should be equal. For non vertical tracks, the difference in drift distances is given by $tg\alpha z_0$.

Taking into account a non zero δ_h, this becomes

$$v_4 t^i_4 - \delta_h - v_{10}t^i_{10} = tg\alpha z_0 \tag{5.18}$$

where $tg\alpha$ is, from equation (5.16), given by:

$$tg\alpha = \frac{v_{10}t^i_{10} + v_{11}t^i_{11} - w}{e} \tag{5.19}$$

leading to a second constraint equation:

$$-z_0 w + z_0(v_{10}t^i_{10} + v_{11}t^i_{11}) + e(v_{10}t^i_{10} - v_4 t^i_4) + e\delta_h = 0 \tag{5.20}$$

The method described above has been applied to the hodoscope to find the parameters v_k, taking into account the two constraint equations (5.17) and (5.20) and the measured variables t^i_k for a set of tracks (typically 100).

Once the v_k are known, the next step is to determine the d^0_k from the mean of the residual distributions of a minimum χ^2 fit to a straight line of the impact point coordinates of each track given by (5.15), with d^0_k=0. This is done by minimizing the quantity (see appendix B):

$$\chi^2 = \sum_k \frac{(x^i_k - a^i z_k - b^i)^2}{\sigma^2_k} \tag{5.21}$$

where k=11, 10, 4 and 5 for sector a, z_k and σ_k are respectively the vertical position and the measurement error on x_k; a^i and b^i are the slope and intercept for the ith reconstructed track. In each chamber, the residual is given by:

$$Res^i_k = x^i_k - a^i z_k - b^i \tag{5.22}$$

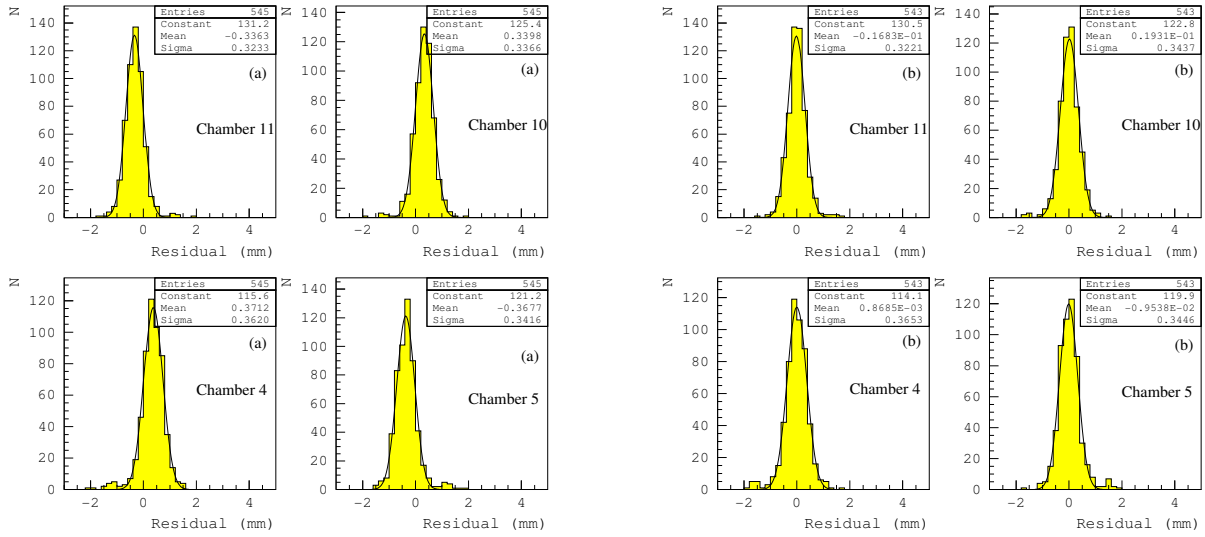

Figure 5.8: *Residual distributions of the four chambers of sector a before (a) and after (b) corrections for the d_k^0 parameters.*

Cham.	1	2	3	4	5	6	7	8	9	10	11	12
proj.	y	y	y	x	x	x	y	y	y	x	x	x
σ_k	600	480	430	360	344	404	480	470	488	340	322	370
v_k	0.099	0.134	0.116	0.116	0.118	0.117	0.117	0.118	0.115	0.113	0.129	0.118
d_k^0	-0.64	0.50	-0.17	0.18	-0.19	-0.6	0.32	0.30	.40	-0.35	0.18	0.14

Table 5.1: *Standard deviation in μm of the residual distribution, computed drift velocity v_k in mm per TDC unit and delay parameter d_k^0 in mm of the twelve drift chambers of the cosmic rays hodoscope.*

The residual distributions of the four chambers of sector a are given in figure 5.8(a). They fit a Gaussian function but non centred on zero because of the non adjusted d_k^0 parameters. After adjusting these parameters by centring these distributions on zero, we obtained the distributions of figure 5.8(b). This procedure has been applied to the three other sectors. The standard deviation of the residual distributions obtained for the twelve drift chambers are summarized in table 5.1 as well as some typical values of the fitted parameters. In the x projection, the standard deviation is smaller thanks to the larger lever arm. Chamber 1 of the y projection was malfunctioning and its parameters are not well estimated. Its distribution is thus broad. The resolution of the drift chambers derived from the residuals is about 660 μm, for sector c, for instance, in agreement with previous results obtained with these chambers [106]. Since the drift velocity depends on the pressure and the temperature, the calibration has to be done regularly.

The track angle with respect to the vertical incidence are denoted α and β respectively in the x and y projections. Figure 5.9 (a) and (b) show the distribution of $tan\alpha$ and $tan\beta$ respectively showing that the acceptance is [-16^0,16^0] in α and [-20^0,20^0] in β. The non-uniformity of these distributions is due to the rejection , during the data taking, of tracks passing in the vicinity of an anode wire, a region where the electric field is not uniform and therefore relation (5.1)

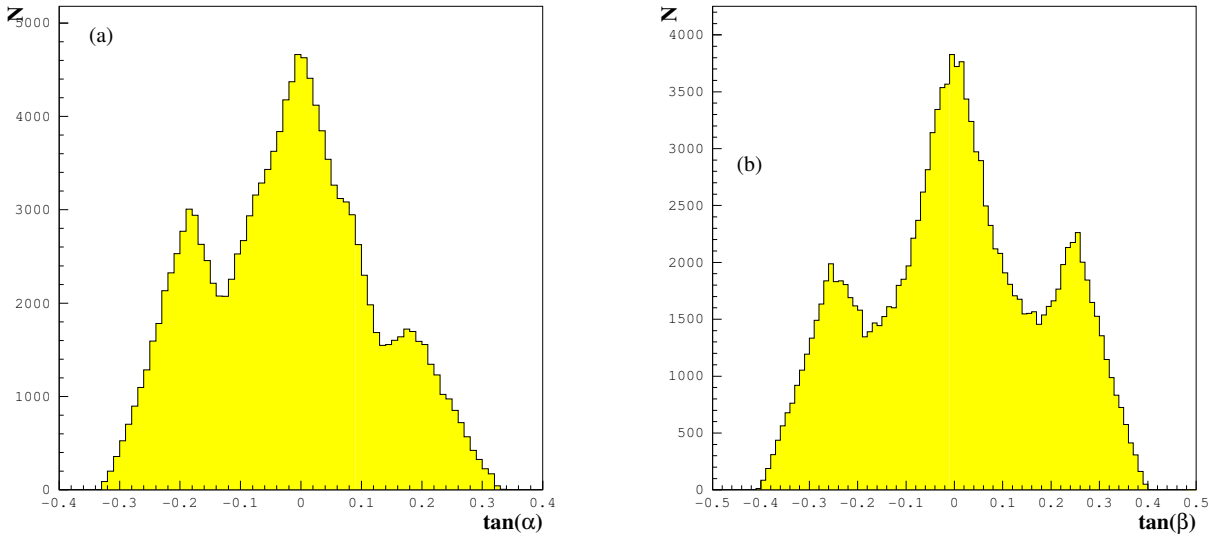

Figure 5.9: *Distribution of the tangent of incidence angle of particle tracks reconstructed by the hodoscope in the projections parallel (a) and perpendicular (b) to the MSGC strips.*

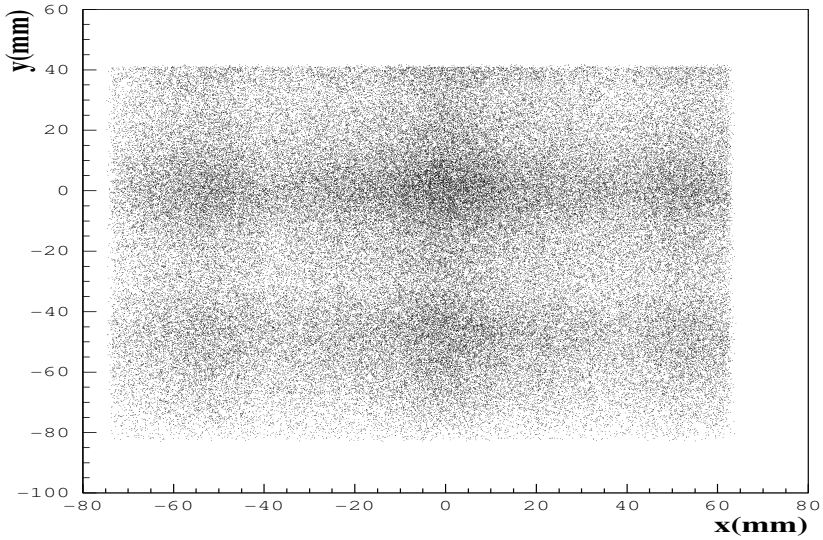

Figure 5.10: *Impact point position of the reconstructed tracks, in the mid-plane of the hodoscope.*

does not hold [15].

Figure 5.10 shows a scatter plot of the impact points position in the middle of the hodoscope, where the MSGC's under test are placed. It is also non uniform. The selected area is 14×12 cm^2. It is largely sufficient since the active area of the MSGC's is 10×10 cm^2.

5.2 MSGC data analysis

The charge generated by the ionizing particle is spread over one or more MSGC strip depending on the track incidence angle and on the diffusion of electrons in gases. The signals collected on these strips are grouped into clusters after pedestal subtraction, common mode correction and noise calculation.

5.2.1 Pedestal subtraction and common mode correction

The raw data ADC_i^k recorded by the Scirocco Flash ADC for the *ith* strip in the *kth* event is a superposition of three contributions:

$$ADC_i^k = S_i^k + P_i + C_i^k \tag{5.23}$$

where S_i^k is a possible ionizing particle charge signal, P_i is the strip pedestal and C_i^k is a possible common shift of the baseline in a group of channels of the same readout chip.

For each MSGC channel, the pedestal is defined as the average value of the Gaussian distribution of the channel pulse height in the absence of a particle signal. However, in the MSGC data taken in the hodoscope, the strip may have a signal corresponding to an ionizing particle. The pedestal subtraction has thus to be done in an iterative way in order to remove the contribution of these particle signals.

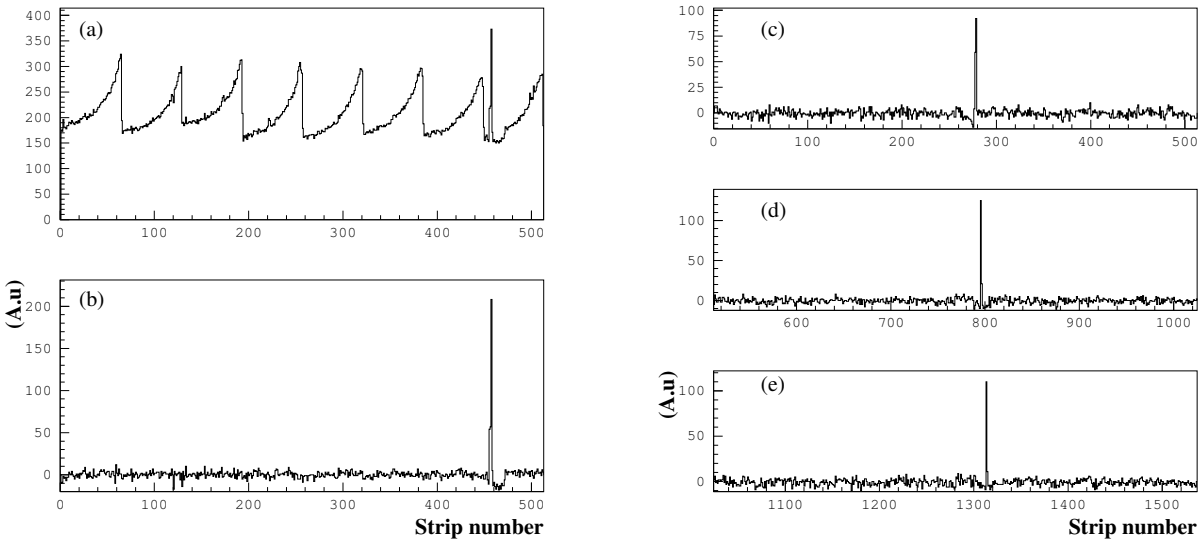

Figure 5.11: *ADC signal measured for each strip for one particular event in an MSGC of 512 channels, without any correction (a) and after pedestal and common mode subtraction (b). In (c), (d) and (e) a similar event is shown, after correction for the three MSGC counters in the hodoscope.*

The channel charge average is computed for each set of 100 events for each run as well as the RMS of its distribution. In order to reject events for which the strip may have been hit by a particle, in the second iteration, signals larger than three times the RMS, over the average value, are discarded and the average and RMS are recalculated. We found that two iterations are sufficient to determine the pedestals. Once the pedestal value P_i is known, it is subtracted from the raw data. The common mode for each event is then defined as the average of the remaining signals in the 64 strips connected to the same APC chip taking care to remove strips which may have had a particle signal. This is also done in two iterations. After pedestal and common mode correction, the same sample of a 100 events is used to determine the strip noise σ_i; it is defined as the standard deviation of the remaining signal distribution.

The signal measured for each strip in ADC units (A.u)[1] is shown in figure 5.11(a), for one event in one chamber, before pedestal subtraction. A clear signal of an incident particle around strip 458 is observed. The pedestal value increases from the first to the last channel of an APC chip. This is a known defect of the version of the APC chips we used [107]. After pedestal subtraction and common mode correction, the remaining signal looks as shown in figure 5.11(b). Adjacent channels to those with the main pulse, detect signals of reverse polarity. This is a consequence of the grouping of cathodes (16) to the high voltage as explained in section 4.1. In plots (c), (d) and (e) of figure 5.11, a muon track detected in the three MSGC chambers is shown.

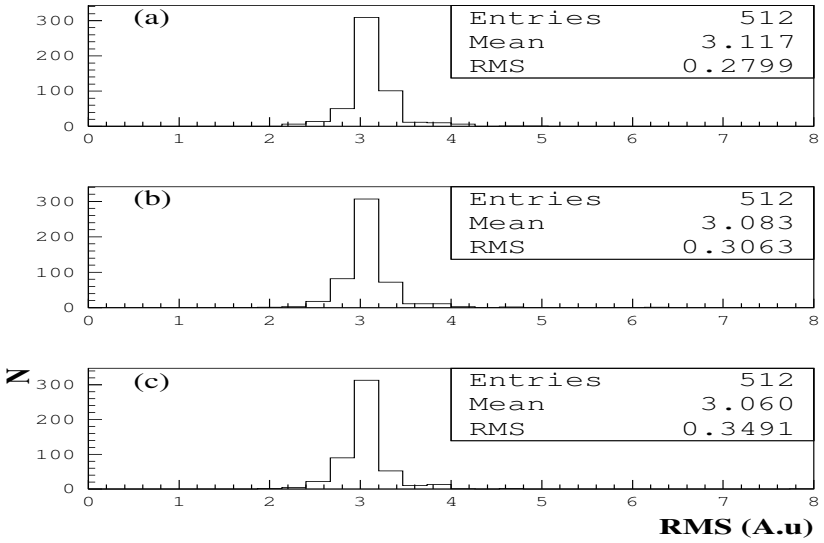

Figure 5.12: *RMS strip noise distributions for the 512 channels of each of the three chambers.*

The strip R.M.S noise distribution for the 512 channels in each of the three chambers are shown in figures 5.12 (a), (b) and (c). The average strip noise is around 3 ADC counts. The strip is defined as noisy or dead if its RMS noise is more than 6 or less than 1.5 ADC counts respectively. Such strips are excluded from further analysis.

5.2.2 Impact point reconstruction and cluster characteristics

The MSGC counters are placed in the middle of the hodoscope in such a way that their strips are, in first approximation, parallel to the x axis of the hodoscope reference frame.

[1] 1 ADC unit is equivalent to 250 electrons.

To find the impact points of ionizing particles in the counter, clusters of strips with a signal are formed. First, a threshold of 10 ADC counts is applied to the strip signals. Then the signals of adjacent strips passing this threshold are added together and a threshold on the total cluster charge $Q^{cluster}$ is applied. This cut is discussed later. To allow for dead channels, one strip with a signal below threshold can be accepted within a cluster.

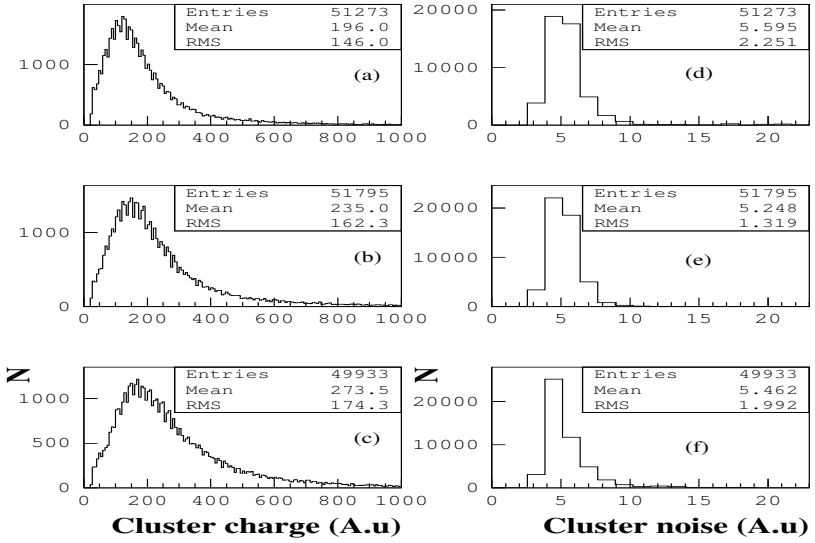

Figure 5.13: *Cluster charge (a), (b) and (c), and cluster noise (d), (e) and (f) distributions for the three chambers filled with Ne/DME 50/50 % and operated at a cathode strip voltage of -540 V and at a drift voltage of -2200 V.*

The coordinate, in strip number, of the impact point in a direction perpendicular to the strips is computed as the barycentre of the cluster:

$$y_{cog} = \frac{\sum_{i=1}^{N} n_i S_i}{\sum_{i=1}^{N} S_i} \tag{5.24}$$

where n_i is the strip number, S_i its signal. The sum is performed over the strips having an accepted signal within the cluster. The total cluster charge is proportional to the energy released in the detector by the ionizing particle. The cluster charge distributions for chambers 1, 2 and 3 are shown in figures 5.13 (a), (b) and (c) respectively. The counters were filled with a Ne/DME 50/50 % gas mixture and operated at a drift voltage of -2200 V and at a cathode strip voltage of -540 V. The resulting drift field is 5.6, 6.1 and 6.8 kV/cm for counters 1, 2 and 3. This increase of the drift field intensity from chamber 1 to chamber 3, due to the different gas gaps, leads to an increase of the pulse height, in agreement with results from other groups [68]. In the plots (d), (e) and (f) of the same figure, the corresponding cluster noise distributions are displayed. The cluster noise, given by:

$$\sigma^{cluster} = \sqrt{\sum_{i=1}^{N} \sigma_i^2} \tag{5.25}$$

is of the order of 5 for the three chambers.

The number of strips in a cluster defines the cluster size. It depends on the particle incidence angle and on the diffusion of electrons in the gas. Therefore the cluster characteristics defined

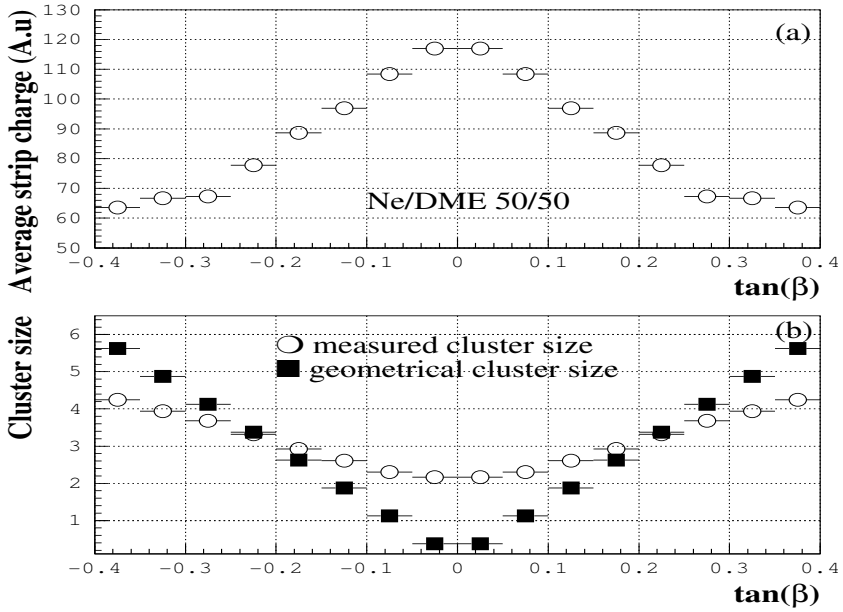

Figure 5.14: *Average strip charge (a) and cluster size (b) measured as a function of the track slope in Ne/DME 50/50 %; the square marks in the lower plot represent the cluster size calculated.*

above are expected to vary with the particle incidence angle [108]. Indeed if the track angle β is different from zero the electrons deposited by the particle are spread over many strips. The charge collected by each strip is proportional to the ionization in the gas column above the strip. The probability to have no ionization at all above a strip is thus higher at large β angles. This is the case, in CMS, for particles with low p_T ($p_T \leq 2$ GeV/C) which pass the detectors at large incident angles ($\beta \geq 0.15$ rad).

In figure 5.14 (a) the average strip charge is shown as a function of the tangent of the angle β. The charge per strip is observed to drop rapidly with increasing angle. The strip detection efficiency is thus expected to decrease with increasing β.

The average number of strips in a cluster, which is a measurement of the cluster size, is shown in figure 5.14(b) as a function of the tangent of β. As expected there is a clear widening of the clusters with the angle. For comparison the length of the particle path projected on a direction perpendicular to the strips, in the strip plane, expressed in number of strips, called the geometrical cluster size is also shown in figure 5.14(b) as a function of the tangent of β. It is observed that for small angles ($|\beta| \leq 0.17$ rad), the measured cluster size is well above the geometrical value. This is due to the diffusion of the primary electron swarm during the drift in the Ne/DME 50/50 % gas mixture. The test of MSGC's with CO_2/DME 40/60 % gas mixture, by other groups [109] showed this effect only at very small angles ($|\beta| \leq 0.06$ rad) as the electron transverse diffusion in this gas is smaller (see reference [110]). On the contrary for large angles, the electron diffusion has less influence on the cluster size, the experimental data are well below the geometrical values as the strip inefficiencies increase at this acceptance. The results are in good agreement with those of other groups [109]. The cluster size at normal incident angle is 2.1 strips as obtained previously [111]. At large angles, in order to include all the detected hits in the cluster definition it is necessary to allow for several zeros in the clusters. This is rarely possible in a real experiment as the two track separation will be affected. At best one strip without signal can be allowed, but even that might spoil the two track resolution [14].

5.2.3 Measurement of the particle detection efficiency

Before studying the MSGC detection efficiency, the MSGC counters were aligned to the hodoscope reference frame. The coordinates of the MSGC clusters found are converted to the hodoscope reference frame by correcting for translations of the MSGC counter along y and z axes, and rotations in the xy plane; the other rotations have negligible effects. This is done by minimizing the function:

$$\chi^2 = \sum_{i=1}^{N} \frac{y_{hod}^i - y_m^i}{\sigma_{hod}^2} \tag{5.26}$$

where y_{hod}^i and y_m^i are the impact point coordinates for the i-th track respectively predicted by the hodoscope and calculated by the centre of gravity method, both expressed in microns. σ_{hod} is the error on y_{hod}^i, taken as the same for all tracks. For the j-th MSGC counter, the χ^2 is minimized with respect to the parameters Δy_j, Δz_j, α_{hj} and α_{vj}. $\Delta y_j(\Delta z_j)$ is the translation of the MSGC counter along the $y(z)$ axis, and $\alpha_{hj}(\alpha_{vj})$ is the rotation angle of the MSGC strip plane in the $yoz(xoy)$ plane. This procedure is described in details in reference [112].

Figure 5.15 (a), (b) and (c) show the distribution of the difference between the corrected measured impact point coordinate and that predicted by the hodoscope, in counters 1, 2 and 3 respectively, for the full angular acceptance of the hodoscope. The curves are fitted to a Gaussian function. The standard deviations of the distributions are close to 370 μm. This is in qualitative agreement with the resolution of the drift chambers prediction 330 μm and of the MSGC measurement, being more than 40 μm as track angles up to 400 mrad are included in the statistics.

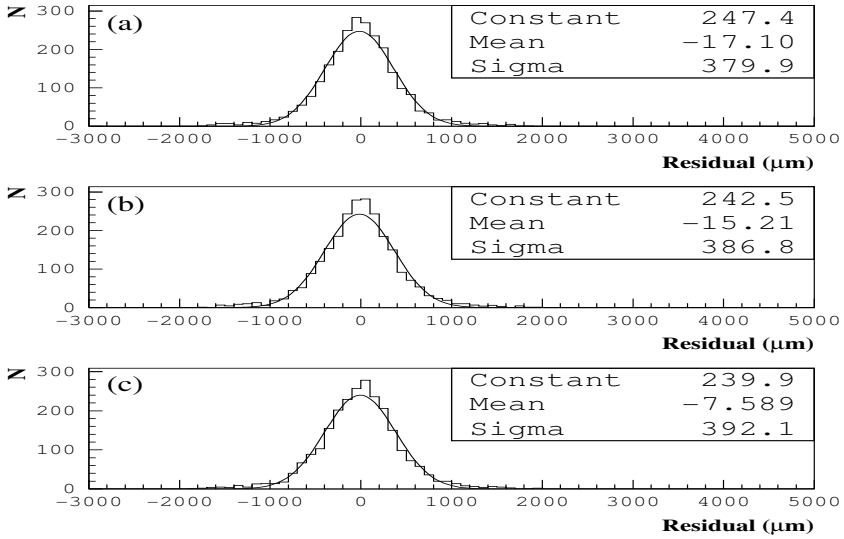

Figure 5.15: *Distributions of the residuals between the coordinate of the impact point predicted by the hodoscope and this measured in each of the MSGC counters.*

Due to a data acquisition problem 20 % of the triggers accepted and reconstructed by the drift chambers are not sent to the APC controller. To give an exact estimation of the MSGC detection efficiency, this latter is measured for the second MSGC using tracks reconstructed by the hodoscope and producing at least one cluster in one of the two other MSGC's. Then this impact point has to be in agreement with the one predicted by the hodoscope in the MSGC

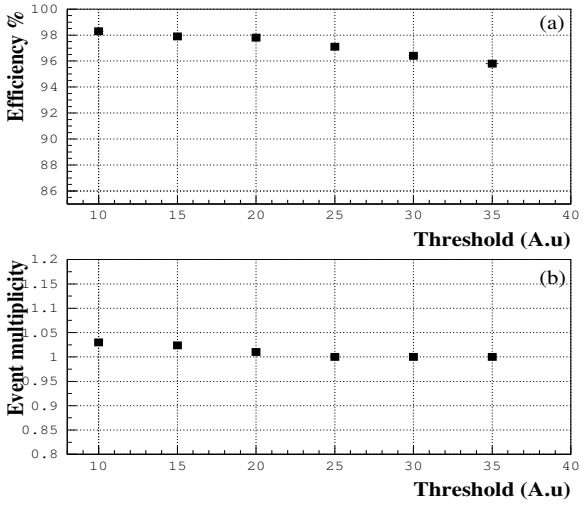

Figure 5.16: *Detection efficiency (a) and event multiplicity (b) versus the threshold on the cluster charge.*

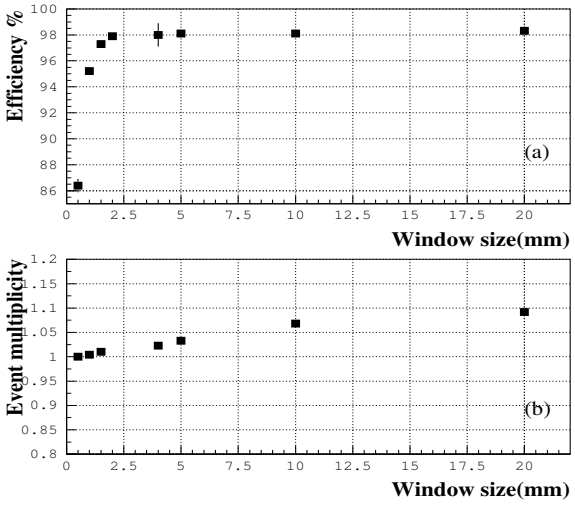

Figure 5.17: *Detection efficiency (a) and event multiplicity (b) versus the size of the window set on each side of the hodoscope prediction to accept an MSGC cluster.*

plane, within a certain window. The efficiency is defined as the fraction of these tracks detected by the second counter, using the same window.

In setting up the threshold on the cluster charge and on the size of the prediction window, one has to compromise between rejection of false clusters and an acceptable detection efficiency of true clusters. The plots (a) and (b) of figure 5.16 show respectively the detection efficiency and the average event multiplicity of one counter as a function of the threshold on the cluster charge. For a threshold value below 20, there is more than one cluster per event. Choosing a threshold value equal to or more than 25 reduces the detection efficiency to less than 97 %. Consequently, a value between the two, that is 22, has been chosen. On the other hand, a window of 2.5 mm, on each side of the prediction impact point, seems to keep the detection efficiency at 98 % without increasing the number of clusters per event as can be seen from figure 5.17(a) and (b) where the detection efficiency and the event multiplicity are shown as a function of the size of this window.

Detection efficiency results will be presented for several gas mixtures in section 5.4.

5.2.4 Spatial resolution study

To determine the spatial resolution of the MSGC's under test, expected to be of the order of 40 μm, use is made of the counters themselves as the hodoscope prediction accuracy is poor (330 μm). The hodoscope is only used to perform an angular selection of the incident particle.

The alignment of the MSGC counters with respect to the hodoscope, described briefly in section 5.2.3, is also not precise enough. The relative displacements of the MSGC counters, in a direction perpendicular to the strips, are measured using vertical tracks selected by the hodoscope ($|\beta| \leq 7$ mrad), and by requiring events with cluster of at most one or two hits ,in each MSGC, in the 2.5 mm window around the drift chambers prediction. This selection means that the track projection onto the substrate is at most 23 μm. To avoid the influence of edge

effects, strips numbered below 50 and above 470 in each counter are not used in the alignment procedure. In addition to that, the two half pieces of substrate 2 are treated separately. Once the relative displacement of the MSGC's are determined, we look for the relative tilt angles of the MSGC's in the xoy plane using a χ^2 minimization similar to the one described in section 5.2.3. It should be noticed that the positions of the counters in the vertical coordinate z are evaluated to an accuracy σ_z=250 μm using the hodoscope predictions for inclined tracks ($|\beta| \geq$ 0.1 rad).

The spatial resolution is studied for counter 2 using the points measured in counters 1 and 3. The residuals between the coordinate of the points extrapolated from counters 1 and 3 and this measured in counter 2 can be written as follows:

$$R = (\frac{y_{c1} - y_{c3}}{z_1} z_2 + y_{c3}) - y_{c2} \tag{5.27}$$

where y_{ci} is the measured impact point coordinate in counter i after alignment, and z_i its vertical position, with $z_3 = 0$. The standard deviation of this distribution is given by:

$$\sigma_R = \sqrt{\sigma_{track}^2 + \sigma_2^2} \tag{5.28}$$

where σ_2 is the resolution in counter 2 and σ_{track} is the error on the extrapolation made from counters 1 and 3. σ_{track} is given by:

$$\sigma_{track}^2 = (\frac{z_2}{z_1})^2 \sigma_1^2 + (\frac{z_1 - z_2}{z_1})^2 \sigma_3^2 + (\frac{z_1^2 + z_2^2}{z_1^4})(y_{c1} - y_{c3})^2 \sigma_z^2 \tag{5.29}$$

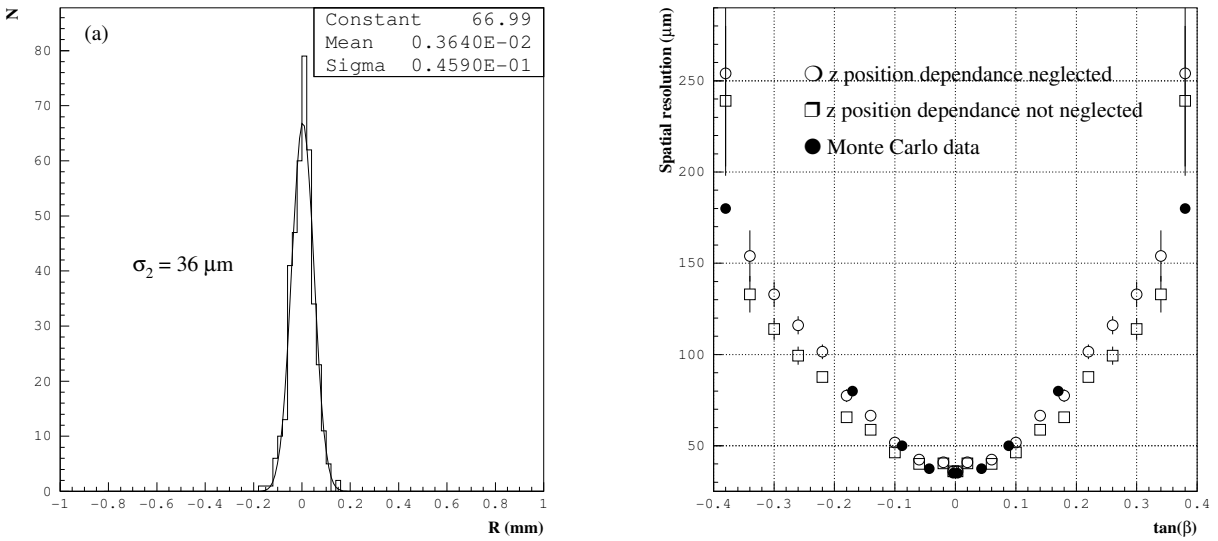

Figure 5.18: *(a) Distribution of the difference between the coordinate predicted by the two reference MSGC's and the one measured in the second counter, for perpendicular tracks ($|\beta| \leq$ 70 mrad). (b) Dependence of the measured spatial resolution on the track slope when the term on σ_z of expression (5.29) is taken into account and when it is neglected ; the Monte carlo data are taken from reference [113]. The MSGC's are filled with a Ne/DME 50/50 % gas mixture and operated at a cathode strip voltage of -540 V and at a drift voltage of -2200 V.*

The distribution of variable R, as defined in (5.27), is shown in figure 4.16(a) for tracks orthogonal to the substrate ($|\beta| \leq$ 70 mrad). The angular selection has been released here,

compared to the selection made for alignment, in order to have enough statistics. The MSGC's were filled with a Ne/DME 50/50 % gas mixture. The drift voltages were -2200 V and the cathode strip voltages, -540 V. The distribution fits a Gaussian function with a mean compatible with zero and a standard deviation $\sigma_R = 46$ μm. The corresponding spatial resolution is found to be $\sigma_2 = 36$ μm using relations (5.28) and (5.29), assuming the same resolution for all three counters. This result is in good agreement with previous experimental results [14, 111] and monte carlo simulations [113] where the resolution was found to be 35 μm in MSGC's operated with the same gas mixture.

The right hand side of expression (5.29) comprises a term that depends on σ_z and on the difference $y_{c1} - y_{c3}$ between the impact point coordinates measured in counters 1 and 3 respectively. This term is expected to increase with the particle incidence angle and to affect thus the absolute value of the spatial resolution. Figure 5.18 (b) shows the spatial resolution as a function of the track slope when the term in σ_z of expression (5.29) is taken into account and when it is neglected (set to zero). The data are compared to previous monte carlo results [102, 113]. A common feature of these curves is the degradation of the spatial resolution with the angle both in experimental and Monte Carlo data. Indeed, when the incidence angle differs significantly from normal incidence, the charge starts to be collected by several strips. Because of large fluctuations in the individual strip signals within the cluster, the impact position of the cluster also fluctuates. This implies a degradation of the spatial resolution with the angle of incidence. This effect has been observed many times [14, 109].

Comparing the two experimental curves shows that at small angles the two curves are identical as the difference $y_{c1} - y_{c3}$ is very small and the term on σ_z is therefore not significant. At large angles this difference becomes important and can reach up to a few millimetres. This explains the 10 % discrepancy between the two curves. Since the monte carlo data do not include any correction for the extrapolation error due to the MSGC positions along the z axis, there is agreement with the experimental data when the term in σ_z is neglected.

5.3 Description of the simulation of MSGC performances

In order to understand the behaviour of MSGC counters filled with different gas mixtures, operated at different voltages or more simply having different geometry, a simulation of the detector performances has been done. For this purpose, a program called GARFIELD [114] has been used. Originally this program has been written for the simulation of two-dimensional drift chambers. Since then it has been subject to extensive study in order to adapt it to the simulation of thin electrode devices such as the MSGC's. A precise calculation of the drift velocity and the diffusion coefficient was needed as well as the energy loss of charged particles in gases. In addition, use of electric field maps computed with specific programs was desirable. As shown in figure 5.19, it is actually interfaced to three programs: MAXWELL [115], HEED [116] and MAGBOLTZ [117], that provide the necessary inputs. Interfaced to these programs, GARFIELD computes the electron and ion drift paths, the arrival time distributions of the charges, the signal induced on the electrodes by the moving charges, etc. It also computes the gas gain by an integration of the first Townsend coefficient. In the following a brief description of these programs is given and a complete description of the program can be found in reference [114].

- **MAXWELL 2D Field Simulator**: it is a two-dimensional finite elements analysis program for the simulation of electromagnetic fields. It comprises several types of solvers, among them the electrostatic solver used in this thesis. It computes the static electric field that exists in a structure, given a set of voltages and a distribution of static charges. This

is based on the Gauss's law which indicates that the net electric flux passing through any closed surface is equal to the net positive charge enclosed by that surface. In differential form, this law reads:

$$\nabla.\mathbf{D} = \rho \tag{5.30}$$

where $\mathbf{D}(x, y)$ is the electric flux density and $\rho(x, y)$ is the charge density. The electric flux density is related to the electric field $\mathbf{E}$ by:

$$\mathbf{D} = \varepsilon_r \varepsilon_0 \mathbf{E} \tag{5.31}$$

where ε_r is the material relative permittivity and ε_0 is the permittivity of free space. Equation (5.30) becomes then:

$$\nabla.(\varepsilon_r \varepsilon_0 \mathbf{E}(x, y)) = \rho \tag{5.32}$$

Since in a static field:

$$\mathbf{E} = -\nabla\phi \tag{5.33}$$

where $\phi(x, y)$ is the electric potential, equation (5.32) becomes:

$$\nabla.(\varepsilon_r \varepsilon_0 \nabla\phi(x, y)) = -\rho \tag{5.34}$$

The electrostatic solver solves this equation, for the electrostatic potential, using the finite element analysis. Once the solution of the potential is generated, the program computes the electric field and the electric flux density using respectively relations (5.33) and (5.31). In the present study Maxwell provides three input files to GARFIELD. They contain respectively the maps of the potential, of the electric field and of the dielectric constant.

- **MAGBOLTZ**: it computes the electron transport parameters, as the drift velocity and the diffusion coefficients, for a large variety of gases. It is based on the numerical solution of the Boltzmann transport equation described in section 3.2.2.

- **HEED**: this program computes in detail the energy loss of charged particles in gases, taking into account the delta electrons emitted and optionally the multiple scattering. It can also compute the number of electron clusters created per centimetre of track, the cluster size distribution and the range of delta electrons.

5.4 Study of the appropriate filling gas

Many of the MSGC performances are related to the gas mixture filling the counter. The major requirements for the filling gas at LHC conditions have been presented in section 4.2.2, which also includes a brief history on the different tests that have been made to find a suitable gas mixture for MSGC's at LHC conditions. Before the beginning of gas studies in Brussels, in 1994, the best candidates were CO_2/DME and Ar/DME [43, 75]. In 1994, F. Angelini et al. operated Micro-Gap counters with mixtures of neon and DME and observed very large proportional gains up to 2×10^4 in Ne/DME 70/30 % [77]. This behaviour has been attributed to the high excitation and ionization potentials of neon, 17 and 21 eV respectively, as compared to the ionization potential of argon, about 15 eV. The electrons have only elastic collisions with

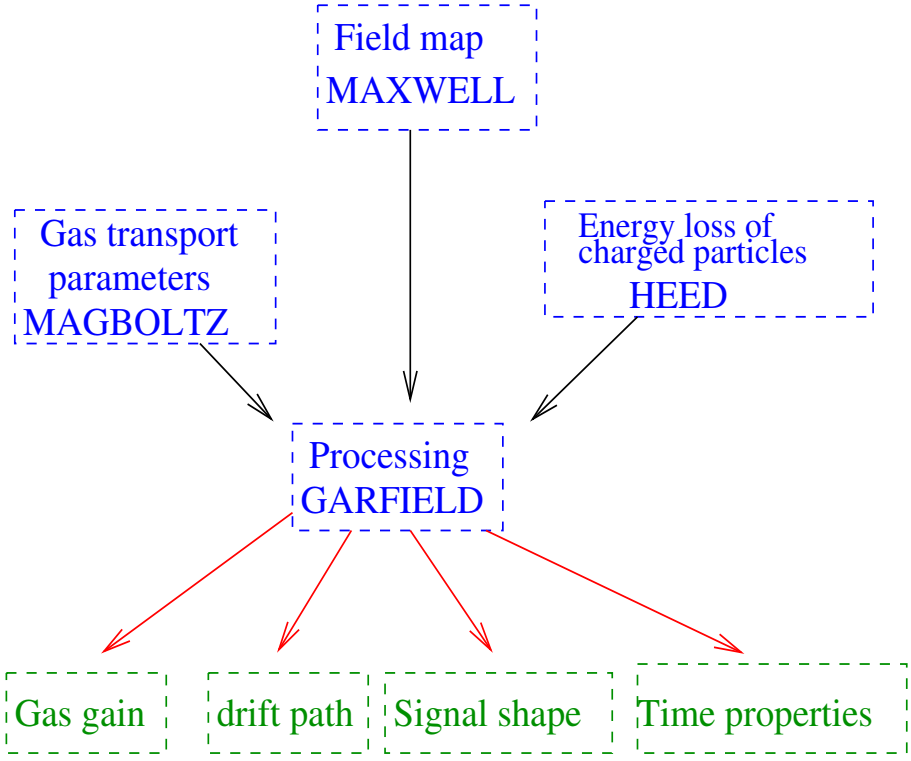

Figure 5.19: *Diagram showing the different sub-programs used for the simulation of the MSGC performances.*

the neon atoms and therefore neon acts as an inert diluant providing thus the same advantages as working with pure DME at low pressure. In addition, for the same reason the photon feedback is strongly suppressed.

However the detection efficiency had to be measured in Ne/DME mixtures as well as the length of the efficiency plateau since the primary ionization density of neon is low and might spoil the detection efficiency.

In a first attempt MSGC's filled with Ne/DME gas mixtures were tested in the cosmic rays hodoscope. The signal pulse height and the detection efficiency were measured, and the results presented by P. Vanlaer in his thesis [102] and also published [113], are summarized in section 5.4.1.

We then investigated the possibility to replace neon by a cheaper gas like helium (or even argon for comparison) and to add CO_2 since it is known for its high drift velocity. Pure DME was also tried. We have thus measured the signal amplitude and the detection efficiency for these mixtures. The spatial resolution was also measured for some of them. The electron drift velocity in these mixtures had to be measured to check if the CMS timing requirements could be fulfilled. This has been done in a laser setup in Antwerp by T. Beckers, together with a measurement of the transverse diffusion coefficient. Results from these tests that were published [110], are summarized and compared to the simulation we have done, in section 5.4.2.

5.4.1 MSGC operation with Ne/DME gas mixtures

For this study the MSGC counter used had a gas gap of 2.7 mm and the drift voltage was kept at -2200 V. The mean collected charge, taken as the average of the cluster charge distribution, is shown in figure 5.20 as a function of the cathode strip voltage, for Ne/DME 20/80 %, 40/60 % and 50/50 %. A measurement with CO_2/DME 40/60 % at a cathode strip voltage

of -625 V is also shown for comparison. The measurements start at cathode strip voltages corresponding to almost full efficiency and stop at the voltages where the counter trips more than three times within a period of a few hours. The same signal amplitude as in CO_2/DME is obtained in Ne/DME mixtures at a much lower cathode strip voltages, between -520 V and -540 V depending on the neon content. This demonstrates the advantage of adding a noble gas to DME. Indeed the mean free path between inelastic collisions then increases due to the high excitation potential of noble gases. The drifting electrons acquire thus larger kinetic energy. In addition, since the ionization potential of DME is much lower than the excitation potential of neon, more collisions are ionizing allowing therefore larger gains.

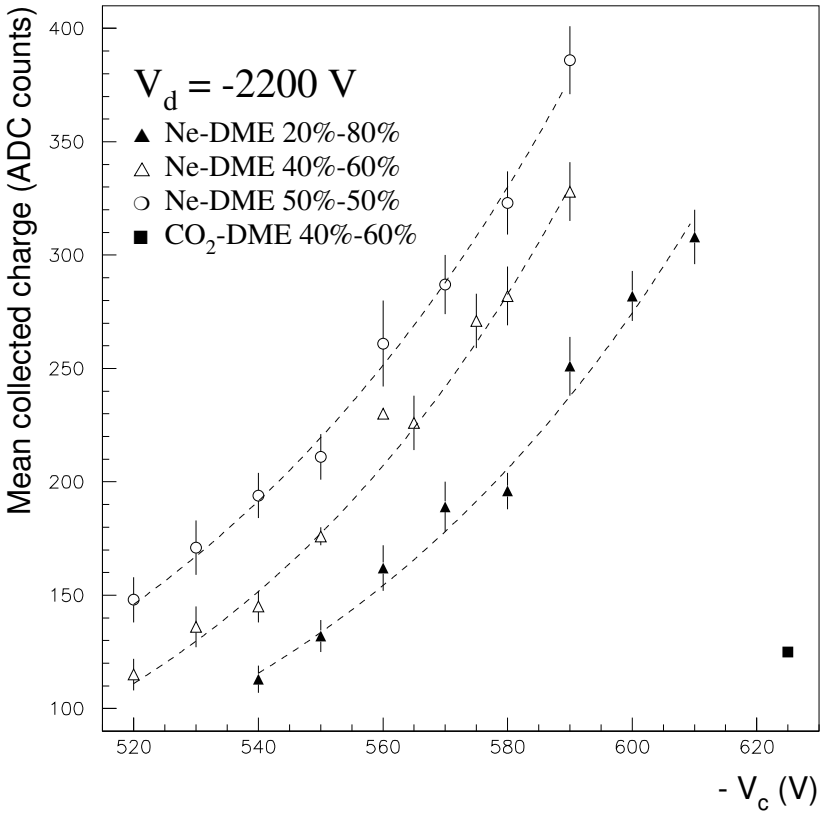

Figure 5.20: *Mean collected charge measured for cosmic rays in Ne/DME 20/80 %, 40/60 % and 50/50 %, as a function of the cathode strip voltage, at a drift voltage of -2200 V and for a gas gap of 2.7 mm. A measurement in CO_2/DME 40/60 % is also shown. The lines are exponential curves.*

At identical voltages, the mixture with the highest neon content yields the largest pulse height. This is in agreement with the explanation given above: although the total ionization density decreases with increasing neon content, the gas gain increases, compensating thus the decrease of primary ionization. In addition, the detector can be operated safely up to cathode strip voltages yielding three or four times the maximum attainable signal in CO_2/DME gas mixture.

The measured detection efficiency is shown in figure 5.21 as a function of the cathode strip voltage for the same gas mixtures as above. Detection efficiencies of 98 % at least are reached in all mixtures in a range of cathode strip voltages of more than 70 V. Although the primary ionization density of neon is low, the gas gain is sufficient to produce signals exceeding the thresholds. Even with the gas with the highest content of neon, a detection efficiency of at

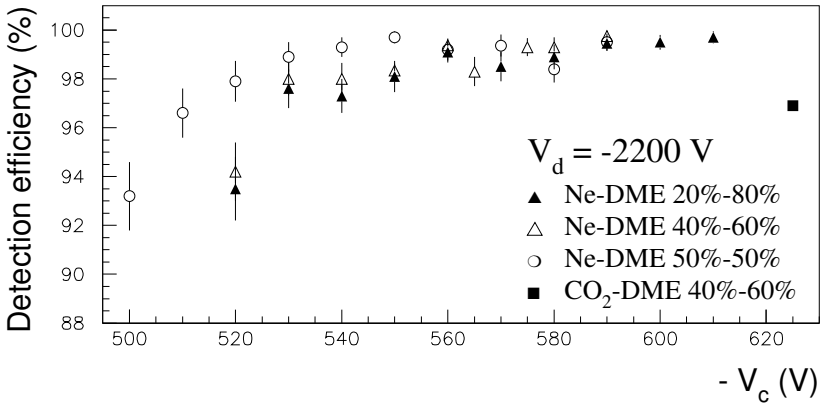

Figure 5.21: *Detection efficiency for cosmic rays in Ne/DME 20/80 %, 40/60 % and 50/50 %, as a function of the cathode strip voltage, at a drift voltage of -2200 V and for a gas gap of 2.7 mm. A measurement in CO_2/DME 40/60 % is also shown.*

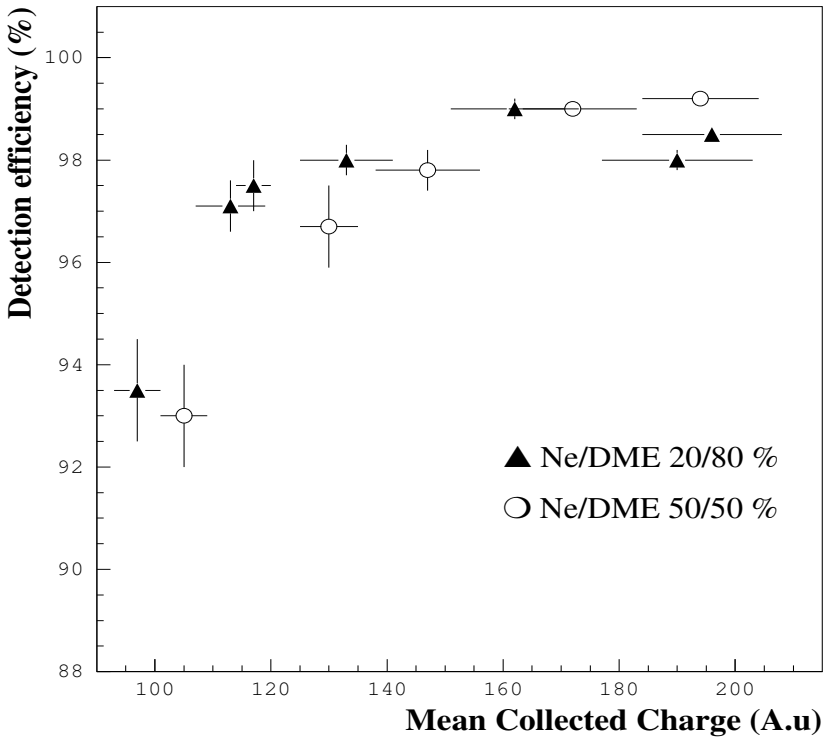

Figure 5.22: *Detection efficiency for cosmic rays in Ne/DME 20/80 % and in Ne/DME 50/50 % as a function of the mean collected charge.*

least 97 % starts at a cathode strip voltage of -510 V instead of -625 V in CO_2/DME 40/60 %. This is an advantage as operating at low cathode strip voltages reduces the energy released in case of a spark, which minimizes the risk of strip damage. The efficiency plateau starts earlier in Ne/DME 50/50 % than in Ne/DME 20/80 %, due to the signal increase with increasing neon content at a given cathode voltage.

The detection efficiency is shown in figure 5.22 as a function of the mean collected charge both for Ne/DME 50/50 % and Ne/DME 20/80 %. A full detection efficiency seems to require a higher signal amplitude in gases with a higher neon content. This is because the smaller primary ionization of these mixtures leads to an increase of the signal fluctuations, requiring therefore a higher signal to obtain a full efficiency.

5.4.2 Test of the performances of MSGC's filled with DME based mixtures

The study of Ne/DME gas mixtures has revealed that these mixtures are very promising as shown in the preceding section. However because of the relatively high cost of neon, we tried to replace it by helium or argon. To increase the drift velocity in these mixtures, addition of a fraction of CO_2 has been investigated.

This study has been done with respect to five parameters: the signal to noise ratio, the detection efficiency, the spatial resolution, the electron drift velocity and the transverse diffusion coefficient. The first three ones are measured in the cosmic rays hodoscope, whereas the last two ones are measured in a laser setup in the University of Antwerp.

5.4.2.1 Signal to noise ratio, detection efficiency and spatial resolution study

For this study the MSGC counter used had a gas gap of 3 mm and the drift voltage was kept at -2200 V.

The signal to noise ratio, SNR, is defined, in this work, as the average value of the distribution of the quantity:

$$\frac{Q^{cluster}}{\sigma^{cluster}} \tag{5.35}$$

where $Q^{cluster}$ is the cluster charge and $\sigma^{cluster}$ its noise.

A typical signal to noise ratio distribution is shown in figure 5.23 for Ne/DME 50/50 % and at a cathode strip voltage of -560 V. As expected it exhibits a Landau-like shape distribution.

The average signal to noise ratio is shown in figure 5.24 as a function of the cathode strip voltage for various gas mixtures: Ne/DME 50/50, Ar/DME 50/50, He/DME 50/50, Ne/DME/CO_2 45/45/10, Ne/DME/CO_2 40/40/20, He/DME/CO_2 40/40/20 and pure DME.

Although DME has the largest total ionization density (180 electrons cm^{-1}, as reported in reference [14]), at a given cathode strip voltage the largest signal to noise ratio is obtained by replacing part of the DME by a noble gas, 50 % in the present work. The largest signal to noise ratio is obtained with Ar/DME mixture, argon also having the largest ionization density among the noble gases considered here (see table 4.1). Helium has very low ionization yield and thus leads to a signal amplitude only 15 % higher than in pure DME. Adding 10 % of CO_2 to Ne/DME does not affect significantly the signal to noise ratio. Indeed Ne/DME 50/50 % and Ne/DME/CO_2 45/45/10 have a total ionization density of 110 and 109 cm^{-1} respectively and only 5 % of neon is replaced by CO_2. On the contrary, adding 20 % of CO_2 decreases the signal of both Ne/DME and He/DME by up to 35 %. Indeed, although the ionization densities

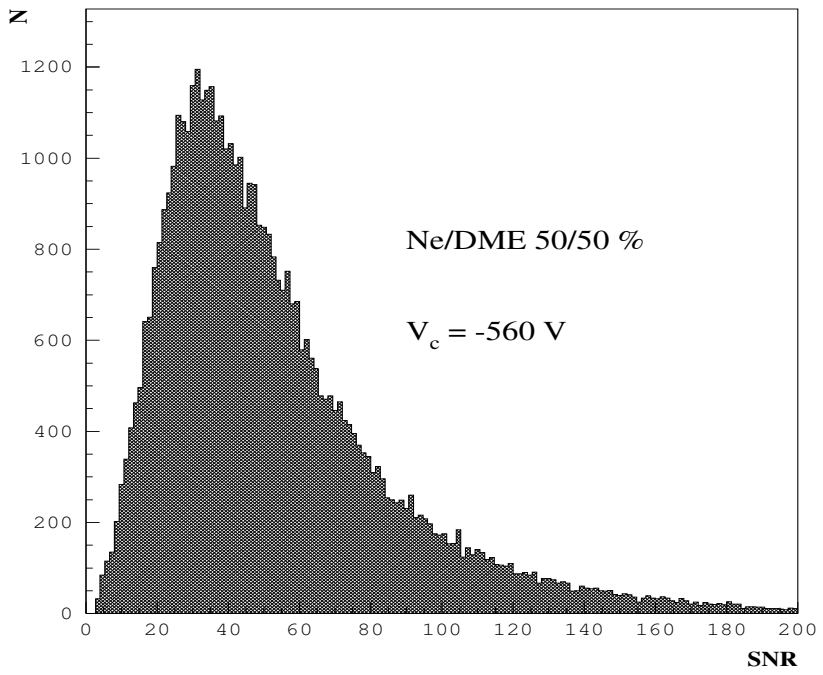

Figure 5.23: *Typical signal to noise ratio distribution in an MSGC filled with Ne/DME 50/50 % gas mixture and operated at a cathode strip voltage of -560 V.*

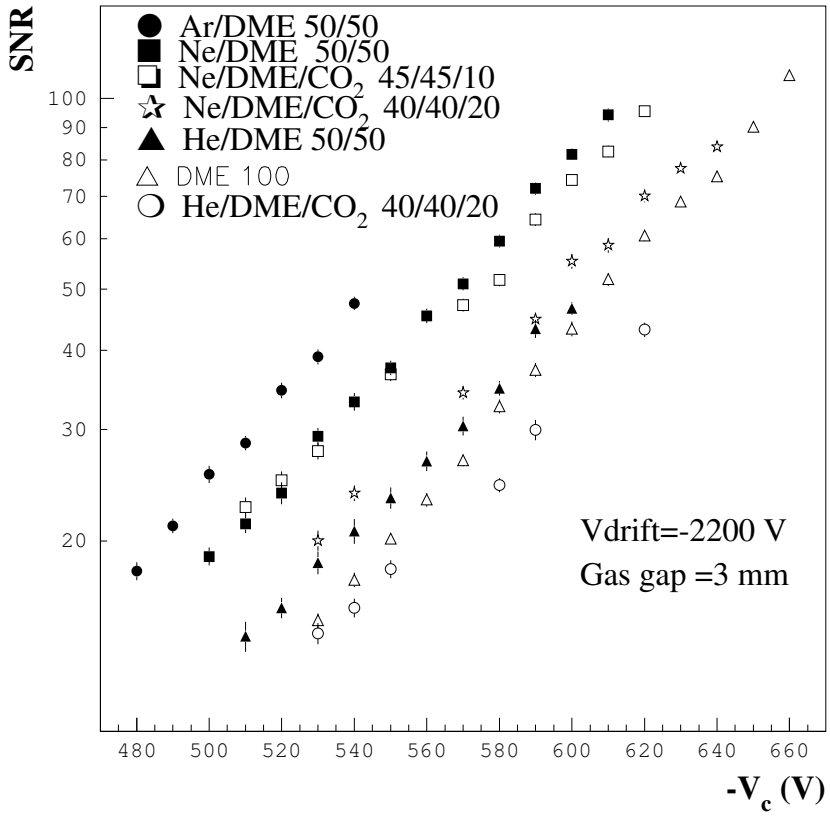

Figure 5.24: *Average signal to noise ratio as a function of the cathode strip voltage, at a drift voltage of -2200 V, for various gas mixtures.*

of Ne/DME 50/50 % and Ne/DME/CO_2 40/40/20 % are comparable (110 and 108 cm^{-1} respectively) and those of He/DME 50/50 and He/DME/CO_2 40/40/20 are also comparable (94 and 95 cm^{-1} respectively), the amount of the noble gas is reduced by 10 % when adding 20 % of CO_2 and therefore the effect becomes significant.

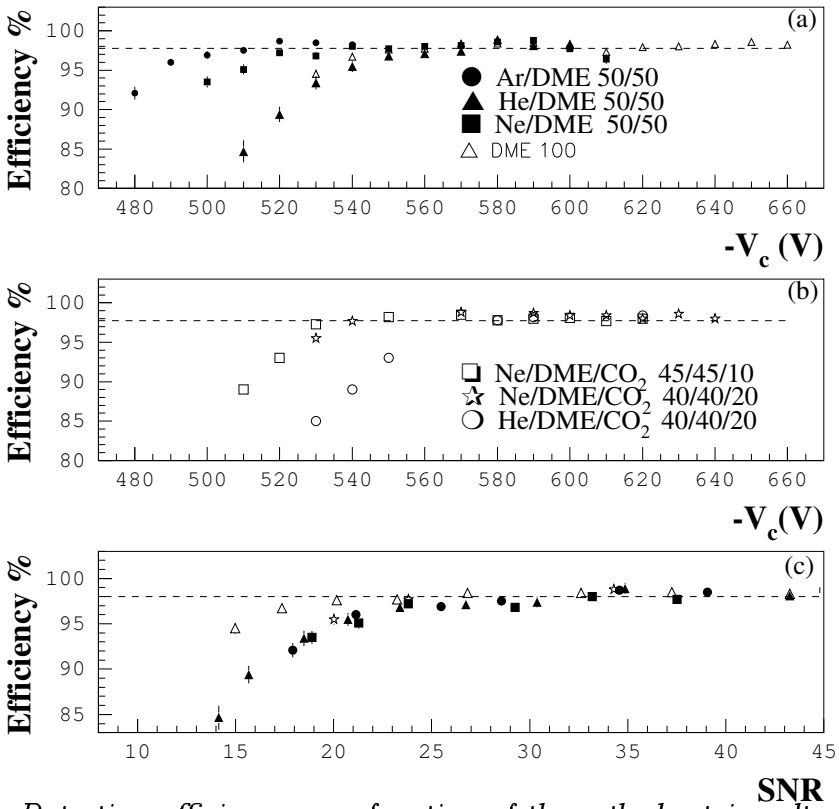

Figure 5.25: *Detection efficiency as a function of the cathode strip voltage (a) and (b), and of the average signal to noise ratio (c), for various gas mixtures. The drift voltage is -2200 V and the gas gap is 3 mm.*

Although at a fixed cathode strip voltage, pure DME leads to a smaller signal amplitude, the largest signal can be obtained with pure DME as its good quenching properties allow to work safely at much higher cathode strip voltages. However this can only be achieved at high cathode strip voltage which is undesirable. On the contrary, the largest signal to noise ratio measured for Ar/DME mixture is a factor two lower than for the corresponding Ne/DME mixture. This behaviour is attributed to the presence of photon feedback as the ionization potential of argon is lower than that of neon. Similar limitations have been encountered in Micro-Gap Chambers filled with Ar/DME with respect to Ne/DME mixtures [119]. However, the authors of reference [118] did not see this earlier breakdown in Ar/DME mixtures. An explanation might be that the trip level was set at 20 μA in that experiment instead of 80 nA in our case.

The behaviour of the signal to noise ratio with the cathode strip voltage for the different gas mixtures reflects in the variation of the particle detection efficiency with the cathode strip voltage. Figures 5.25 (a) and (b) show the detection efficiency as a function of the cathode strip voltage, for the different gas mixtures considered above. The efficiency plateau is set at 98 % and ends as for the signal to noise ratio measurements. Let us recall that an efficiency plateau starting at low cathode voltages is needed as well as a long efficiency plateau. The plateau starting at the lowest cathode voltage is obtained for Ar/DME. However this gas mixture

together with He/DME and He/DME/CO_2 have an insufficient plateau length, not more than 50 V, and therefore are rejected.

Among the remaining gas mixtures, Ne/DME comes first with an efficiency plateau starting 20 V higher than that of Ar/DME and having a length of 90 V. The last one is pure DME starting 30 V higher than for Ne/DME and having an efficiency plateau length of 110 V.

Adding 20 % of CO_2 to Ne/DME moves the start of the efficiency plateau by 20 V towards higher cathode strip voltages but increases the efficiency plateau length by 10 V since the quencher proportion is then increased. It must be noticed that the data reported here for Ne/DME 50/50 % can not be compared directly to those reported in section 5.4.1 since the gas gap of the chambers is different.

	V_{start} (V)	Length of plateau (V)	Maximum SNR
He/DME 50/50%	560	50	47
Ne/DME 50/50%	520	90	95
Ar/DME 50/50%	500	40	48
DME 100%	550	110	109
Ne/DME/CO_2 45/45/10%	530	90	96
Ne/DME/CO_2 40/40/20%	540	100	84
He/DME/CO_2 40/40/20%	570	50	43

Table 5.2: Starting point and length of the efficiency plateaus, and maximum stable SNR for the various gas mixtures.

The starting points and the lengths of the efficiency plateaus are summarized in table 5.2 as well as the maximum signal to noise ratio reached. Looking at this table and at figure 5.24, it can be seen that the long efficiency plateaus obtained correspond to a factor 3.4, 3.8 and 5 between the signal to noise ratio at the end and at the start of the efficiency plateau for Ne/DME/CO_2 45/45/10 %, Ne/DME 50/50 % and pure DME respectively.

As seen in section 5.4.1, the start of the efficiency plateau is linked to the average cluster charge and thus to the signal to noise ratio. The detection efficiency is shown in figure 5.25(c) as a function of the signal to noise ratio for some of the gas mixtures studied. The efficiency plateau starts at a signal to noise ratio of about 24. However, the gases with high primary ionization density like DME reach full efficiency already at a 20 % smaller signal to noise ratio. This can be explained if we look at figure 5.26 where the cluster charge distribution of Ne/DME 50/50 % and of pure DME at voltages leading to comparable signal to noise ratios are displayed. The gas with the largest primary ionization density, that is DME, has less fluctuations of the number of primary electrons and leads to a narrower distribution. Therefore the probability to have a signal below threshold is smaller for gases with a high primary ionization statistics. The width of the cluster charge distribution has been measured for several gas mixtures at cathode voltages leading to comparable signal to noise ratio, and is shown in figure 5.27 as a function of the primary ionization density. It shows clearly that the higher the primary ionization density, the narrower the cluster charge distribution.

For the Ne/DME mixture, it is observed in figure 5.25(c) that the minimum signal to noise ratio to have a full detection efficiency is about 24. This value is much higher than that obtained by another group, about 13, and which is set as the working point for MSGC's in CMS [14]. Two comments can be made about this difference. First, the value reported in reference [14] corresponds to a mixture of Ne/DME of 30/70 % having a larger primary ionization density than the Ne/DME 50/50 % used in this work, and therefore it allows to work efficiently at

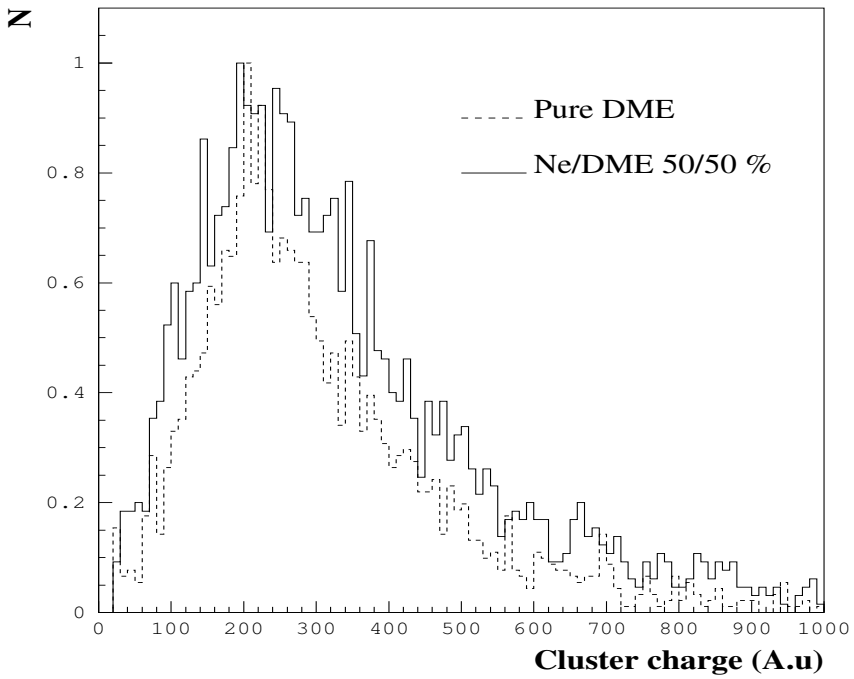

Figure 5.26: *Cluster charge distribution in Ne/DME 50/50 % and in pure DME at identical average signal to noise ratios.*

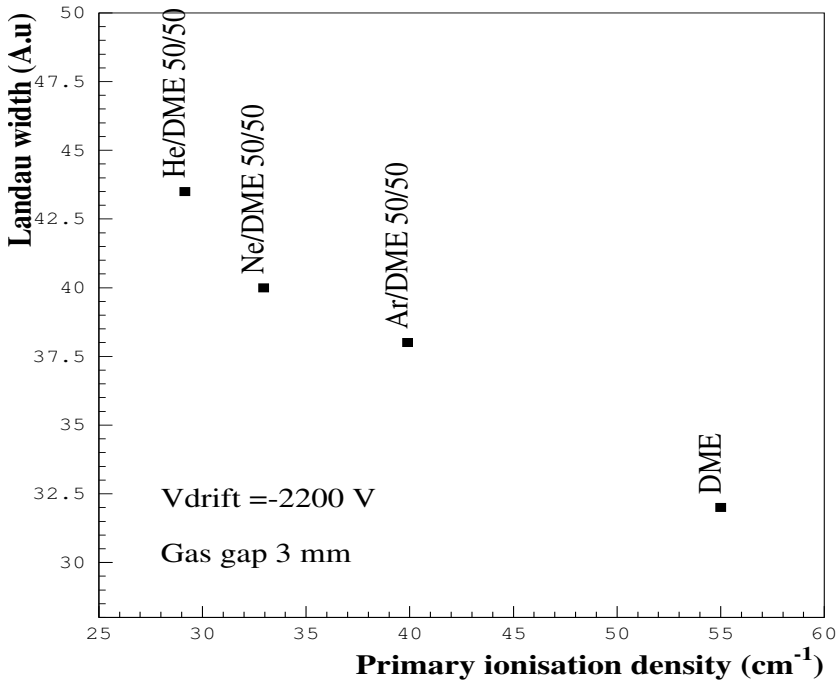

Figure 5.27: *Full width at half maximum of the cluster charge distribution versus the primary ionization density, for various gas mixtures operated at cathode strip voltages leading to comparable signal to noise ratio.*

a lower signal amplitude. However, this can not explain this difference since it is seen from figure 5.22 that this can lead to only 10 % of the difference between the two mixtures in the signal amplitude value at the start of the efficiency plateau. The second explanation comes from the difference in the particle incidence angle. Indeed in reference [14], the data are reported from a test beam where the maximum angular acceptance, in the direction perpendicular to the MSGC strips, is not more than 70 mrad, while in our case it extends up to 400 mrad. In case of a large incidence angle, the charge is distributed over more than one or two strips, and because of the strip inefficiency at large angles this charge might not exceed the threshold and therefore higher signals are needed to pass the threshold and to reach the full detection efficiency.

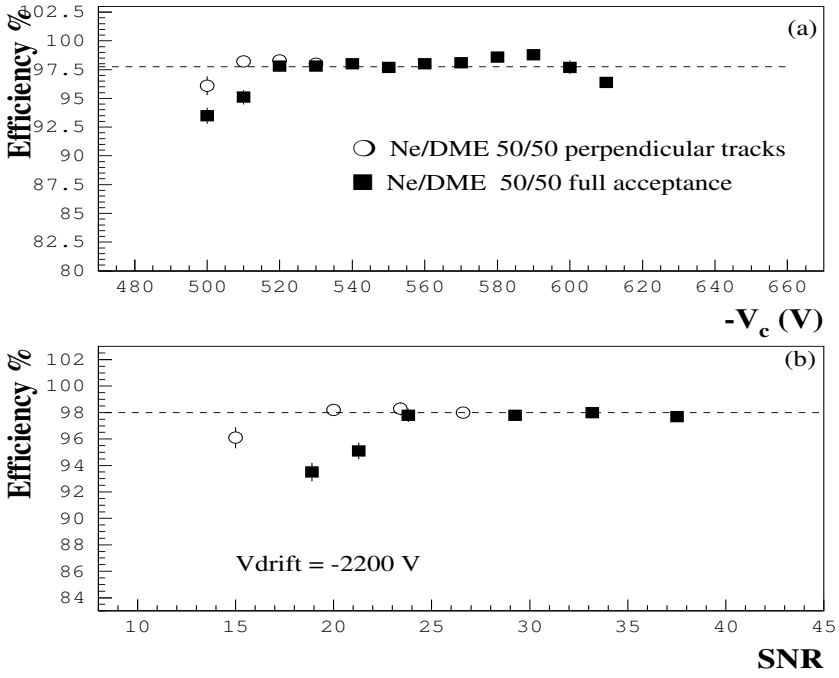

Figure 5.28: *Detection efficiency as a function of the cathode strip voltage (a) and of the signal to noise ratio (b) for tracks with an angle of incidence $|\beta| \leq 70$ mrad, and for the full hodoscope angular acceptance $|\beta| \leq 400$ mrad. For perpendicular tracks, only the points around the start of the plateau are displayed.*

To check this statement, we used the same data as for figure 5.25 and studied the detection efficiency for perpendicular tracks. Figure 5.28(a) shows the detection efficiency in Ne/DME 50/50 % for tracks with an angle of incidence ($|\beta| \leq 70$ mrad), and for tracks with the full hodoscope angular acceptance. Only the points around the start of the efficiency plateau are displayed for perpendicular tracks. It is clear that, in case of perpendicular tracks, the detection efficiency starts at a cathode strip voltage of -510 V instead of -520 V for full acceptance tracks. The length of the efficiency plateau is thus extended by 10 V. Figure 5.28(b) shows the detection efficiency as a function of the signal to noise ratio for both angular cuts. In case of perpendicular tracks, a signal to noise ratio of about 19 is sufficient to reach full efficiency instead of a value of 24 for tracks with full acceptance. This confirms the statement made above and contributes to the explanation of the difference mentioned above. However, even taking into account the different gas proportions and the angular acceptance, the minimum signal to noise ratio quoted in reference [14] is underestimated by 17 %.

The spatial resolution has also been studied for some of these gas mixtures. It has been

	Cluster size (*number* of strips)	resolution (μm)
He/DME 50/50%	1.7 $\pm$ .1	32 $\pm$ 2
Ne/DME 50/50%	2.0 $\pm$ .1	36 $\pm$ 2
Ar/DME 50/50%	1.9 $\pm$ .1 [10]	35 [120]
DME 100%	1.5 $\pm$ .1 [10]	30.0 $\pm$ 1.1 [121]
Ne/DME/CO_2 45/45/10%	1.8 $\pm$ .1	-
Ne/DME/CO_2 40/40/20%	1.8 $\pm$ .1	-

Table 5.3: Cluster size and spatial resolution for the various gas mixtures.

shown that the spatial resolution in MSGC's degrades rapidly with the particle incidence angle in the direction perpendicular to the strips (see section 5.2.4). In order to compare our data to previous results obtained in test beams and to minimize the effect of the track incidence angle, the position accuracy is measured with an angle of incidence less than 70 mrad. Since this requires important statistics, it has only been measured for He/DME and Ne/DME 50/50 %, at a signal to noise ratio of about 30. The results are 32 $\pm$ 2 μm and 36 $\pm$ 2 μm respectively. All the studies carried out in the past have shown that the position resolution of MSGC's with 200 μm anode pitch is between 30 and 40 μm for perpendicular tracks. The spatial resolution is strongly related to the cluster size and thus to the electron diffusion in the gas. Indeed, if the diffusion is too small, the particle signal is almost entirely collected by a single anode strip, leading to a position resolution of about the anode pitch divided by $\sqrt{12}$, that is 58 μm in case of a 200 μm anode pitch. On the contrary, if the cluster size increases, due to diffusion, the charge is spread over two strips allowing thus a better measurement of the impact point position.

Table 5.3 presents the cluster size and the position resolution obtained either in this work or in references [10, 120, 121] for perpendicular tracks. The largest cluster size is obtained for Ne/DME and the smallest one for pure DME. This is to be expected since DME has a small diffusion coefficient as seen in section 3.2. The spatial resolution varies only between 30 and 36 μm. Since it is affected by the particle incidence angle, the spatial resolution is not an important parameter in the gas choice for an MSGC tracker, as long as it does not exceed 40 μm for perpendicular tracks.

5.4.2.2 Drift velocity and transverse diffusion

An important parameter in the choice of the gas mixture is the electron drift velocity. For a typical drift velocity of 50 μm/ns, the total drift time of electrons in a 3 mm gas gap is 60 ns. A gas with a higher drift velocity will thus improve the MSGC performances at CMS (see section 4.2.3). The drift velocity was measured in a laser setup, installed in Antwerp, by T. Beckers [110]. In the following, these results are summarized and compared to the simulation we have performed as described in section 5.3. The electric field, both in the measurements and in the simulation, is defined as the difference between the cathode drift voltage of the MSGC and the effective voltage on the substrate which is approximately two third of the nominal cathode strip voltage, divided by the gas gap. The dependence of the electron drift velocity on the electric field is shown in figure 5.29 for various Ne/DME mixtures as well as for pure DME. The errors on the experimental data in this figure and the following figures are smaller than the size of the markers. The lines on the figure are results from our calculations described in section 5.3. The measurements extend to large electric fields which are commonly used in

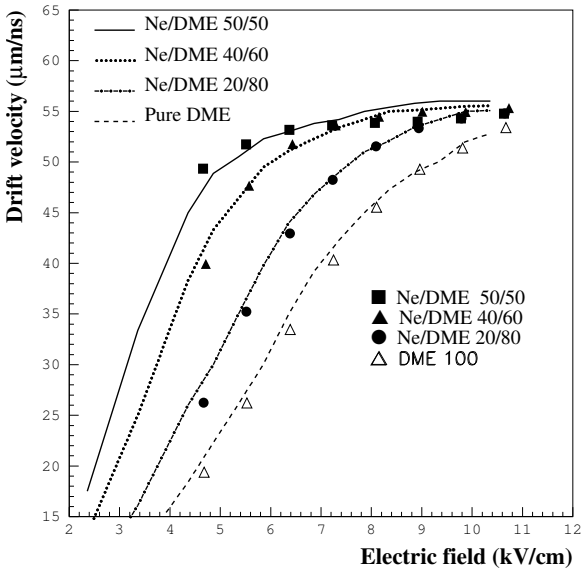

Figure 5.29: *Measured (points) and calculated (lines) drift velocity versus the electric drift field in pure DME and in Ne/DME gas mixtures.*

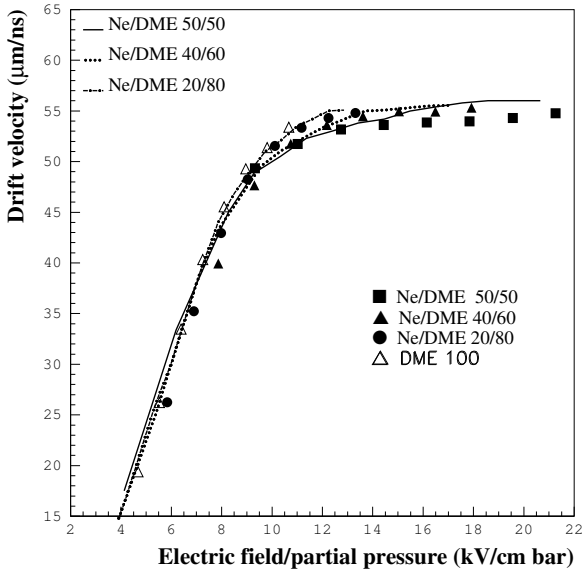

Figure 5.30: *Measured (points) and calculated (lines) drift velocity, in pure DME and in Ne/DME gas mixtures as a function of the electric drift field divided by the DME partial pressure.*

MSGC's (around 10 kV/cm in CMS). Both the simulation and the experimental results show that all mixtures saturate below a value of 55 μm/ns. At a given electric field, DME has the lowest drift velocity. Adding neon increases the drift velocity and causes the saturation to occur earlier. These drift velocities can be shown as a function of the electric field normalized to the partial pressure to verify whether neon only acts as a diluant as suggested above. Figure 5.30 shows that indeed this is a valid assumption, and both simulation and experimental results agree within less than 10 % in the worst case. In a previous work, the authors of reference [123] have seen the same behaviour in drift chambers filled with He/DME mixtures and operated at electric fields below 2 kV/cm. Indeed the dependence of the drift velocity u on the electric drift field E can be approximated by the relation [28]:

$$u \simeq \frac{1}{\varepsilon\sigma(\varepsilon)}\frac{ET}{P} \tag{5.36}$$

where ε is the characteristic energy of the electrons, σ is the momentum transfer cross section, P is the pressure and T is the temperature. Since DME is a thermal gas, its characteristic energy remains close to the thermal values. In this range of characteristic energy its momentum transfer cross section is about 10^{-14} cm^2, which is larger than that of neon, about 10^{-16} cm^2. The free path of electrons in Ne/DME mixtures is therefore mostly determined by the DME molecules as was explained above. Thus the drift velocity may scale with the ratio E/P_{DME}, where P_{DME} is the DME partial pressure.

Figure 5.31 shows the drift velocity versus the electric drift field, for Ne/DME, Ar/DME and He/DME 50/50 % gas mixtures. The drift velocity in Ar/DME and He/DME saturates at values below this of the Ne/DME gas mixture, before reaching an electric field of 10 kV/cm. Again the simulation agrees with the experimental data within less than 10 %.

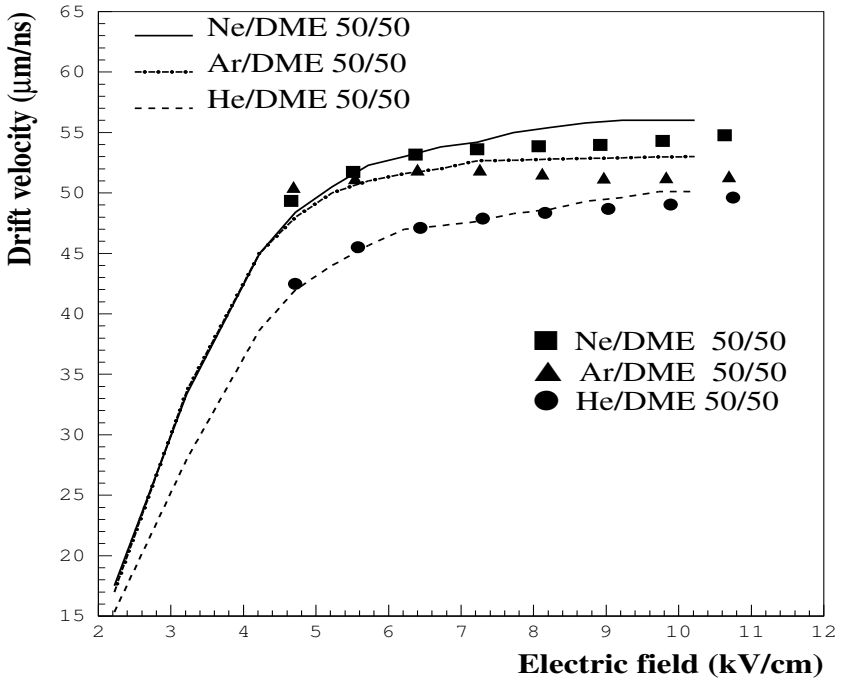

Figure 5.31: *Measured (points) and calculated (lines) drift velocity as a function of the electric field in mixtures of DME with noble gases.*

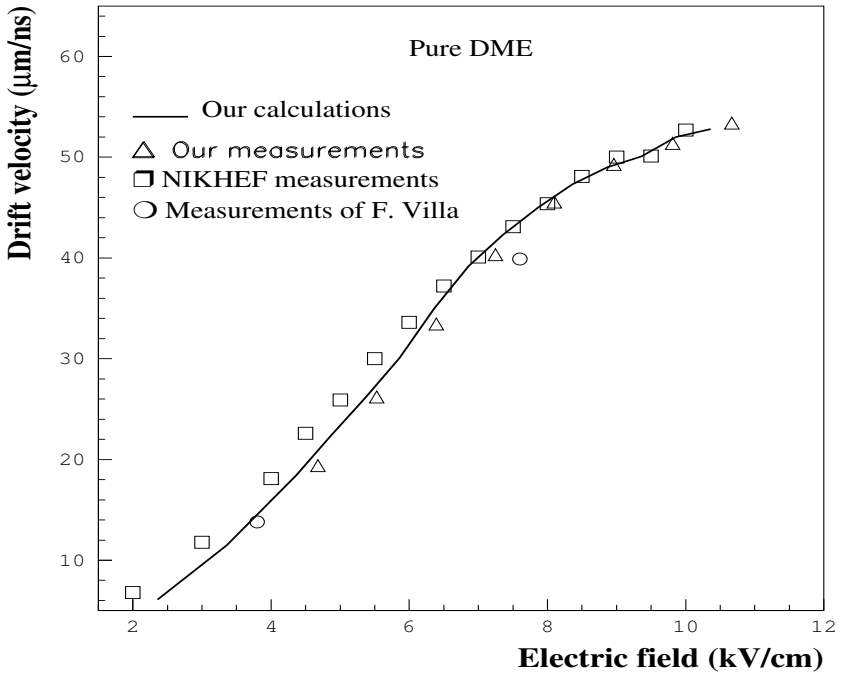

Figure 5.32: *Comparison of our measured (square marks) and calculated (lines) drift velocity as a function of the electric field, in pure DME, with previous measurements [75] and [124] (triangles and circles respectively).*

For comparison our measurements of the drift velocity as a function of the electric field in pure DME and our corresponding simulation are shown in figure 5.32 together with the measurements done by NIKHEF [75] and those done by F. Villa [124]. At relatively low electric fields ($E \leq 6$ kV/cm), there is a discrepancy of up to 15 % between the measurements of NIKHEF and our data, both experimental and simulation. This is attributed to the fact that, in the measurements of NIKHEF, the electric field is computed as the difference between the cathode drift voltage and the cathode strip voltage divided by the gas gap. This value is thus underestimated by one third the cathode strip voltage divided by the gas gap, with respect to our electric drift value. At high electric drift field values this difference becomes less significant and both measurements and simulation agree. However, there is a discrepancy with the values measured by F. Villa, where the way in which the electric drift field has been computed is not indicated.

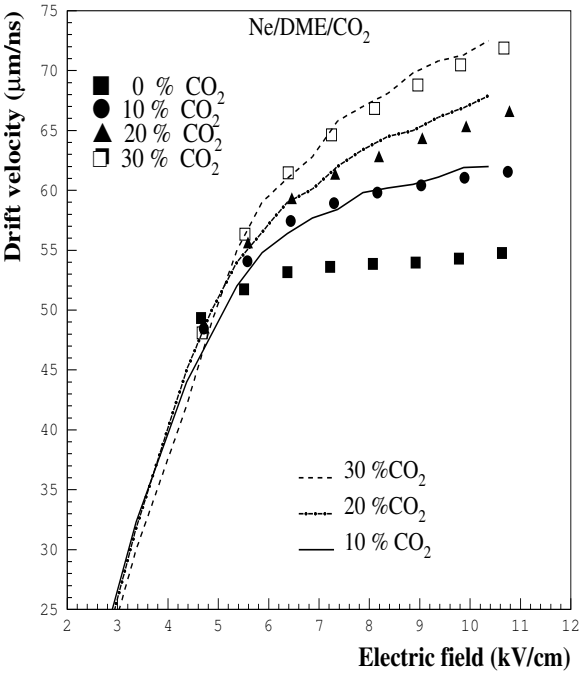

Figure 5.33: *Measured (points) and calculated (lines) drift velocity as a function of the electric field in gas mixtures with equal amounts of neon and DME with increasing CO_2 content.*

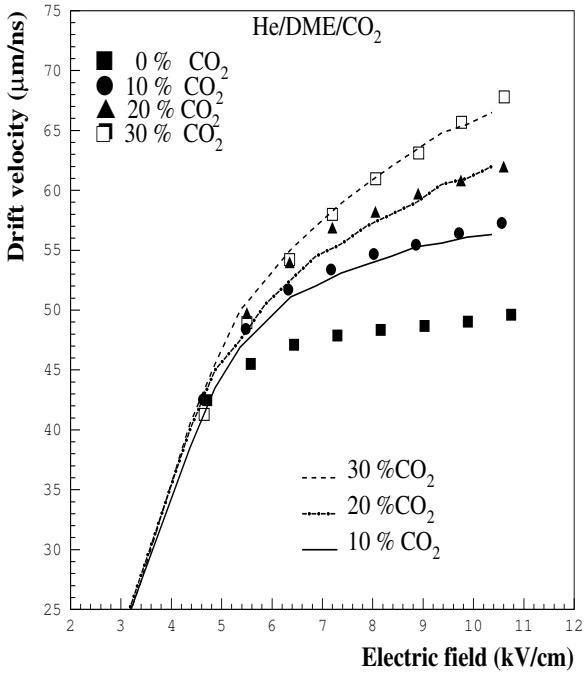

Figure 5.34: *Measured (points) and calculated (lines) drift velocity as a function of the electric field in gas mixtures with equal amounts of helium and DME with increasing CO_2 content.*

From the above measurements we can conclude that the binary mixtures of DME with noble gases are not fast enough for operation at CMS. Indeed, the maximum drift velocity, obtained with Ne/DME 50/50 %, is 55 μm/ns. The corresponding drift time in the 3 mm gas gap is thus about 54 ns. In such a mixture the primary ionization is low and all the ionizations produced would be needed to reach the efficiency plateau. In the case of CMS, this goal would be fulfilled if the drift time is less than two LHC bunch crossing intervals, that is less than 50 ns. Since the addition of CO_2 to DME has been shown to improve the drift velocity from 52 μm/ns to 68 μm/ns at an electric field of 10 kV/cm [75], we tried to add CO_2 to some of these binary mixtures. Figures 5.33 (5.34) shows the drift velocity , from both simulation and measurements, as a function of the electric field for Ne/DME/CO_2 (He/DME/CO_2) with equal amount of neon (helium) and DME, and with different CO_2 content. At low electric fields,

there is no influence of CO_2 on the drift velocity as can be seen from both the simulation and the measurements. This can be attributed to the fact that at low electric field, the electrons characteristic energy does not vary too much and consequently the momentum transfer cross section leading to a negligible effect of the CO_2 content. At electric fields above 5 kV/cm, the effect of CO_2 becomes significant and the larger the CO_2 content the higher the drift velocity. At a given electric field strength and at a given CO_2 content the drift velocity is higher in mixtures with neon than those with helium. At an electric field of 10 kV/cm, addition of 10, 20 and 30 % of CO_2 to Ne/DME mixtures leads to drift velocities of 60, 65 and 71 μm/ns respectively. The corresponding drift times in a 3 mm gas gap are respectively 50, 46 and 42 ns. It turns out that the addition of CO_2 is favourable for operation at LHC, for two reasons: on one hand, it increases the drift velocity allowing the full collection of primary ionization within two LHC bunch crossing intervals, and on the other hand, in case of a variation of the external magnetic field, the Lorentz angle, in the CMS barrel region, can be kept constant by adjusting the drift velocity with a slight variation of the amount of CO_2. The presence of up to 20 % of CO_2 in the Ne/DME mixtures does not change significantly the detection characteristics of these mixtures.

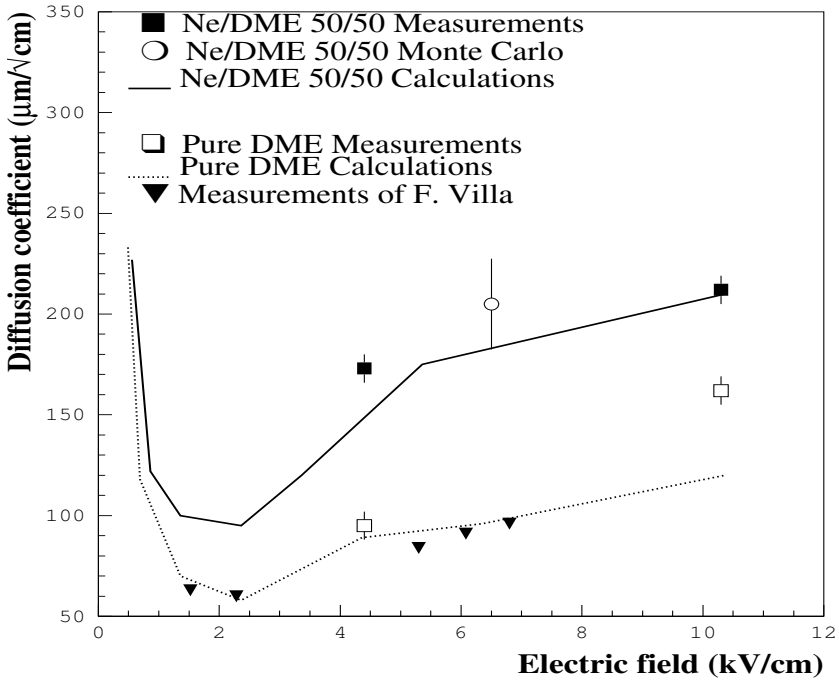

Figure 5.35: *Measured (square marks) and calculated (lines) transverse diffusion coefficient versus the electric drift field. A Monte Carlo estimation [113] (circle) and previous measurements [124] (triangles) are also shown for comparison.*

With the laser setup, it is also possible to measure the transverse diffusion coefficient $D_T^{'}$ of relation (3.17). The transverse diffusion can be calculated by generating an ionization spot at a given height above the substrate and measuring the RMS width of the electron cloud arriving on the substrate.

Figures 5.35 shows the measured (square marks) and calculated (lines) transverse diffusion coefficient as a function of the electric field in pure DME and in Ne/DME 50/50 % gas mixtures. A previous Monte Carlo estimation in Ne/DME 50/50 % [113] is also shown as well as previous measurements in pure DME [124]. The results agree qualitatively except for pure DME at an

	Diffusion Coefficient in ($\mu m/\sqrt{cm}$) at 4.4 kV/cm	Diffusion Coefficient in ($\mu m/\sqrt{cm}$) at 10.3 kV/cm
DME 100%	95	162
Ne/DME 50/50%	173	212
Ne/DME/CO_2 45/45/10%	177	216
Ne/DME/CO_2 40/40/20%	166	181
Ne/DME/CO_2 35/35/30%	168	188
He/DME 50/50%	148	193
Ar/DME 50/50%	168	214

Table 5.4: Transverse diffusion coefficients for different gas mixtures at two different electric field strengths.

electric field of 10 kV/cm. Calculations done by A. Sharma [110] lead to results similar to our calculations. Table 5.4 presents the measured diffusion coefficient for the different gas mixtures and for two values of the electric field. The errors on the values are of the order of 5 $\mu m/\sqrt{cm}$. As expected the diffusion coefficient in pure DME is the smallest one. The transverse diffusion coefficients in triple gas mixtures are comparable to that of Ne/DME 50/50 and He/DME 50/50. Therefore the spatial resolution in these mixtures is expected not to exceed 40 μm for perpendicular tracks.

5.4.2.3 Simulation of the Lorentz angle

The presence of the 4 T magnetic field, orthogonal to the electric field, in the CMS barrel part changes the direction of drift of the ionization electrons by an angle α_L given by relations (3.11) and (3.12). The situation is identical to the detection of a particle with an incidence angle α_L with respect to the normal to the substrate. The spatial resolution is thus worsened. In CMS, the MSGC's will be tilted by an angle α_L in order to compensate for this effect. The Lorentz angle can also be minimized by working at the highest possible electric field. However each attempt to increase the detector speed by increasing the electrons drift velocity will result in an increase of the Lorentz angle (see equation (3.12)). The addition of CO_2 is thus expected to increase the angle α_L. Since we didn't have the opportunity to test MSGC's in a magnetic field, we performed calculations of α_L with the simulation tools.

To check the reliability of our calculations, results from these simulations were compared with existing data in magnetic fields and were found to be consistent [15, 120]. As an example figure 5.36 shows the calculated Lorentz angle and this measured by F. Angelini et al. [120], as a function of the intensity of the magnetic field for a mixture of Ar/DME 80/20 %. The simulation agrees with the data.

Figure 5.37 shows the Lorentz angle as a function of the magnetic field, at an electric drift field of 10 kV/cm for Ne/DME gas mixtures with various CO_2 content. As expected all curves are linear functions of the magnetic field. At a given magnetic field, the larger Lorentz angle obtained with the mixture with the highest CO_2 content is explained by the highest drift velocity (see figures 5.29 and 5.33) as the Lorentz angle is proportional to the drift velocity (see equation (3.12)). Adding either 10 %, 20 % or 30 % of CO_2 to the Ne/DME 50/50 % gas mixture brings the Lorentz angle from 16^0 to 18.4^0, 19^0 and 20.3^0 respectively. In the present design of the CMS barrel part the MSGC's are tilted by an angle of 14^o to compensate for the

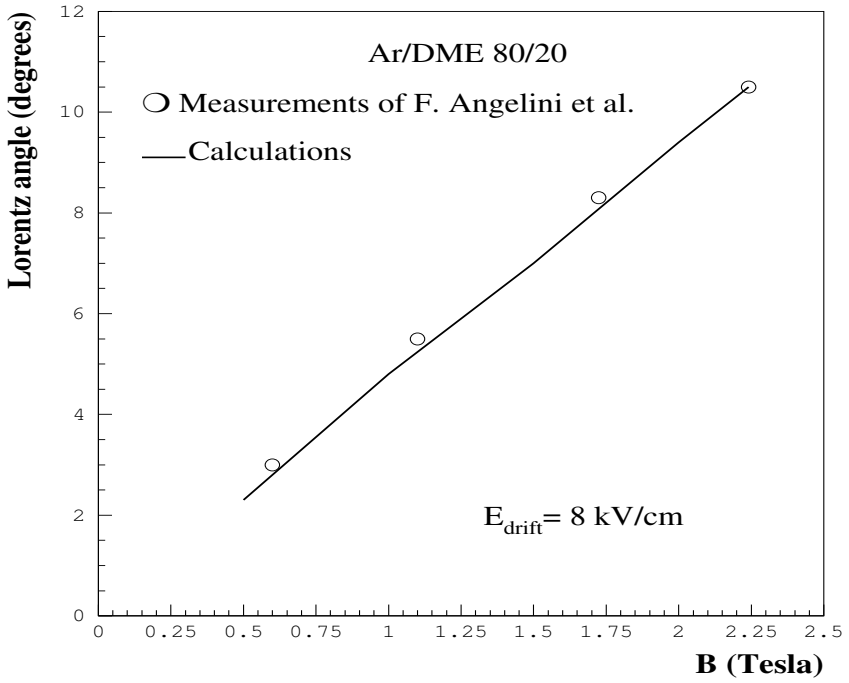

Figure 5.36: *Calculated (line) and measured (points) Lorentz angle as a function of the magnetic field in Ar/DME 80/20 % at an electric drift field of 8 kV/cm. The measurements are taken from reference [120].*

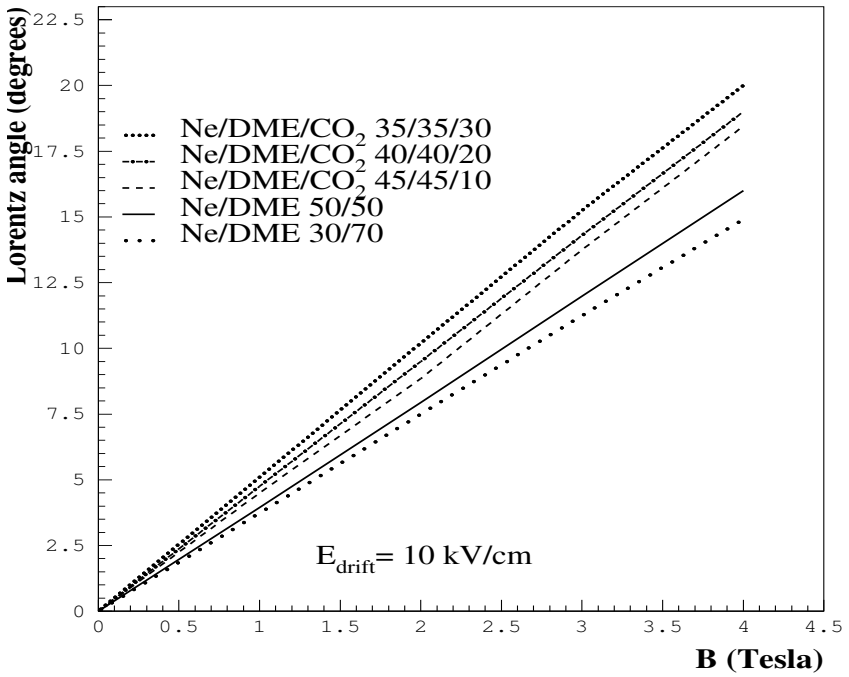

Figure 5.37: *Calculated Lorentz angle as a function of the magnetic field and at an electric field of 10 kV/cm, in Ne/DME gas mixtures with different CO_2 content.*

Lorentz angle in the Ne/DME 30/70 %. Use of the Ne/DME/CO_2 40/40/20 % instead would increase the particle angle of incidence by 5^0. The spatial resolution for high p_t particles would thus change from 35 μm to 50 μm (see figure 5.18).

5.5 MSGC response to a high intensity Hadron beam

We discussed in section 4.2.4 several problems that have been met during the test of MSGC's with low energy pions or protons due to discharges induced by heavily ionizing particles (HIP's). The solution proposed to suppress the discharges or to limit the damage produced by them is the advanced passivation technique. Although this technique has shown promising features in controlled laboratory tests with α-particles, its feasibility had to be proven in a real high intensity beam of hadrons producing HIP's, with a large dynamic range of deposited energy. The MSGC group of CMS has thus carried out tests in high intensity hadron beams. This section reports on the first of them with five MSGC's in the high intensity hadron beam T10 at the CERN PS. Section 5.5.1 describes the MSGC counters that were tested and section 5.5.2 the experimental setup. The results are reported in section 5.5.3.

5.5.1 MSGC counters

Five MSGC's, 10×10 cm^2 each, have been produced and assembled according to the CMS baseline specifications that were introduced in section 4.2.4. Four of these MSGC's have been assembled by the PISA MSGC group and are labelled: P_1, P_2, P_3 and P_4. The fifth counter, labelled B_1, was assembled in our laboratory. The substrates are made of DESAG D263 glass 300 μm thick, under-coated by a semi-conductive layer. The resistivity and the type of coating are given in table 5.5. The strips are made of gold and are 10 cm long, 0.5 μm thick. The anodes are 7 μm wide, the cathodes 90 μm. The anode pitch is 200 μm. Each detector has 512 anode strips.

The strip ends are passivated on 2 mm by a 3 μm thick polyimide film (standard passivation) and the cathode strip edges by a 3 μm polyimide film, 4 μm wide (advanced passivation). All cathodes are connected to the high voltage but the first and last ones of the Pisa counters, which are grounded to optimize the electric field configuration at the counter edges. The four Pisa counters have drift planes made of 500 μm thick PEEK[1], metallized with gold. Counter B_1 drift plane is a 300 μm thick D263 glass plate coated with 5 nm of chromium. This leads to a high resistivity of the drift plane. The gas gap in all counters is 3 mm. The counters are filled with a Ne/DME 30/70 % gas mixture. Counter B_1 is assembled following the open design layout of the CMS forward tracker (see section 4.4.3); its service board is thus different from this of the Pisa counters. As shown in table 5.5, the Pisa counters have about 10 dead strips per counter, which are mostly due to artwork defects. Counter B_1 lost 86 strips during the assembly procedure. In addition to the five MSGC's, two Micro-Gap Counters (MGC's) have been placed in the beam by the Lyon group. However no result will be given regarding these two counters since it is beyond the scope of this work. The anode strips are read out by PreMux128 chips [125]. One chip consists of 128 preamplifiers, shapers and a multiplexer. The working principle of one channel of this chip is illustrated in figure 5.38. The strip signal is sampled two times by opening the switches S_1 and S_2. S_2 is closed at the maximum of the signal and S_1 is closed when the pulse returns to the baseline. The time constant of the RC stages is made very small (3.5 ns) compared to the rise time of the amplifier ($\sim$ 40 ns) so that the voltage on both capacitors follows the voltage on the input. By opening S_2 and S_1 these voltages are stored on the capacitors. The difference of the voltages on the capacitors is amplified by an external differential amplifier and gives the output signal. To collect the maximum charge, one has to adjust the timing between the arrival of the trigger and the opening of S_2, and thus to make the so called "delay curve".

[1] Poly-Ether-Ether-Keton

	Coating resistivity $\Omega/\square$	number of dead strips	drift plane
P_1	(Pestov) 1.2 10^{16}	10	PEEK+Au
P_2	(Pestov) 9 10^{15}	10	"
P_3	(Pestov) 5 10^{15}	10	"
P_4	(DLC) 1 10^{15}	10	"
B_1	(Pestov) 4.8 10^{15}	86	D263 glass + 5 nm Cr

Table 5.5: Some characteristics of the MSGC's tested.

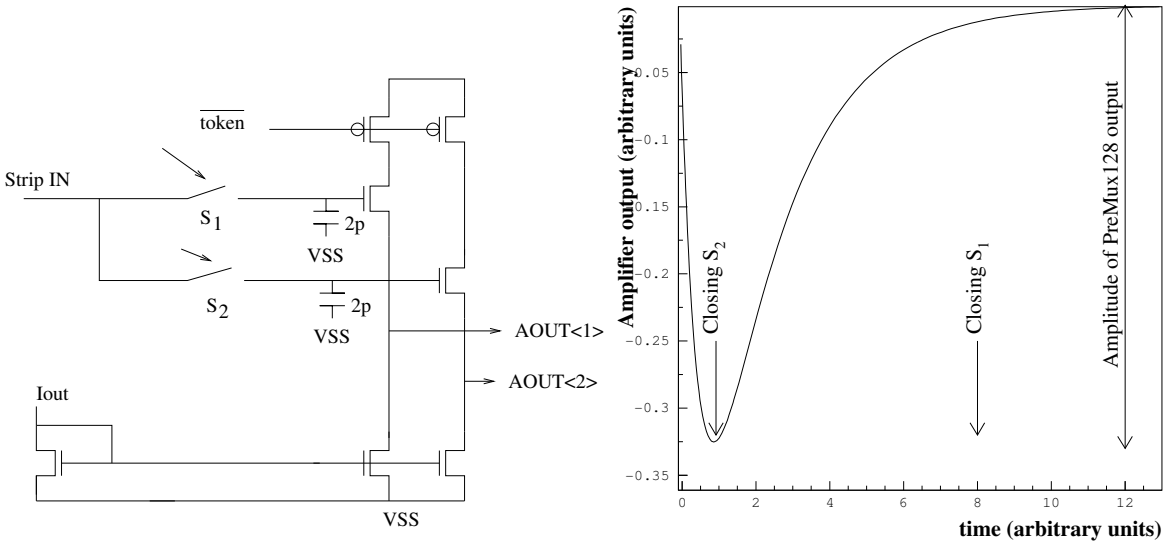

Figure 5.38: *Schematic diagram and working principle of the PreMux128 readout chip [125].*

5.5.2 Experimental setup

The detectors have been placed on a bench as shown in figure 5.39 at the CERN PS T10 test facility. All detectors read out the x coordinate but counter B_1, reads out the y coordinate. The beam is a 3 GeV/c pion beam of intensity that can be varied up to 4 kHz/mm^2. The beam spill lasts on average 300 ms every 7 s yielding thus a duty cycle of 5 %. The beam is estimated to have a Gaussian distribution in the directions orthogonal to the beam, with a standard deviation of about 2.5 cm. Two scintillators of active area of 5×5 and 10×10 cm^2 respectively delivered the trigger signals. A finger scintillator of 0.5×0.5 cm^2 active area was used for rate measurements. The interaction length is estimated to be 70.5 cm in the PEEK drift planes, 49 cm in the drift plane of counter B_1 and 43 cm in its 50 μm thick aluminium cover, and slightly less than 49 cm in the substrates; these lengths have been estimated using the pion inelastic cross sections in different materials given in reference [126]. The probability of nuclear interaction of a single pion is therefore at least 0.13 % per detector. Taking into account the number of detectors present in the bunch, the HIP rate during a spill is comparable to that at the LHC [127].

The anode signals are digitized by a Scirocco Flash-ADC. The electrode voltages are set by means of a CAEN high voltage power supply with a trip level set at 1 μA. For counter B_1, an additional opto-coupled electrometer is used to control the cathode drift current. The trip level was also set at 1 μA.

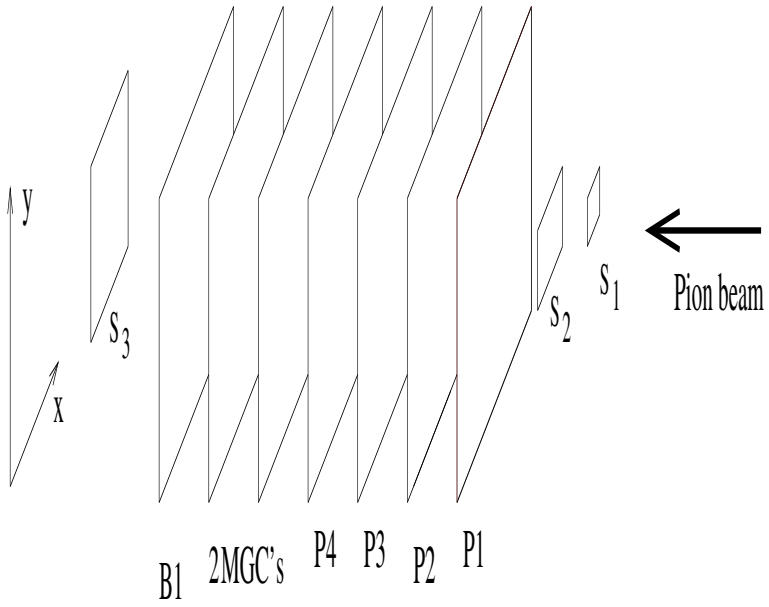

Figure 5.39: *Schematic view of the experimental setup. S_1, S_2 and S_3 are scintillators and P_1, P_2, P_3, P_4 and B_1 the MSGC's under test. The two Micro Gap counters are not analyzed here.*

The data acquisition (DAQ) is performed with a VME crate and a computer. All raw data are written to EXABYTE tapes for offline analysis. In parallel a subset of data are analyzed and visualized on line in order to provide monitoring.

5.5.3 Results

The detectors were exposed during 11 days to the hadron beam operated at a high intensity of a few kHz/mm^2. In order to monitor the uniformity of the response of the counters, two low intensity ($\sim$ 200 Hz/mm^2) runs per day were taken. The data analysis procedure is similar to that described in section 5.2. After pedestal subtraction and correction for common mode shift, clusters are formed with adjacent channels having a signal above the threshold. The threshold on the strip charge is set to 4(5) times the strip RMS noise and that on the cluster charge is set to 4(5) times the cluster noise for the Pisa chambers (counter B_1). These thresholds have been chosen by an appropriate study of the detection efficiency and of the noise in the chambers, similar to the one performed in section 5.2.3. The higher threshold set for counter B_1 is due to the higher noise, due probably to the use of a different service board for this counter. Among the selected clusters in a given chamber, the one with the highest charge is chosen, in order to reject possible noisy clusters. The detection efficiency has been measured for a given counter using tracks producing at least one cluster in two of the other MSGC counters. The efficiency is thus defined as the fraction of these tracks detected by the counter considered. No correction for dead strips has been made neither for false reference tracks. This is not important as the aim was to find the start of the efficiency plateaus and to monitor the evolution of the counter response with the duration of exposure to the beam. The analysis is mainly devoted to check the chamber stability and to look for possible damage of the strip pattern due to discharges.

5.5.3.1 Cluster characteristics and signal to noise ratio at low intensity

Before starting any measurements, the timing of the signal sampling has to be adjusted in order to record the maximum possible charge. A delay box has been inserted in the trigger line between the arrival of the trigger and the opening of the PreMux128 channel switch S_2. Figure 5.40 shows the cluster charge as a function of this delay for counter B_1. A delay between 35 and 45 ns yields the maximum charge. A value of 40 ns has thus been chosen. The same delay has been applied to the other counters.

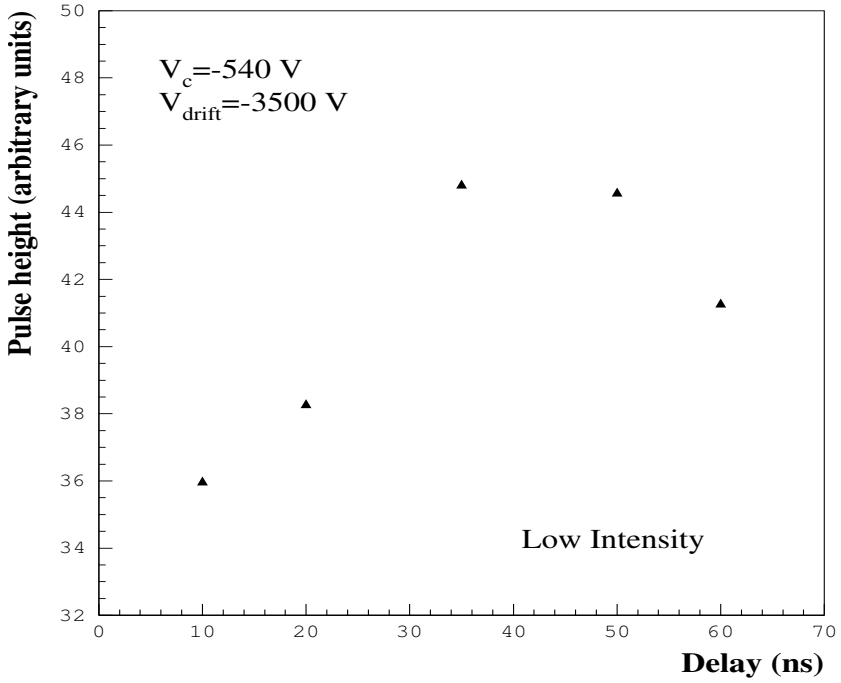

Figure 5.40: *Average cluster charge versus the trigger delay for counter B_1.*

Figures 5.41 and 5.42 show the distributions of the cluster charge (a), the average strip noise (b), the cluster size (c) and the number of clusters per event (d), in a low intensity run for counters P_3 and B_1 respectively. The cathode strip voltage is -540 V and the drift voltage is -3500 V. Since the substrates have the same resistivity, the average cluster charge distributions are comparable. However the average strip noise is 40 % higher in B_1 than in P_3, probably due to the different service board used in counter B_1. Therefore the signal to noise ratio is lower in counter B_1. The event multiplicity and the cluster size are lower in B_1, due to the higher thresholds applied for this counter. Although the hadron beam is approximately perpendicular to the counters, the cluster size is 40 % higher than the one also obtained for Ne/DME gas mixtures in section 5.4.2 for P_3 and 17 % for B_1. Part of this difference is attributed to the different electric fields leading to different transverse diffusion coefficients. In the present case, the electric field is about 10 kV/cm (compared to 5 kV/cm in section 5.4.2) leading to a transverse diffusion coefficient 22 % higher and consequently to a larger spread of the electron cloud.

A first measurement was done to find the working point of the MSGC counters by performing a high voltage scan in a low intensity beam. Figure 5.43 shows the signal to noise ratio as a function of the cathode strip voltage for the Pisa counters at a drift voltage of -3500 V. For the safety of the counters, measurements are not pushed to cathode strip voltages higher than -560 V. All curves show the expected exponential dependence of the signal to noise ratio on the cathode voltage. At a given cathode voltage the signal to noise ratio increases with the

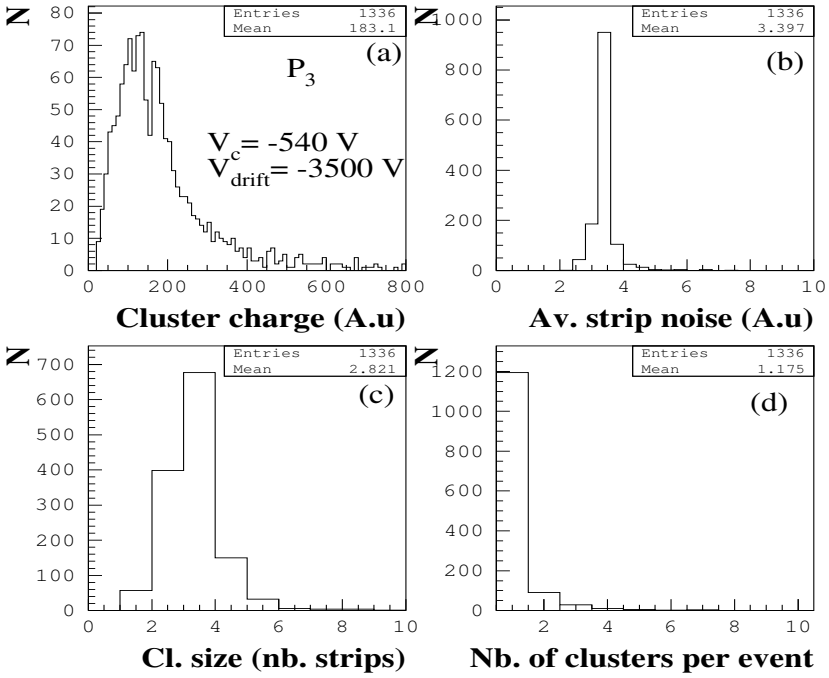

Figure 5.41: *Distributions of the cluster charge (a), the average strip noise (b), the cluster size (c) and the event multiplicity (d) for counter P_3 in a low intensity beam.*

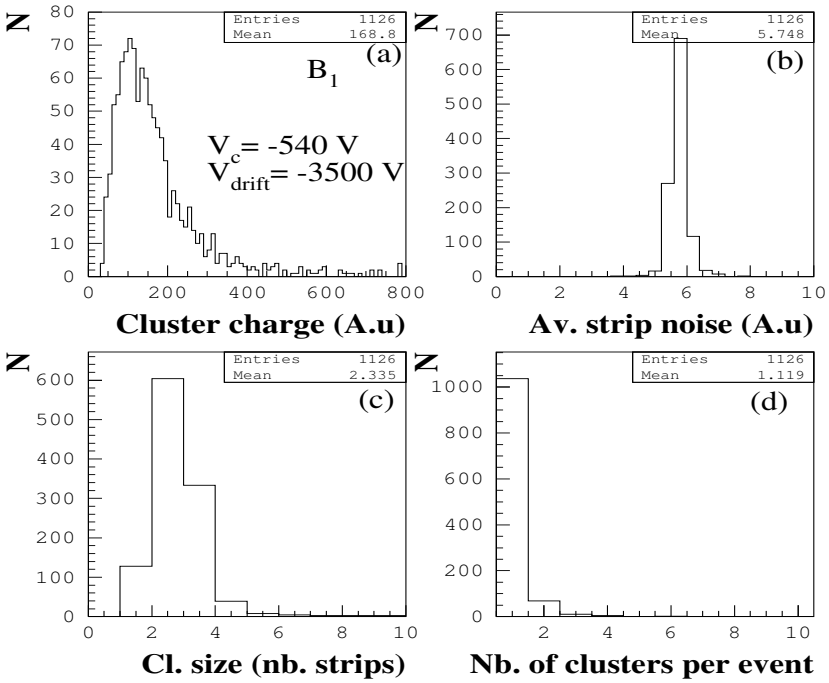

Figure 5.42: *Distributions of the cluster charge (a), the average strip noise (b), the cluster size (c) and the event multiplicity (d) for counter B_1 in a low intensity beam.*

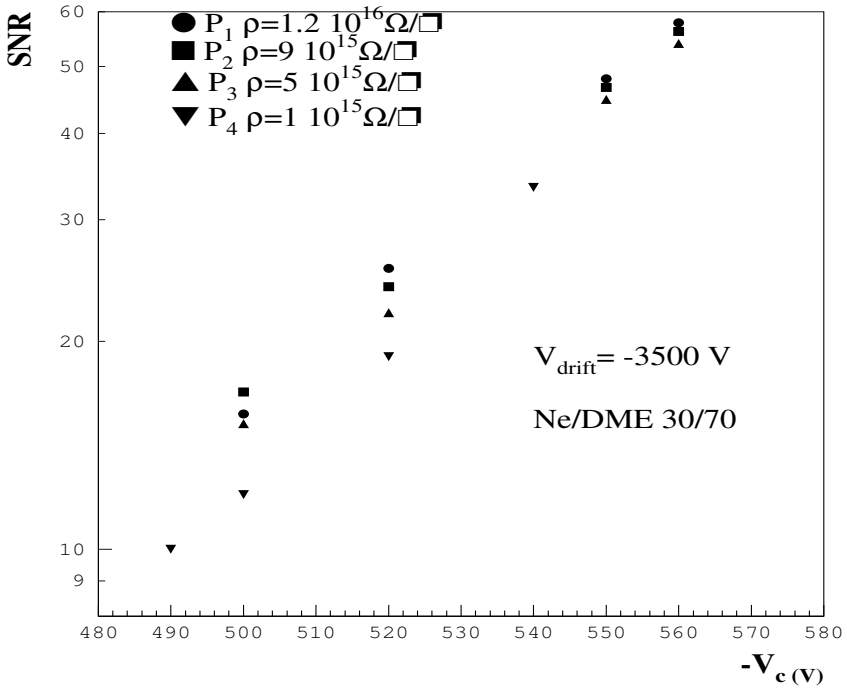

Figure 5.43: *Dependence of the signal to noise ratio on the cathode strip voltage for counters P_1, P_2, P_3 and P_4 having a substrate with surface resistivities in the range 1.2 10^{16}- 10^{15} $\Omega/\Box$, in a low intensity beam.*

substrate surface resistivity. This was expected since a lower substrate resistivity decreases the anode electric field and consequently the pulse height as explained in section 4.2.1. A decrease of the substrate resistivity by an order of magnitude reduces the pulse height by up to 30 %. However this gain reduction affects slightly the beginning of the efficiency plateau as we can see on figure 5.44(a) and (b) showing respectively the dependence of the detection efficiency on the signal to noise ratio and on the cathode strip voltage, for counters P_1 and P_4 operated at a drift voltage of -3500 V. For a given gas and for a given detector geometry the efficiency plateau is expected to start at a signal to noise ratio independent of the gain variations occurring from one substrate to another. Indeed the data points of both P_2 and P_4 seem to fit a single curve in figure 5.44(a). We thus estimate that the minimum signal to noise ratio required to reach a full efficiency of at least 98 % is 19, for both counters. This value corresponds to cathode strip voltages of -510 V and -520 V respectively for counters P_1 and P_4 (see 5.44(b)). Thus a difference on the surface resistivity of one order of magnitude moves the efficiency plateau by only 10 V.

5.5.3.2 Counters behaviour under high intensity of hadrons

The scope of this test is to study the behaviour of the MSGC counters when exposed to a high intensity beam of hadrons. To do so, the detectors have been operated at their nominal working point determined in the preceding section, -3500 V on the drift plane and -520 V on the cathode strips.

Figure 5.45 shows the average pion rate versus the integrated running time as measured by the 0.5×0.5 cm^2 scintillator placed a few millimetres off the beam centre. Considering the 5 % duty cycle of this beam and the integrated time of 155 hours, the beam test period amounts therefore to about 7h 45mn of continuous beam at a rate of 2 kHz/mm^2 or more, always larger

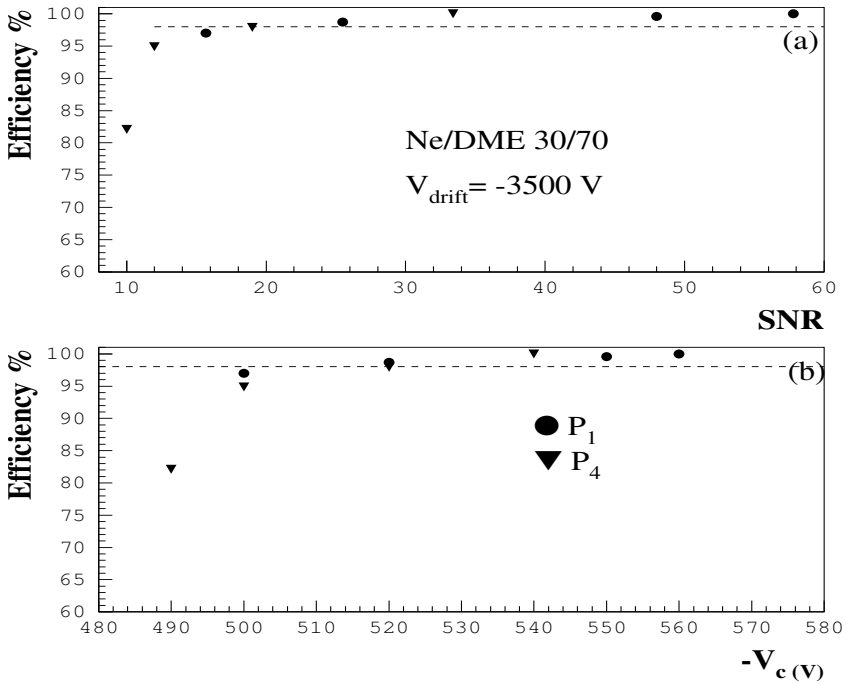

Figure 5.44: *Dependence of the detection efficiency on the cathode strip voltage (a) and on the signal to noise ratio (b) for counter P_1 having a substrate resistivity of 1.2 10^{16} $\Omega/\Box$ and counter P_4 having a substrate resistivity of 1 10^{15} $\Omega/\Box$, in a low intensity beam.*

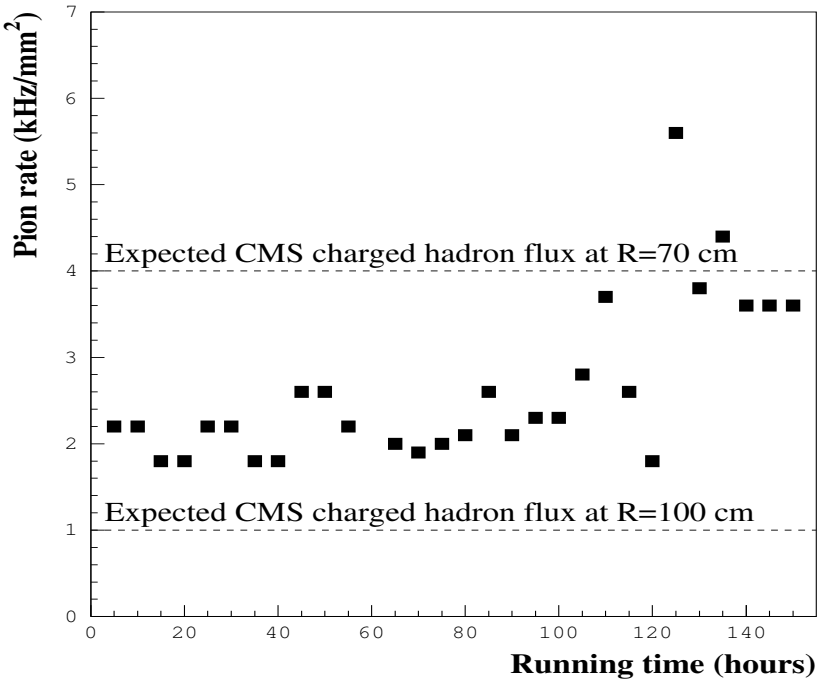

Figure 5.45: *Average pion rate as a function of the integrated running time, measured by the 0.5×0.5 cm^2 scintillator set close to the region of maximum beam intensity.*

than the one expected at the LHC at a radial distance of 100 cm from the beam pipe[1].

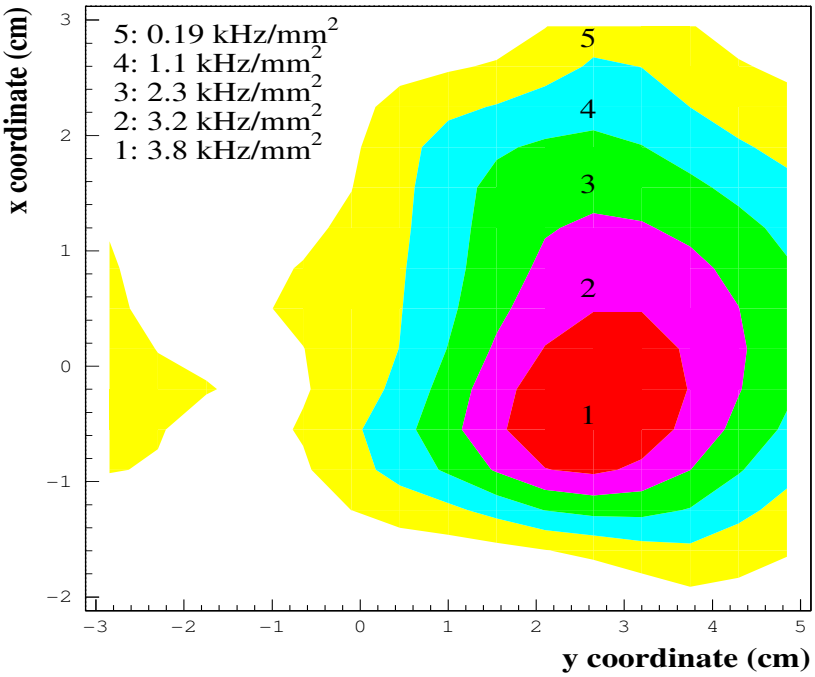

Figure 5.46: *Contour plot showing five regions of different particle rates in the MSGC active area.*

Since both coordinates were measured for beam particles, the x coordinate by Pisa counters and the y coordinate by counter B_1, it was possible to estimate the irradiated area of the chambers and the corresponding particle rate. Figure 5.46 shows the distribution of particles in the x-y plane. The irradiated area is divided into five regions with different particle rates. The area with the maximum number of impact points in the MSGC plane is assumed to correspond to the rate recorded by the 0.5×0.5 cm^2 scintillator. The rates in the other regions are deduced from the rate in the central region, scaled by the numbers of impact points. When working at high intensity the high resistive drift plane of counter B_1 could not sustain the high voltage because of charging up. The situation is made worse by the fact that a non negligible fraction of the beam intensity ($\sim$ 2 kHz/mm^2) reaches the edge of the drift plane, as seen in figure 5.46. As a result frequent discharges, from the drift plane to the substrate, took place creating in some cases serious damage to the strip pattern. It should be mentioned that the first and last cathode strips of this counter are not grounded as done for the other counters. During the few first runs at high intensity, counter B_1 lost seven strips after several trips of the drift plane. This is illustrated in figure 5.47 where the strip RMS noise of counter B_1 is shown as a function of the strip number before (a) and after (b) the discharges. The strip noise depends on the strip capacitance which in turns depends linearly on the strip length. Thus an interrupted or broken anode will result in a decrease of its RMS noise. The dips seen already in figure 5.47 (a) correspond to the 86 strips that were lost during the assembly procedure. In figure 5.47 (b) the same dips are observed but in addition the right edge shows seven additional strips with low RMS noise which were lost during the drift plane trips. In order to prevent the counter from loosing further strips, the drift voltage of counter B_1 was reduced to -2600 V and the cathode voltage was increased to -560 V during the whole test period. The other counters,

[1]The average charged pions fluence at 98 cm from the interaction point is estimated to be 0.29 10^{13} cm^{-2} for an integrated luminosity of 5 10^5 pb^{-1} which leads to a charged pion rate of 1.6 kHz/mm^2 [14].

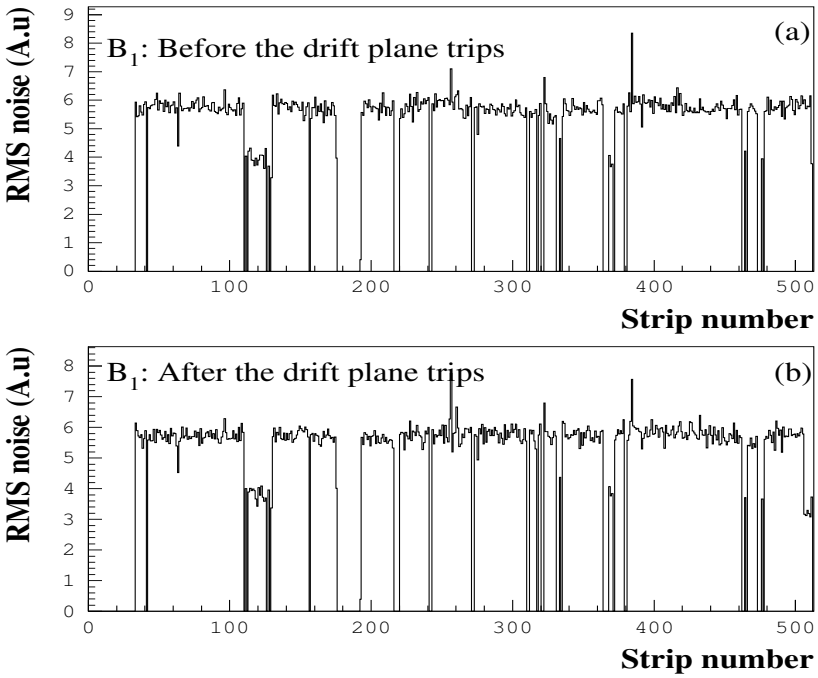

Figure 5.47: *RMS strip noise versus the strip number for counter B_1 before (a) and after (b) the drift plane trips.*

with a different drift plane, could be operated at -3500 V without trips, even at the highest intensity.

Figure 5.48 shows the distributions of the event multiplicity (a) and of the cluster charge (b), for counter P_1 at three different beam intensities. At low intensity the number of clusters per event is almost equal to 1. This number increases at high intensity and can reach more than 8 clusters per trigger. At the highest intensity the cluster charge distribution shown moves slightly towards higher values because we always choose the cluster with the highest charge among the many simultaneous signals at high intensity.

The high rate of particles might cause some charging up of the substrate. To investigate this assumption, runs with the highest intensity have been selected and a study of the uniformity of the collected charge as a function of the event number in a spill has been performed. This has been done for the substrate with the highest surface resistivity for which the effect is expected to be the largest. The results are reported in figure 5.49 where the average cluster charge is shown as a function of the event number in a spill, for counter P_1 and at an intensity of 3.5 kHz/mm^2. The dashed dotted line represents the average value of these measurements and the dotted lines correspond to a deviation of 10 % from that mean. All measured values are within less than 10 % from the mean value and compatible with the average value, indicating that there is no significant effect due to the charging up of the substrate.

The stability of the counters during the test is checked by looking at the evolution of their response with time. Figures 5.50, 5.51 and 5.52 show, for counters P_1, P_2 and P_3 respectively, the average cluster charge (a), the average strip noise (b), the average cluster size (c) and the average event multiplicity (d), versus the integrated running time. The data are from both low and high intensity runs. For all counters, the event multiplicity is higher at high intensity than at low intensity as expected. After an integrated time of 100 h, the event multiplicity increases significantly because of the very high intensity reached at that time as can be seen in figure 5.45. The cluster charge and the strip noise are stable for all counters both at low

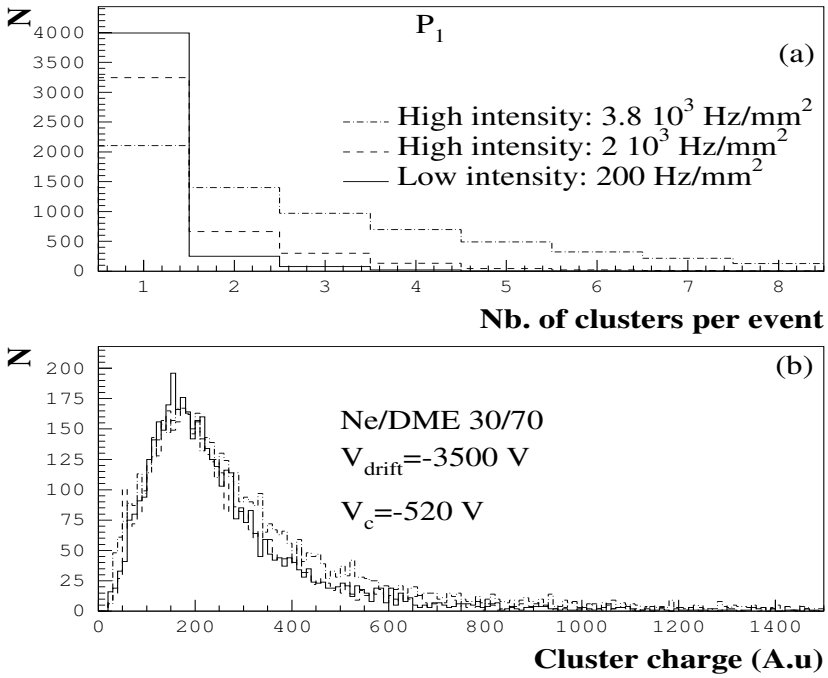

Figure 5.48: *Distribution of the event multiplicity (a) and of the cluster charge (b) for counter P_1 for three different beam intensities.*

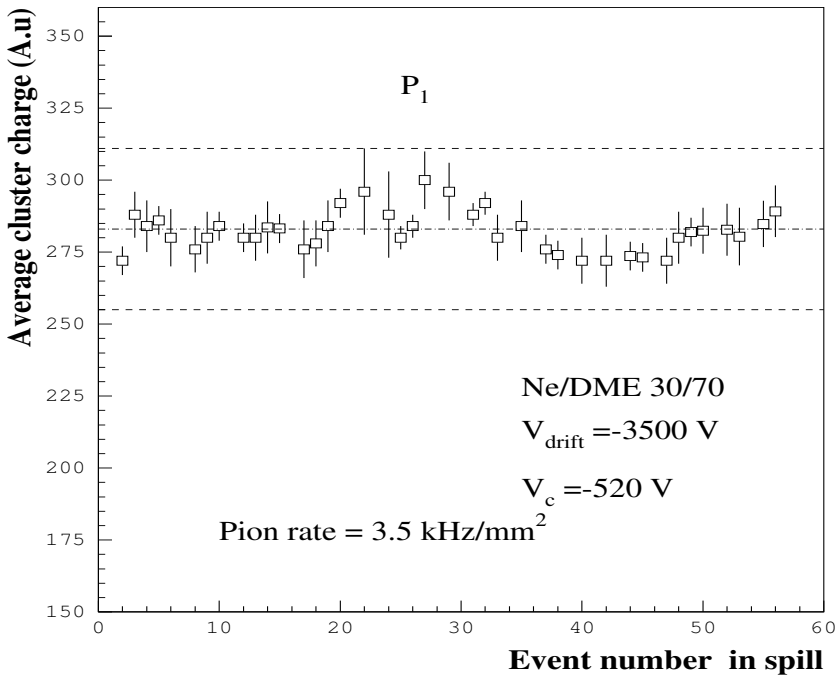

Figure 5.49: *Average cluster charge as a function of the event number in a spill, for counter P_1, at a beam intensity of 3.5 kHz/mm^2.*

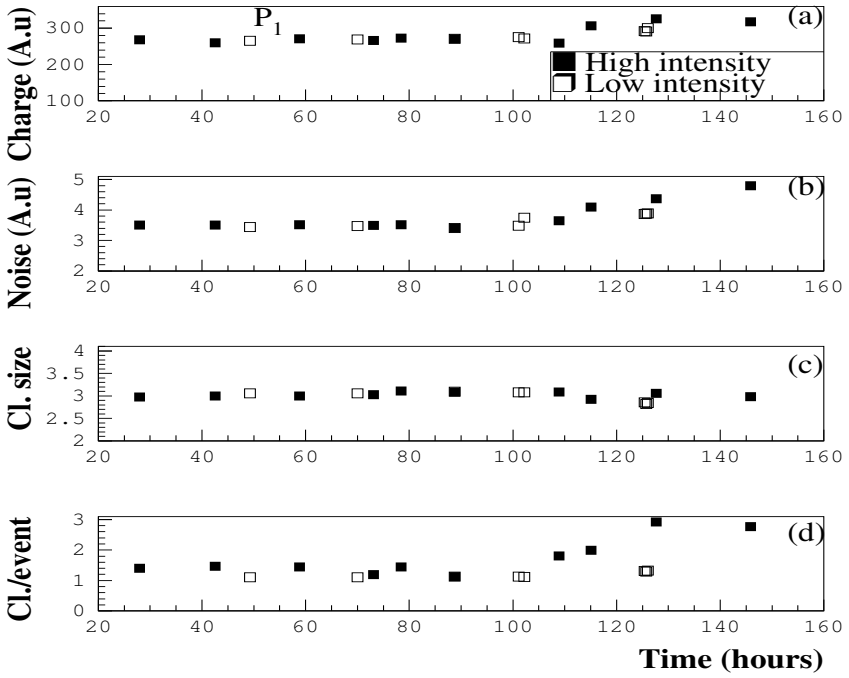

Figure 5.50: *Average cluster charge (a), average RMS strip noise (b), average cluster size (c) and event multiplicity (d) as a function of the integrated running time, for counter P_1. The open marks are for low intensity runs, the full marks for high intensity runs.*

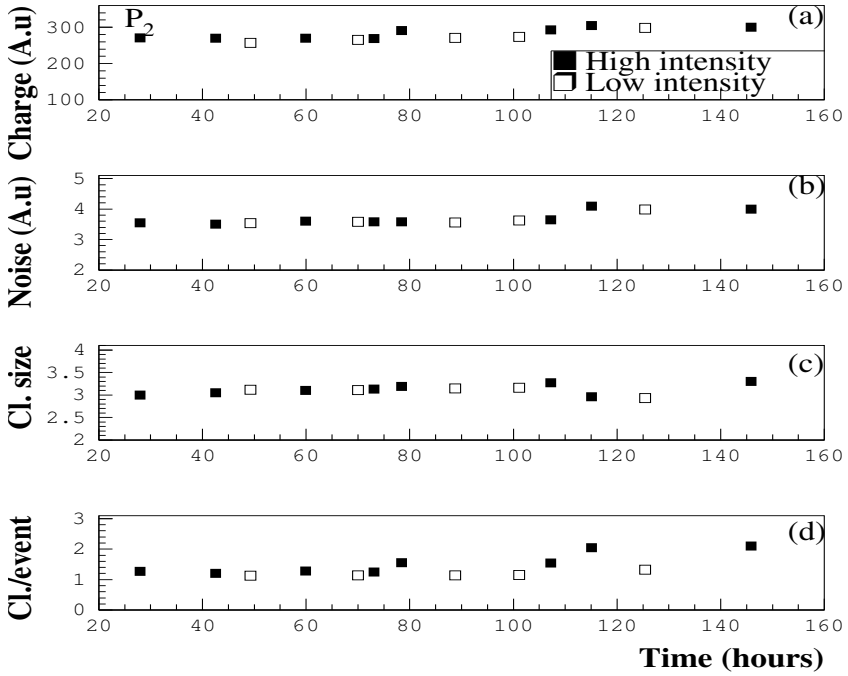

Figure 5.51: *Average cluster charge (a), average RMS strip noise (b), average cluster size (c) and event multiplicity (d) as a function of the integrated running time, for counter P_2. The open marks are for low intensity runs, the full marks for high intensity runs.*

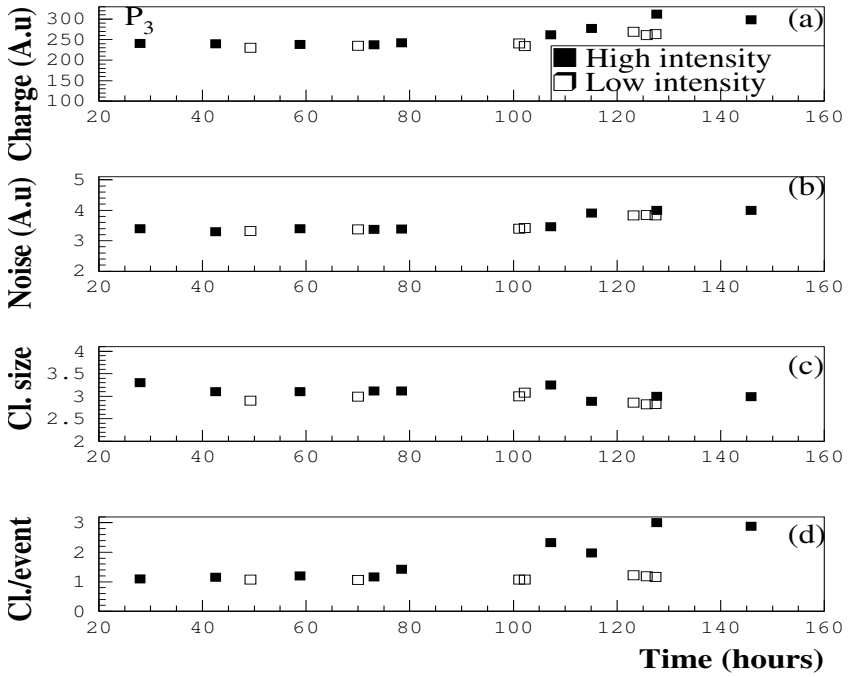

Figure 5.52: *Average cluster charge (a), average RMS strip noise (b), average cluster size (c) and event multiplicity (d) as a function of the integrated running time, for counter P_3. The open marks are for low intensity runs, the full marks for high intensity runs.*

and high intensities. However in some counters, they show a slight increase (less than 8 %) at high intensity runs after 100 h. The increase in the average cluster charge has been explained above. The increase of the strip noise at the highest intensity is due to imperfect rejection, during pedestal and noise calculation, of the many simultaneous signals in the counters. The cluster size is stable for all counters. The other counters have shown similar stability.

In addition to the counters stability with time, we have checked the number of active strips in the counters before and after irradiation. As explained above, discharges can be induced by large energy deposition caused by HIP's, produced in nuclear interaction, or by a very large integrated rate. The amount of energy released in a spark might be sufficient to melt the gold strips locally, leading to a shortening of the strip active length. To look for broken or interrupted strips, two approaches can be used. The first is based on the beam profile of the counter. A dead or interrupted strip would be revealed by a local inefficiency of this strip, accompanied by an enhancement of counting efficiency on the neighbouring strips, since the electrons released above the dead strip are deviated towards the neighbouring ones by the electric field. The second approach to look for damaged strips already seen uses the strip RMS noise. This latter is the most reliable and is used in this work. As an example, figures 5.53 and 5.54 show the strip RMS noise versus the channel number, for counters P_2 and P_4 respectively, at the beginning (a) and at the end (b) of the test. The difference between the RMS noise after the test and before the test is shown in the plot (c) of each figure. A damaged strip would give a clear dip in this plot. Counter P_2 shows one clear dip (around strip 316) corresponding to an interrupted strip since its RMS noise is comparable to that of broken anodes. The dip observed, around strip 480, of this counter is due to a strip having different noise levels as can be seen from the upper plots. Counter P_4 does not loose any strip. The other counters did not lose any strip too. Thus during the whole test period and at the nominal working point of the counters, only one strip, this of counter P_2, is lost among the 2400 working strips.

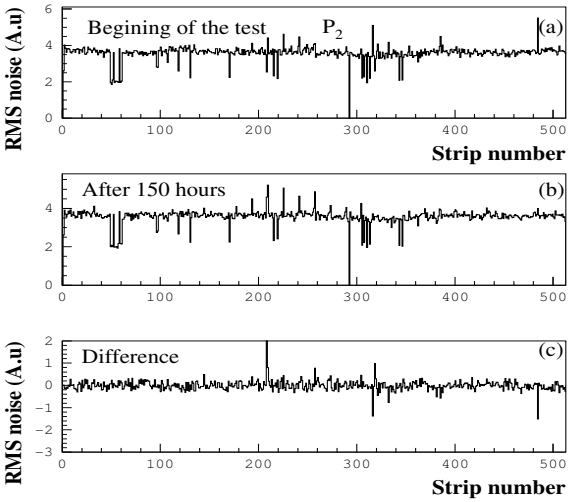

Figure 5.53: *RMS noise versus the strip number in counter P_2, at the beginning of the test, and after 150 hours of running time (b). In (c) the difference between the second and first histogram is shown.*

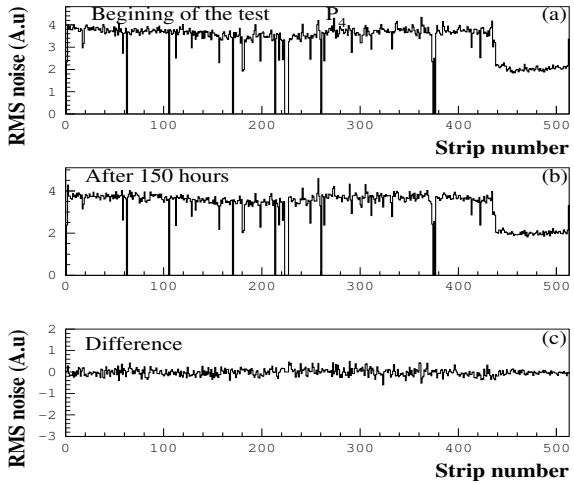

Figure 5.54: *RMS noise versus the strip number in counter P_4, at the beginning of the test, and after 150 hours of running time (b). In (c) the difference between the second and first histogram is shown.*

This test has proven the efficiency of the advanced passivation technique in extending the MSGC lifetime in a high intensity beam of hadrons. To increase the total integrated rate on the chambers and to study the behaviour of the counters under a continuous hadron beam, a second test was performed at the pion beam at PSI[1]. The beam was composed of pions of 400 MeV/c with a proton contamination between 5 and 40 %. The pion rate in this beam was up to 10 kHz/mm^2, which is higher than the LHC rate at the innermost of the MSGC tracker, expected to be slightly below 5 kHz/mm^2. Operated at their nominal working points leading to 98 % efficiency, the detectors were exposed during 161 hours to the high intensity beam. They showed no sign of high voltage instability and did not lose any strip [14]. Counter B_1 has been exposed to a fast neutron beam, at LLN[1], having an average energy of 20 MeV and an intensity of 7.10^3 kHz/mm^2. A fluence equivalent to that of 3 years of LHC operation has been accumulated without damages to the detectors [128]. Thus the advanced passivation technique allows the MSGC's to meet the CMS requirements in terms of the stability under high intensity beams of hadrons.

5.6 Conclusion

This chapter was devoted to study several aspects of the MSGC's and to check if this technology allows to build tracking detectors that meet the CMS requirements in terms of the detection efficiency, the spatial resolution, the response time and the stability of operation.

In the first part of this chapter we have demonstrated that MSGC's can meet satisfactorily the demands in terms of the detection efficiency, the spatial resolution and the response time.

[1]Paul Scherrer Institute, Zurich

[1]Louvain La Neuve test facility, Belgium.

Indeed, we have studied the response of MSGC's filled with selected DME based mixtures and made the following conclusions:

- a detection efficiency of at least 98 % has been reached in all the gas mixtures studied;
- a spatial resolution of less than 40 μm can be achieved;
- the Ne/DME gas mixtures, chosen by the CMS collaboration as the filling gas for MSGC's, enable to reach the required efficiency already at cathode strip voltages between -510 V and -540 V, much lower than for pure DME. This is a big advantage since the energy released in case of a spark is reduced and consequently the risk of strip damage. In addition these mixtures present a long efficiency plateau, more than 70 V, compared to Ar/DME mixtures. However we measured and calculated the drift velocity in these mixtures, and found that it does not exceed 55 μm/ns. In a 3 mm gas gap, as foreseen in CMS, this results in an electron drift time of 54 ns, that is more than two LHC bunch crossing intervals. In such a mixture the primary ionization is low and all the primary ionization produced would be needed to reach full efficiency. To increase the drift velocity, we added amounts of CO_2 to Ne/DME mixtures and found that Ne/DME/CO_2 40/40/20 %, for example, allows a 65 μm/ns drift velocity at an electric field of 10 kV/cm. In this gas mixture, the cathode strip voltage has to be increased by 20 V, with respect to Ne/DME 50/50 %, in order to reach full efficiency. The increase in the drift velocity leads to the increase of the Lorentz angle from 15^0 in Ne/DME 50/50 to 19^0. In the barrel region of CMS, this will lead to a spatial resolution of 50 μm for high p_t particles. If this triple mixture is to be used, it is recommended to modify the tilt angle of the counters. If this is done, the presence of CO_2 is then an advantage as the Lorentz angle can be kept constant, in case of a variation of the external magnetic field, by adjusting the drift velocity with a slight variation of the amount of CO_2.

The second part of this chapter was devoted to the study of the MSGC response to a high intensity beam of hadrons. This study has proven that the advanced passivation technique extends the lifetime of MSGC's in an environment such as at the LHC. It protects the strip from damage. Indeed several MSGC's were exposed to a high intensity pion beam during a test period amounting to 7.7 hours of continuous beam at a rate larger than the one expected at the LHC, at a radial distance of 100 cm from the beam pipe. The counters showed a uniform response during the test period, and no indication of charging-up of the substrates has been noticed. Among the 2400 working strips, only one has been damaged during the test period.

Since the duty cycle of this beam was only 5 %, this test had to be repeated in a continuous high rate of HIP's. In addition, higher rates had to be tested as the MSGC tracker reaches a radius of 70 cm. Thus two tests took place after the completion of this work. The first one at the PSI test facility, where the chambers were exposed to a continuous high intensity beam of hadrons, in which an integrated rate equivalent to 170 hours at LHC operation at the innermost layers of the MSGC tracker has been accumulated. The second one took place at the LLN neutron test facility and where one counter was exposed to a neutron fluence equivalent to that of three years of LHC operation. In both tests the counters showed extremely stable behaviour and no sign of strip damage has been reported.

These studies prove that MSGC's with the advanced passivation technique meet the CMS requirements to build a tracker at a radial distance of 70 cm or more from the beam pipe.

Chapter 6
Study of elements of the MSGC forward tracker

Introduction

Whereas chapter 5 deals with the study of MSGC's for CMS, the present chapter is devoted more precisely to the forward MSGC tracker. In this part of CMS, it is foreseen to place several trapezoidal MSGC substrates side by side in a detector module providing a common gas volume. A detailed description of this approach is given in section 4.4. However the stability of operation, the uniformity of the response of multisubstrates modules over the full length of wedge shaped counters and the detection efficiency mainly in between two adjacent counters was still to be checked. We have thus carried out several tests to study these parameters.

Results from the test of a wedge shaped chamber and its response to MIP's are given in section 6.1. To study the edge effects with adjacent substrates, two prototypes have been built. The analysis of their performances and response to MIP's is described in section 6.2.

To prove the feasibility of the forward tracker design, the CMS forward MSGC tracker collaboration was asked by the LHC Committee to build several multisubstrates modules and to test them in a beam. To fulfil this request (the MF1 milestone), the six participating institutions have constructed one full scale MSGC module each, with a total of 38 wedge shaped counters. Section 6.3 provides the motivations for this milestone as well as the description of the MSGC modules. A preliminary test of one of these modules with cosmic rays is described in section 6.4. Section 6.5 discusses the problems encountered during the assembly procedures of the MSGC modules. The 38 MSGC's were exposed to a muon beam at the CERN SPS facility. In sections 6.6 and 6.7 results on gain uniformity, detection efficiency, spatial resolution and dead spaces are presented together with results from simulations. Section 6.8 discusses the improvements to be done in order to meet all the challenges that this project raises.

6.1 Behaviour of a wedge shaped MSGC

Although MSGC's with parallel strips have been extensively tested, wedge shaped MSGC's with varying anode pitches have just began to be investigated. The possibility to reach stable operation with such a counter was still to be proved as well as the uniformity of the response along the strips. To investigate this point a trapezoidal counter has been mounted and tested in the cosmic rays hodoscope described in section 5.1.

6.1.1 Experimental setup

The trapezoidal MSGC has a base of 123 mm and a height of 103 mm and comprises 512 anode strips. The substrate is made of DESAG D-263 glass of 300 μm thickness. The anode pitch varies from 190 μm at the short base of the substrate to 241 μm at the large base. The anodes are 10 μm wide. For this first wedge shaped counter, no attention was paid to adapt the other

substrate parameters to the varying pitch and the anode-cathode distance was kept to 50 μm implying a variation of the cathode width from 80 μm to 131 μm. The rule (4.1) proposed by NIKHEF to maintain the gain constant along the strips is thus not fulfilled. The strips are connected to the front-end electronics (64 channels APC chips) as for the three MSGC's with parallel strips (see section 5.1). The pitch adapter used was conceived for MSGC's with 200 μm pitch. To correct for the larger pitch in this case, 82 strips on one side of the counter as well as 12 electronic channels of each of the 7 APC chips are not connected. Thus, only 346 strips are read out. The cathode strips are connected to the high voltage in groups of sixteen. The drift plane consists of a 300 μm thick aluminized glass placed 3 mm above the substrate.

As this counter was also used to study edge effects in counters placed side by side in a common gas volume (see section 6.2), both the wedge shaped substrate and the drift plane are cut into two pieces placed side by side and aligned with respect to each other. The alignment of the two pieces of substrate is done in such a way that the distance between the two anodes adjoining the strip less region is twice the nominal pitch on the substrate.

The whole counter is placed in a flat carbon fibre box similar to the model proposed for the so-called "open-design" of the CMS forward tracker (see section 4.4). This gas box is placed in the cosmic rays hodoscope, 50 mm above the gas box containing the three square MSGC's. The central strip of the trapezoidal counter is, in first approximation, parallel to the square MSGC's strips.

The data analysis procedure is done in a way similar to that of the square MSGC's. However, before attempting to form a cluster, it was necessary to make the correspondence between the electronic channels and the geometrical position of the strips, thereby taking into account the APC channels that are not connected to strips. In the next section, we describe the alignment procedure for this particular detector geometry.

6.1.2 Alignment procedure

The spatial resolution study requires a careful alignment of the detector under test with respect to the reference external tracking device. This device, in our case, can be either the hodoscope or a combination of the hodoscope and the three square MSGC's.

In the trapezoidal MSGC, the local coordinate system (u, v) is taken with u along the central strip (taken as strip 256) and v along the short base of the substrate as shown in figure 6.1.

For event i, the coordinates of the impact point M_p^i predicted in the MSGC plane placed at height z, are given in the external reference frame by:

$$M_p^i = \begin{pmatrix} x_p^i \\ y_p^i \end{pmatrix} = \begin{pmatrix} a_x^i z + b_x^i \\ a_y^i z + b_y^i \end{pmatrix} \tag{6.1}$$

where a_x^i (a_y^i) and b_x^i (b_y^i) are respectively the slope and the intercept of the track reconstructed by the external tracking device in the x (y) projection. These track parameters are calculated by a least square fitting procedure described in appendix B. To go from the reference coordinate system to the local one, one has to perform the following transformation:

$$\begin{pmatrix} u_p^i \\ v_p^i \end{pmatrix} = \begin{pmatrix} cos\psi & sin\psi \\ -sin\psi & cos\psi \end{pmatrix} \begin{pmatrix} x_p^i \\ y_p^i \end{pmatrix} + \begin{pmatrix} u^0 \\ v^0 \end{pmatrix} \tag{6.2}$$

where ψ is the rotation angle around the z axis and u^0 (v^0) is the translation along the $u(v)$ axis of the MSGC local frame (see figure 6.1) . These alignment parameters are unknown and have to be determined.

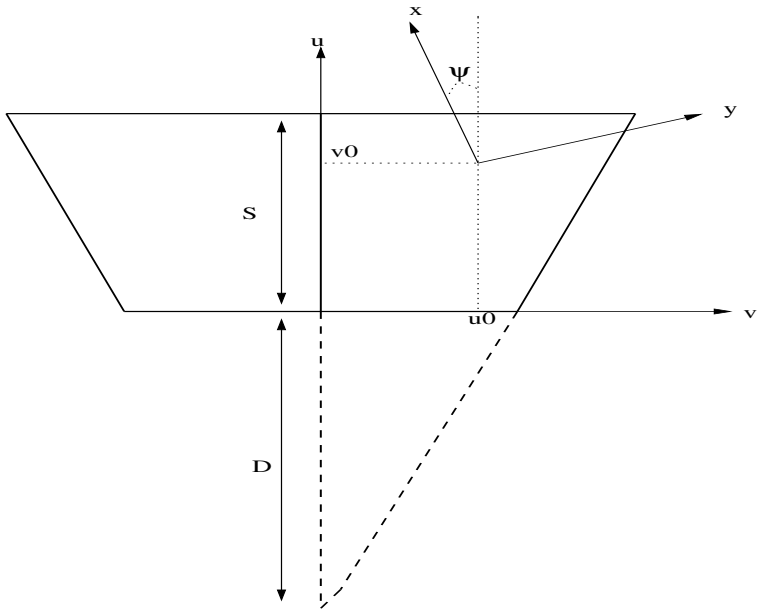

Figure 6.1: *Schematic view of the coordinate systems used for the trapezoidal MSGC alignment.*

The MSGC strip number that should be hit by the particle is given by:

$$S_p^i = 256 + \frac{v_p^i}{P_1 + \frac{P_2 - P_1}{S} u_p^i} \tag{6.3}$$

where P_1, P_2 and S are respectively the smallest anode pitch, the largest anode pitch and the central strip length of the wedge shaped substrate.

The alignment parameters follow from the minimisation of:

$$R = \sum_{i=1}^{N} \frac{(R^i)^2}{\sigma_i^2} \tag{6.4}$$

with

$$R^i = S_c^i - S_p^i \tag{6.5}$$

where S_c^i is the cluster position, expressed in strip number, computed from the centre of gravity of the cluster charge. The error σ_i is given by:

$$\sigma_i^2 = \sigma_{S_c^i}^2 + \sigma_{S_p^i}^2 \tag{6.6}$$

where $\sigma_{S_c^i}$ is the intrinsic detector resolution and $\sigma_{S_p^i}$ is the error due to the extrapolation from the tracking device to the MSGC plane and to the errors on the MSGC alignment parameters.

Neglecting correlations, this later is given by:

$$\sigma_{S_p^i}^2 = (\frac{\partial S_p^i}{\partial x_p^i})^2 \sigma_{x_p}^2 + (\frac{\partial S_p^i}{\partial y_p^i})^2 \sigma_{y_p}^2 + (\frac{\partial S_p^i}{\partial \psi})^2 \sigma_\psi^2 + (\frac{\partial S_p^i}{\partial u^0})^2 \sigma_{u^0}^2 + (\frac{\partial S_p^i}{\partial v^0})^2 \sigma_{v^0}^2 \tag{6.7}$$

where σ_{x_p} and σ_{y_p} are the errors on x_p and y_p given by equation (6.1); σ_ψ, σ_{u^0} and σ_{v^0} being the errors on the unknown parameters obtained from the fitting procedure.

In figure 6.2 the distribution of the residues defined in (6.5) is shown when only the hodoscope alone is used as a tracking device. The distribution fits a Gaussian function with a standard deviation of 400 μm, comparable to that obtained for the square MSGC's (see figure 5.15).

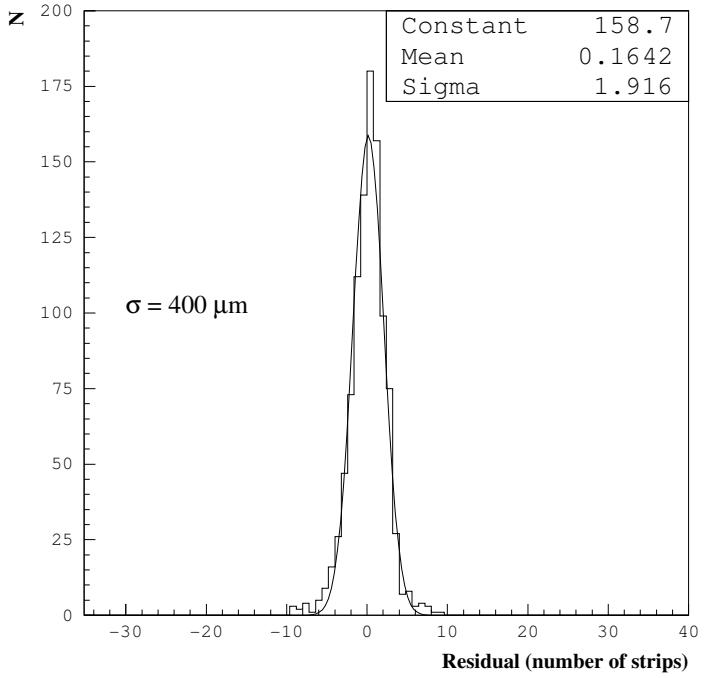

Figure 6.2: *Distribution of the residues defined in (6.5) for the trapezoidal MSGC.*

6.1.3 High voltage behaviour and uniformity studies

During the whole test, the gas mixture was Ne/DME 50/50 % and the drift voltage was kept at -2200 V for all counters. A typical cluster charge distribution is shown in figure 6.3 (a) and (b) respectively for the second square MSGC and for the trapezoidal one. The cathode strip voltage is -550 V. The signal amplitude is higher in the case of the square counter. This is to be attributed to the smallest anode width of this counter (7 μm instead of 10 μm for the trapezoidal one) and to the pitch difference between the two counters, the average pitch of the trapezoidal counter being 215 μm compared to 200 μm for the square MSGC. The cluster size is also shown in figure 6.3(c) and (d), in number of strips, respectively for the square and the trapezoidal counter. Converting the average cluster size to microns, to take into account the different anode pitches, one obtains 550 μm $\pm$ 5 and 537 μm $\pm$ 6; the difference is thus not significant. The positions of the impact points in the counter active area are shown in figure 6.4 in the local reference frame. The trapezoidal shape is clearly seen in the figure. The asymmetry observed is due to the 82 strips that are not connected on one side.

The signal to noise ratio has been measured, for both counters, as a function of the cathode strip voltage. The result is shown in figure 6.5(a). The dependence of the signal to noise ratio on the cathode strip voltage looks similar for both counters, with a lower signal in the trapezoidal MSGC due to the counter geometry as was already explained for figure 6.3 (a) and (b). Measurements are continued up to voltages at which the counter trips more than three times within a period of a few hours. The trapezoidal counter becomes unstable at a cathode strip voltage above -600 V, 10 V below the square counter.

Since the detection efficiency is strongly related to the value of the signal to noise ratio, the efficiency plateau ($\geq$ 97 %) starts at a cathode voltage of -540 V in the trapezoidal chamber instead of -520 V for the square one (figure 6.5(b)). It is observed from figure 6.5(a) that the signal to noise ratio is the same in both counters at these voltages and of the order of 23. This value is higher than the one required as the working point for MSGC's at CMS, which is around 13 for tracks with normal incidence [14]. This is due to different reasons. On one

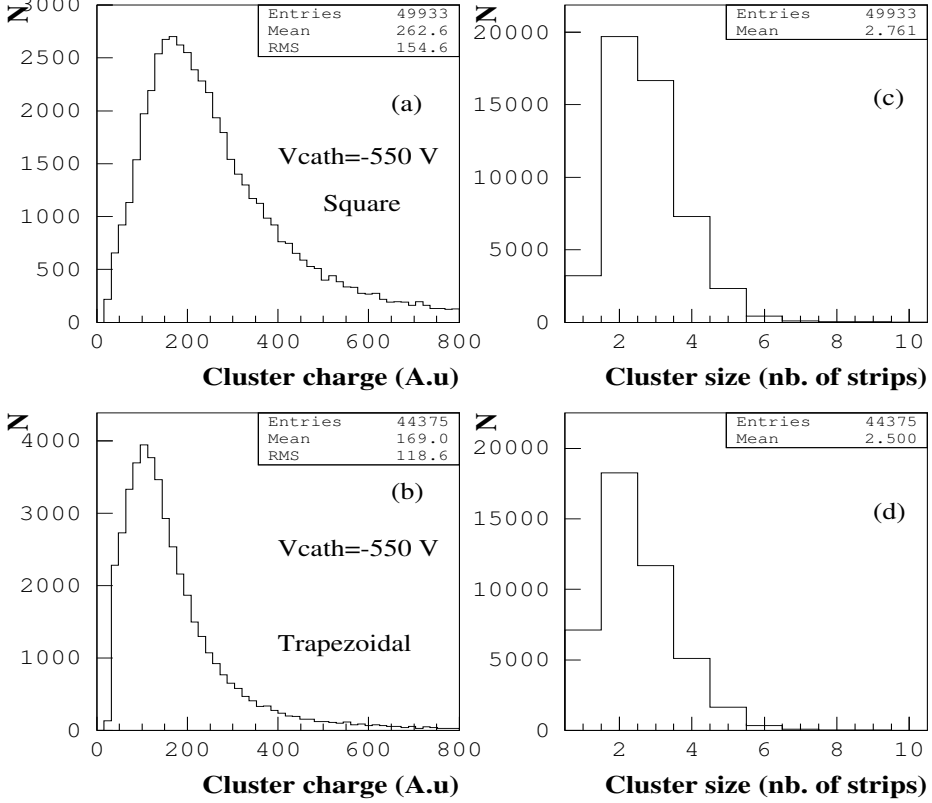

Figure 6.3: *Cluster charge (a) and (b) and cluster size (c) and (d) distributions in Ne/DME 50/50 % at a drift voltage of -2200 V for the square and the trapezoidal counter respectively.*

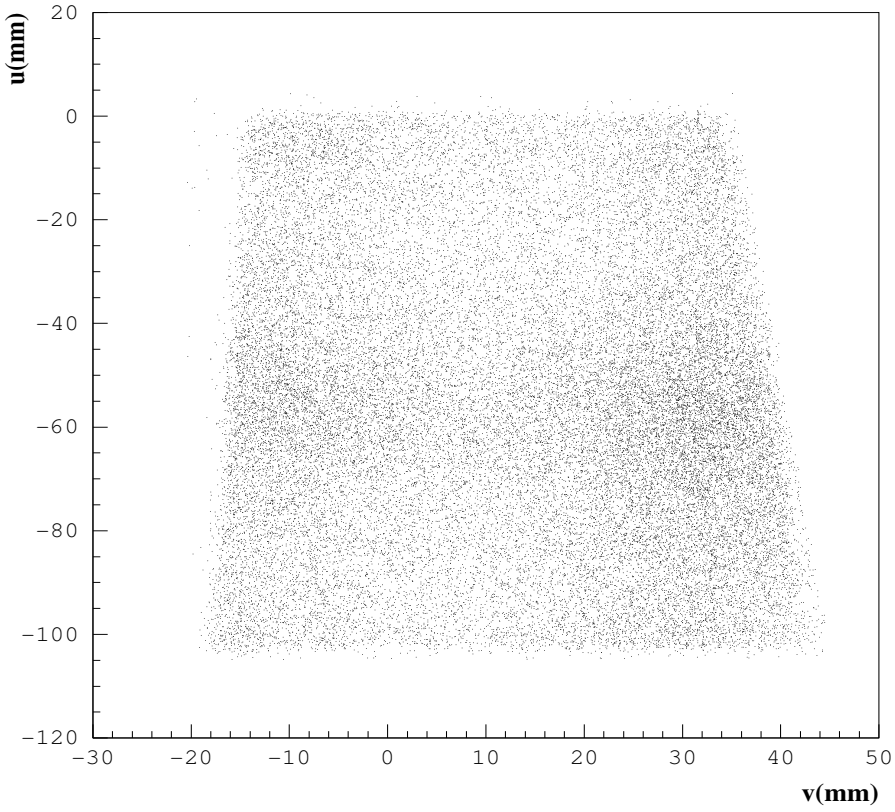

Figure 6.4: *Impact point positions in the active area of the trapezoidal counter.*

hand, as explained in section 5.4 this difference can be due to the larger angular acceptance of the hodoscope which decreases the detection efficiency. A full efficiency is thus reached at higher average signal to noise ratio. On the other hand, the gas mixture used in reference [14] is Ne/DME 30/70 % which has a higher primary ionization density than Ne/DME 50/50 %, enabling therefore the detection efficiency to start at a lower signal to noise ratio. Eventually the efficiency plateau is 30 V shorter in the trapezoidal chamber.

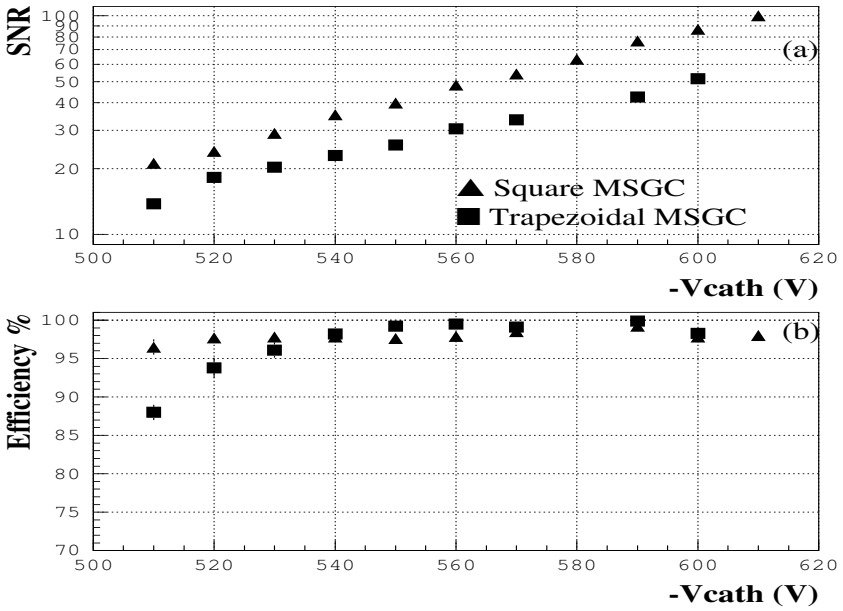

Figure 6.5: *Dependence of the signal to noise ratio (a) and detection efficiency (b) on the cathode strip voltage, in a trapezoidal and in a square counter, operated at a drift voltage of -2200 V. The gas mixture is Ne/DME 50/50 %.*

In the design of the present substrate, the rule (4.1) was not followed and thus the gain is expected to vary with the anode pitch. The average signal to noise ratio is shown in figure 6.6(a) as a function of the anode pitch. The cathode strip is -550 V. The signal to noise ratio is increasing linearly with the pitch. A variation of the signal to noise ratio of 47 % is observed between the large and the short side of the substrate. At both edges of the chamber, the signal to noise ratio decreases due to the electric field distortion in these regions. The variation of the signal to noise ratio with the anode pitch affects the detector performances. Indeed, it is seen from figure 6.6(a) that although the detector is operated at a cathode strip voltage of -550 V, that is 10 V above the starting point of the efficiency plateau of this counter, the region of smaller pitch is not efficient at 97 %. One needs to increase the cathode strip voltage by 10 V to reach a signal to noise ratio allowing to obtain an efficiency in excess of 97 % in this region (see figure 6.5). In other words, the real starting point of the efficiency plateau for this counter is -560 V and not -540 V leading to an efficiency plateau length of only 40 V. Therefore a uniform signal to noise ratio along the strips is of great importance.

To better understand the experimental results, we performed calculations using the codes MAXWELL [115] and GARFIELD [114]. The former computes the electrostatic field and the latter the gas gain as explained in section 5.3. Figure 6.6(b) shows the relative gain as a function of the pitch, both for the experimental and simulation results. The simulation shows a good agreement with the experimental data. We also investigated the relative electric field both at the anode and cathode strips edges since most of the gain variations can be interpreted as

alteration of the electric field. The results are shown in figure 6.6(c). The anode (cathode) strip field shows a 10 % increase (decrease) between the short and the large side of the substrate. The gain increase from one end to the other can be seen as a consequence of the anode electric field variation; a higher anode field leading to a higher amplification. The region of lower pitch not only has a lower signal to noise ratio, but also a higher cathode electric field compared to other regions of the counter, which might favour streamers development.

Previous measurements with trapezoidal chambers showed the same gain variations from one end of the geometry to the other, if a constant anode-cathode distance is kept along the strips [92].

Figure 6.6(d) gives the cluster size, expressed in number of strips, as a function of the anode pitch for nearly perpendicular tracks ($|\beta| \leq 80$ mrad). The cluster size is 380 $\pm$ 15 μm and 438 $\pm$ 10 μm respectively at the short and the large base of the substrate. This can be explained as follows: at the large base, the gain is higher which favours the amplification of small charges collected on the strips at the border of the cluster.

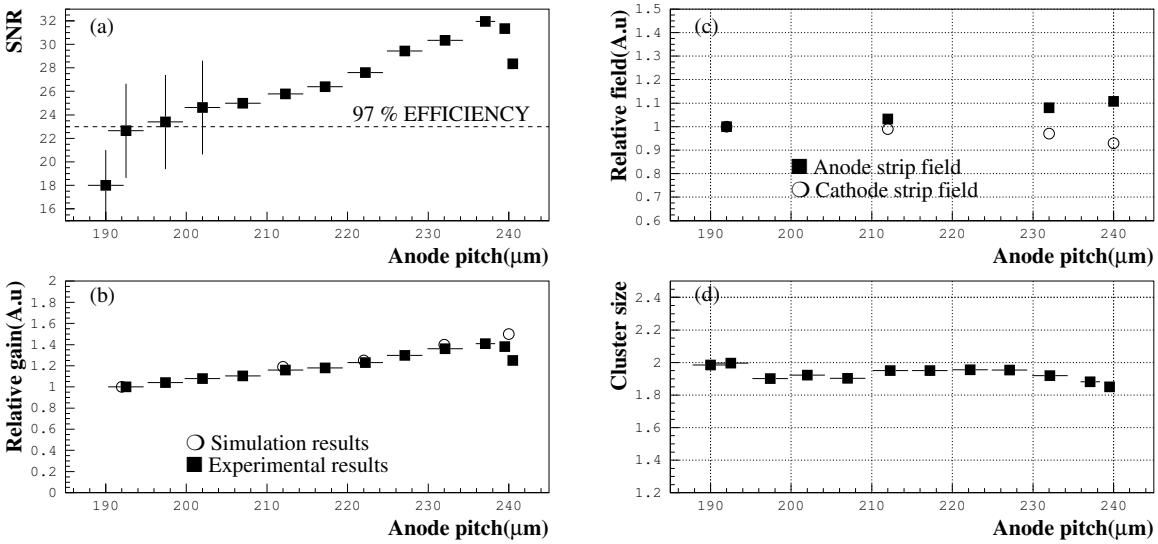

Figure 6.6: *(a) Measurements of the signal to noise ratio versus the anode pitch. (b) Comparison of the experimental relative gain, derived from plot (a), and simulation results as a function of the anode pitch. (c) Variations of the relative electric anode and cathode fields, with the anode pitch, as obtained from the simulation. (d) Average cluster size versus the anode pitch for perpendicular tracks ($|\beta| \leq 80$ mrad). The MSGC is filled with Ne/DME 50/50 % and operated at a cathode strip voltage of -550 V and a drift voltage of -2200 V.*

6.1.4 Spatial resolution

The distribution obtained for the difference between the impact point position predicted with the hodoscope and the one measured by the trapezoidal MSGC is 400 μm, too wide compared to the expected MSGC resolution (see figure 6.2). The three square MSGC's were used to predict the impact point coordinate along the strips for spatial resolution determination; the coordinate along the strips being still provided by the hodoscope. In figure 6.7, the resulting distribution of residues , in number of strips, is shown, for one half of this substrate and for tracks with an angle of incidence $|\beta| \leq 100$ mrad. The standard deviation of this distribution

is 120 μm. Taking into account the extrapolation error, computed to be 90 μm, one obtains a spatial resolution of 80 μm. This is 30 % larger than the spatial resolution measured for a 200 μm pitch MSGC at the same angular acceptance. To explain this difference, we investigate the spatial resolution along the strips. In figure 6.8, the detector spatial resolution is shown as a function of the anode pitch. The spatial resolution varies from 60 μm at the large base to 90 μm at the short base of the substrate. To check if this is not due to a misalignment along the strips, figure 6.9 shows the mean of the residual distribution along the strips.

The variation of the spatial resolution with the pitch is a consequence of the non-uniformity of the signal to noise ratio and of the cluster size along the strips; a higher signal to noise ratio leads to a better impact point localisation and thus to a better spatial resolution. This can be explained if we take figures 5.14 and 5.18. It is seen that the degradation of the signal to noise ratio of 25 % can cause a degradation of the spatial resolution by up to 40 %. A uniform signal to noise ratio would thus ensure constant spatial resolution.

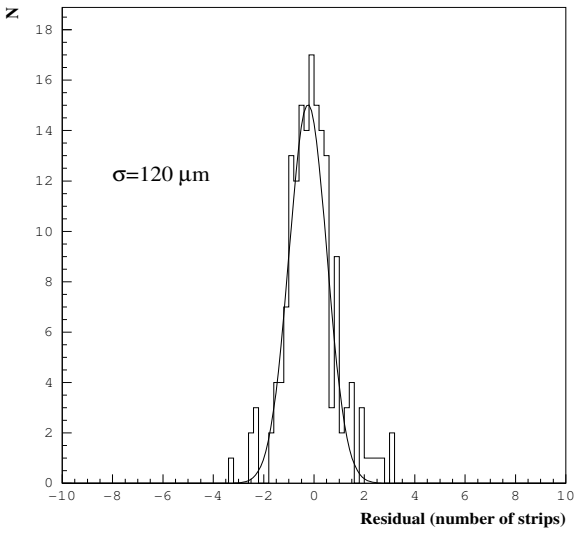

Figure 6.7: *Residual distribution of (6.5), of the trapezoidal counter, obtained after a combination of the three square MSGC' and the hodoscope.*

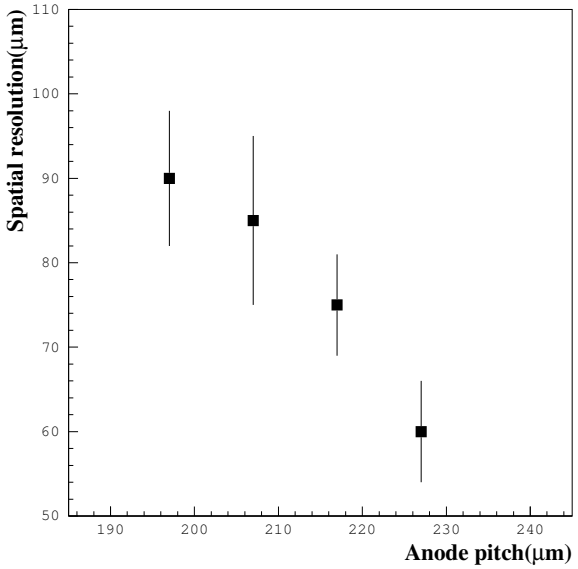

Figure 6.8: *Spatial resolution versus the anode pitch for the trapezoidal counter.*

6.2 Edge studies

An essential feature of the design of the forward MSGC tracker is the joining of several substrates side by side, without overlap, in a common gas volume. This idea comes from the fact that no loss of efficiency was observed in MSGC's with a single interrupted anode strip. In this case, the electric field near the broken anode strip deviates electrons released in this region to the neighbouring anode strips, enabling their detection. To test this feature two MSGC prototypes have been built and tested in the cosmic rays hodoscope. One is the second square reference MSGC of the cosmic hodoscope, made of a substrate cut into two pieces and placed side by side and a single drift plane (see section 5.1). The second prototype used to study the

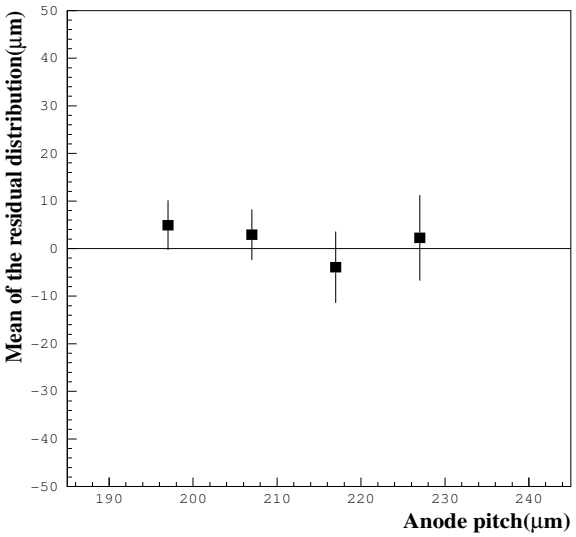

Figure 6.9: *Mean of the residual distribution of (6.5) versus the anode pitch for the trapezoidal counter.*

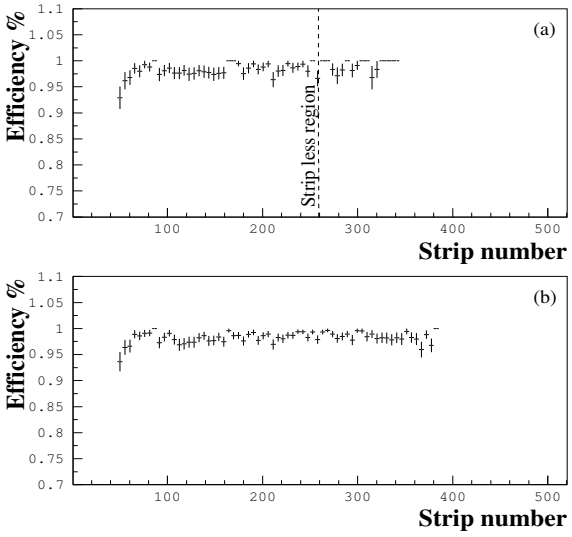

Figure 6.10: *Detection efficiency across the strips for tracks with $|\beta| \leq 70$ mrad (a) and for inclined tracks (b), for the square counter.*

edge effects is the trapezoidal counter described in section 6.1 for which both the drift plane and the substrate are cut into two pieces placed side by side. The alignment of the two pieces of substrate is done in such a way that the distance between the anodes adjoining the strip less region is twice the nominal pitch elsewhere in the substrate. Therefore no loss of efficiency is expected in this region. On the contrary to the detection efficiency, the spatial resolution could be affected as was observed in detectors with broken anode strips [131]. Indeed, since the released electrons are deviated to the neighbouring anode strips, the centre of gravity of the charge signal is also displaced and the spatial resolution is worsened. The purpose of the test is to measure the detection efficiency and the spatial resolution in these regions.

For the square counter, the presence of a dead strip at two strips from the strip less region affects the detection efficiency [132]. This is illustrated in figure 6.10 (a) and (b) representing the efficiency of the square MSGC across the strips for perpendicular tracks ($|\beta| \leq 70$ mrad) and inclined tracks ($|\beta| \geq 70$ mrad) respectively. The full efficiency is at the level of 98 % in both plots. In the strip less region, the dead strip reduces the efficiency to 96.5 ± 0.6 % for perpendicular tracks. The efficiency becomes 97.5 ± 0.4 % in this region for inclined tracks as the particle is still seen by enough strips to be detected. The spatial resolution has been measured for perpendicular tracks and was found to be 67 μm instead of 36 μm for the rest of the counter [112]. This deterioration of the spatial resolution is partly attributed to the dead strip present in this region. Therefore another test of the edge effect was needed.

The trapezoidal counter is suitable to test the edge effects since it has both the substrate and the drift plane cut into two pieces. The efficiency of the trapezoidal counter across the strips is shown in figure 6.11(a) for perpendicular tracks. The efficiency is constant (≥ 98 %) in particular in the strip less region. The detection efficiency along the strips in the strip less region (800 μm on each side) is shown in figure 6.11(b) per steps of 2 mm, for perpendicular tracks. The detection efficiency is constant (≥ 97.5 %) along the strips in this particular region. At two mm from the strip edges the efficiency decreases and reaches 95 % because of edge effects.

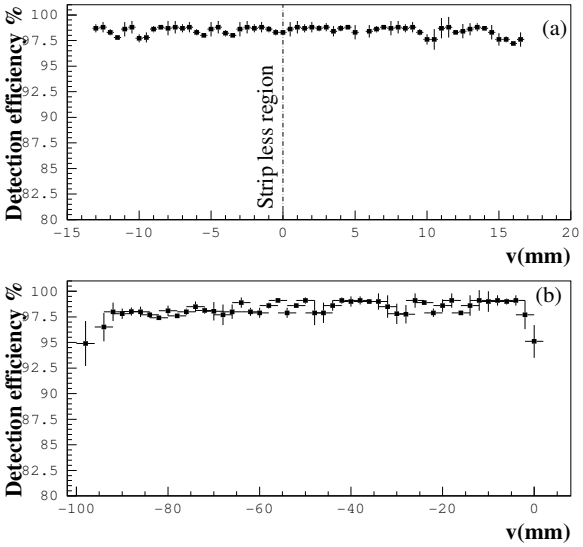

Figure 6.11: *Detection efficiency across the strips (a) and along the strip less region (b), for tracks with $|\beta| \leq 70$ mrad (a), for the trapezoidal counter.*

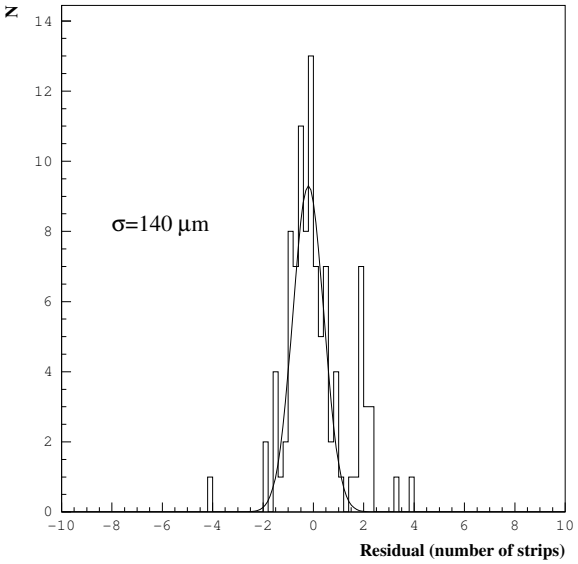

Figure 6.12: *Residual distribution as defined in (6.5) in the strip less region (800 μm on each side).*

The spatial resolution in the strip less region of the trapezoidal counter has been studied. Figure 6.12 shows the distribution of the residues with impact point at less than 800 μm on each side of this region, as defined in (6.5), for perpendicular tracks ($|\beta| \leq 100$ mrad). The width of this distribution is 140 μm leading to a spatial resolution of 107 μm after correcting for the extrapolation error. As discussed in section 6.1.4, the spatial resolution estimated for this counter is not as good as usual: 80 μm instead of $\sim$ 55 μm for this angular acceptance. Nevertheless, it is degraded by 20 % with respect to another region elsewhere on the substrate. A similar degradation have been observed many times in the region of dead strips [133, 131].

6.3 The MF1 milestone

The MF1 milestone was set in order to evaluate the system aspects of the CMS forward-backward MSGC tracker as described in section 4.4. The main purposes of this test were:

1. to learn how to build such full scale modules keeping in mind the mass production of MSGC's for the whole CMS detector;
2. to compare the various designs and the different substrate industrial productions;
3. to perform a large scale test of the high voltage and gas distributions.
4. to study the uniformity of response of the counters;
5. to check the alignment procedures of the substrate within the modules.

In order to compare the various design options (see section 4.4), four of the six MSGC modules were constructed following the so-called "open" approach, referred to in the text as O_1, O_2, O_3

and O_4, and two modules following the "closed" design: C_1 and C_2. Module C_2 is a variant of the closed design (see figure 4.26).

6.3.1 Description of the MSGC counters

6.3.1.1 Substrates

The substrates were made on DESAG D263 glass, 300 μm thick and the strips were made of aluminium for all counters but C_1, having gold strips. They were produced by various manufacturers: SRON [134], VOSTOK [135], OPTIMASK [136] and IMT [137].

For this milestone two wedge shaped masks have been designed corresponding, respectively, to the outermost and innermost rings of a CMS forward MSGC disk. The variation along the strips of the electrode widths and their relative distances follow the homothetic rule (4.1) (see section 4.4). The main characteristics of these masks are presented in table 6.1 and the layout of the outer ring mask is shown in figure 6.13.

	Outer ring	**Inner ring**
number of anodes	512	512
Pitch(μm)	250 to 212	200 to 185
Anode width(μm)	10	7
Cathode width(μm)	138 to 110	103 to 92
Anode-cathode gap(μm)	51 to 46	45 to 43
Central anode length(mm)	170	40
Large base width(μm)	128	102

Table 6.1: *Parameters characterising the MF1 milestone masks.*

6.3.1.2 Drift planes

All modules, but C_2 and O_4, had 300 μm thick DESAG 263 glass as drift planes, coated with a 5 *nm* chromium layer. The chromium layer was made so thin to make the drift plane transparent to allow an easy alignment of the counters in the case of the open design. Unfortunately, the high resistance of chromium, leading to drift plane charging up, prevented us from working with high drift voltages.

Module O_4 had also 300 μm thick DESAG 263 glass drift planes but coated with a 50 *nm* nickel layer.

The C_2 module had drift electrodes made of honeycomb, 3 mm thick. The core was made of NOMEX(aramide) and the skins, 200 μm thick, were made of 2 layers of glass fibres.

The drift planes were placed 3 mm above the substrates for all counters.

6.3.1.3 High voltage supply and readout electronics

For each counter two ceramic hybrids located on each side of the strips were used for high voltage supply and readout.

The anode strip signals were read out by PreMux128 chips [125] mounted on the hybrid at the large side of the counters. These chips hold 128 preamplifier/shaper with 45 *ns* shaping

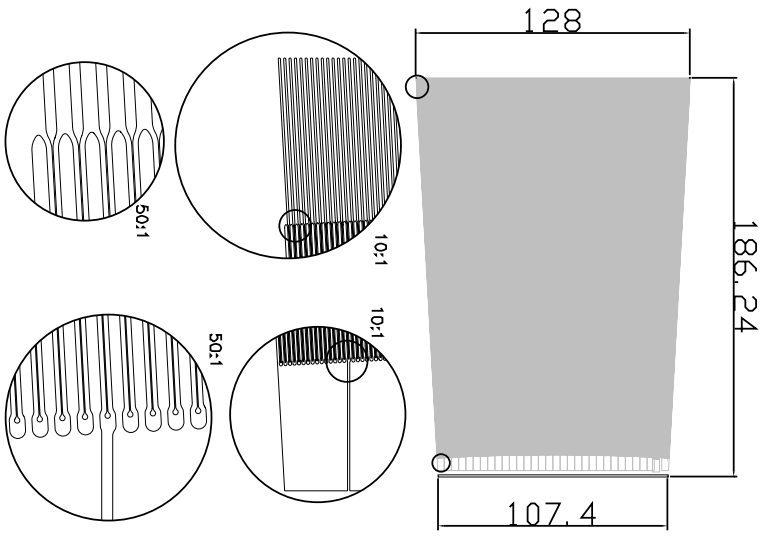

Figure 6.13: *Layout of the mask designed for outer ring substrates. Dimensions are given in millimetres.*

time combined with a 1 MHz multiplexer (see section 5.5.1). The readout hybrid had to be designed for the MF1 milestone and completed by a service board [1].

The cathode strips were connected in groups of sixteen to the high voltage bus, located in the hybrid at the short side of the counters, via a 4.7 MΩ protective resistor. The same hybrid was used to bring the high voltage to the drift plane[2]. This hybrid also holds a high voltage filter with 4.7 MΩ resistor and decoupling capacitors (1000pF,-2kV). Some detector modules were equipped with fuse resistors (400 Ω) integrated in the bonding pads of the pitch adaptors at the input of the PreMux128 chips. A diode bypassed the 4.7 MΩ protection resistor. These diodes were supposed to conduct only a positive bias voltage applied in case of short circuit to blow the corresponding resistor fuse. Erroneous reverse mounting of these diodes made the detector module more vulnerable since the protection resistors to the cathode groups were bypassed in normal operations. As a consequence, loss of strips, due to discharges, was observed in modules equipped with these fuse resistors.

6.3.2 Detector modules

The modules O_1, O_2, O_3 and C_1 had eight counters each whereas C_2 and O_4 modules had respectively 4 and 2 counters as shown in table 6.2. All modules had outer ring substrates except O_4, having inner ring substrates. C_1 module consisted of two modules of four substrates each. The water cooling pipes were mounted only in the "open" modules but were not used to

[1] The design was made at BINP Novosibirsk, the production of the PreMux128 hybrids was done at CERN and the service boards were produced at IEKP Karlsruhe.

[2] These hybrids have been designed and realized at IReS Strasbourg.

Module	Ring	Strips material	number of substrates	working substrates
O_1	Outer	Al	8	8
O_2	Outer	Al	8	8
O_3	Outer	Al	8	5
O_4	Inner	Al	2	1
C_1	Outer	Au	8	8
C_2	Outer	Al	4	4

Table 6.2: *Some characteristics of the MF1 milestone modules.*

cool the readout hybrids.

A full description of open and closed designed modules was given in section 4.4. The six MF1 milestone modules were built by the different institutes involved in this part of the project: Aachen, Belgium, Karlsruhe, Lyon, Novosibirsk and Strasbourg.

6.4 Test of the O_1 module with cosmic rays

As module O_1, built at the IIHE, was the first to be ready, each counter of this module was tested individually in a separate gas box with cosmic rays, and then again, after the assembly. This was done in order to investigate the stability of operation of the eight counters and the dependence of the signal over noise ratio on the cathode and drift voltages. It also helped to define the dead and noisy strips of the counters before the final test.

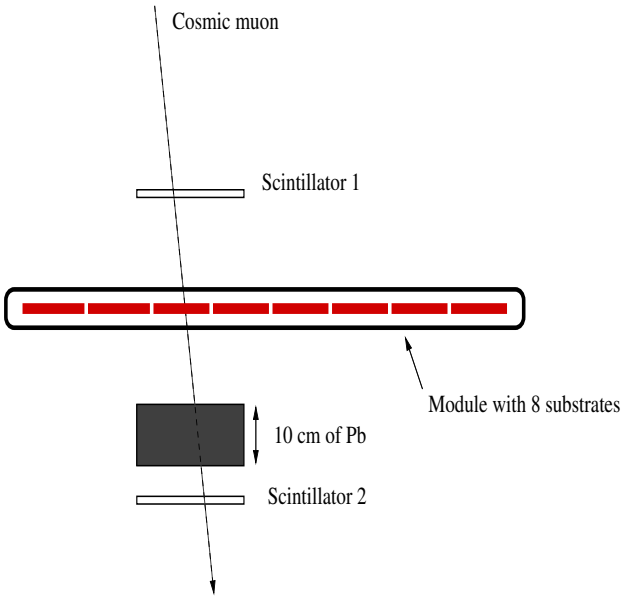

Figure 6.14: *Lateral view of the setup used for the cosmic rays test of the O_1 module.*

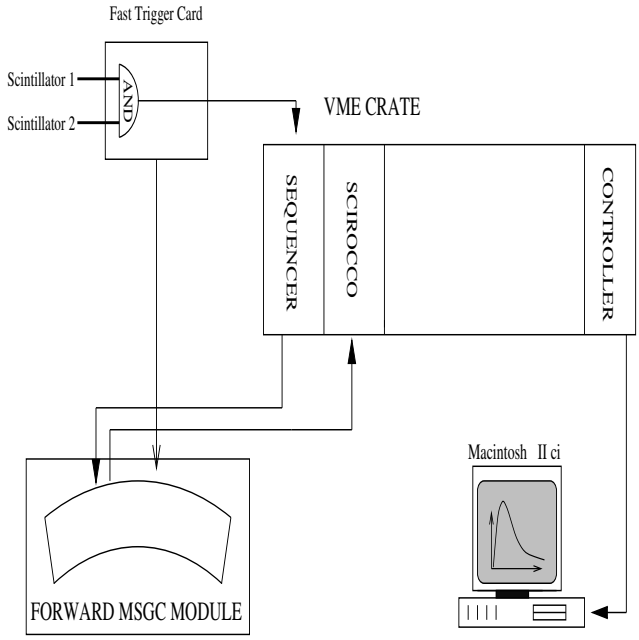

Figure 6.15: *Readout chain of the cosmic rays test setup.*

The experimental setup was very simple and is shown in figure 6.14. The MSGC module, filled with a Ne/DME 30/70 % gas mixture, was placed between two 15×15 cm^2 scintillators.

A piece of lead , 10 cm thick, was used to absorb all low momentum muons. The scintillators and the piece of lead could be moved horizontally to enable the scanning of the whole module active area.

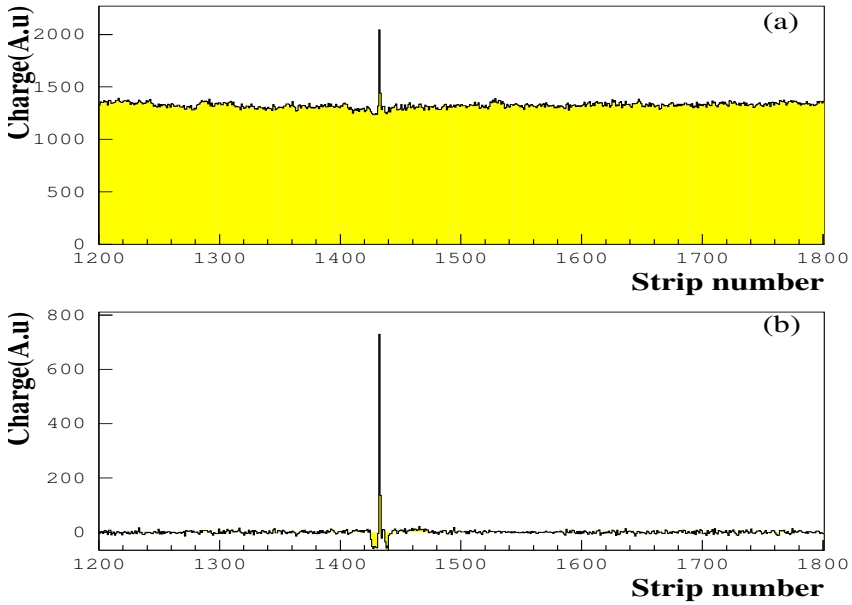

Figure 6.16: *The charge collected by each strip for a substrate of module O_1 before (a) and after (b) pedestal subtraction.*

As shown in figure 6.15, the readout sequence was initiated by trigger signals from the coincidence of the two scintillators. A fast trigger card provided a fast hold signal needed for the PreMux128 chips and a trigger signal for the sequencer module. The latter generated all control signals for the front end electronics. The digitization of the analog data was performed by a 12-bit resolution ADC converter: the VME Scirocco [138]. The data acquisition system was based on Lab View operating on a VME+Mac platform. The raw data were stored in a hard disk for later offline analysis.

The procedure followed during the offline analysis was very similar to that described in section 5.2.

The charge collected by each strip is shown in figure 6.16, for a single event, before (a) and after (b) pedestal and common mode subtraction with a clear signal from an incident particle around strip 1440. One can also notice the signals of reverse polarity on the channels adjacent to the one with the main pulse. This phenomenon, due to cross talk, is explained in section 4.1. For this preliminary test, raw data were not corrected for this undershoot.

The 8 MSGC's were connected to the same analog bus for the readout. The effective time constant of the bus was increased. At a readout clock of 1 MHz, an effect similar to pile-up took place. This effect increased the number of strips in a cluster as can be seen on figure 6.17(a) showing the number of strips in a cluster at a readout frequency of 1 MHz. The average cluster size is 3.7 instead of 2 usually obtained for this gas mixture [139, 140]. Reducing the readout frequency to 100 kHz solved the problem and led to normal cluster sizes (see figure 6.17(b)). This change didn't affect the signal over noise ratio as can be seen from figures 6.17(c) and (d).

In figure 6.18(a) the signal over noise ratio is plotted as a function of the cathode voltage for a given substrate when it was tested and read out individually in a separate gas box, and

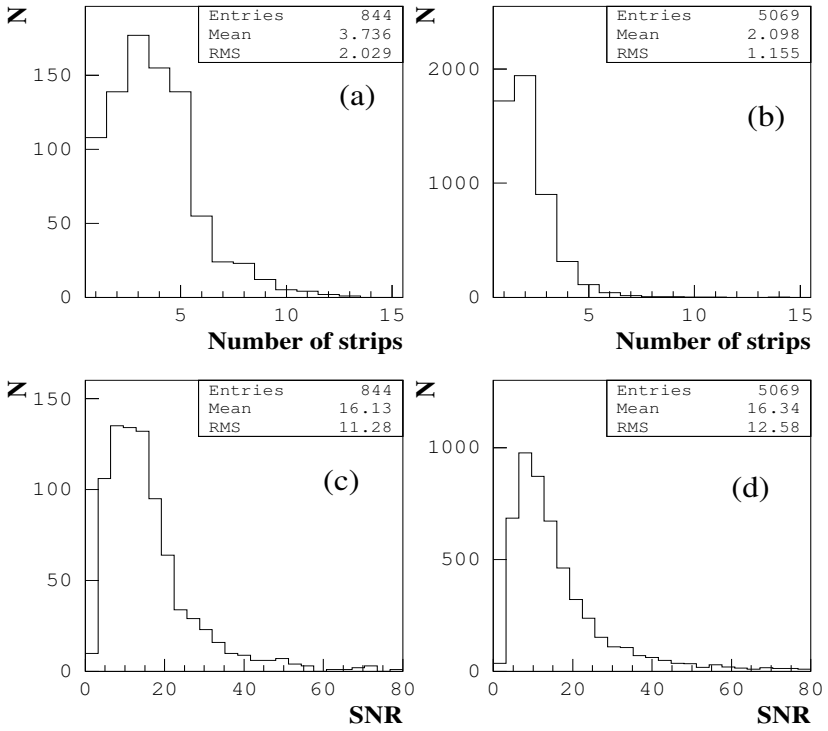

Figure 6.17: *Cluster size and signal to noise ratio distributions, in module O_1 , at a readout frequency of 1 MHz (a) and (c), and 100 kHz (b) and (d), during the cosmic rays test.*

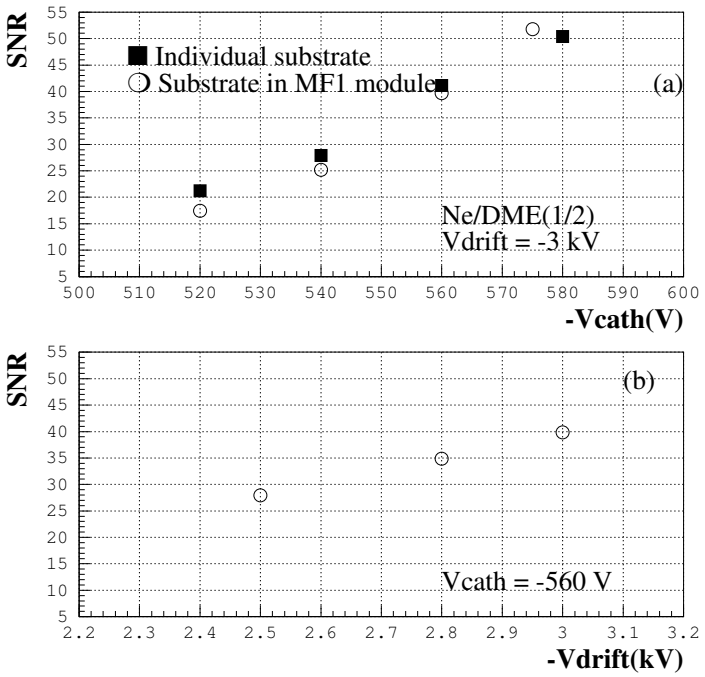

Figure 6.18: *Signal over noise ratio as a function of the cathode voltage(a) and the drift voltage(b) for module O_1, during the cosmic rays test.*

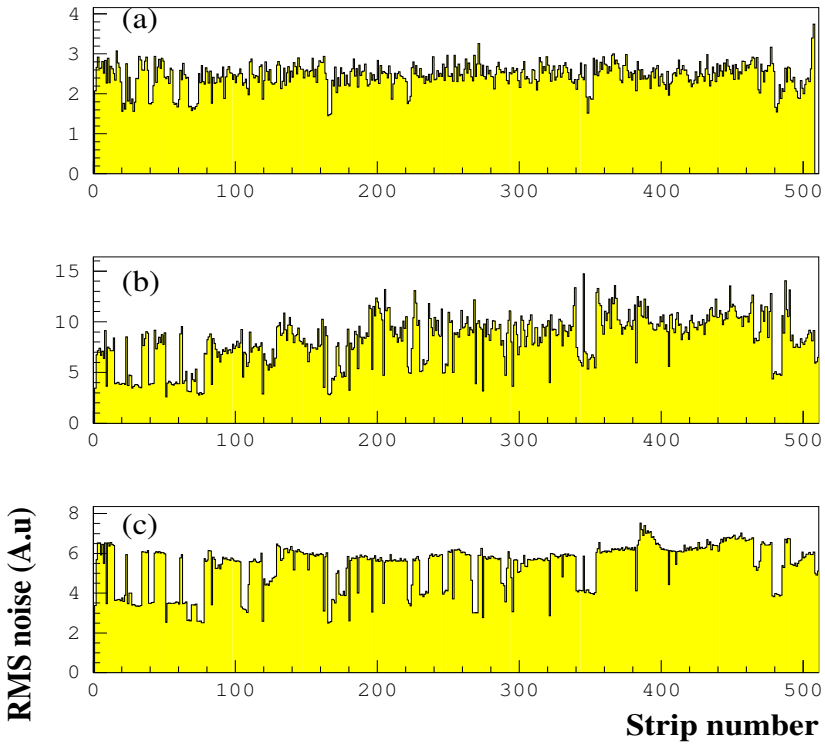

Figure 6.19: *RMS noise per strip for one of the eight substrates before the accident with DME(a), just after the accident(b) and two weeks later(c).*

after being mounted and read out inside the module with the other counters. The drift voltage was set to -3 kV. No significant change is noticed. The signal over noise ratio as a function of the drift voltage, at a cathode voltage of -560 V, is shown in figure 6.18(b) with the linear expected shape [42, 68]. As the drift planes used were of the same type of those used in the T10 test (see section 5.5), it was hard to maintain stable operation for drift voltages of more than 3 kV.

During the initial testing of this module a gas flush rate of three times the nominal one, which is 0.5 volume/hour, was used. When starting a cooling test, this led to DME condensation at the exit of the small inlet holes in the gas box. This condensation was due to the combined effect of the cooling and the overpressure caused by the very high flush rate. As the high voltage was on, the shorts produced by this accident with the reversely mounted diodes damaged 20 % of the active area. The RMS noise per strip is shown for one of the counters in figure 6.19 before the accident (a), just after (b) and after two weeks of operation (c). The damage is clearly distributed everywhere in the counter. It also shows that no further strip damage was induced in the substrate after this accident. The difference in the absolute value of the RMS noise from one figure to the other is due to a different tuning of the Scirocco amplification.

This preliminary test with cosmic rays helped us to verify some performance capabilities of the counters. The MSGC's have shown stable operation at high voltage up to 3 kV on the drift plane. A signal to noise ratio of around 19 is reached at a cathode strip voltage of -520 V and at a drift voltage of -3 kV. This value should lead to detection efficiencies above 97 %.

6.5 Outcome of the construction and assembly procedures

Before the final assembly into the detector modules, the MSGC substrates were optically inspected to detect interrupted or shorted anode strips. In some laboratories, an electrical test was performed using probe stations [14].

Since for the open design modules the substrates are connected to the readout electronics before module assembly, a high voltage test was performed in a nitrogen filled box as described in detail in reference [93]. In this test, each individual counter was brought to 80 % of the working point voltages.

In the closed design, the readout electronics is connected after module assembly. In both cases, shorted anode strips were disconnected by removing the corresponding bonding wire.

To avoid the DME condensation problem encountered with module O_1 and explained in section 6.4, the other open modules were built with larger gas inlet holes.

During the mounting procedure of the first 4-fold C_1 half module, some problems were encountered while aligning the three different frames (see section 4.4) one over the other, leading to a misaligned module with gas leak problems. In a gas leak search, water entered the module and caused shorts which damaged 30 % of the active area. The mounting procedure was then improved and the second C_1 half module was built with only a few damaged strips.

For module O_3, the recommended cleaning procedure of the substrates was not followed resulting in high currents (1-10μA) driven by the five working substrates and leading to poor performances of these counters.

6.6 The MF1 milestone test in a muon beam

After the assembly, the six detector modules have been tested in a muon beam at the CERN SPS test facility. In this section this test, called the MF1 milestone, is described and the results are reported.

6.6.1 Experimental setup

The test beam setup, shown schematically in figure 6.20, consisted of two independent benches. The first one carried the scintillator trigger, the track defining telescope, and several detectors to be tested by the CMS silicon group. The second one supported the six MSGC modules. The reference frame is also shown in figure 6.20: the beam was along the z axis whereas the x axis was roughly parallel to the MSGC strips. Thus the various detector planes, in first approximation, were parallel to the xy plane.

To provide fast trigger signals, two out of three plastic scintillators were used. The first was always 12×12 cm^2 and the second one was either 6×6 cm^2 or 2×2 cm^2.

During this test, we used a 100 GeV muon beam, obtained from the primary SPS proton beam [142]. The readout rate was 80 triggers per spill of 2.4 s when the trigger with an area of 2×2 cm^2 was used.

6.6.1.1 MSGC modules bench

A special support structure has been designed and built at IReS-Strasbourg to hold the six forward MSGC modules, as shown in figure 6.21. Each module was mounted on a thick aluminium plate (6 mm) supporting also the service board modules, the gas and cooling connectors and

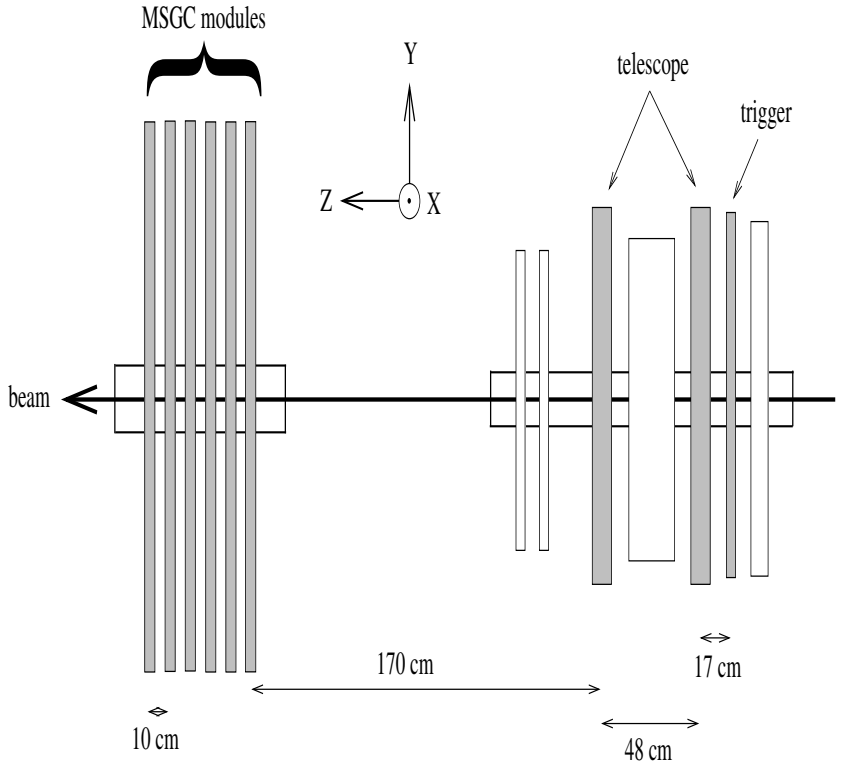

Figure 6.20: *Schematic view of the test benches from top.*

the high voltage lines. Five survey mirrors were installed on each plate allowing mechanical alignment. The aluminium plate had also a hole of the size and shape of the forward module to minimize the Coulomb multiple scattering.

The whole platform was mounted on a movable support enabling translations, of the six modules together, in x and y directions. The maximum excursion allowed to scan the whole active area of the MSGC modules. Figure 6.22 shows a picture of the MSGC bench in the CERN's test area.

A single gas rack delivered a mixture of Ne/DME 30/70 %. The six modules were flushed in parallel. The high voltage for the cathode strips were connected separately to each individual counter. For the drift high voltage, there were three lines per module for the open design modules; one line for each of the two edge counters and the third one for the rest of the counters. In the case of the closed design modules there was one drift voltage line per 4-fold half module.

The six modules were placed in such a way that the muon beam hit in turn O_1, O_2, C_1, O_3, C_2 and finally O_4.

6.6.1.2 Telescope

The telescope used for track reconstruction consisted of 4 silicon modules [143], referred to in the following as T_1, T_2, T_3 and T_4. Each module consisted of a double sided silicon microstrip detector(n-side and p-side), 300 μm thick, with an effective area of 1.92×1.92 cm^2. The readout pitch was 50 μm, so that each detector had 384 readout strips on each side. The n-side strips were perpendicular to the p-side strips. On the p-side, measuring the y coordinate, an intermediate p^+ strip was implemented between two readout strips, in order to improve the linearity of the charge collection whereas on the n-side, measuring the x coordinate, a p-stop

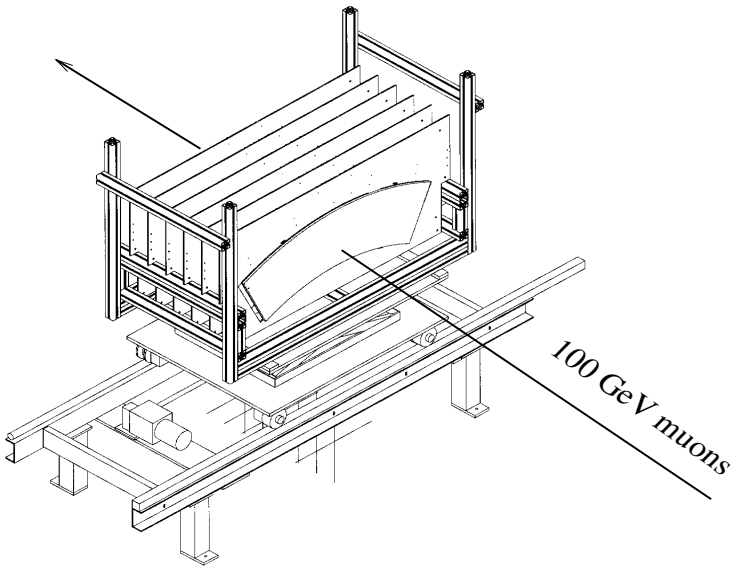

Figure 6.21: *Schematic view of the MSGC support structure.*

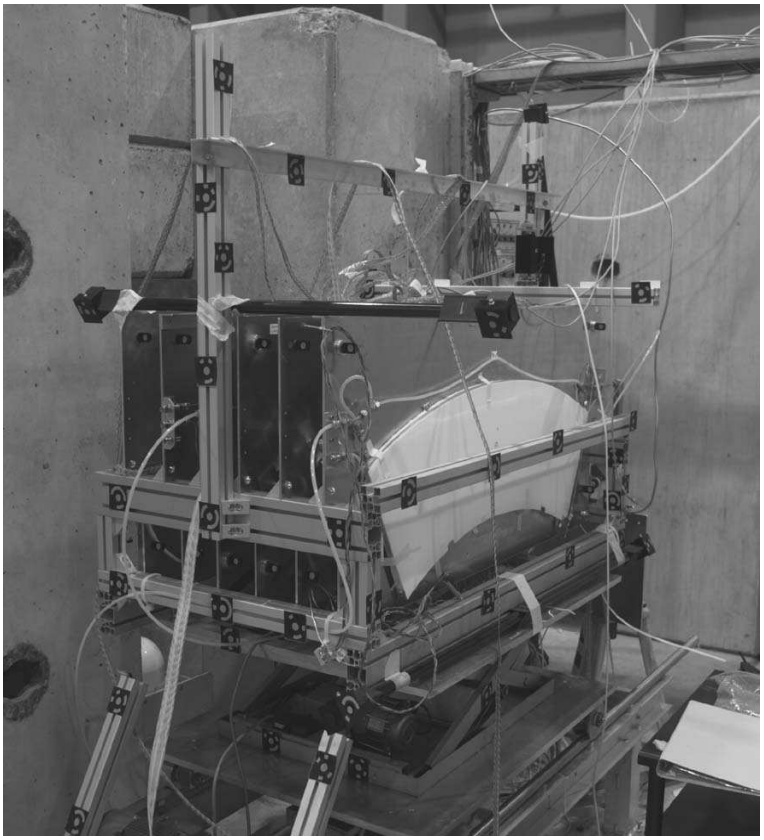

Figure 6.22: *Photograph of the support structure holding the six MSGC detector modules.*

strip was inserted in between two readout strips, to avoid charge spread. As a result of this asymmetry between the p and n-sides, the spatial resolution on the y coordinate was expected to be better than this of the x coordinate (see section 6.6.3). A detailed description of the silicon strip technology can be found in reference [144].

The strips were read out using the VIKING amplifier-multiplexer chips [145].

6.6.1.3 DAQ system and readout

The DAQ system was performed by a distributed system designed by GRPHE Mulhouse [146]. The system was divided into a front-end and an event builder part. Because of the large number of counters, the front-end system was segmented into several front-end crates as shown in figure 6.23.

In each front-end crate a sequencer synchronized the VME FADC and sent the readout signals necessary for the front-end chips. The trigger had to start all the sequencers and wait for the end of the readout of all ADC's before starting a new event cycle. The multiplexed analog outputs of the entire detector front-end electronics were transmitted by means of the Fast Intelligent crate Controller (FIC) to the FADC's where they were digitized, demultiplexed and stored. The data were then transferred to the event builder via a daisy chained fast data link.

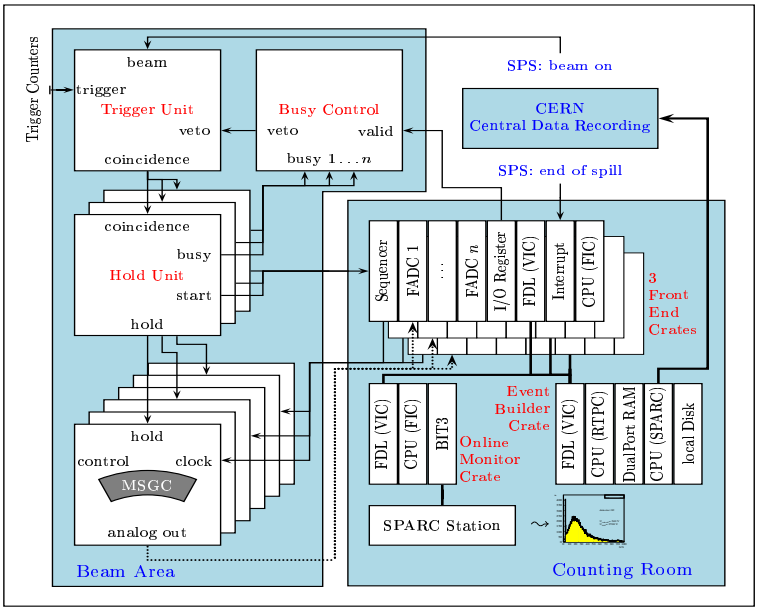

Figure 6.23: *The data acquisition system for the MF1 milestone test.*

The event builder ensured the synchronization between the front-end crates, created Zebra format data banks [129] and transferred them to a dual port memory. Data were then written to disk and sent via Ethernet to the CERN Central Data Recording. Due to the large number of silicon detectors also under test, only the two MSGC's that were in the beam were read out but the high voltage was on during the whole period for all the MSGC counters. However a few runs were successfully taken reading out together all the MSGC counters.

Another crate holds the Slow Control Module [148] which communicated with the PreMux128. It allowed the monitoring of the low voltages and the control of the front-end electronics. The triggering scheme of the whole system can be found in details in reference [147].

Data quality was checked on-line, with a PAW displayer [130], thanks to a monitoring program developed at INP Lyon.

6.6.2 Cluster definition

6.6.2.1 MSGC

The retrieval of the particle related signal from raw data requires a careful computation of the pedestals and of the common mode shifts. The pedestal for each strip was defined as the average of the ADC counts of that channel, evaluated for the 500 first events of each run, taking care not to include those events in which the strip may have been hit by a particle. Figure 6.24 shows the average pedestal per strip for two substrates of modules O_2 and C_2. The pedestal is uniform from one strip to another, with a few exceptions, for module O_2. A bad electrical connection for C_2 affects dramatically the pedestals uniformity even for strips connected to the same chip. The fluctuations are also bigger for module C_2. After correction of the raw data for the pedestals, the common mode was computed for each event, following a procedure similar to the one used in pedestals calculation, for sets of 128 contiguous strips connected to the same readout chip. After this correction, the strip noise σ_i was estimated as the RMS of the distribution of the remaining signal S_i^k (see equation (5.23)), in the absence of an incident particle. The RMS noise per strip is shown in figure 6.25 for two substrates of modules O_2 and C_1. The RMS value ranges between 10 and 12 ADC counts. Some dips, corresponding to dead or broken strips, are also observed. The strips were identified as dead or noisy if their RMS noise is less than half the average noise or more than three times that average respectively. They were therefore excluded from further analysis.

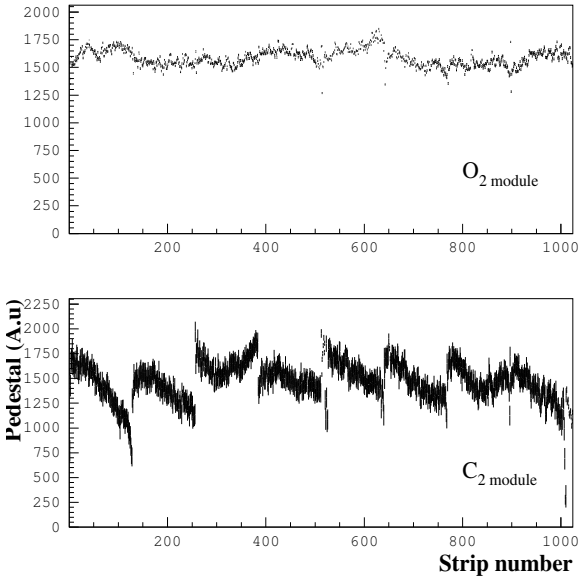

Figure 6.24: *Pedestal as a function of the strip number for two substrates of modules O_2 and C_2 respectively.*

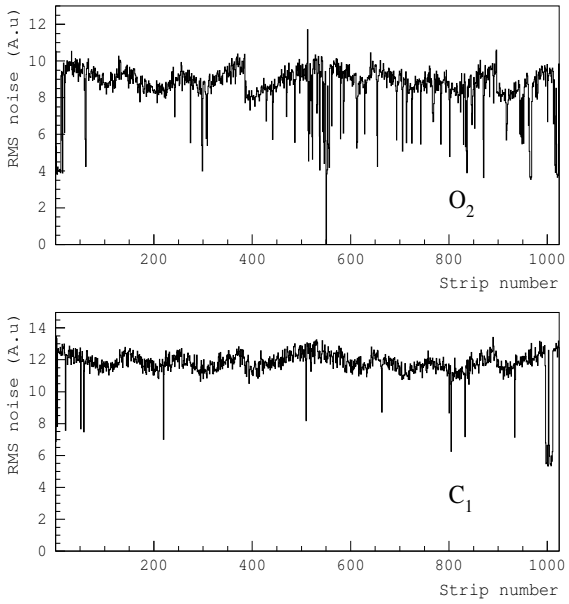

Figure 6.25: *RMS noise per strip for two substrates of modules O_2 and C_1 respectively.*

Clusters of adjacent strips having a signal were then formed. A strip was considered to have a signal if $S_i^k/\sigma_i > 3$. Adjacent strips satisfying this criterion were added together till no more strips having signal above threshold were found. To allow for dead strips, one strip with a signal below the threshold could be accepted within a cluster.

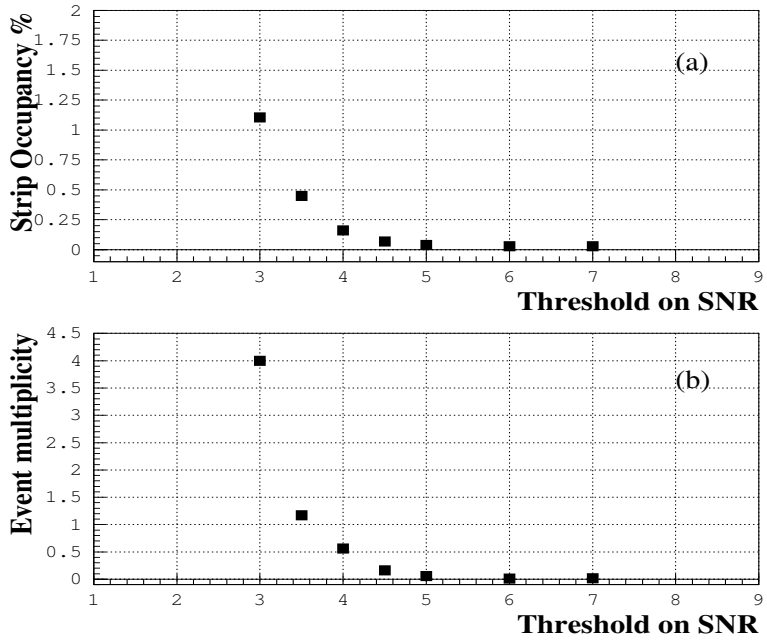

Figure 6.26: *Strip occupancy in percent(a) and event multiplicity (b) as a function of the threshold on the signal to noise ratio in a pedestal run.*

A second cut is then applied on the signal to noise ratio defined as the cluster charge divided by the cluster noise (see equation (5.35)). Figures 6.26 (a) and (b) show, respectively, the strip occupancy and the average event multiplicity as a function of the threshold applied to the signal to noise ratio, for a pedestal run taken with 2000 random triggers. The strip occupancy is defined as the average number of strips with a signal over threshold divided by the number of strips in the counter, expressed in percent. The channel occupancy and the fake hits rate decrease with threshold and reach values of 0.03 % and 0.05 respectively at a threshold of about five. Rising this threshold did not decrease these numbers significantly but affected the detection efficiency. We therefore applied a threshold of five on the signal over noise ratio during the analysis.

6.6.2.2 Telescope

The telescope information was needed to compute the spatial resolution as it will be shown below. Use was made of the telescope only in case of a 2×2 cm^2 trigger as with a 6×6 cm^2 trigger only 11 % of events were in the telescope active area.

Pedestal and common mode shift corrections together with cluster finding were performed in a way similar to the one described above for the MSGC's. However no strip with a signal below threshold was accepted within a cluster and the cluster signal to noise ratio had to exceed 15. In addition, events with more than one cluster in a telescope plane were rejected as well as those corresponding to particles coming outside one or more of the telescope active planes. With this selection, 13 % of events were removed from further analysis.

6.6.3 Alignment procedures

In order to determine the spatial resolution and the detection efficiency of the tested detectors using the information provided by the telescope, the entire setup had to be aligned. This has been done in two stages. First the eight planes of the telescope were aligned with respect to

a given reference frame, then the MSGC's were aligned with respect to this reference frame. These alignment procedures will be described below.

6.6.3.1 Telescope alignment

For the *ith* event, eight impact point coordinates x_j^i and $y_j^i, j = 1,4$ were registered by the telescope; x_j^i and y_j^i are the local x and y coordinates measured by the *jth* double sided detector T_j; the local x and y axes are aligned to the p and n side strips respectively. The local x and y axes of the first double sided silicon detector T_1 encountered by the beam were used as the reference frame. For the three other detectors, it was necessary to transform the measured coordinates x_j^i and y_j^i into coordinates in the common reference frame by rotations and translations.

In what follows, we will describe this change of reference frame taking into account only translations along x (x_j^0) and y (y_j^0), and rotations about the z axis (θ_j^0) as the other rotations were found to have negligible effects. Translations along the z axis having less influence will be introduced later.

The corrected coordinates x_{cj}^i and y_{cj}^i were related to the local ones via the following relation:

$$M_{cj}^i = R_j M_j^i + T_j^0 \quad (j = 1,4), \tag{6.8}$$

where:

$M_{cj}^i = \begin{pmatrix} x_{cj}^i \\ y_{cj}^i \end{pmatrix}$; $M_j^i = \begin{pmatrix} x_j^i \\ y_j^i \end{pmatrix}$; $R_j = \begin{pmatrix} cos\theta_j^0 & sin\theta_j^0 \\ -sin\theta_j^0 & cos\theta_j^0 \end{pmatrix}$; $T_j^0 = \begin{pmatrix} x_j^0 \\ y_j^0 \end{pmatrix}$,

and taking for the first detector T_1:

$\theta_1^0 = 0$ and $x_1^0 = y_1^0 = 0$.

In order to find the above unknown parameters: x_j^0, y_j^0 and θ_j^0, j=2,3,4, an iterative procedure using the minimum χ^2 method was used. Each track was fitted to a straight line both in the yz and xz projection plane leading to four new unknown parameters per track: the slopes, a_x^i and a_y^i, and the intercepts, b_x^i and b_y^i, for the *ith* track. The quantity to minimize is then

$$\chi^2_{total} = \sum_{i=1}^{N} (\chi^2_{x,i} + \chi^2_{y,i}), \tag{6.9}$$

with

$$\chi^2_{x,i} = (X_{ct}^i - H_x A_x^i)^T V_x^{-1} (X_{ct}^i - H_x A_x^i) \tag{6.10}$$

and

$$\chi^2_{y,i} = (Y_{ct}^i - H_y A_y^i)^T V_y^{-1} (Y_{ct}^i - H_y A_y^i), \tag{6.11}$$

where $X_{ct}^i = \begin{pmatrix} x_{c1}^i \\ x_{c2}^i \\ x_{c3}^i \\ x_{c4}^i \end{pmatrix}$, $Y_{ct}^i = \begin{pmatrix} y_{c1}^i \\ y_{c2}^i \\ y_{c3}^i \\ y_{c4}^i \end{pmatrix}$, $H_x = \begin{pmatrix} 1 & z_{x1} \\ 1 & z_{x2} \\ 1 & z_{x3} \\ 1 & z_{x4} \end{pmatrix}$, $H_y = \begin{pmatrix} 1 & z_{y1} \\ 1 & z_{y2} \\ 1 & z_{y3} \\ 1 & z_{y4} \end{pmatrix}$,

$A_x^i = \begin{pmatrix} b_x^i \\ a_x^i \end{pmatrix}$ and $A_y^i = \begin{pmatrix} b_y^i \\ a_y^i \end{pmatrix}$.

The z_{xj} and z_{yj} are the positions along the z axis of the j^{th} detector plane reading x and y coordinates respectively. V_x and V_y are the 4×4 covariance matrices. These matrices were supposed to be diagonal as the Coulomb multiple scattering through the detector planes

was negligible (0.7 μm) compared to the expected silicon detector resolution of several microns [150]. Therefore their diagonal elements were taken as the intrinsic spatial resolution of the corresponding plane as expected from reference [143].

As too many parameters appear in the χ^2 expansion (6.9) to perform a single fit, an iterative procedure was applied:

1. giving the starting values for the rotation and translation parameters, the track parameter matrices A_x^i and A_y^i were computed by minimizing the χ^2 (6.10) and (6.11) independently for each event.

2. an upper threshold on the χ^2 (6.10) and (6.11) was then applied in order to reject bad events for the next iteration. This threshold was decreased after each iteration.

3. the new track parameters are then used to minimize the χ^2 (6.9) in order to find better estimations of the rotation and translation parameters.

4. these new values are then used as starting values for the next iteration.

A similar minimization procedure was applied to search for z_{xj} and z_{yj}.

The residual distributions of the eight planes after the first iteration are shown in figure 6.27. After 3-4 iterations we obtained stable final values. An example of the values obtained from a given set of data is shown in table 6.3. A translation up to 430 μm was observed.

	θ_j^0 $(mrad)$	x_j^0 (μm)	y_j^0 (μm)
T_1	0	0	0
T_2	5.43	47.71	39.55
T_3	3.88	51.98	-430.22
T_4	-1.68	0.32	67.87

Table 6.3: *Correction parameters for the rotation θ_j^0 and translations, x_j^0 and y_j^0.*

The residual distributions after correction fit a Gaussian function as shown in figure 6.28. The standard deviations of these distributions, including the extrapolation error, are of the order of 5 μm for the y coordinate and 10 μm for the x coordinate. This latter is less precise as expected (see section 6.6.1.2). Correcting for track extrapolation errors leads to spatial resolutions of 3.5 μm and 7 μm for y and x coordinates respectively, in good agreements with previous measurements [143]. As shown in figure 6.29, the distributions of the χ^2 per degree of freedom of the fit in x and y projections have a mean close to 1 reflecting the quality of the fitting procedure. The difference in statistics between the x and y projections is due to two inefficient planes in the x projection.

6.6.3.2 Alignment of MSGC's to the telescope

In the *kth* MSGC placed at the position z_k along the beam, the local coordinate system (u_k, v_k) is taken with u_k along the central strip and v_k along the short base of the substrate as shown in figure 6.1.

The alignment of the *kth* MSGC to the telescope is similar to the method described in section 6.1.2. The residual distribution (6.5) is shown in figure 6.30 for one substrate of each module, after alignment; the residual is expressed in number of strips.

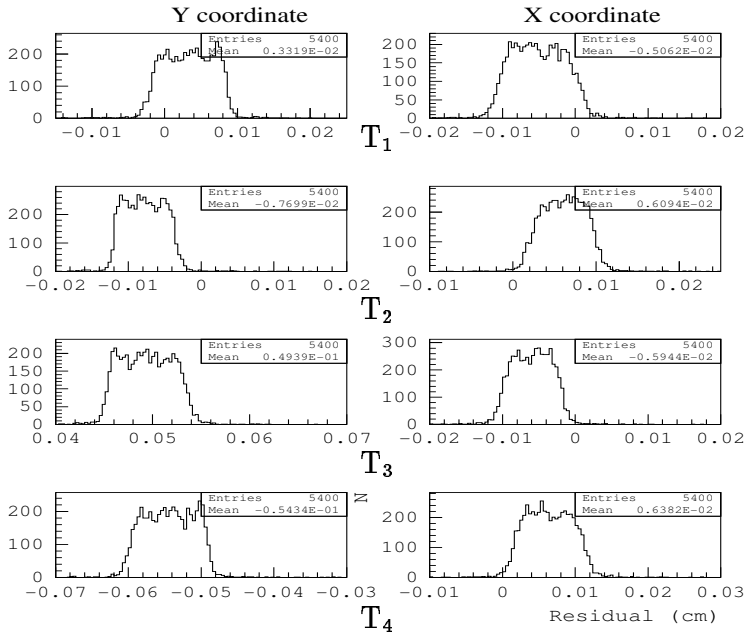

Figure 6.27: *Residual distribution of the telescope planes at the first iteration.*

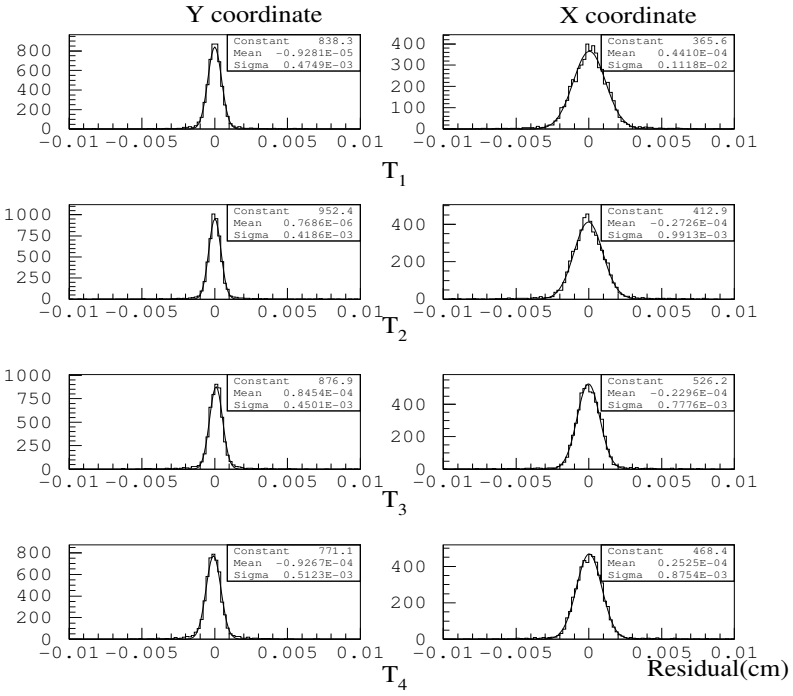

Figure 6.28: *Residual distribution of the telescope planes after alignment.*

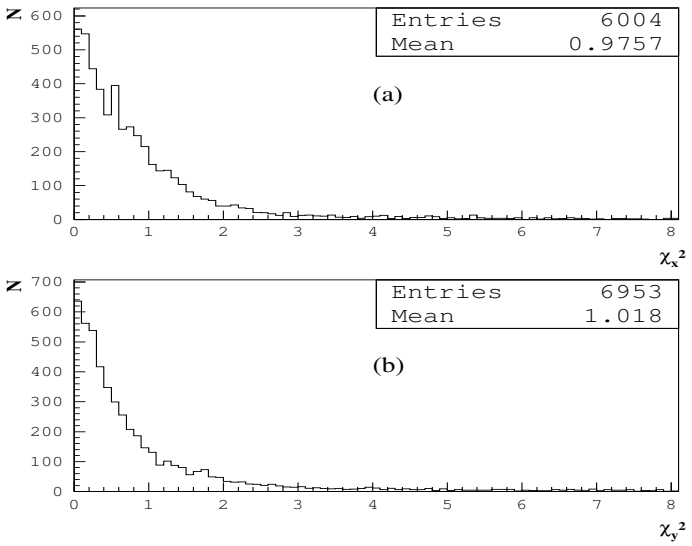

Figure 6.29: χ^2 *per degree of freedom distribution of the fit for the telescope planes alignment for x (a) and for y (b) projections.*

	$\sigma_{S_{pk}}$ (μm)	σ_{R_k} (μm)
O_1	15	98
O_2	16	100
C_1	19.5	133
C_2	20	115
O_3	21	116
O_4	24	121

Table 6.4: *Error on the predicted position and standard deviation of the residual distribution (6.5) for the six MSGC detector modules.*

Given the position of the MSGC modules along the beam axis, the distance between the telescope and the modules is increasing from module O_1 to module O_4. As a result the extrapolation error $\sigma_{S_{pk}}$ increases from module O_1 to module O_4, as can be seen in the second column of table 6.4. This increase can be also observed in the standard deviation σ_{R_k} of the distribution of the MSGC modules, shown in the third column of table 6.4. The distribution for module C_1 is larger, due to the fact that the beam was hitting a bad substrate, with many dead strips.

However, the values of $\sigma_{S_{pk}}$ and σ_{R_k} shown in table 6.4 do not match the MSGC spatial resolution expected to be of the order of 40 μm [10, 14, 110]. This can be explained by independent vibrations, of the telescope and the MSGC modules benches, not taken into account in the procedure.

For this reason, the position prediction from the telescope alone can not be used to determine the MSGC spatial resolution but it is sufficient to calculate the detector efficiency. An improvement of the alignment method, in order to estimate the spatial resolution, will be described in section 6.7.6.

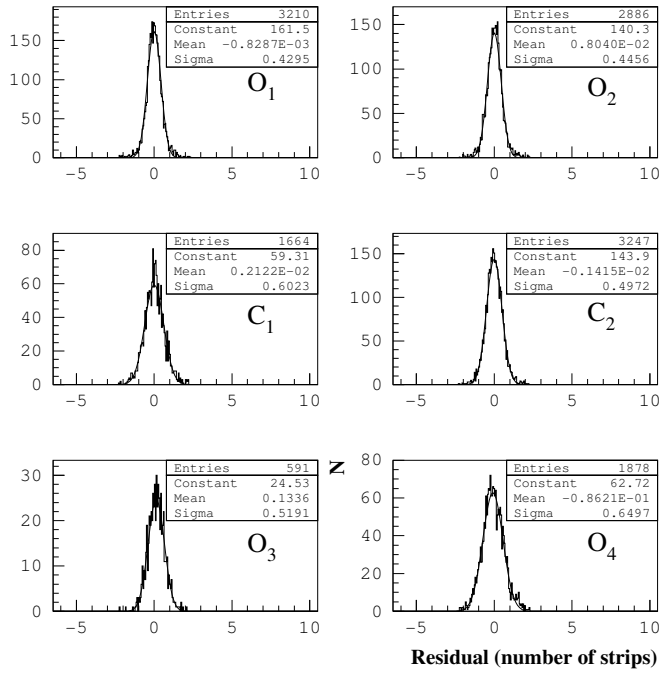

Figure 6.30: *Residual distribution obtained for equation (6.5) for one counter of each module.*

6.7 Results

6.7.1 Trigger timing adjustment

As explained in section 5.5, the timing of the signal sampling is of great importance when front-end electronics based on double correlated sampling method is used. For this purpose a delay box was inserted in the trigger line. Figure 6.31 shows the average cluster charge versus this delay for two MSGC detector modules, O_1 and C_1. In both cases the optimal delay was of the order of 20 ns. This value was used for the rest of data taking.

6.7.2 Cluster characteristics

Figure 6.32 (a) and (b) show respectively a typical cluster charge distribution and a cluster noise distribution for an outer ring substrate; the cluster noise is defined as in equation (5.25). These data were taken with a drift voltage of -2700 V and a cathode voltage of -510 V leading to a signal over noise ratio of 21.

As can be seen on figure 6.32(c) the average cluster width for the same detector is 2.3 strips as usual with Ne/DME 30/70 % gas mixture for the same angular distribution [140]. As shown in figure 6.32(d), 1.1 clusters were found on average for each trigger, with 1024 MSGC channels read out. This number is to be attributed mainly to true beam particles since the fake hit rate was found to be only 0.05 (see section 6.6.2). For the inner ring substrate, figure 6.33 shows the same quantities from a set of data taken with a drift voltage of -1500 V and a cathode voltage of -510 V, leading to a signal over noise of 20. The average number of clusters per event is 1.2.

The signal amplitude (the cluster noise) in ADC units of the two counters can not be directly compared as these two counters were connected to two different scirocco's having different amplifications. Since the anode width of module O_4 is smaller, it enables to reach a signal to noise ratio comparable to that of outer ring modules even if its voltages are lower. As the average pitch for the inner ring substrate is 192 μm instead of 231 μm in case of the outer

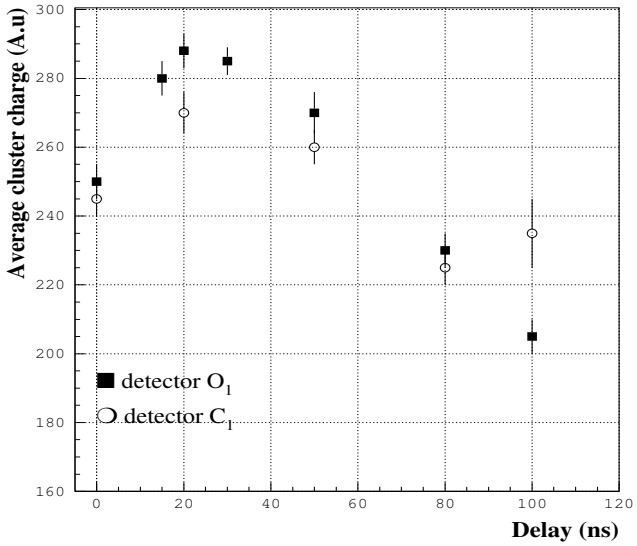

Figure 6.31: *Average cluster charge versus the trigger delay for two MSGC detector modules, O_1 and C_1.*

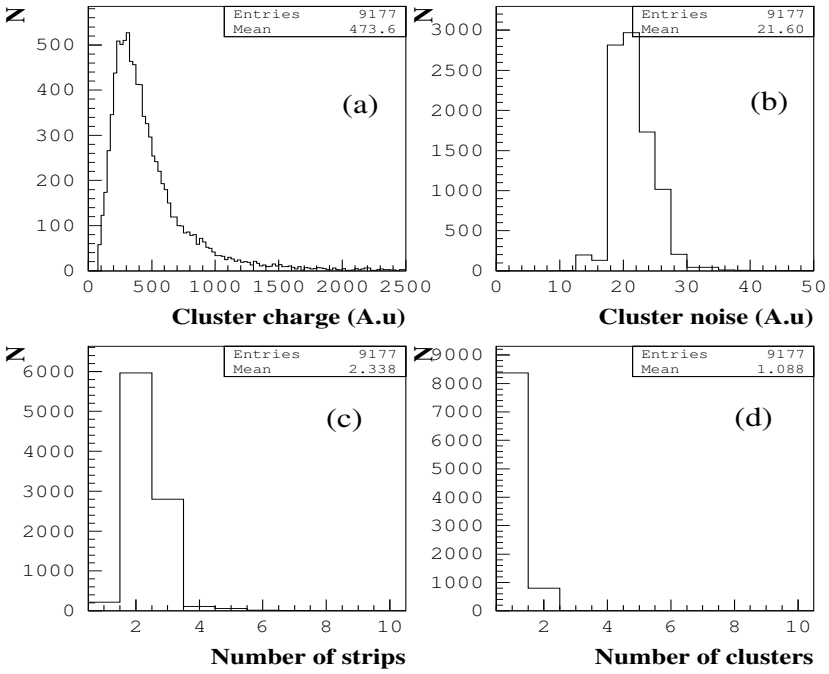

Figure 6.32: *Cluster charge (a), cluster noise (b), cluster size (c) and event multiplicity (d) distributions for one outer ring MF1 counter. The cathode strip voltage is -510 V and the drift voltage is -2700 V.*

ring substrates, the number of strips in a cluster should be larger in the case of the inner ring substrates. It is indeed observed, but converting these values to microns, leads to 690 $\pm$ 3 μm and 543 $\pm$ 2 μm for inner and outer ring counters respectively, which is not expected. Indeed the inner (outer) ring module is operated at an electric drift field of 3.8 kV/cm (7.8 kV/cm), leading to a transverse diffusion coefficient of about 130 $\mu m/\sqrt{cm}$ (160 $\mu m/\sqrt{cm}$) as can be deduced from figure 5.35, for Ne/DME 30/70 % gas mixture.

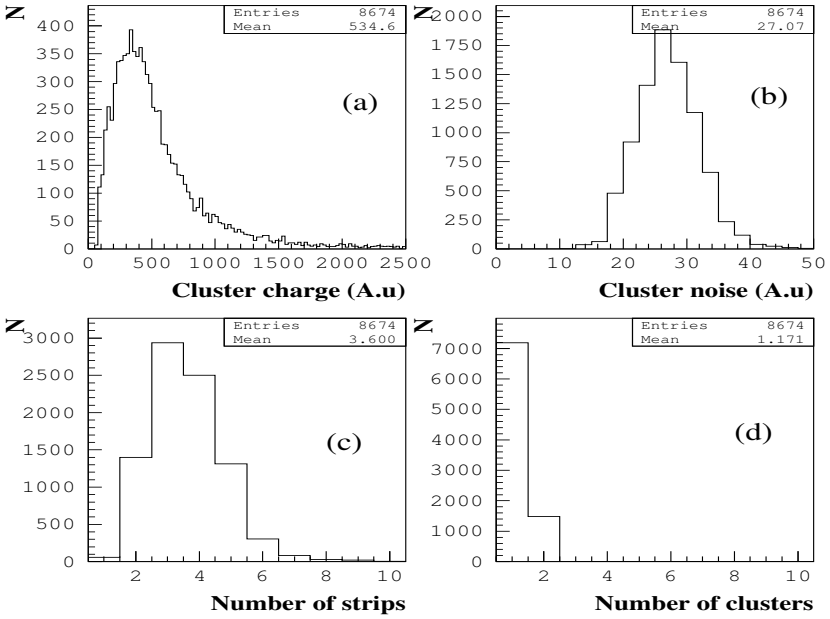

Figure 6.33: *Cluster charge (a), cluster noise (b), cluster size (c) and event multiplicity (d) distributions for the inner ring MF1 counter. The cathode strip voltage is -510 V and the drift voltage is -1500 V.*

6.7.3 Beam profile

Figure 6.34 shows the position of the strip having the highest charge in the cluster obtained in the two 4-fold C_1 modules. Each plot shows a different position of the module with respect to the beam. Substrates 5 to 8 present a large number of dead strips damaged during the assembly procedure as outlined in section 6.5. The neighbouring strips collect the charge released by the particle on the dead strip and present therefore a higher counting rate. Counters 1 to 4 show only a few dead strips since the assembly procedure was improved.

6.7.4 High voltage scan and efficiency plateau

During this test, a first set of measurements was dedicated to find the MSGC working conditions by measuring the efficiency plateaus. The detection efficiency was computed as the fraction of reconstructed tracks, traversing the MSGC active area, that lead to a cluster compatible with the impact point predicted by the telescope, within a certain window on each side of this prediction.

The dependence of the detection efficiency on the size of this window is shown in figure 6.35(a) for an MSGC of module C_2. A maximum efficiency of 97.5% is obtained if this window is set at least to 700 μm; *i.e* 6 times the width of the C_2 MSGC module residual distribution of figure 6.30. The detection efficiency versus the strip number is shown in figure 6.35(b)

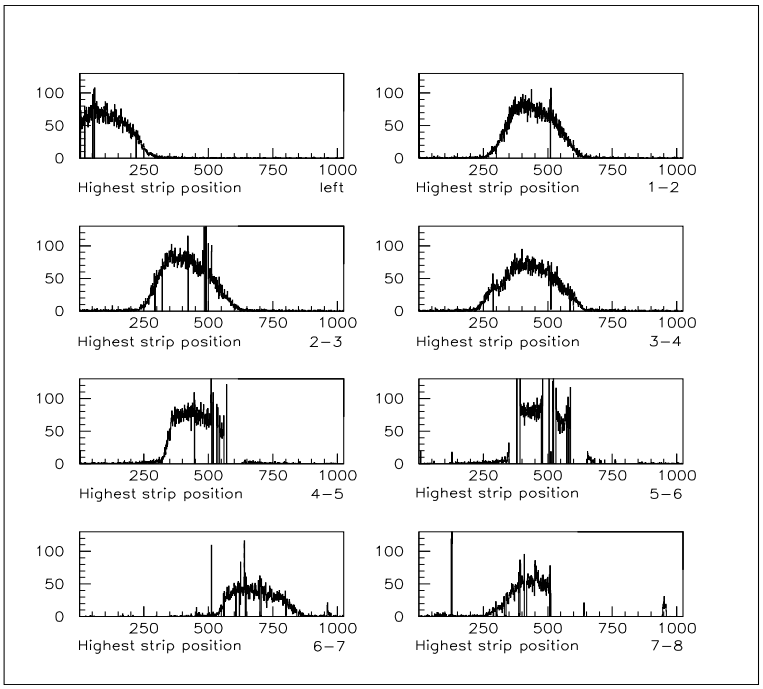

Figure 6.34: *Beam profile across counter pairs of module C_1.*

for the same counter with a window size of 700 μm. No dead strip is observed in this substrate. Indeed, all efficiency values are equal to 97.5 % within the statistical error of the order of 1 %.

For a given gas mixture and a fixed detector geometry, the detection efficiency is determined by the signal over noise value [14]. In other words, detectors with the same nominal geometry operated with the same gas mixture, would be fully efficient at the same signal over noise value (see chapter 5) although they could need different voltages to reach it, due to small differences in cathode widths. As it was difficult to measure it as a function of the cathode strip voltage for all counters, the efficiency plateau was measured for a few counters. Figures 6.36 show respectively the detection efficiency as a function of the applied cathode strip voltage (a) and as a function of the average signal over noise ratio (b), for modules O_1 and O_2. The drift voltage is of -2500 V for O_1 and -2700 V for O_2. Considering a maximum efficiency of 97.5 % , the efficiency plateau starts at a cathode voltage of about -520 V for O_1 and around -505 V for O_2 corresponding, in both cases, to an average signal over noise ratio of about 17 completely in agreement with previous measurements made with identical chambers with the same gas mixture [151]. It is also in agreement with the value of 19 obtained for MSGC with parallel strips operated with Ne/DME 50/50 %, in section 5.4.2.1. The slight difference between the two values is attributed to the different in the primary ionization densities for the gas mixtures used. However, it is higher than the value required as working point for MSGC's with parallel strips in CMS which is 13, using the same definition of the signal to noise ratio [14]. In order to prevent the strips from possible sparks, the cathode strip voltage was not pushed too high and thus the end of the efficiency plateau is expected at values higher than 560 V. With other modules we see the same behaviour of the average signal over noise ratio.

The signal over noise ratio is shown in figure 6.37(a) as a function of the cathode strip voltage, for O_1, C_1 and O_2 modules. This latter was operated with a drift voltage of -2700 V, instead of -2500 V for the two others, raising the signal over noise by 30 % at -520 V. The cathode strip voltage scan for module O_4 operated with a drift voltage of -1500 V is shown in figure 6.37(b). Thanks to the small anode width of this device, resulting in a higher amplification [42, 66], a

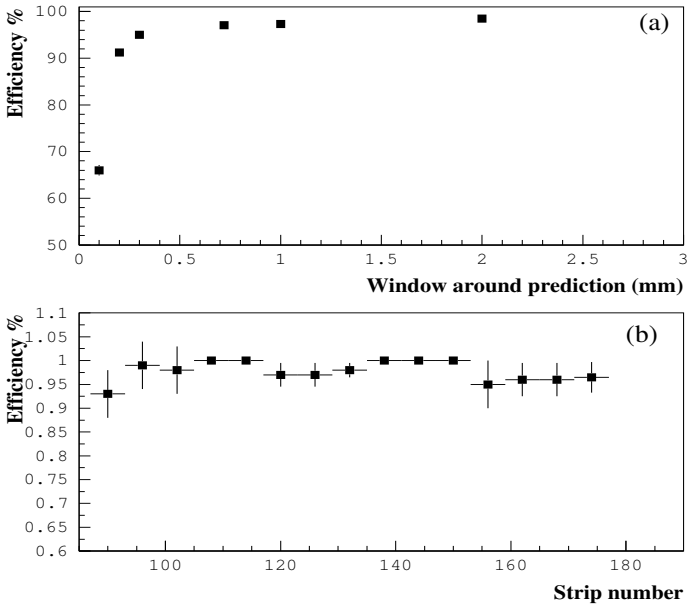

Figure 6.35: *Efficiency as a function of the size of the window on each side of the telescope prediction (a) and across the strips (b), for a MF1 substrate without dead strips.*

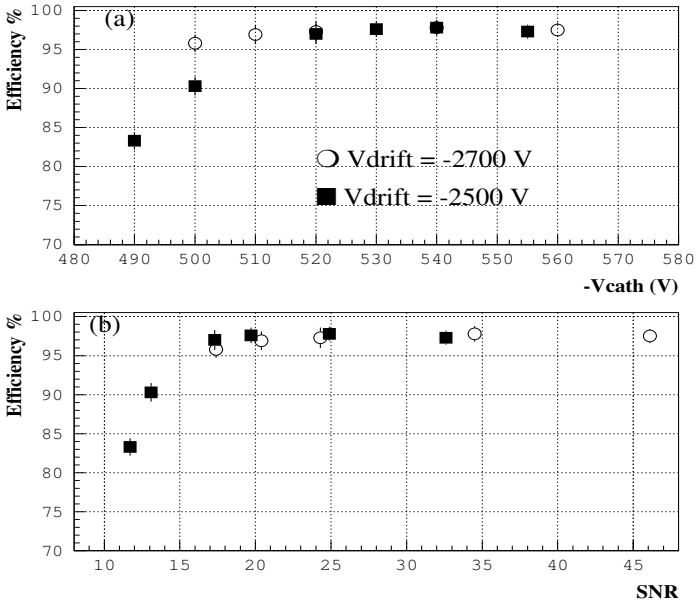

Figure 6.36: *Efficiency as a function of the cathode strip voltage (a) and of the signal to noise ratio (b), for O_1 and O_2 modules.*

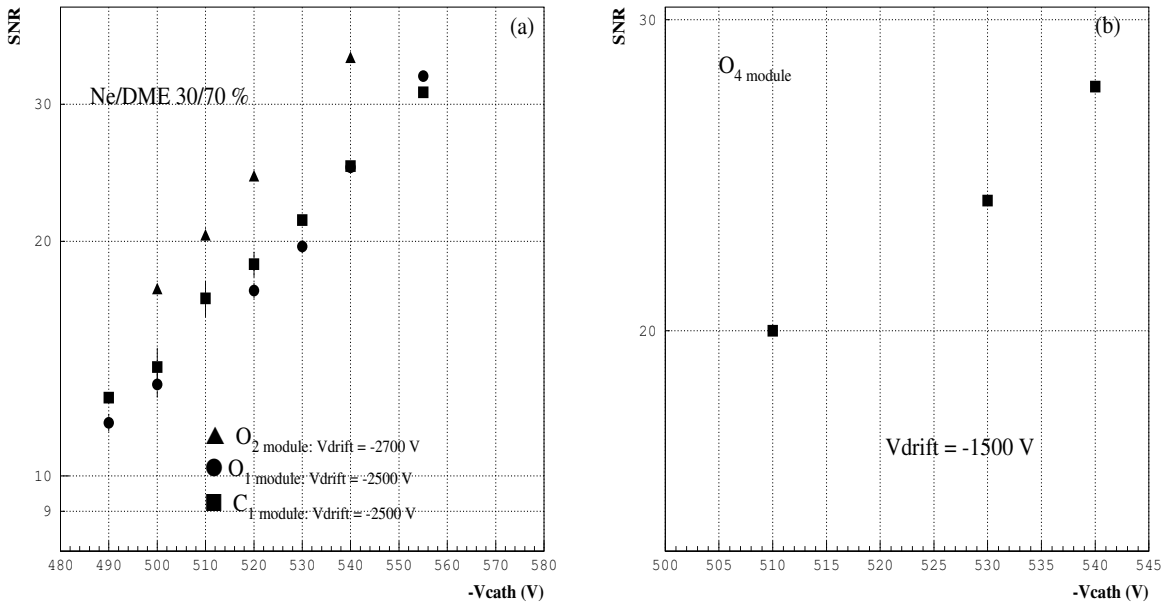

Figure 6.37: *Signal over noise ratio versus the cathode strip voltage for O_1, O_2 and C_1 modules(a), and for O_4 module (b).*

signal to noise ratio of 20 is obtained already at -510 V.

A drift voltage scan was performed for module C_2 alone since the drift planes of the other modules did not allow to apply voltages higher than 3 kV (see section 6.3.1.2). Figure 6.38 shows the dependence of the signal to noise ratio on the drift voltage for a fixed cathode strip voltage of -530 V. For comparison, one point at -510 V is also shown. It demonstrates that an increase of about 500 V on the drift voltage allows to decrease the cathode voltage by 20 V. This means that full efficiency can be reached at a lower cathode voltage with a higher drift voltage. This has the advantage of minimizing the spark rate and therefore the risk of damaging strips with sparks is decreased [14, 52, 152] (see also section 4.2.4).

Six months later, counters of an open design module have been successfully tested in the same beam with new drift planes allowing to operate with drift voltages up to -3800 V as shown in figure 6.39. The cathode voltage was -530 V and the gas mixture was Ne/DME 40/60 %. The drift voltage was easily raised up to -3.8 kV corresponding to an electric field of 11 kV/cm which is above the working point of MSGC in CMS [14]. These drift planes have also shown stable behaviour in a high intensity beam of hadrons.

6.7.5 Uniformity study

In an experiment as CMS, a uniform gain in a given counter and from one counter to another is mandatory because of the large number of counters foreseen. For this reason, a scan has been performed along the strips for each module and across the strips for all counters.

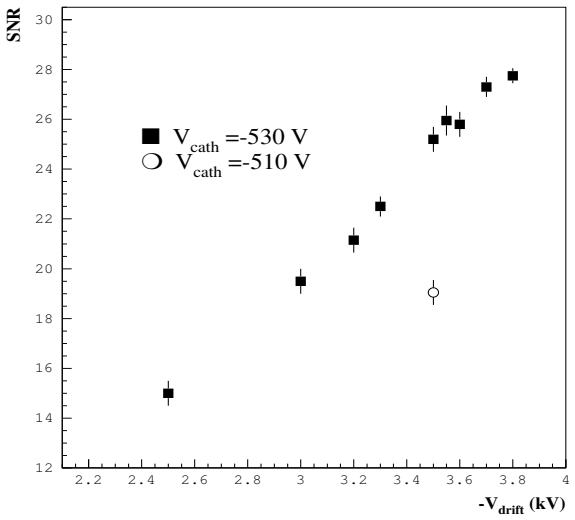

Figure 6.38: *Signal to noise ratio versus drift voltage for module C_2 at two cathode strip voltages: -530 V and -510 V.*

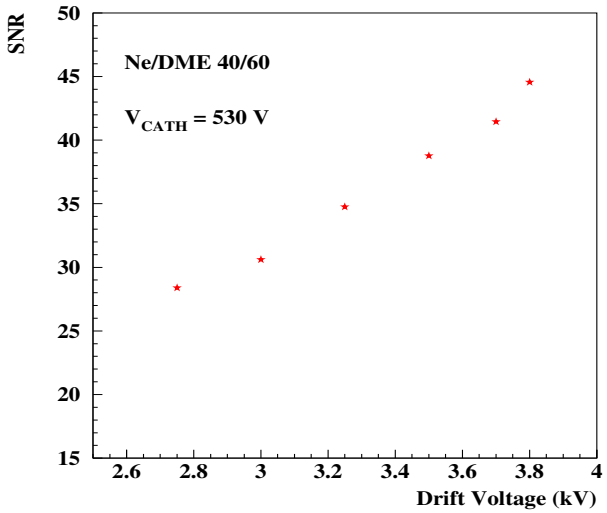

Figure 6.39: *Signal to noise ratio versus drift voltage for an "open" module with a new drift plane, measured at a cathode strip voltage of -530 V, in another test beam.*

6.7.5.1 Scan along the strips

As, due to the trapezoidal shape of the counters, the anode pitch varies along the strips, one of the aims of this test was to check that the gain does not vary too much along the strips.

Figure 6.40 shows the signal over noise ratio as a function of the anode pitch, for the six MSGC modules. Since the aim was to check the uniformity within a given counter, no attention was paid to operate the counters at the same voltages. Thus the cathode strip voltage was -520 V for O_2 and O_3, and -530 V for O_1, C_1 and C_2. The drift voltage was -2700 V for O_1, O_2 and C_1, -2500 V for O_3, and -3000 V for C_2. The inner ring module O_4 was operated with -510 V on the cathode strips and -1500 V on the drift plane. In order to allow precise tracking with the telescope, the 2×2 cm^2 trigger was used.

In the case of module O_3, the 60 % lower signal observed was due to the high current (1 μA) drawn by most of the counters in this module. Due to the bad electrical connections leading to a larger noise, module C_2 was operated at a higher drift voltage, to allow to reach a full efficiency signal to noise ratio; this ratio was still 20 % lower than for O_1, O_2 and C_1.

For modules O_1, O_3, C_1 and O_4, shown in figures 6.40 (a) and (c), the signal over noise ratio is uniform along the strips; the variations are less than 10 % which is acceptable. On the contrary, for modules O_2 and C_2 shown in figure 6.40 (b) and for which the substrates were produced by OPTIMASK, a decrease up to 20 % is observed with increasing pitch although the same mask was used to pattern the strips as for O_1, O_3 and C_1. Indeed, it was observed that the substrate quality affects strongly the uniformity of response along the strips [92]. Nevertheless, these results are very promising with respect to the uniformity study done in section 6.1.3 for substrates having a constant anode-cathode gap where the gain variation reaches 47 %.

In order to better understand these results and to complete our knowledge of these detectors, we have performed extensive simulations including electric field computations with MAXWELL [115] and a combination of GARFIELD [114] and MAXWELL (see section 5.3) to compute the relative gain along the strips of a trapezoidal MSGC. For this purpose we have

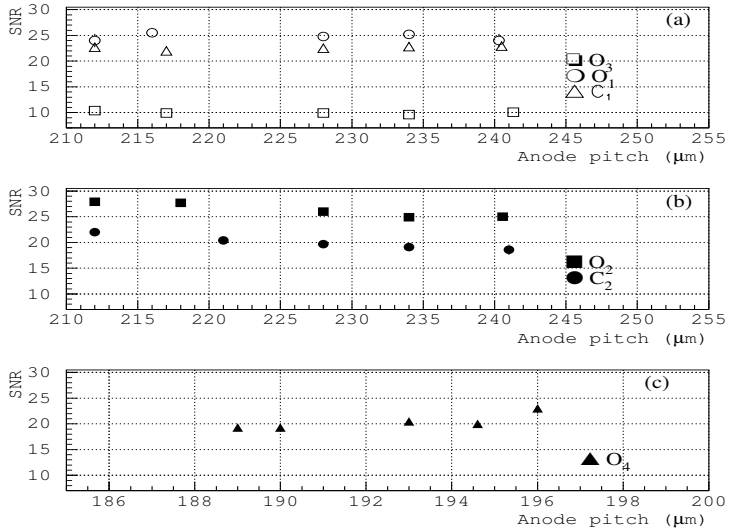

Figure 6.40: *Signal to noise ratio along the strips, for modules O_1, C_1 and O_3 (a), for modules O_2 and C_2 (b) and for module O_4 (c).*

made four models which characteristics are shown in table 6.5. The substrate for each model consists of 300 μm thick glass. The strips are in aluminium and the gas gap is 3 mm. The gas mixture is Ne/DME 30/70 %. For models 1 and 2, the anode width, the cathode strip and drift voltages are chosen as for the outer and inner ring substrates in the MF1 milestone. Model 3 is similar to Model 2 but the drift voltage is set to -3000 V in order to check the uniformity along the strips at higher electric drift fields. Model 4 allows to check the behaviour of counters with larger anode width (13 μm).

During the simulation, the emphasis is put on the relative gain variations as a function of the anode pitch.

	Model 1	Model 2	Model 3	Model 4
Pitch(μm)	160 to 400	140 to 300	180 to 300	200 to 360
Anode width(μm)	10	7	7	13
Cathode width(μm)	70 to 250	58 to 178	88 to 178	97 to 219
Anode-cathode gap(μm)	40 to 70	37.5 to 57.5	42.5 to 57.5	45 to 65
$V_{drift}(V)$	-2500	-1500	-3000	-3000
$V_{cath}(V)$	-530	-510	-510	-520

Table 6.5: *Parameters characterising the simulated models.*

The relative gain as a function of the anode pitch is shown in figure 6.41 for the four simulated models. A first look into this figure reveals that the gain is not constant everywhere. The gain is constant only over a certain range of pitch values called the uniformity plateau. In model 1, corresponding to the outer ring substrates of the MF1 milestone, the gain is constant between pitch values of 210 μm and 320 μm which is in agreement with experimental results reported above in figure 6.40(a). However below 210 μm, the gain is not constant while it is in the experimental values of module O_4 (figure 6.40(c)). However the experimental module O_4 has an anode width of 7 μm while the simulation model 1 has a 10 μm anode width. Indeed, results from the simulated model 2 with an anode width of 7 μm shows that the gain

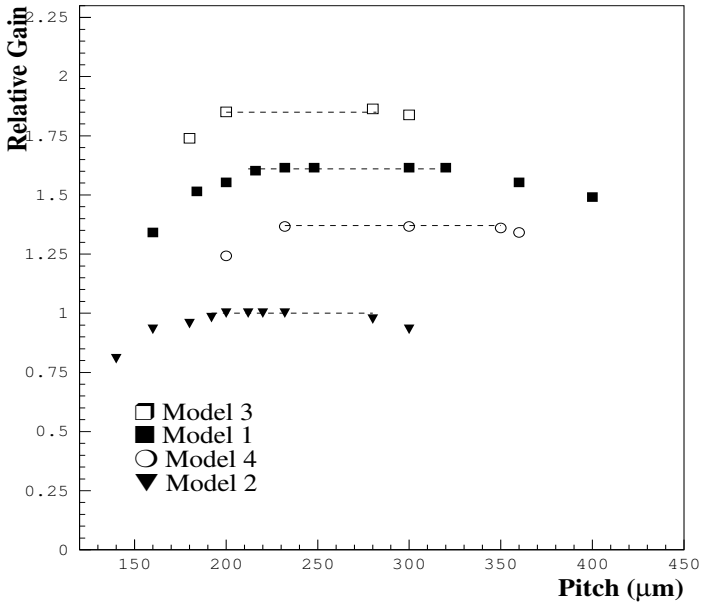

Figure 6.41: *Relative gain as a function of the anode pitch for the four simulated models. Their characteristics are listed in table 6.5. The dashed lines indicate the length of the uniformity plateaus.*

is uniform between pitches of 190 μm and 280 μm which is in agreement with experimental values of module O_4. The uniformity plateau is thus shifted and depends on the anode width. Model 4 also shows the same behaviour with a shift of the uniformity plateau towards higher pitches since the anode width is higher (13 μm). Increasing the electric drift field does not affect the uniformity plateau as can be seen from the comparison of models 2 and 3. Results from reference [92] shows that the ratio between the gain at the large base to this at the short base of the trapezoidal substrate depends strongly on the drift voltage. Two comments can be made about these results. First none of the tested substrates verified the scaling law (4.1). Secondly, their boron implemented SiO_2 substrates show charging-up with positive ions. Indeed, the dependence on the drift voltage of the gain ratio disappeared after the substrate has fully charged up [92].

The behaviour of the gain as a function of the pitch for several anode widths leads us to make the plot of figure 6.42 where the beginning and the end of the uniformity plateaus of figure 6.41 are reported as a function of the anode width. The points are aligned and lead to one uniformity region which is between the two straight lines. With simple calculations, we can show that two additional conditions have to be added to the rule (4.1) and are given by:

$$0.8a + 38\mu m \leq G = \frac{P}{8} + 20\mu m \leq 1.4a + 45\mu m \tag{6.12}$$

where a, G and P are respectively the anode width, the anode cathode distance and the anode pitch.

In table 6.6, several chambers that were tested, in the framework of this study or by other groups, are listed. All the results agree with the condition (6.12). The results reported in reference [151] are from a substrate having 10 μm anode width and a pitch between 180 μm and 200 μm. It shows up to 30 % of variations of the pulse height along the strips in some regions of the counter. This is in agreement with the simulation results of model 1. These

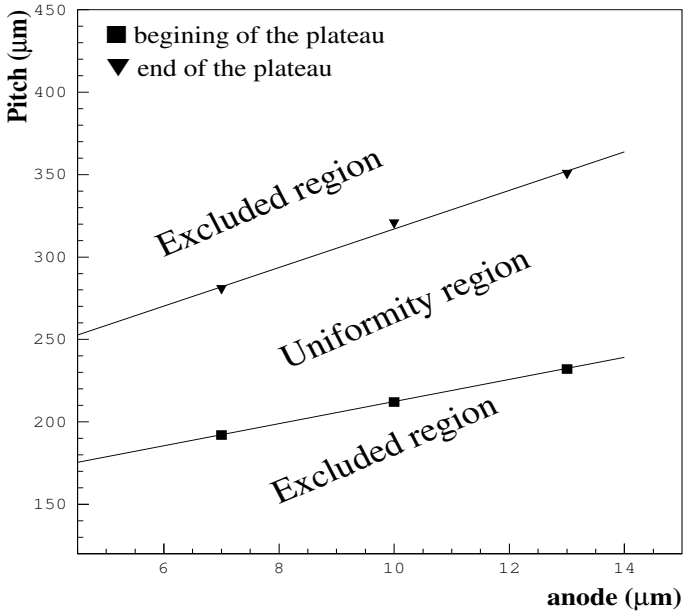

Figure 6.42: *Beginning and end of the uniformity plateau in anode pitch as a function of the anode width. The lines are a linear fit through the corresponding points.*

	Ref.	gain variations (%)	rule (4.1)	rule (6.12)
O_4	this work	≤ 10	yes	yes
O_1,O_3 and C_1	this work	≤ 10	yes	yes
4 substrates	[92]	up to 70	no	no
1 substrate	section 6.1	up to 47	no	no
1 substrate	[151]	10 to 30	yes	no

Table 6.6: *Summary of the experimental results obtained by different groups.*

results together show that it is still possible to ensure a constant gain along the strips in the CMS MSGC tracker where the range of pitches and anode widths correspond to models 1 and 2 but attention must be paid to the anode width (and the quality of the substrate).

6.7.5.2 Scan perpendicular to the strips

Tuning the high voltage for each individual MSGC, in order to reach full efficiency, must be avoided in an experiment such as CMS where a large number of counters will be used [10, 14]. For this reason, the uniformity of the response in a direction perpendicular to the MSGC strips was also checked. The MSGC bench has been moved during this scan in order to have the beam in different regions of each counter. So we could check the cluster position distribution, the signal amplitude and the cluster noise in each MSGC detector.

Figure 6.43 shows the variation of the signal to noise ratio from one MSGC to another for modules O_1, C_1, O_2 and C_2. During this particular scan , modules O_3 and O_4 were not in the beam. Module C_2 was operated at a drift voltage of -3500 V. The different marks correspond to different positions of the beam in each corner of the substrates.

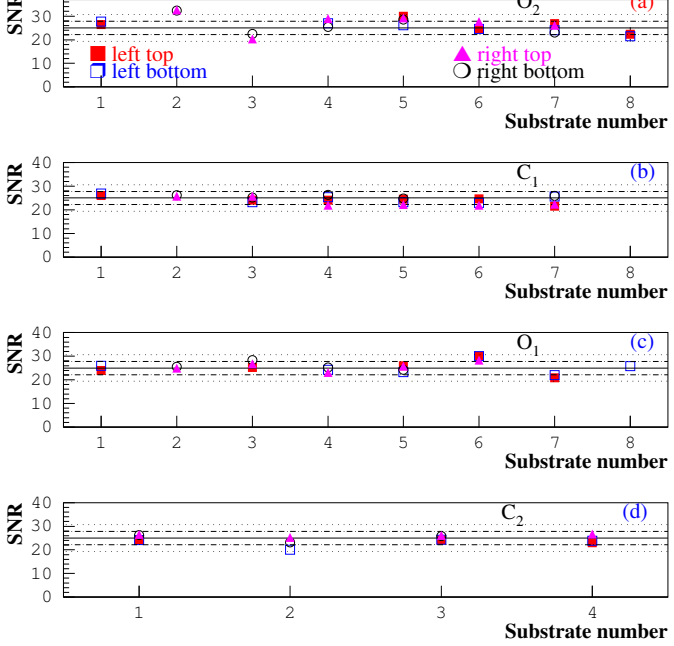

Figure 6.43: *Variations of the signal to noise ratio as a function of the counter number in modules O_2, C_1, O_1 and C_2. The square(round or triangle) marks correspond to beam positions in a left(right) corner of the substrates. The open(closed) marks correspond to positions in a bottom(top) corner of the substrates. The full lines correspond to the average value of all measurements. The dashed and dotted lines are at one and two standard deviations , respectively, from that mean.*

The full lines correspond to the average signal to noise ratio of 25 obtained for all measurements of the four displayed modules. The dashed and dotted lines are, respectively, at one and two standard deviations from that mean. In C_1 module, the 8^{th} counter was pushed to very high cathode voltages resulting in a short; as a consequence it was not possible to operate it during this scan. The presence of only one or two measured points for some counters is due to the lack of statistics. Variations less than 10 % are observed except for three counters where the variations are up to 25 %. One of these has a broken substrate, the second one draws a high current (1-10 μA) and the third one presents many dead strips.

For module O_4, containing only one working counter, the signal to noise ratio has been studied across the strips. Figure 6.44 shows the signal to noise ratio as a function of the distance of the average beam impact position to the central strip of this counter. The gain variations observed are less than 15 %.

This uniformity study demonstrates that it is possible to operate all MSGC counters of a given module at the same voltages. A constant gain along the strips can be reached provided the rule 6.12 is satisfied and a qualified producer is chosen. Gain variations up to 25 %, in the worst cases, were observed in some counters showing some defects.

Noise performances of the counters were also studied. Figure 6.45 shows the average cluster noise (a) and strip noise (b) versus the substrate number for modules O_1, O_2, C_1 and C_2. The bad electrical connections for module C_2 has led to higher noise; this lowered the signal to noise ratio for this module as seen for example in figure 6.43. The lower values obtained for O_2 are due to a different tuning of the FADC amplification used for this module. Indeed the signal to noise ratio was the same as for O_1 and C_1 at the same conditions.

Only substrates 3 and 7 of module O_2 had 400 Ω protective resistors between the anodes

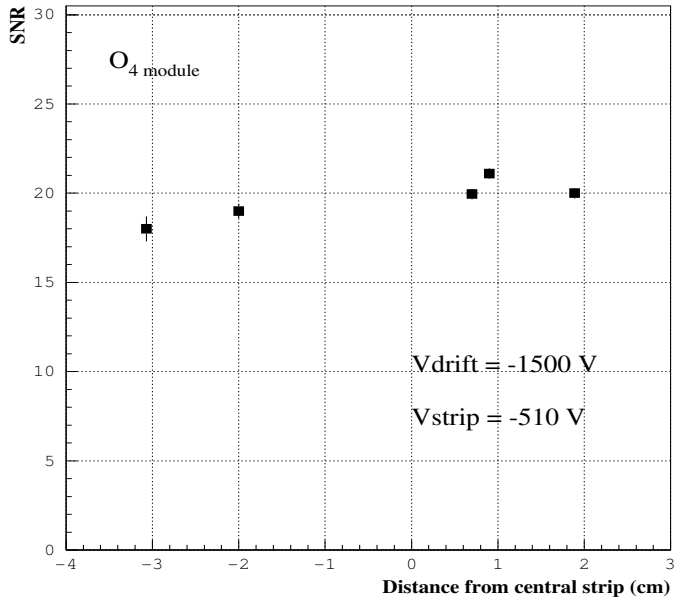

Figure 6.44: *Variations of the signal to noise ratio as a function of the distance from the central strip in the O_4 counter.*

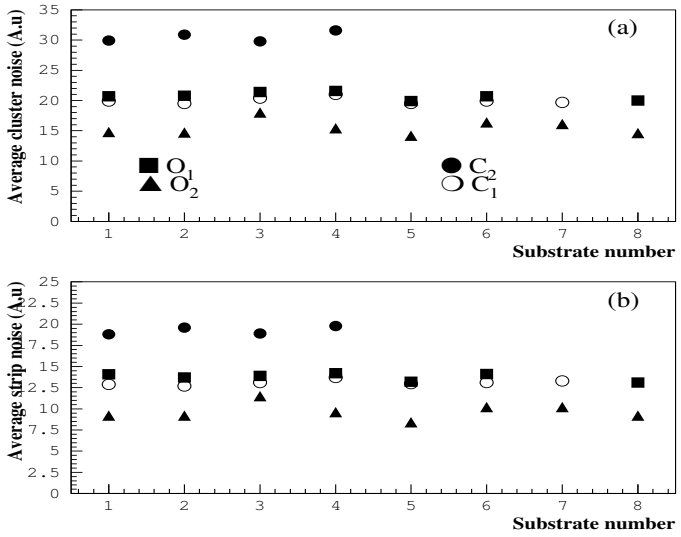

Figure 6.45: *Average cluster noise (a) and average strip noise (b) per counter for some MF1 modules.*

and the input of the PreMux128 channels; the six remaining counters of that module have an average cluster noise of 9.3 ADC counts whereas for substrates 3 and 7 it is 11.5 and 10 ADC counts respectively. However substrate 3 was partially broken. As shown in figure 6.43, the signal to noise ratio of counters 3 and 7 of module O_2 were not significantly different from the other values which is in agreement with previous tests [149]. Although the 400 Ω resistor brings an essential protection for the electronics, its effect on the signal amplitude has to be studied in details. Indeed the IReS group obtained a difference of 20 % , in the signal amplitude, between MSGC's with and without these resistors.

6.7.6 Spatial resolution

The poor accuracy of the telescope prediction (see section 6.6.3.2) prevented us from using only the telescope information to evaluate the spatial resolution of the MSGC's, expected to be of the order of 40 μm. Therefore the MSGC's themselves were also used; the information from the telescope was used to determine the coordinate along the strips in order to find the appropriate anode pitch as will be explained below.

After alignment of each concerned MSGC counter with respect to the telescope as described in section 6.6.3, the nearest cluster measured with a position S^i_{ck}, within $\pm$ 400 μm from the telescope prediction, is accepted. This can be used to estimate the azimuthal angle ϕ^i_{ck} in the local (u,v) frame of the MSGC (see figure 6.1):

$$tg\phi^i_{ck} = \frac{P_2 - P_1}{S} S^i_{ck} \tag{6.13}$$

where P_1, P_2 and S are , respectively, the smallest, the largest pitch and the central strip length of the counter.

As can be seen in figure 6.1, the v local coordinate can be obtained from

$$v^i_{ck} = (u + D)tg\phi^i_{ck}, \tag{6.14}$$

where D can be derived from:

$$D = \frac{P_1}{P_2 - P_1} S. \tag{6.15}$$

As u cannot be measured by a single sided MSGC, it is taken from the telescope prediction: u^i_{pk}. This leads to

$$v^i_{ck} = (u^i_{pk} + D)tg\phi^i_{ck}. \tag{6.16}$$

To study the spatial resolution in an MSGC of the kth module, we have used the measured coordinates of modules $(k-1)$ and $(k+1)$. The residual between the point measured in the kth counter and this extrapolated from the $(k-1)th$ and $(k+1)th$ counters can be written as follows:

$$R^i_{vk} = v^i_{ck} - \left(\frac{v^i_{c(k-1)} - v^i_{c(k+1)}}{z_{k-1} - z_{k+1}}(z_k - z_{k-1}) + v^i_{c(k-1)}\right) \tag{6.17}$$

where z_k is the position of the kth MSGC along the beam axis. The standard deviation of this distribution is given by:

$$\sigma_{R^i_{ck}} = \sqrt{\sigma^2_{track} + \sigma^2_k} \tag{6.18}$$

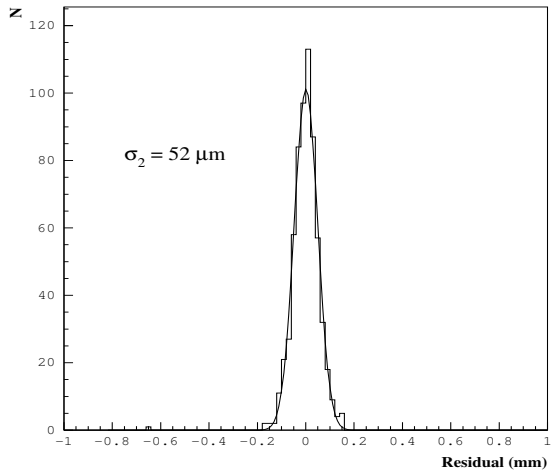

Figure 6.46: *Residual distribution of (6.17) obtained after combining the inter-MSGC modules tracking and the telescope prediction.*

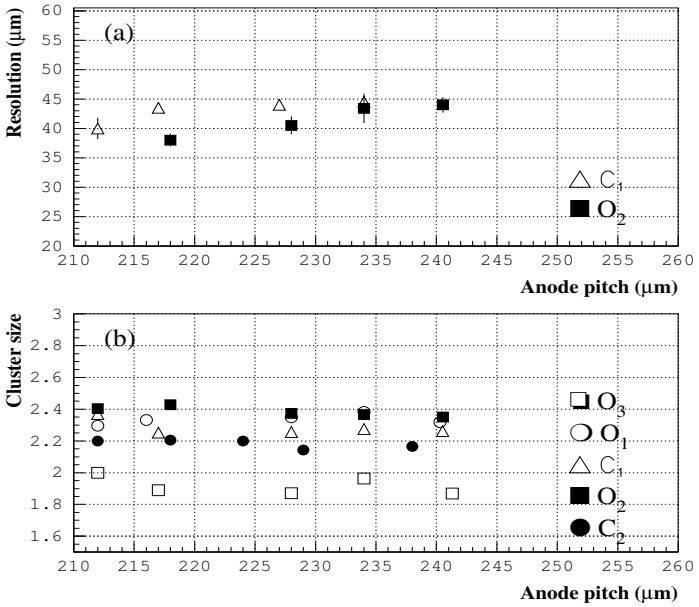

Figure 6.47: *Variation of the spatial resolution in μm versus the anode pitch for O_2 and C_1 modules(a) and variations of the measured cluster size as a function of the anode pitch for modules O_1, O_2, O_3, C_1 and C_2 (b).*

where σ_k is the resolution in the kth detector module and σ_{track} is the extrapolation error.

The distribution of the variable R^i_{vk} defined in (6.17) is shown for one counter of module O_2 in figure 6.46; MSGC's of module O_1 and C_1 were used to form the track. This distribution fits a Gaussian distribution with a mean compatible with zero and a standard deviation of 52 μm; the corresponding resolution was found to be 42 μm, assuming the same resolution for the three counters as they have been produced with the same mask. This results is in agreement with previous measurements taken with parallel strips in a Ne/DME 50/50 % [112, 110], and measurements with trapezoidal detectors [131].

In figure 6.47(a) the measured resolution versus the anode pitch is shown for modules O_2 and C_1. For O_2, the position accuracy varies from 38 μm at the lower pitch to 44 μm at the higher pitch. For a given gas mixture and track angular acceptance, the spatial resolution depends on two major parameters: the cluster size and the signal to noise ratio. The cluster size in strip number versus the anode pitch is shown in figure 6.47(b) for all outer ring modules. A constant cluster size is observed for all modules, in particular O_2. This was not expected. Indeed, converting these numbers into microns, the cluster size is increasing from 510 μm to 580 μm, going from 212 μm to 240 μm. As the electric drift field is the same, the diffusion is the same and the cluster size should not be affected by the substrate geometry. As the cluster size in strip number is constant along the strips, we believe that the 20 % variation of the signal to noise ratio along the strips observed in case of module O_2 is responsible for the variation of the spatial resolution with the anode pitch. For C_1, the gain is constant along the strips (see figure 6.40), three point seem to give a uniform resolution of the order of 44 μm and since the cluster size is 10 % higher at the point measured at the narrow side this results in a spatial resolution of 40 μm. The overlap of the two curves occurred at a pitch value where the signal over noise ratio of both modules are the nearest as shown in figure 6.40. Comparing figures 6.8 and 6.40 one realizes the importance of a uniform signal over noise ratio on the detector performances, in particular for the localization accuracy.

6.7.7 Alignment and edge studies

A good tracking performance requires not only counters with good spatial localization but also a good alignment between adjacent counters in a given module. Optical alignment was performed for the open design modules. To check, with real data, the relative alignment of two neighbouring substrates, the following procedure was followed for O_1 and O_2.

A given substrate of each module was aligned with respect to the telescope following the procedure described in section 6.6.3.

The histograms (a) and (c) of figure 6.48(6.49) show for the aligned counter of $O_1(O_2)$ the distribution of the difference between the particle impact point coordinate predicted by the telescope and the coordinate measured by the MSGC (see relation 6.5), for two different anode pitches. The histograms (b) and (d) of these figures show the distributions of the same quantity for the neighbouring substrate, estimated without changing the alignment parameters, assuming that the strips of both counters point to a common point and that the distance between the two outermost anodes was twice the nominal pitch. For all of these distributions, the difference on the horizontal axis is given in number of strips. A broadening of the distributions (b) and (d) is observed together with a shift of the average value. This shift amounts to 67 μm and 43 μm for O_1 and 0 and -39 μm for O_2. As an example, for O_1, the rotation angle ψ_2 as defined in equation (6.2) had to be increased by 90 $mrad$ to align the right counter, in addition to the shift of 43 μm in the direction orthogonal to the strips. Therefore, the optical alignment method used here is not precise enough and an additional alignment with particles is necessary.

For the closed design it is foreseen to use a special machine which provides the possibility of

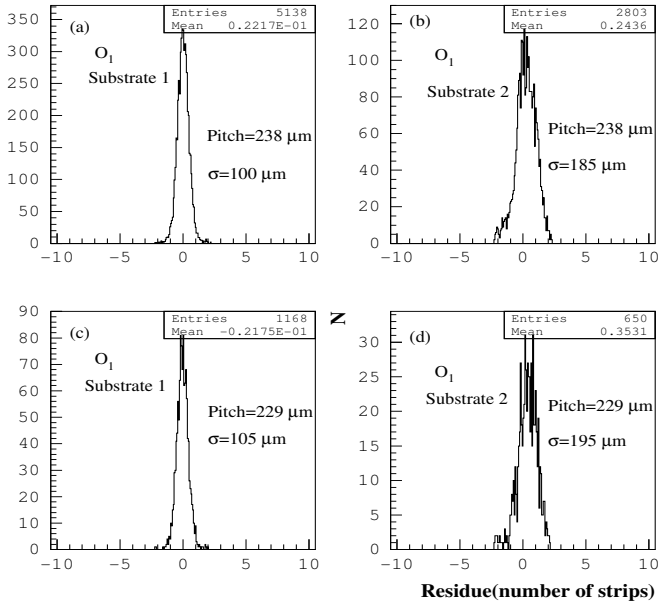

Figure 6.48: *Distribution of the difference between the impact point coordinate predicted with the telescope and the one measured by the MSGC of module O_1. The distributions to the left are for one counter aligned to the telescope, those to the right are for its neighbouring counter. The results are shown for two different anode pitches.*

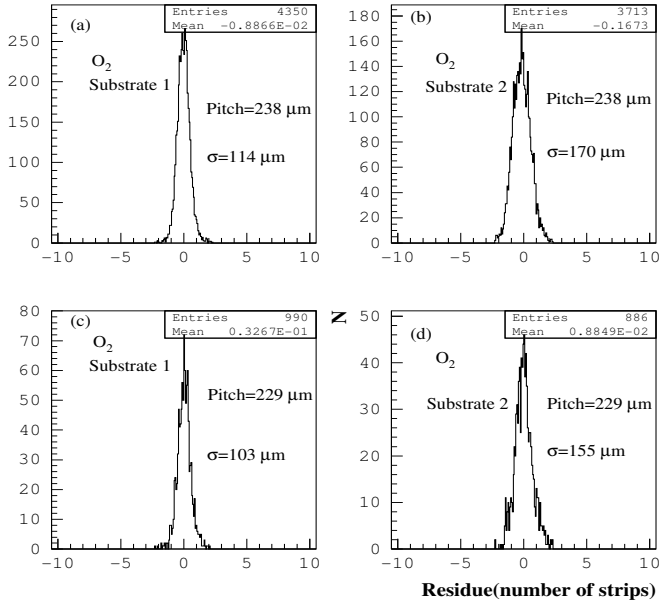

Figure 6.49: *Distribution of the difference between the impact point coordinate predicted with the telescope and the one measured by the MSGC of module O_2. The distributions to the left are for one counter aligned to the telescope, those to the right are for its neighbouring counter. The results are shown for two different anode pitches.*

controlling the substrate positions within a module with great precision [14, 96]. Unfortunately, the lack of statistics with particles hitting the edges of two neighbouring good substrates for these modules, prevented us to check their alignment procedure with data.

Following the CMS forward-backward tracker design with the substrates put side by side without overlap in the azimuthal angle, the performance of the substrate common edges has to be checked. Indeed in this region the electric field is modified and gain variations might occur. As mentioned in section 6.5, several accidents and mistakes occurred during the construction and assembly phases. This had a serious impact on the detector quality mainly in the region between two adjacent counters. As an example, due to the DME condensation problem encountered in module O_1, six out of the seven common edges were damaged. Among the 23 common edges in modules $O_1(7)$, $O_2(7)$, $C_1(6)$ and $C_2(3)$, 16 were damaged during the construction. During the test beam we found only three regions with no dead strips; the other ones were probably damaged by discharges as the erroneous mounting of the diodes bypassed the strips protective resistors.

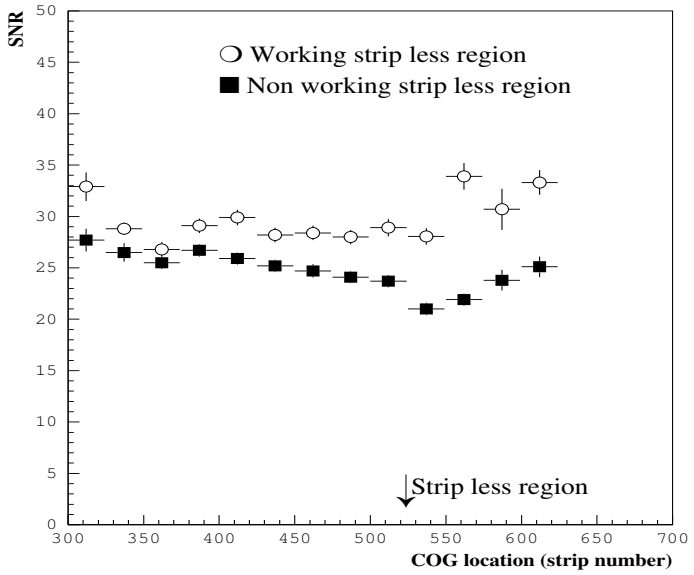

Figure 6.50: *Variations of the signal over noise ratio as a function of the particle position for module O_2. The square(round) marks are for two substrates presenting a large(very small) number of dead strips around their common edge.*

Figure 6.50 shows the signal over noise ratio versus the cluster position in strip number near two common edge regions of module O_2. One of these regions had a large number (more than 10 %) of dead strips resulting in a clear variation of the signal to noise ratio around the strip less region; the second one corresponds to a working strip less region with a few (less than 4 %) dead strips around leading to a uniform signal over noise ratio. It is expected to have gain variations of the order of 30 % on the few, one or two, strips surrounding the edge. It can not be seen in the figure as the histogram binning is of the order of 25 strips per bin.

6.7.8 Dead space studies

The dead space between two modules has to be as small as possible, and of the order of 1% (see section 4.4). This could be studied only for module C_1 containing two 4-fold modules placed side by side on the same support plate, using the same method as this used to check

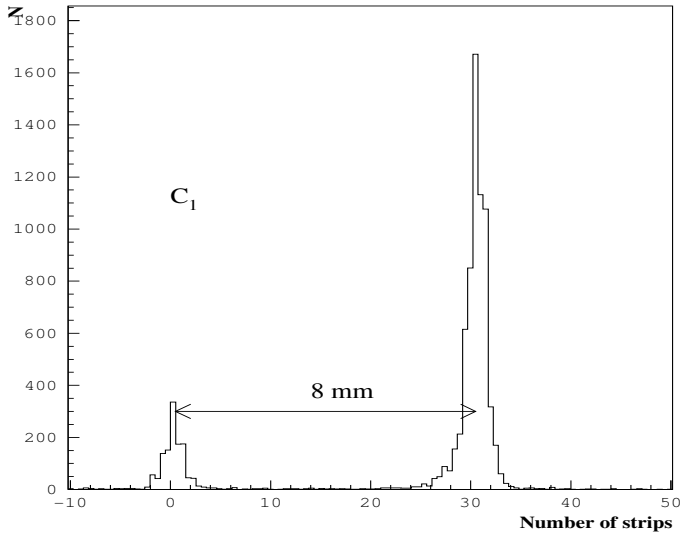

Figure 6.51: *Distribution of the difference between the impact point coordinate predicted with the telescope and the one measured by on of the two counters adjoining the region between the two 4-counters of module C_1.*

the substrate alignment in section 6.7.7. Figure 6.51 shows the distribution of the difference between the particle impact point coordinate predicted by the telescope and the coordinate measured by one of the counters adjoining the region between the two 4-fold module. Two peaks are clearly observed, the left one corresponding to particles hitting the counter aligned to the telescope. The two peaks are separated by 8 mm which corresponds to 1.7 % of dead space in the azimuthal angle ϕ. However it should be pointed out that for this milestone, the two C_1 half modules were not mounted with the foreseen procedure. It is hoped that for the final mounting, the dead space will be decreased to 6 mm to reach the 1.2 % dead space for outer ring modules [14].

6.8 Summary

The aim of this chapter was to study the MSGC forward tracker of CMS and the different designs proposed to build it as described in section 4.4. This study covered the main questions that had to be answered regarding: the stability of operation of several MSGC's in a common gas volume, the behaviour of wedge shaped counters, the effect of the varying anode pitch on the counter response, the detection efficiency in the strip less region, the amount of dead space between consecutive modules and the alignment of the substrates within modules. This has been done either in the cosmic rays hodoscope with two half substrates placed side by side or in a muon beam at CERN with six MSGC modules (MF1 milestone), with a total of 38 wedge shaped MSGC counters:

- we have proven the stability of operation of wedge shaped counters by studying their response during four months in a cosmic rays hodoscope for one of them and during two weeks for 38 of them in a low intensity muon beam. The counters were operated at their nominal working points leading to detection efficiencies of more than 97 %;

- we have studied, both experimentally and with simulation, the effect of the varying anode pitch in wedge shaped counters and demonstrated that it is possible to achieve a uniform response, provided care is taken to the strips geometry.

  In a first study, no attention was paid to adapt the strip geometry and the anode-cathode distance was kept constant. As a consequence, we observe a signal to noise ratio variation of up to 47 % along the 10 cm long strips, both in experimental data and in simulation. This could be attributed to electric field variations. Consequently, the efficiency plateau starts at a cathode strip voltage 20 V higher reducing its length by 30 %; the spatial resolution is also drastically affected along the strips, showing 50 % variation.

  In contrast, the 38 wedge substrates of the MF1 milestone have been built following the NIKHEF rule in which the anode-cathode distance and the cathode width vary with the anode pitch following an homothetic rule. In this case a constant signal to noise ratio, within 10 %, along the strips has been demonstrated for all modules but two. Since the substrates of these two modules were produced by a common producer, one can suspect the substrate quality production to be responsible of the 20 % variations observed. The beginning of the efficiency plateau is observed at the same cathode strip voltage than for MSGC's with parallel strips. The spatial resolution at different positions along the strips has been measured for all modules and it is of the order of 40 μm. For the two modules having 20 % variation in the signal to noise ratio, the measured spatial resolution varies between 38 μm and 44 μm; these values are still within the range of the CMS requirements.

  With the help of a simulation of the gain uniformity along the strips for several electrode geometries, we had a deeper insight in the limit of validity of the above rule. We have demonstrated that this rule leads to a uniform gain only over a limited range of anode pitches called uniformity plateau. The limits of this plateau depends on the anode width which leads to two constraint conditions:

  $$0.8a + 38\mu m \leq G = \frac{P}{8} + 20\mu m \leq 1.4a + 45\mu m$$

  where a, G and P are respectively the anode width, the anode-cathode distance and the anode pitch. The simulation shows that this new rule is not affected by electric drift field variations;

- not only the uniformity of the response along the strips has been proven, but also from one counter to another. A signal to noise ratio variation of less than 10 % was obtained from one counter to another, for counters with less than 4 % of dead strips. Comparing the noise of different counters has revealed that the presence of a 400 Ω protective resistor at the input of the preamplifier of some of them does not affect significantly the noise performances of the counters;

- a full detection efficiency of more than 97 % was reached in the region between two adjacent counters, containing no dead strips around. The presence of one dead strip in the neighbourhood of this region reduces this value to 96.5 %;

- we have studied the alignment procedure between adjacent substrates in the open design and found shifts up to 70 μm with respect to the nominal position as well as a rotation of up to 90 $mrad$. This alignment method has to be improved to reach the required precision of 10 μm on the position of substrates within modules. The lack of statistics prevented us to test the alignment procedure of the closed design counters with data;

- a dead space of 8 mm was observed between two contiguous closed design modules. This corresponds to 2 % of dead space in the azimuthal angle. It is hoped to reach 1.2 % of dead space when using the final mounting procedure of these modules onto disks.

Although this study has proven the feasibility of the forward tracker for both designs, the problems encountered during the assembly of the modules demonstrates the difficulty to built such a large system and the need for all participating institutions to gain experience with the final design. Since it was decided to adopt the closed design, as the construction requires less human intervention, new prototypes should be built by all the institutes, using the final CMS performance substrates equipped with the closest approximation to the final electronics. Indeed, it has been shown that the substrate quality affects the gain uniformity, in particular the coating, and the signal to noise ratio will be affected by the behaviour of the different electronics. For this pre-mass production we should measure the final working point, the efficiency plateau length, the signal to noise ratio and the alignment of the substrates within modules. The emphasis should be put on the quality of strips at the edge of the counters.

Chapter 7
Conclusions

This thesis is a contribution to the study and optimization of microstrip gas counters (MSGC's) for the CMS tracker, in particular for the endcap regions. The CMS experiment is one of the two general purpose experiments that will be installed at the Large Hadron Collider (LHC). It is designed as an attempt to elucidate the origin of particle masses, in particular by discovering the standard model Higgs boson, and to discover new physics beyond the standard model. To perform these studies the LHC will collide bunches of protons at a centre of mass energy of 14 TeV with a luminosity of 10^{34} Hz/cm^2. This results in a high interaction rate of 10^9 Hz. This harsh environment puts stringent constraints on the performances of the detectors: their granularity must be fine enough to cope with the high track density, they must sustain the high radiation levels and be able to measure the energy and momentum of high transverse momentum particles, up to a few TeV/c, with a high precision in this hostile environment.

More specifically, the MSGC tracker should provide the measurements of six points on average along the tracks of high momentum charged particles, with a detection efficiency of 98 % and an accuracy of 50 μm in $R\phi$. It is also requested to have a response time below 50 ns, 2 times the LHC bunch crossing interval.

Five Belgian groups of high energy physics participate to the design, the construction and the test of the MSGC endcap tracker of CMS. This region will be occupied by eleven disks on each side of the barrel tracker. The disks will be equipped with trapezoidal MSGC's. To build the endcap tracker, the Belgian groups have proposed to place several trapezoidal MSGC counters side by side at less than 100 μm distance, in a module with a single gas volume. This layout minimizes the dead space between counters and the amount of material inside the tracker.

To meet the above requirements on efficiency, spatial resolution and response time, the choice of the gas mixture filling the MSGC's is of great importance. In addition, it influences the short and long term stability of the counters. This is why our work started with a search for the best gas mixture for MSGC's at LHC. When we started the gas study, the gas mixtures considered at that time were: DME/CO_2 and Ar/DME. Ne/DME gas mixtures were found to lead to very high proportional gas gains, up to 2×10^4, but the detection efficiency in the 3 mm gas gap was still questioned, because of the low primary ionization of neon. The study of Ne/DME gas mixtures in a cosmic rays hodoscope in Brussels has revealed that the required 98 % efficiency is reached in these mixtures already at cathode strip voltages between -510 V and -540 V, a 100 V lower than for DME/CO_2. This is a big advantage since the energy released in case of a spark is reduced and consequently the risk of strip pattern damage. In addition, these mixtures present a long efficiency plateau, more than 70 V, compared to Ar/DME mixtures. Due to the high cost of neon, we tried to replace it by helium. We investigated also pure DME. However, He/DME mixtures present a small efficiency plateau length, only 50 V. On the contrary, pure DME leads to a 100 V plateau length but starting at a higher cathode strip voltage, about -550 V. The spatial resolution was then measured in Ne/DME mixtures and was found to be 35 μm for tracks perpendicular to the substrate. At this point Ne/DME mixtures looked as

the best choice. However, in such mixtures the primary ionization density is low and all the primary ionization produced would be needed, within 50 ns, to reach full efficiency, requiring therefore a high enough drift velocity. We have thus measured and calculated the drift velocity in these mixtures, and found that it does not exceed 55 μm/ns. In a 3 mm gas gap, this results in an electron drift time of 54 ns, that is slightly too much. To increase the electron speed, we have added amounts of CO_2 to these mixtures, and found that Ne/DME/CO_2 40/40/20 %, for instance, allows a drift velocity of 65 μm/ns at an electric field of 10 kV/cm. To reach the 98 % efficiency plateau in this triple gas mixture, the cathode strip voltage has to be increased by 20 V, with respect to that of Ne/DME 50/50 %. The increase of the drift velocity leads to an increase of the Lorentz angle from 15^0 in Ne/DME 50/50 % to 19^0. This would degrade the spatial resolution to 50 μm for high p_t particles, in the barrel region if the tilt angle of the counters is kept at 14^0. To avoid this degradation of the accuracy, it is recommended to increase the tilt angle to 19^0. The presence of CO_2 has then another advantage since the Lorentz angle can be kept constant, in case of a variation of the external magnetic field, by adjusting the drift velocity with a slight variation of the amount of CO_2.

The appearance of discharges at some critical applied voltage is a problem in all gaseous detectors with thin electrodes as MSGC's. In CMS, the counters will be exposed to a high flux of hadrons which may generate heavily ionizing particles (HIP's), by nuclear interactions in the counter material. The presence of HIP's increases the probability of discharges in the counter. To suppress these discharges in MSGC's or to limit the subsequent damages, the advanced passivation technique was proposed. This solution had to be proven in a high intensity beam of hadrons. We have thus carried out a test of several MSGC's, in collaboration with the MSGC group of Pisa, in a 3 GeV/c pion beam of an intensity up to 4 kHz/mm^2, with a duty cycle of 5 %. The counters were exposed to this beam during a period equivalent to 7.7 hours of continuous beam at a rate larger than the one expected at the LHC, at a radial distance of 100 cm from the beam pipe. The counters showed a uniform response during the whole test period, and no indication of charging up of the substrates has been noticed. Among the 2400 working strips, only one has been damaged during the test period. However there were some worries that such a good result could not be reproduced in a continuous high rate of HIP's. In addition, higher rates had to be tested as the MSGC tracker reaches a radius of 70 cm. To verify that, two tests took place, after the completion of this work. The first one at PSI, where the counters were exposed to a continuous high intensity hadron beam in which the integrated rate is equivalent to the one that would be accumulated during 170 hours at LHC, at the innermost layer of the MSGC tracker. The second test took place at the LLN neutron test facility: one counter was exposed to a neutron fluence equivalent to that of 3 years of LHC operation. All the counters tested showed extremely stable operation and no sign of strip loss has been reported.

The last part of this work was devoted to the study of some particular aspects of MSGC operation related to the design of the endcap tracker.

- The MSGC counters in this design have a trapezoidal shape, with a varying anode pitch which was never tried before. To ensure the uniformity of the gain along the strips, the MSGC group of NIKHEF proposed a rule in which both the cathode width and the anode-cathode distance vary with the anode pitch. This rule has been used to build six modules with a total of 38 wedge shaped counters. We have shown that a constant gain along the strips can be obtained. The beginning of the efficiency plateau is then at the same cathode strip voltage as for MSGC's with parallel strips. The spatial resolution is also constant and is measured to be 40 μm. However for two modules from a same producer there were gain variations of 20 % leading to variation of the spatial resolution

from 38 to 44 μm. This shows that not only attention must be paid to the mask used to pattern the electrodes but also to the production process of the substrates. With the help of a set of simulation programs, we have also studied the gain along the strips to verify the limit of the NIKHEF rule. We have thus demonstrated that the gain is uniform only over a limited range of anode pitches called the uniformity plateau. The limits of this plateau depend on the anode width which leads to two constraint conditions:

$$0.8a + 38\mu m \leq G = \frac{P}{8} + 20\mu m \leq 1.4a + 45\mu m$$

where a, G and P are respectively the anode width, the anode-cathode distance and the anode pitch. We have also shown that the uniformity of the response along the strips is not affected by varying the electric drift field.

- We have proven the stability of operation of wedge shaped counters by studying their response during four months in a cosmic rays hodoscope for one of them and during two weeks for the 38 counters in a low intensity muon beam. The counters were operated at their nominal working points leading to detection efficiencies of more than 97 %.

  The uniformity of the response from one counter to another was also demonstrated. A signal to noise ratio variation of less than 10 % was obtained from one counter to another for counters with less than 4 % dead strips.

- By placing MSGC's side by side in a common gas volume in the forward tracker design, the aim was to minimize the dead space in the azimuthal angle, the hope being to have no dead space between adjacent counters and a limited dead space between modules. Indeed, we have shown that 97 % efficiency is reached in the region between two counters, provided no dead strip is present in the neighbourhood. A dead space of 8 mm was observed between two contiguous modules. This corresponds to 2 % dead space in the azimuthal angle. It is hoped to reduce this dead space to 1.2 % when using the final mounting procedure.

With these studies, we have contributed to a research program which has lasted for several years, in order to study and optimize the MSGC counters for operation at LHC. Having in mind the above results, we conclude that the MSGC is an adequate counter which fulfils the requirements of the outermost CMS tracker. In particular, the distinctive features of the forward tracker design have been validated.

Bibliography

[1] The LHC study group, *The Large Hadron Collider, Conceptual Design*, CERN/AC/95-05, 1995.

[2] F. Abe et al., CDF Collaboration *Observation of Top quark production in $\bar{p}p$ collisions with the collider detector at Fermilab*, *Phys. Rev. Lett.* **74** (1995) 2626.

[3] S. Abachi et al., D0 Collaboration *Observation of the Top quark*, *Phys. Rev. Lett.* **74** (1995) 2632.

[4] F. Englert and R. Brout, *Phys. Rev. Lett.* **13** (1964) 321.

[5] P.W. Higgs, *Phys. Rev.* **145** (1966) 1156.

[6] A. Masiero, *CP violation for the pedestrians*, Lectures given at the 1993 European school on high energy physics, 1993, Zakopane, Poland.

[7] J. Ellis, *Beyond the standard model for hillwalkers*, Lectures given at the 1998 European school on high energy physics, 1998, St-Andrew, Scotland.

[8] M. Paulini, *Brief report from the Tevatron*, Symposium on Lepton-Photon interactions, Stanford, 1999.

[9] M. Dittmar, *Searching for the Higgs and other exotic objects, a "how to" guide from LEP to the LHC*, CMS CR 1999/009, 1999.

[10] CMS Collaboration, *Technical proposal*, CERN/LHCC 94−38, 1994.

[11] CMS Collaboration, *The Muon Project*, CERN/LHCC 97-32, 1997.

[12] CMS Collaboration, *The Electromagnetic Calorimeter Project*, CERN/LHCC 97-33, 1997.

[13] CMS Collaboration, *The Hadron Calorimeter Project*, CERN/LHCC 97-31, 1997.

[14] CMS collaboration, *The Tracker Project*, CERN/LHCC 98-6, 1998.

[15] W. Blum and L. Rolandi, *Particle Detection with Drift Chambers*, Accelerator Physics, Springer-Verlag, 1994.

[16] P. Rice-Evans, *Spark, Streamer, Proportional and drift chambers*, The Richelieu Press, London, 1974.

[17] W.R. Leo, *Techniques for Nuclear and Particle Physics Experiments*, Springer-Verlag, 1987.

[18] J.H. Cobb, W.W.M Allison and J.N. Bunch, *The ionisation loss of relativistic charged particles in thin gas samples and its use for particle identification; theoretical predictions*, Nucl. Instr. and Meth. A **133** (1976) 315.

[19] D.L Landau, *On the energy loss of fast particles by ionization*, *J. Phys. USSR* **8**(1944)201.

[20] O. Blunck and S. Leisang, *Zeit. Phys.* **128** (1950) 500.

[21] K.A. Ispirian, A.T. Margarian and A.M. Zverev, *A monte-carlo method for calculation of the distribution of ionization losses*, Nucl. Instr. and Meth. A **117** (1974) 125.

[22] Review of particle physics, *Eur. J. Phys.* **3** (1998) 1.

[23] D.H. Perkins, *Introduction to High Energy Physics*, Third edition, Addison-Wesley, 1987.

[24] F. Sauli, *Principles of operation of Multiwire Proportional and Drift Chambers*, CERN Yellow Report 77-09 (1977).

[25] J. Va'vra, *Gaseous wire detectors*, Lectures given at ICFA Instrumentation School, Guanajuato, Mexico, June 7-19, 1997.

[26] T. Lohse and W. Witzeling, *The Time Projection Chamber*, Adv. Series on Directions in High Energy Physics, Vol. 9, Editor F. Sauli, 1992.

[27] A. Peisert, F. Sauli, *Drift and diffusion of electrons in gases: a compilation*, CERN report 84-08 (1984).

[28] V. Palladino and B. Sadoulet, *Application of classical theory of electrons in gases to drift proportional chambers*, Nucl. Instr. and Meth. A **128** (1975) 323.

[29] K. Kumar et al., Aust. J. Phys. 33(1980)343.

[30] K.F. Ness and R.E. Robson, *Phys. Rev.* **A38** (1988) 1446..

[31] P.M. Morse, W.P. Allis and E.S. Lamar, *Phys. Rev.* **48** (1935) 412.

[32] S.F. Biagi, *Accurate solution of the Boltzmann transport equation*, Nucl. Instr. and Meth. A (273) 1988 533.

[33] S.F. Biagi, *A multiterm Boltzmann analysis of drift velocity, diffusion, gain and magnetic-field effects in Argon-Methane-Water-Vapour mixtures*, Nucl. Instr. and Meth. A **283** (1989) 716.

[34] M. Atac, *Wire chamber ageing and wire material*, IEEE Transactions on Nuclear Science, Vol. 34 (1987).

[35] J.A. Kadyk, *wire chamber aging*, Nucl. Instr. and Meth. A **300** (1991) 436.

[36] L.B. Loeb, *Basic Processes in Gaseous Electronics*, University of California Press, Berkely, CA, 1961.

[37] H. Raether, *Electron Avalanches and Breakdown in Gases*, Butterworth, London, 1964.

[38] M. Atac, A.V. Tollestrup and D. Potter, *Self-Quenching Streamers*, Nucl. Instr. and Meth. A **200** (1982) 345.

[39] G. Charpack et al., Nucl. Instr. and Meth. **62** (1968) .

[40] A.H. Walenta et al., Nucl. Instr. and Meth. **92** (1971) 373.

[41] A. Oed, Nucl. Instr. and Meth. A **263** (1988) 351.

[42] R. Bellazzini and M. A. Spezziga, *Electric Field, Avalanche Growth and Signal Development in Micro-Strip Gas Chambers and Micro-Gap Chambers.*, *Rivista Del Nuovo Cimento* **17** (12) 1994.

[43] T. Beckers et al., *Optimisation of MSGC design and operating conditions*, Nucl. Instr. and Meth. A **346** (1994) 95.

[44] F. Angelini et al., *Further progress in the development of microstrip gas counters*, Proc. LHC Workshop, Aachen 1990, Ed. by G. Jarlskog and D.Rein.

[45] R. Bouclier et al., *Performance of Gas MicroStrip Chambers on glass substrates with electron conductivity*, Nucl. Instr. and Meth. A **332** (1993) 100.

[46] R. Bouclier et al., *Ageing of MicroStrip Gas Chambers : Problems and Solutions*, CERN-PPE/96-33.

[47] A. Oed, *Properties of microstrip gas chambers and recent developments*, Proc. of the 7*th* International Wire Chamber Conference, Vienna, Austria, 1995.

[48] F. Angelini et al., *Results from the first use of MSGC's in a high energy physics experiment*, Nucl. Instr. and Meth. A **315** (1992) 21.

[49] M.K. Ballintijn et al., *Results from the MSGC tracker at SMC*, Nucl. Phys. **B** (Proc. Suppl.) **44**(1995)268.

[50] J. Blouw et al., *Operational experiences with the Large Microstrip gas Tracker of HERMES*, Proc. of the Int. Workshop on MSGC's, november-december 1995, Lyon, France.

[51] R. Bouclier et al., *High Rate operation of Micro-Strip Gas Chambers*, 1995, IEEE Nuclear Science Symposium and Medical Imaging Conference, San Francisco, 1995.

[52] B. Schmidt, *Microstrip gas chambers: Recent developments, radiation damage and long-term behaviour.*, Proc. of the 8*th* International Wire Chamber Conference, Vienna, Austria, February, 1998, Nucl. Instr. and Meth. A **419** (1998) 230.

[53] F. Sauli, *Development of MicroStrip Gas Chambers for radiation detection and tracking at high rates, final status report*, RD-28 status report, CERN/LHCC 96-18.

[54] R. Bouclier et al., *Some factors affecting the lifetime of Micro-Strip Gas Chambers operated at high rates in laboratory conditions*, Proc. Int. Workshop on MSGC's, Lyon, 1995. Eds. D. Contardo and F. Sauli.

[55] J.T.M. Baines et al., *Work at RAL on the ageing properties of gas microstrip detectors*, Proc. Int. Workshop on MSGC's, Lyon, 1995. Eds. D. Contardo and F. Sauli.

[56] R. Bouclier et al., *Development of microstrip gas chambers on thin plastic supports*, Nucl. Instr. and Meth. A **315** (1992) 521.

[57] Yu.N. Pestov and L.I. Shekhtman, *Influence of the bulk resistivity of glass with electronic conductivity on the performance of microstrip gas chamber*, Nucl. Instr. and Meth. A **338** (1994) 368.

[58] J. Bohm et al., *High rate operation and lifetime studies with micro-strip gas chambers*, Nucl. Instr. and Meth. A **360** (1995) 34.

[59] R. Bouclier at al., *Development of Micro-Strip Gas Chambers for high rate operation*, Nucl. Instr. and Meth. A **367** (1995) 168.

[60] S. Brons et al., *Use of ultra thin semiconductive layers as passivation in microstrip gas chambers*, Nucl. Instr. and Meth. A **342** (1994) 411.

[61] W.G. Gong, J.W. Harris and H. Wieman, *Microstrip gas chamber on thin-film Pestov glass and micro gap chamber*, Nucl. Instr. and Meth. A **360** (1995) 30.

[62] R. Bouclier et al., *High rate and long term operation of micro-strip gas chambers on Diamond coated glass*, Proc. Int. Workshop on MSGC's, Lyon, 1995. Eds. D. Contardo and F. Sauli.

[63] F. Angelini et al., *Operation Of MSGCs with gold strips built on surface treated thin glasses*, Proc. Int. Workshop on MSGC's, Lyon, 1995. Eds. D. Contardo and F. Sauli.

[64] W.G. Gong et al., *Tests of MSGC's with Pestov-glass coatings*, Proc. Int. Workshop on MSGC's, Lyon, 1995. Eds. D. Contardo and F. Sauli.

[65] M.R. Bishai et al., *Plastic MSGC's with two-sided readout*, Proc. Int. Workshop on MSGC's, Legnaro, 1994. Eds. G. Della Mea and F. Sauli.

[66] J. J. Florent et al., *The electrostatic field in microstrip chambers and its influence on detector performance.*, Nucl. Instr. and Meth. A **329** (1993) 125..

[67] J.E. Bateman et al., *The experimental characterization of gas microstrip detectors*, RAL-94-114(1994).

[68] F.D. Van den Berg at al., *Gas gain stability of MSGCs operating at high rates*, NIKHEF/ 97- 014, (1997).

[69] B. Boimska et al., *Noise in MSGC with resistive strips*, CMS TN/95-203.

[70] R. Bouclier et al., *On some factors affecting discharge conditions in micro-strip gas chambers*, Nucl. Instr. and Meth. A **365** (1995) 65.

[71] A.V. Zarubin, *Properties of wire chamber gases*, Nucl. Instr. and Meth. A **283** (1989) 409.

[72] A. Pansky et al., *Applications of gaseous electron counting detectors*, Nucl. Instr. and Meth. A **323** (1992) 294.

[73] R. Sachdeva, *Signal processing for MSGC's at CMS*, CMS TN/94-215.

[74] J. Va'vra, *Wire chamber gases*, Nucl. Instr. and Meth. A **323** (1992) 34.

[75] M. Geijsberts et al., *Tests of the performance of different gas mixtures in microstrip gas counters*, Nucl. Instr. and Meth. A **313** (1992) 377.

[76] R. Bouclier et al., *Results of wire chamber ageing tests with CH_4- and DME-based mixtures*, Nucl. Instr. and Meth. A **346** (1994) 114.

[77] F. Angelini et al., *A large area, high gain micro-gap counter*, Nucl. Instr. and Meth. A **362** (1995) 273.

[78] M. Raymond et al., *The APV6 Readout Chip for CMS Microstrip detectors*, CERN/LHCC/97-60.

[79] S. Gadomski et al., *The deconvolution method of fast pulse shaping at hadron colliders*, Nucl. Instr. and Meth. A **320** (1992) 217.

[80] F.G. Sciacca, *Readout of a Micro Strip Gas Chamber prototype with the APV66 Front-end chip*, CMS NOTE 1998/093, 1998.

[81] F.G. Sciacca, *Impact of fast shaping at the front-end on signals from Micro Strip Gas Chambers*, CMS NOTE 1997/105, 1997.

[82] P. Fonte et al., *Feedback and breakdown in parallel-plate chambers*, Nucl. Instr. and Meth. A **305** (1991) 91.

[83] A. Bressan et al., *High rate behaviour and discharge limits in micro-pattern detectors*, Nucl. Instr. and Meth. A **424** (1999) 321.

[84] V. Peskov et al., *Surface streamer breakdown mechanisms in microstrip gas counters*, Nucl. Instr. and Meth. A **392** (1997) 89.

[85] F. Sauli and A. Sharma, *Micro-Pattern Gaseous Detectors*, submitted to Ann. Rev. of Nucl. and Part. Sc.

[86] R. Bellazzini et al., *Technique for the characterization of discharges in micro-strip gas chambers*, INFN PI/AE 97/01, 1997.

[87] B. Schmidt, *MSGC development for HERA-B*, talk given at the 36th workshop of the INFN ELOISATRON PROJECT on new detectors, Erice, November 1997.

[88] F. Sauli, *Gas Detectors: Recent Developments and future perspectives*, Nucl. Instr. and Meth. A **419** (1998) 189.

[89] J.F. Clergeau et al., *Performance of a small gap chamber* Nucl. Instr. and Meth. A **401** (1997) 238.

[90] F. Sauli, Nucl. Instr. and Meth. A **386** (1997) 531.

[91] V. Chorowicz et al., *Behaviour of Small gap Chambers in a high intensity hadron beam*, Nucl. Instr. and Meth. A **419** (1998) 464.

[92] S. Kiourkos et al., *Comparison of experimental measurements and electrostatic simulations of keystone geometry microstrip gas chambers*, Nucl. Instr. and Meth. A **348** (1994) 351.

[93] O. Bouhali et al, *A possible approach for the construction of the CMS forward-backward tracker*, CMS NOTE 1997/081 (1997).

[94] S. Claes et al., *Material specification and evaluation of the mechanical support structure for the CMS forward tracker*, CMS/TN 95-087(1995).

[95] S. Claes et al., *Material specification and evaluation of the mechanical support structure for the CMS forward tracker*, CMS/TN 96-034(1996).

[96] S. Bachmann et al., *The Closed MSGC Design: Detectors and Mechanical Structure.*, I. and III. Physikalisches Institut, RWTH Aachen, 1997.

[97] M. Ageron et al., *Assembly of a closed module of 4 MSGC's for the CMS forward tracker*, CMS NOTE 1998/022 (1998).

[98] F. Stichelbaut, *La détection des muons dans l'expérience DELPHI et son rôle dans l'étude de l'interaction* $e^+e^- \rightarrow \mu^+\mu^-$, thèse de doctorat, Université Libre de Bruxelles, 1993.

[99] R. Horisberger and D. Pitzl, *A novel readout chip for silicon strip detectors with analogue pipeline and digitally controlled analog signal processing*, Nucl. Instr. and Meth. A **326** (1993) 92.

[100] The APC controller and STIN were designed by F. Hartjes, NIKHEF-H, according to specifications mentioned in [99].

[101] CERN EP-Electronics note 90-01.

[102] P. Vanlaer, *Contribution to the study of the central tracking system of the CMS detector, at the future proton collider LHC*, thèse de doctorat, Université Libre de Bruxelles, 1998.

[103] S. Cittolin et al., *MacUA1: Macintosh-based development system data acquisition, control and monitoring applications*, CERN UA1 Technical Note 90-01.

[104] W.T. Eadie, D. Drijard, F.E. James, M. Roos and B. Sadoulet, *Statistical methods in experimental physics*, Eds. North-Holland Publishing Company, Amsterdam, 1971.

[105] D. Bertrand, private communication, IIHE 1992.

[106] J. Buytaert et al., *The forward muon detector of the DELPHI experiment at LEP*, Nucl. Instr. and Meth. A **310** (1991) 596.

[107] N. de Groot et al., *The MSGC at SMC*, Proc. of the Int. Workshop on MSGC's, november-december 1995, Lyon, France.

[108] ATLAS MSGC, ATLAS Inetrnal Note, INDET-NO-076, December 1994.

[109] F.D. v.d. Berg et al., *Study of inclined particle tracks in micro strip gas counters*, Nucl. Instr. and Meth. A **349** (1994) 438.

[110] O. Bouhali et al., *Operation of microstrip gas counters with DME-based gas mixtures*, Nucl. Instr. and Meth. A **413** (1998) 105..

[111] B. Baiboussinov et al., *Performance of MSGC in high longitudinal magnetic field*, Proc. of the Int. Workshop on MSGC's, november-december 1995, Lyon, France.

[112] O. Bouhali et al., *Experimental study of the spatial resolution with MSGC filled with a Ne/DME 50/50 % gas mixture*, IIHE internal note, IIHE 96/001.

[113] O. Bouhali et al., *Operation of microstrip gas counters with Ne/DME gas mixtures*, Nucl. Instr. and Meth. A **378** (1996) 432.

[114] R. Veenhof, *GARFIELD, a drift chamber simulation program, http://consult.cern.ch/writeup/garfield*, Version 6.27, CERN.

[115] MAXWELL 2D field simulator, Ansoft corporation, 1994.

[116] I. Smirnov, *HEED, program to compute energy loss of particles in gases*, CERN.

[117] S. Biagi, *MAGBOLTZ, program to compute transport parameters in gases*, CERN.

[118] R. Bouclier et al., *Optimization of design and beam test of microstrip gas chambers*, Nucl. Instr. and Meth. A **367** (1995) 163.

[119] P. Pralavorio, *Violation de CP dans le système B^0-$\overline{B^0}$ avec le détecteur CMS à LHC et étude des chambres gazeuses à micropistes*, thèse de Doctorat, CNRS-IN2P3 et Université Louis Pasteur, Strasbourg, France, 1997.

[120] F. Angelini et al., *Behaviour of microstrip gas chambers in strong magnetic field*, Nucl. Instr. and Meth. A **343** (1994) 441.

[121] O. Adriani et al., *Performance of a prototype of the CMS central detector*, Nucl. Instr. and Meth. A **367** (1995) 189.

[122] M. Raymond, L. Jones, RD20, Preshape32 User Manual.

[123] V. Cindro et al., *Measurement of spatial resolution and drift velocities in a drift chamber filled with a helium-DME mixture*, Nucl. Instr. and Meth. A **309** (1991) 421.

[124] F. Villa, *DIMETHYLETHER: A low velocity, low diffusion drift chamber gas*, Nucl. Instr. and Meth. A **217** (1983) 273.

[125] LL Jones, PreMux128 Specification, Version 2.3, January 1995.

[126] S.P. Denisov et al., *Absorption cross section for pions, kaons, protons and antiprotons on complex nuclei in the 6 to 60 GeV/c momentum range*, *Nucl. Phys.* **B61** (1973) 62.

[127] M. Hutinen, *factors to scale highly ionizing particle rates in MSGC irradiation tests to the LHC radiation environment*, CMS NOTE 1997/073, 1997.

[128] W. Beaumont et al., *MAGC test with fast neutrons*, CMS NOTE 1998/014, 1998.

[129] CN/ADS Group and J.Zoll/ECP, *Zebra user's guide, Program Library Q121*, CERN 1993.

[130] CN/ADS Group, *PAW user's guide, Program Library Q100*, CERN 1993.

[131] S. Bachmann et al., *Spatial resolution of a wedge shaped MSGC module*, CMS NOTE 1997/077 (1997).

[132] O. Bouhali et al., *Operation of MSGCs with Ne/DME gas mixtures and study of edge effects with side to side MSGCs*, Int. Workshop on MSGC's, Lyon, December 1995.

[133] E. Albert et al., *Performance of a prototype of the microstrip gas chambers for the CMS experiment at LHC*, Nucl. Instr. and Meth. A **409** (1998) 70.

[134] SRON, Space Research Organisation, Utrecht, the Netherlands.

[135] NPP VOSTOK, Novosibirsk, Russian federation.

[136] OPTIMASK, 12 av. Ferdinand-de-Lesseps, 91420 Morangis, France.

[137] Baumer IMT Industrielle Messetechnik AG, Im Langacher, CH-8606 Greifensee, Switzerland.

[138] G. Clauss, W. Dulinski and A. Lounis, *Strip Detectors Read-out System user's guide* CRN 96-33.

[139] B. Baiboussinov et al., *Performance of MSGC in high longitudinal magnetic field*, CMS TN/95-201 (1995).

[140] M. Kräber et al., *Test results of a MSGC detector module for the CMS forward MSGC-Tracker*, CMS NOTE 1998/037 (1998).

[141] O. Bouhali et al., *CMS Forward-Backward MSGC milestone*, CMS NOTE 1998/025 (1998).

[142] http://nicewww.cern.ch/sl/eagroup/beams.html.

[143] L. Celano et al., *A high resolution beam telescope built with double sided silicon detectors*, Nucl. Instr. and Meth. A **381** (1996) 49.

[144] G. Batignani et al., *Development and performance of double sided silicon detectors* , Nucl. Instr. and Meth. A **310** (1991) 160.

[145] W. Fallot-Burghardt et al.,*Radiation effects on the Viking-2 preamplifier-readout chip*, Nucl. Instr. and Meth. A **340** (1994) 572.

[146] F. Drouhin et al, *A Unix SVR4−OS9 Distributed Data Acquisition for High Energy Physics*, IEEE Transactions on Nuclear Science, Vol. 45 (1998).

[147] B. Schwaller et al., *The trigger system of the CMS barrel and forward milestones*, CMS NOTE 1998/029 (1998).

[148] B. O. Baibusinov, *The Slow Control Modules specification*, Budker Institute, Novosibirsk, Russian Federation.

[149] The forward-backward MSGC milestone status report. Belgium - France - Germany - Russia. IReS internal note, 23 r. du Loess, BP28 - 67037 Strasbourg Cedex 2.

[150] O. Adriani et al., *Beam Test Results for single- and Double-Sided Silicon Detector Prototypes of the CMS Central Detector*, CMS NOTE 1997/006 (1997).

[151] S. Bachmann et al., *Beam test performance of a closed microstrip gas chamber for the CMS forward tracker*, CMS NOTE 1997/063 (1997).

[152] S. Keller et al., *Sparks in MSGC*, Proc. of the 8*th* International Wire Chamber Conference, Vienna, Austria, February, 1998, Nucl. Instr. and Meth. A **419** (1998) 382.

[153] M. Pentia et al., *A fast procedure for geometric parameter determination of a silicon vertex detector*, Nucl. Instr. and Meth. A **369** (1996) 101.

[154] G. Lutz, *Optimum track fitting in the presence of multiple scattering*, Nucl. Instr. and Meth. A **273** (1988) 349.

Appendix A
Pseudorapidity

The angular distribution of particles produced in hadron interactions is often discussed in the terms of the pseudorapidity η, defined as:

$$\eta = \frac{1}{2}\ln(\frac{p+p_z}{p-p_z}) = -\ln\tan\frac{\theta}{2} \tag{A.1}$$

where θ is the angle of emission of the particle with respect to the beam axis (z axis), and p_z=$pcos\theta$ is the z-component of the particle momentum. It has been demonstrated that the distribution of the number of particles $dN/d\eta$ is roughly constant with the pseudorapidity.

Appendix B
Straight line reconstruction

A standard problem in high energy physics experiments is the determination of the track parameters and their errors from measurements along the path of the particle. In the absence of magnetic field, the particle path is a straight line; the Coulomb multiple scattering is neglected.

Consider N+1 detectors at positions z_i (i=0,...,N) where the coordinate y_i of a given track are measured. The determination of the track parameters consists of a least-square fit to the straight line:

$$y = az + b \tag{B.1}$$

This is obtained by minimizing the quantity

$$\chi^2 = \sum \frac{(y_i - az_i - b)^2}{\sigma_i^2} \tag{B.2}$$

where σ_i is the measurement error on the ith detector.

The two conditions $\frac{\partial \chi^2}{\partial a} = 0$ and $\frac{\partial \chi^2}{\partial b} = 0$ lead to the following equations:

$$\begin{aligned} bS_1 + aS_z &= S_y \\ aS_{zz} + bS_z &= S_{zy} \end{aligned} \tag{B.3}$$

where $S_1 = \sum 1/\sigma_2$, $S_z = \sum z_i/\sigma_i^2$, $S_y = \sum y_i/\sigma_2$, $S_{zy} = \sum z_i y_i/\sigma_2$ and $S_{zz} = \sum z_i^2/\sigma_2$.

Solving the two linear equations gives the track parameters a and b:

$$\begin{aligned} a &= (S_1 S_{zz} - S_z S_y)/D \\ b &= (S_y S_{zz} - S_z S_{zy})/D \end{aligned} \tag{B.4}$$

with $D = S_1 S_{zz} - S_z^2$

The covariance matrix of the two parameters is then:

$$\begin{pmatrix} \sigma_a^2 & cov(ab) \\ cov(ab) & \sigma_b^2 \end{pmatrix} = \begin{pmatrix} S_1 & -S_z \\ -S_z & S_{zz} \end{pmatrix} 1/D \tag{B.5}$$

One of the purposes of tracking in experiments is to extrapolate the track at a certain point (vertex detector for example) placed at position z_0. In our simplest case, the error σ_{ext} due to this extrapolation is given by:

$$\sigma_{ext}^2 = \sigma_a^2 z_0^2 + a^2 \sigma_{z_0}^2 + \sigma_b^2 + 2 z_0 cov(ab) \tag{B.6}$$

where σ_{z_0} is the error on position z_0.

A complete procedure for linear fit taking into account the Coulomb multiple scattering can be found in references [153, 154].

Appendix C
List of colour figures

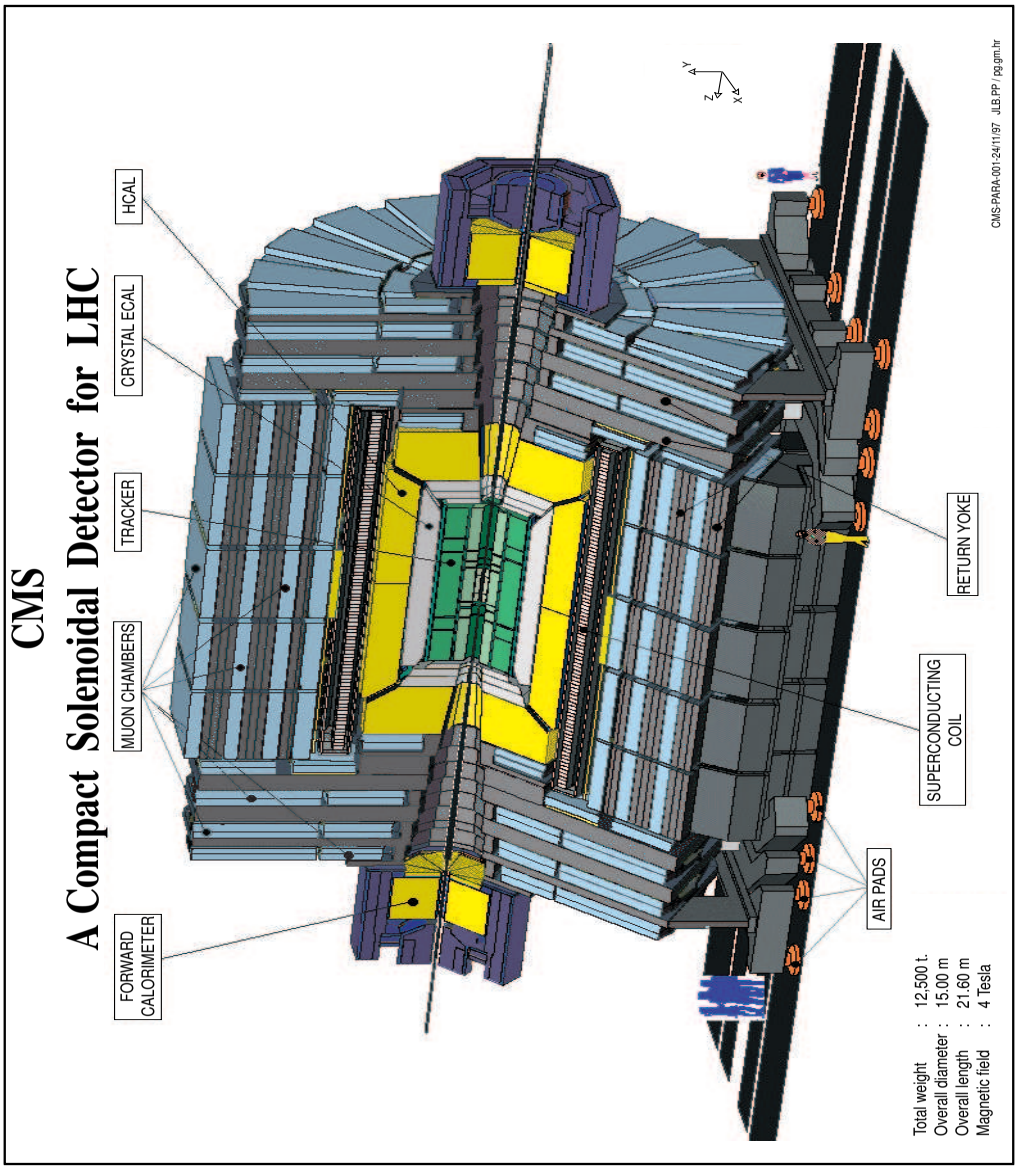

Figure C.1: *Three dimensional view of the CMS detector.*

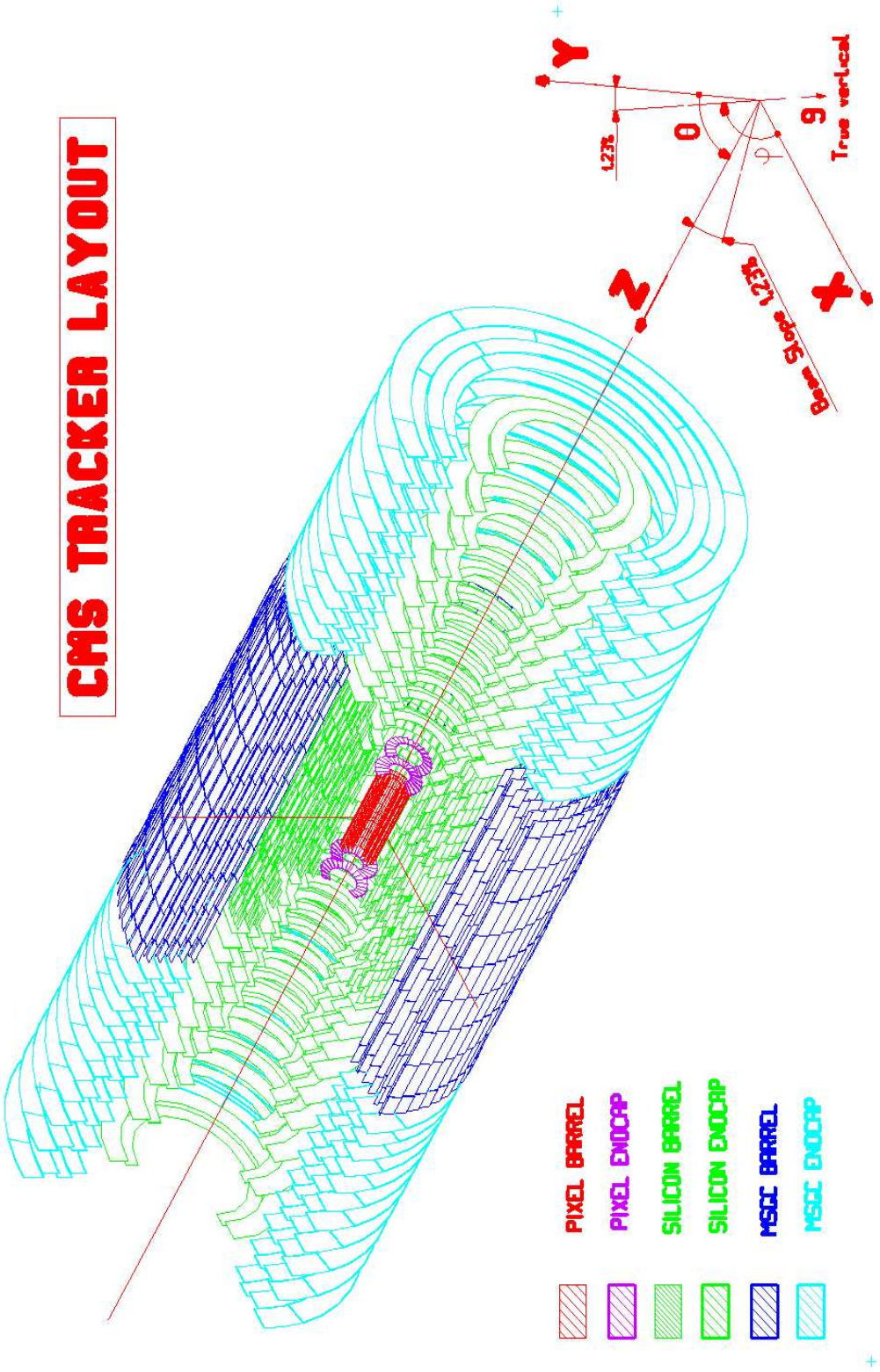

Figure C.2: *Three dimensional view of the CMS central tracker detector.*

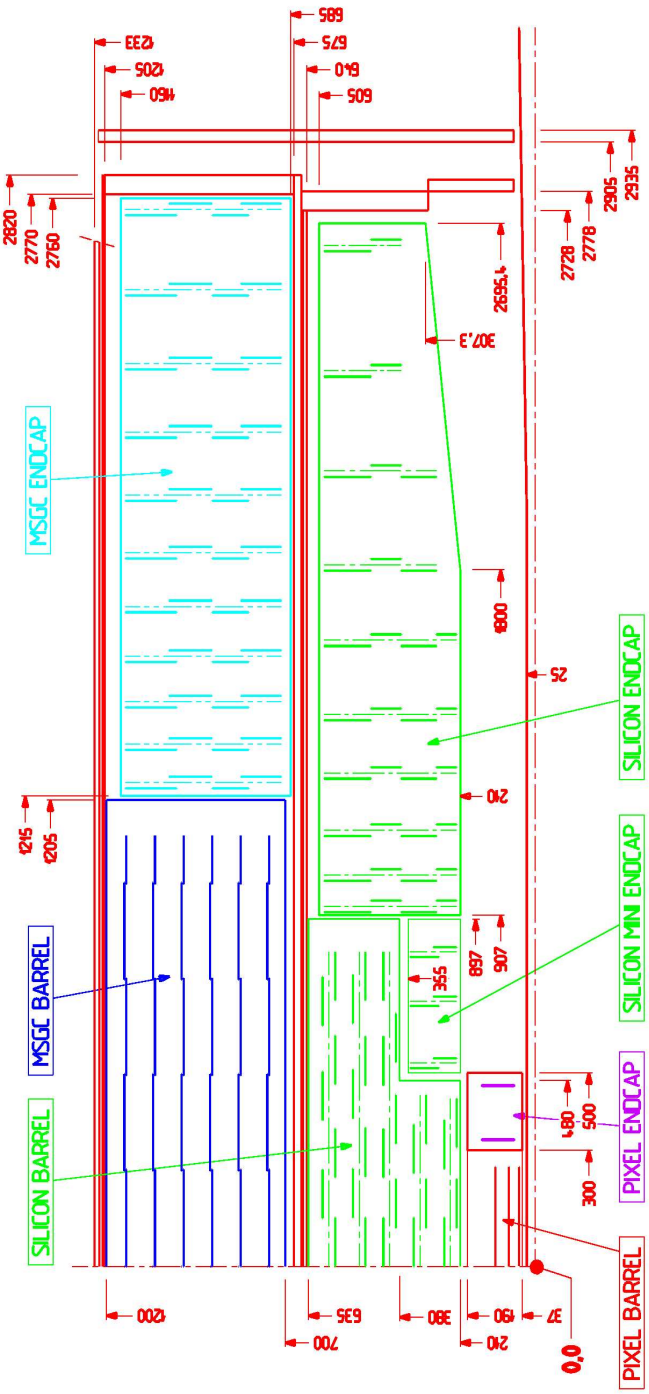

Figure C.3: *View of the CMS central tracker detector.*